Sensing harmful ions in water by using water-gated thin-film transistor sensors

By:

Zahrah Jobran Alqahtani

A thesis submitted in partial fulfilment of the requirements for the degree of Doctor of Philosophy in Physics.

Faculty of Science

Department of Physics and Astronomy

The University of Sheffield

December 2021

I dedicate this thesis to my great parents, my dad Jobran and my mum Mohrah; my lovely husband Saad; beloved sons Ali and Yasir; and my brothers and sisters.

Acknowledgements

Above all, I would like to express my gratitude to **Allah**, who guides me, inspires me and gives me the strength to complete my PhD journey.

My deepest and special thanks to my previous supervisor *Dr. Martin Grell* for his support, patience, motivation, massive knowledge and professional supervision during the first two years of my PhD study. My sincere appreciation and grateful to my current supervisor *Dr. Alastair Buckley* for his unlimited support, patience, encouragement and great advice on my thesis writing. I would like to thank my second supervisor *Prof. Richard Jones.* Special thanks to *Dr. Thomas Robshaw* from the Department of Chemical & Biological Engineering at Sheffield University and his supervisors *Dr. Robert Dawson* and *Dr. Mark D. Ogden* for their contribution and helpful discussions regarding activated Puromet^{TM} MTS9501 resin.

I would like to thank my lab's members, Dr. Abraham Kirwa, Dr. Abbad Al Baroot, Dr. Alhulw Alshammari and Dr. Nawal Alghamdi, for their support, discussion, ideas and help during our work. Also, many thanks for other PhD students in the Department of Chemistry, Saif Althagafi and Abdullah Surry, for their help and support.

I would like to pay my special regards to my family: my parent, husband, sons, brothers and sisters, for their support, love and help. I acknowledge the special support and great love given to me by my little sister and close friend, Bashaier.

My special gratitude to *Alan Lewis* for his invaluable advice, support, and great motivation. Many thanks to all my friends in Saudi Arabia and the UK.

Special thanks to the Saudi Cultural Attaché in London and Taif University in Saudi Arabia for the scholarship.

Publications and conferences

Publications

- N. Alghamdi, **Z. Alqahtani**, and M. Grell, "Sub-nanomolar detection of cesium with water-gated transistor," *J. Appl. Phys.*, vol. 126, no. 6, 2019, doi: 10.1063/1.5108730. **(Chapter 6).**

Formal analysis, Nawal Alghamdi, Zahrah Alqahtani and Martin Grell; **Investigation**, Nawal Alghamdi and Zahrah Alqahtani; **Methodology**, Nawal Alghamdi and Zahrah Alqahtani; **Resources**, Nawal Alghamdi; **Supervision**, Martin Grell; **Writing – original draft**, Nawal Alghamdi, Zahrah Alqahtani and Martin Grell; **Writing – review & editing**, Martin Grell.

- **Z. Alqahtani**, N. Alghamdi, and M. Grell, "Monitoring the lead-and-copper rule with a water-gated field effect transistor," *J. Water Health*, vol. 18, no. 2, pp. 159–171, 2020, doi: 10.2166/wh.2020.186. **(Chapter 7)**

Formal analysis, Zahrah Alqahtani, Nawal Alghamdi and Martin Grell; **Investigation**, Zahrah Alqahtani and Nawal Alghamdi; **Methodology**, Zahrah Alqahtani and Nawal Alghamdi; **Resources**, Zahrah Alqahtani; **Supervision**, Martin Grell; **Writing – original draft**, Zahrah Alqahtani, Nawal Alghamdi and Martin Grell; **Writing – review & editing**, Martin Grell.

- **Z. Alqahtani**, N. Alghamdi, T. Robshaw, R. Dawson, D. Ogden, A. Buckely and M. Grell "Water-gated transistor using ion exchange resin for potentiometric fluoride sensing," *Micromachines*, vol. 11, no. 10, 2020, doi: 10.3390/mi11100923. **(Chapter 8)**

Formal analysis, Zahrah Alqahtani, Thomas Robshaw and Martin Grell; **Investigation**, Zahrah Alqahtani; **Methodology**, Zahrah Alqahtani and Nawal Alghamdi; **Resources**, Zahrah Alqahtani, Thomas Robshaw and Nawal Alghamdi; **Supervision**, Robert Dawson, Mark Ogden, Alastair Buckely and Martin Grell; **Writing – original draft**, Zahrah Alqahtani and Martin Grell; **Writing – review & editing**, Martin Grell.

Poster and oral presentation in the University of Sheffield

- N. Alghamdi, Z. Alqahtani, and M. Grell, "Sub-nanomolar detection of cesium with water-gated transistor," **Poster presentation** in the Octagon-University of Sheffield, Faculty of Science Graduate School Poster Day, United Kingdom (20th March 2019).
- Z. Alqahtani, N. Alghamdi, and M. Grell, "Monitoring the lead-and-copper rule with a water-gated field effect transistor," **(online oral presentation)**, PhD Presentations-Departmental Research Day, Sheffield, United Kingdom, 20th May 2020.

Conferences

- Z. Alqahtani, N. Alghamdi, and M. Grell, “Monitoring the lead-and-copper rule with a water-gated field effect transistor,” **Poster presentation** in the “Sensors and Networks for Environmental Monitoring” Conference, 26 June 2019 at The Royal Society of Chemistry, Burlington House, London.

- Z. Alqahtani, N. Alghamdi, T. Robshaw, R. Dawson, D. Ogden, A. Buckely and M. Grell “Water-gated transistor using ion exchange resin for potentiometric fluoride sensing,” **Online poster presentation** in the 4th International online Conference on Applied Surface Science, 29-30 June 2021**.**

Abstract

This thesis demonstrates the development of a worthy approach to detect harmful waterborne analytes in significantly low concentrations in water by using water-gated thin-film transistors (WGTFTs) as potentiometric ion sensors. The successful gating of thin-film transistor with water to be the gate medium in 2010 paved the way for a new sensor technology, WGTFTs, to detect waterborne analytes in water gate media. WGTFT sensors have been applied to detect waterborne analytes (e.g. K^+, Na^+ and Ca^{2+}) with the help of organic macrocyclic ionophores (sensitisers) incorporated within the membrane in WGTFT's architecture. The response characteristics of such WGTFT sensors underwent the Nikolsky-Eisenman (modified Nernstian) law, with a limit-of-detection (LoD) in the range of 100 nM – 1 µM. This limit is insufficient to monitor drinking water against harmful or toxic ions. Accordingly, ion-exchange sorbents such as zeolites and resin were exploited in this work to sensitise the WGTFTs. These sorbents were embedded within a PVC membrane as a sensitiser and located in the transistor's gate medium, which separated the sample solution (containing an analyte ion) and a reference solution (free of analyte ion) in the composition of WGTFT sensors.

Radioactive- ^{137}Cs is rare in nature but finds its way into water supplies and then into humans and animals due to nuclear accidents. The sensitisation of the WGTFT sensor with Cs^+-selective mordenite zeolite as an ion-exchange ionophore enabled the detection of Cs^+ in very low concentrations. The response of such Cs^+- WGTFT sensor followed the Langmuir adsorption isotherm with a high stability constant and an exceedingly low LoD (33 pM). Such response characteristic enabled to determine very low LoD. The LoD of a Cs^+- WGTFT sensor is much lower than the potability limit of Cs^+ in drinking water (7.5 nM), which has not been obtained by organic macrocyclic sensitisers.

Pb^{2+} and Cu^{2+} are common drinking water pollutants deposited in water resulting from the use of these metals in manufacturing water pipes. To detect these cations in low concentrations, clinoptilolite zeolite was used to sensitised the WGTFT in a similar manner used in previous Cs^+- WGTFT sensors. The threshold shifted in response to increasing Pb^{2+} or Cu^{2+} concentrations following the Langmuir-Freundlich characteristic. Hence, the LoDs were much lower than the action levels of the lead-and-copper rule recommended by the Environmental Protection Agency for drinking water. Such WGTFT sensors achieved respective Pb^{2+} and Cu^{2+} LoDs of 0.9 nM and 14 nM against 72 nM and 20.5 µM as action levels with high selectivity for these metal cations, even with the presence of other interfering cations in the

water sample. Therefore, these features qualify clinoptilolite-sensitised WGTFTs for the monitoring of the lead-and-copper rule.

WGTFTs sensitised with another class of ion-exchange sorbents, La- loading of Purolite™ MTS9501 resin, demonstrated excellent response to fluoride (F^-) anion in a low dynamic range, following the Langmuir-Freundlich adsorption isotherm. This process enabled picomolar LoD and extremely low $c_{1/2}$ concentration. A successful routine was suggested to restrict the interferant from co-solutes. Although, the LoD of F^- was much below practical requirements, this work provides a template for further studies using resins as sensitisers in applications where an extremely low LoD is crucial.

Thesis structure

This thesis is divided into four parts that are subdivided into ten individual chapters, as listed below:

Part 1: Introduction and literature review

Chapter 1 presents the structure and properties of water molecules as a vital part of our lives. This chapter also discusses the problem of water pollution and provides an overview of sensor technologies, including water-gated thin-film transistors (WGTFTs) as potentiometric sensors.

Chapter 2 introduces the theory of thin-film transistors (TFTs), including their structure and operation. Gating TFTs with electrolytes, such as water, and their features in establishing electric double layers are also discussed. In addition, potentiometric ion sensor principles and examples, including WGTFT, are outlined.

Chapter 3 provides the principles of semiconductors in general and solution-processed SnO_2 implemented as the TFT's channel. A quantitative description of TFT, ion-selective membrane, common ionophores and the response characteristics of sensing ions are also discussed.

Part 2: Experimentation

Chapter 4 reports the process of fabricating SnO_2 TFTs and designing WGTFT sensors.

Chapter 5 demonstrates the electrical characteristic of SnO_2 TFT across water as a gate medium; SnO_2 WGTFT.

Part 3: Results and discussion

Chapter 6 displays the results of an initial attempt to incorporate inorganic mordenite zeolite in WGTFTs as a sensitiser to detect Cs^+ cation.

Chapter 7 demonstrates the results of sensing Pb^{2+} and Cu^{2+} using WGTFTs sensitised with clinoptilolite zeolite.

Chapter 8 presents the performance of WGTFT sensors in detecting fluoride anion in water by merging organic resin as a sensitiser.

Part 4: Conclusion

Chapter 9 outlines the overall conclusions of this work and future works.

Table of Contents

List of Figures

List of Tables

Chapter 1 : Introduction

1.1 Fundamentals of water

Water is one of the essential constituents for life on earth. It covers approximately 70% of this planet surface and constitutes between 55% - 78% of the human body, thus playing numerous important roles in this world [1]. Water is a fluid, inorganic compound that is nearly colourless, with a small hint of blue. It is also odourless and tasteless. A water molecule consists of one oxygen (O) atom covalently bonded with two hydrogen atoms (H) in the chemical formula H_2O. The bonding of the hydrogen atoms with the oxygen atom forms a triangle-like shape, as illustrated in Figure 1-1, with an angle of 105^o and an O-H distance of 0.096 nm [2]. Due to the oxygen atom's greater electronegativity compared to hydrogen (i.e., that electrons are more strongly attracted by oxygen than hydrogen), water molecules carry a partially negative charge (δ-) on the oxygen side and partially positive charge (δ+) on the hydrogen side. The existence of different charges on both sides of the water molecule induces a dipole moment in the water molecule based on the polarity of the O-H bonds, thus resulting in a polar water molecule [2]. The water molecule's polarity results in intermolecular forces of attraction between the water molecules and intermolecular forces of attraction between the water molecules and other polar molecules with hydrogen bonds. Thus, one molecule's relatively negative side attracts the relatively positive side of another molecule. These forces of attraction explain the ability of water to act as a solvent for many substances. The strong intermolecular hydrogen bonds in water are also responsible for several other water properties, including its high boiling point and surface tension [2][3].

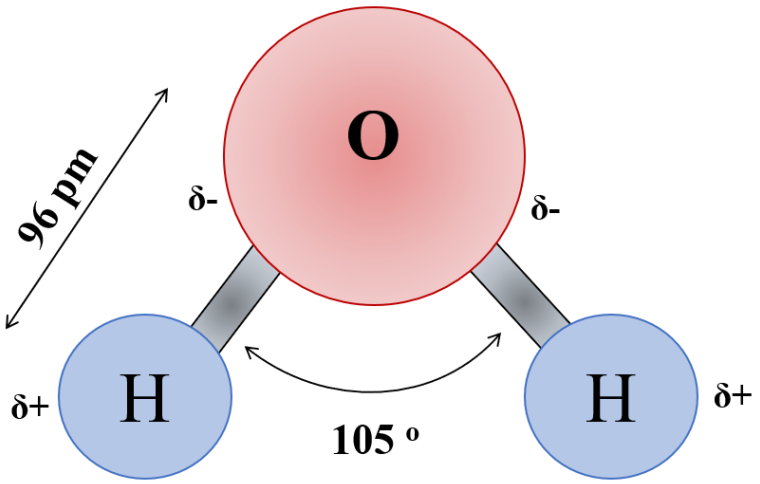

Figure 1-1: *Diagram illustrates the water molecule structure and properties*

Water is known as the universal solvent, and this is attributed to its polarity and its ability to form hydrogen bonds [2][4]. It is an excellent solvent for use with a range of ionic and polar substances. The addition of an ionic solute to water results in the solutes' dissociation into negatively charged ions 'anions' and positively charged ions 'cations.' In such dissociation, the water molecules form a hydration shell (spherical shell of water molecules) around each ion. A single cation is surrounded by several water molecules with their oxygen atoms directed towards this central cation (i.e., the negative ends of the water molecules). In contrast, water molecules surrounding a negative anion will have their hydrogen atoms directed towards this central anion (i.e., the positive ends of the water molecules). Consequently, such molecular organisation maintains ions in a dissolved state in water, they are separated from each other by hydration shells [3].

Substances differ in their solubilities in water and can be designated as either hydrophilic or hydrophobic. The former, hydrophilic substances, completely dissolve in water, while hydrophobic molecules (non-polar) are insoluble in water or are characterised as having low solubility [2].

Moreover, water molecules are known to undergo autoproteolysis, which is the spontaneous dissociation of the water molecules. This process is attributed to the high polarisation of the O-H bonds, thus, resulting in water consisting of OH^- and H_3O^+ ions, as detailed in equation 1-1 under equilibrium conditions:

$$2\,H_2O \leftrightharpoons H_3O^+ + OH^- \qquad 1\text{-}1$$

As one hydroxide anion OH^- is formed for each hydronium cation H_3O^+; the concentration of OH^- and H_3O^+ is noted as $[H_3O^+] = [OH^-] = 1 \times 10^{-7}$ mol/L= 100 nM [2]. Therefore, the concentration of OH^- and H^+ in natural water is 1×10^{-7} mol/L.

A pH meter is used to measure a water's acidity or alkalinity. The pH determines the acidity or basicity of a liquid solution in relation to its concentration of hydrogen ions using equation 1-2:

$$pH = - \log [H_3O^+] \qquad 1\text{-}2$$

The pH scale extends from 0 to 14. An acidic solution has a pH of < 7 and a concentration of H_3O^+ that is higher than OH^-. Conversely, when the concentration of OH^- is higher than H_3O^+ the pH is > 7 and the solution is basic. The pH of pure water is 7. Accordingly, pure water is a neutral solution; it is neither acidic nor alkaline. The pH range of 6.5-8.5 in water is established as safe for human drinking, as noted by the United States Environmental Protection Agency (US EPA) [5].

Pure water is seldom found in nature; instead, water is commonly found in combination with dissolved salts. Surface water (such as rivers, lakes and seas) and ground water are the two notable sources of water, containing a variety of substances in various concentrations [1][6]. The common substances found in water and that are waterborne include cations such as sodium (Na^+), calcium (Ca^{2+}), potassium (K^+) and magnesium (Mg^{2+}), and anions such as fluoride (F^-), chloride (Cl^-), sulphate (SO_4^{2-}), and carbonate (CO_3^{2-}) [7]. When these solutes are present in certain concentrations and in the absence of contaminants, water is safe and beneficial to drink and use.

1.2 Motivation behind the sensing of waterborne analytes

Water contamination is a global issue [1][6][8] that can be described as the polluting of water resources by substances that are hazardous for organisms. Contamination of water can be geological or from man-made resources. Natural contaminants can reach water as a consequence of groundwater moving through soils and sedimentary rocks and picking up

various compounds in excessive concentrations, such as Ca^{2+}, Cl^-, Mg^{2+}, F^- and nitrate (NO_3^-), in its path. The influence of these natural contaminants depends on their concentrations and types [8]. Man-made contamination results from the products of industries and agriculture, which typically involve the use of heavy metals, such as lead (Pb), copper (Cu), mercury (Hg), dyes and other compounds such as insecticides [8]. The releasing of such harmful or toxic elements in water or its overpopulation above certain concentrations makes water dangerous for consumption, whether by humans or living creatures, thereby leading to water pollution. The 'potability limit' or 'action level' are phrases used to describe the maximum acceptance level of certain waterborne substances or pollutants, such as harmful or toxic ions, in water, which is then designated to be sufficiently safe for consumption. Such potability limits have been established by many global organisations, including the World Health Organisation (WHO) [9] and the US EPA [10]. These organisations examine the safety of drinking water and publish international guidelines on the potability limits of certain elements that can be presented in water. These guidelines are updated frequently and serve to incentivise scientists to create new methods for detecting these contaminants at ever-lower concentrations. Table 1-1 lists the potability limit of various waterborne substances, as noted by the WHO.

As previously mentioned, certain waterborne substances (e.g., Na^+, Ca^{2+}, F^-, Cl^-, among others) that present naturally in water are necessary for human health, such as Ca^{2+} and F^- which are essential for bone and teeth health within potability limit concentrations. However, the existence of substances such as F^- above its potability limit of 79 µM (as noted by World Health Organization (WHO)) can lead to serious health problems, such as skeletal fluorosis and/or dental fluorosis [11].

Of note are the heavy metals, which are listed at the top of the inorganic pollutants list given their harmful impact on humans, plants and aquatic organisms [12]. Heavy metals are known to occur naturally within the earth's crust [13][14]. However, large quantities of them are discharged in the environment as a consequence of agricultural and industrial wastes, thereby raising concerns about their negative impact on the environment and human health [15]. The contamination of groundwater with heavy metals across Europe ranks first (31%) compared to other contaminants, such as oil-derived compounds and organic solvents [16]. Furthermore, metal-based industrial operations, such as mining, foundries and smelters, contribute to heavy metal discharges and causes almost 80% of pollution in China [17]. Some heavy metals, such as zinc, iron, copper, cobalt, and manganese, are essential elements in the body in minute amounts for multiple biochemical functions, and these are also usually present in natural water

[12][15]. Other heavy metals are designated as non-essential metals. Some of these are rather highly toxic and poisonous, even in minor quantities, such as arsenic (As), mercury (Hg), cadmium (Cd), lead (Pb) and selenium (Se) [15].

The dangers of heavy metals lie in their tendency to bioaccumulate and disrupt the functioning of vital glands and organs such as the brain, heart, bones and kidneys [14][18]. Essentially, the human consumption of arsenic-polluted water can cause lung, liver and bladder cancer. Arsenic in groundwater poses a real and natural danger in some countries, such as India, Bangladesh, Mexico and Taiwan [13]. In Bangladesh, 52% of drinking water contains > 50 µg/L As [19] and the potability limit of As in water must not exceed 0.01 mg/L as noted in Table 1-1. Cadmium is poisonous and carcinogenic at significantly low levels [13][18]. Human ingestion of water polluted with cadmium may result in lung and kidney damage and in bone fragility [12]. Lead is also a notable toxin of heavy metals. Lead-contaminated water can damage the nervous system, kidneys, liver, heart and brain [13]. The manufacture of lead water pipes is a remarkable means of polluting drinking water with lead [20]. Mercury is also recognised as a global pollutant that can transfer across a wide range of distances in various chemical forms, thereby making it difficult for humans and other organisms to avoid exposure to it [12][13]. Mercury is toxic, and its adverse effects include neurotoxicity, gastrointestinal toxicity, nephrotoxicity and high exposure may lead to death [13][14].

Among the ionic specious that reported in Table 1-1 as a common ions presence in water, arsenic represents in water in different chemical forms: arsenite As(III), arsenate As(V), dimethylarsinic acid (DMA), and monomethylarsonic acid (MMA) [21]. These forms are different in their toxic effects. As(III) is more toxic than As(V) and inorganic arsenicals are more toxic than organic derivatives [21].

Table 1-1: *The maximum acceptance level (potability limits) of some of waterborne analytes in drinking water as noted by the WHO [9]*

Elements	[µM]	[µg/L]
Aluminium	7.4	200
Zinc	76.5	5000
Arsenic	0.133	10
Cadmium	0.027	3
Mercury	0.030	1
Lead	0.048	10
Copper	31.5	2000
Fluoride	79	1500
Caesium	0.0075	1

Radioactive wastes also constitute an environmental threat and concern. Radioactive materials encompass radionuclides which are unstable atoms that have the tendency to disintegrate spontaneously into other radioactive or non-radioactive elements while simultaneously emitting radiation as energy [22]. Radioactive wastes are delivered into the environment from various resources, including through the production and testing of military weapons, electrical power generation, biological and chemical research, medical diagnosis and treatment, mining and industrial activities [23]. Furthermore, they can also result from nuclear accidents. One such example is that of the Fukushima Daiichi nuclear power plant destruction that occurred in Japan in March 2011. The plant's destruction was caused by an earthquake that induced the deposition of a considerable quantity of radioactive elements, such as radiocaesium (^{137}Cs) and radioiodine (^{131}I) into the water and soil [24][25]. From such nuclear accidents, the β^- active radioisotope $^{137}Cs^+$ is released into environments that rarely contain caesium.

Some of the dangers of certain radioactive elements are rooted in their relatively long half-lives (i.e., the time needed to decay to half the initial amount). For example, uranium ^{238}U has a half-life of 4.5 billion years [26], ^{137}Cs has a 30-year half-life [27], the half-life of strontium-90 (^{90}Sr) is 28 years [28], and that of ^{131}I is eight days [23]. Thus, exposure to a high level of radiation can be damaging to DNA, cells and tissues, and it can result in leukaemia, cancers, birth defects and genetic mutations [22].

Besides the contamination of water with harmful ions, the deposition of certain molecules in water can also result in such health issues. For example, benzene is an organic molecule that can be found in the environment and is attributed to both human activities and natural processes such as forest fires and volcanoes [29][30]. Ingesting water with high benzene levels for a long period may have adverse health effects, including the dysfunction of the central nervous system, pancytopenia and an increased cancer risk [30].

Providing safe drinking water is vital for each individual everywhere throughout the world and serves to avoid the previously mentioned potential dangers associated with the contamination of water with harmful substances. Accordingly, to monitor drinking water against contaminants, there is a vital need for the implementation of sensing technologies. Multiple sensors are usually used to disclose the existence of various waterborne analytes and their concentration. Note that the term 'analyte' represents the target chemical component detected by the sensor. Several sensor types are used to monitor the safety of water for consumption. Hence, there is a high demand for sensors that are characterised by a high degree of selectivity and sensitivity as this study investigates.

1.3 Sensor technology overview

Much attention has been paid to sensor technologies due to the increasingly urgent need for them in our lives, a need that parallels the industrial revolution. Sensors play a crucial role in environmental maintenance, specifically, regarding the security and monitoring of human health against water and air pollutants given that these are the primary elements of life. A sensor is an analytical tool that responds to the quantity of a measured object and converts it into a measured signal. Sensors are categorized either as 'physical sensors' that respond to physical quantities such as pressure, mass, temperature, humidity, density, etc. [31], or 'chemical sensors' that respond precisely to the presence of a particular chemical composition in the sample at certain concentrations. Chemical sensors respond to and transduce the chemical interaction between an analyte and the sensitiser (receptor that selectivity binds the analyte) into readable signals. Therefore, most chemical sensors contain a 'sensitiser' and a 'transducer' as its primary elements. The latter usually detects the modification of physical properties due to the analyte-sensitiser chemical interaction then transforms it into a measurable signal.

Electrochemical sensors are widely used to detect a variety of analytes by converting chemical interactions or biological responses into quantifiable electrical signal. This sensor is commonly represented in a potentiometric or amperometric configuration. Potentiometric sensors measure the potential difference between two electrodes separated by a sensitised membrane without a flowing current. The resulting signal is due to the deposition of the analyte at the ion-selective membrane interface (described in sections 2.3 and 3.3), and the resultant potential difference is proportional to the analyte concentration. Conversely, in an amperometric sensor, the analyte-sensitiser reaction is under a constant applied voltage in the sensing system. It results in the production of current, whereby the current is driven by the applied voltage. The ion-selective electrode (ISE) and the field-effect transistor-based sensor are widespread types of potentiometric sensors that are widely utilised in waterborne analyte sensing [32][33][34][35][36].

Optical sensors have also been employed extensively in waterborne analytes sensing [37][38][39]. An optical sensor incorporates a receptor or sensitiser to bind the target analyte and transducer to signal a change in optical properties as a consequence of an analyte-sensitiser complex formation. Based on the format of the output signals, optical sensors can function using colorimetric absorbance or fluorescence emission [40]. Colorimetric optical sensors function by incorporating chromophore molecules as sensitisers that then change their absorption spectrum as a result of binding analytes. In this case, spectrophotometers are widely used as transducers to measure the alteration in light absorption due to the formation of an analyte-chromophore sensitiser complex. Fluorescence-based sensors comprise a fluorophore as a sensitiser and a fluorimeter as a transducer, thus measuring fluorescence enhancement (off → on) or fluorescence quenching of (on → off) when the fluorophore sensitiser binds to an analyte. Fluorophore sensitisers are often organic molecules that can absorb wavelengths in the UV-Vis range while emitting light (fluorescence) in the Vis-near infrared range.

In general, the sensor's performance is considered relative to particular principal parameters such as sensitivity, selectivity, a limit-of-detection (LoD), response time, stability and fabrication cost [41]. The sensor sensitivity represents the ability of the sensor to respond to the ultra-low concentration of the target analyte. Quantitatively, it can be extracted graphically as the slope of the response curve (response *vs* analyte concentration). The ability of the sensor to highly respond to the target analyte over interferants is known as sensor selectivity.

‘Interferants’ are chemicals of a similar size and nature as the target analyte to which the sensor may respond similarly or at a lower level compared to the analyte. Thus, these substances are not the target of the measurement. The sensor’s selectivity is highly reliant on the sensitiser, not on the transducer, which strongly binds the target analyte over others. The sensor selectivity can be evaluated by its selectivity coefficient or the ratio of the binding constant of the analyte-sensitiser and interferant-sensitiser, where a high value reflects the high selectivity of the target analyte [42], as will be elaborated in section 3.4. The LoD refers to the lowest concentration of an analyte that the sensor can detect. Therefore, below a particular LoD, the sensor cannot detect and give a valid response to any analyte concentration [43]. Both the sensitiser and the transducer in the sensor have a role in the LoD characteristics, which can be determined from the analysis of the response curve, as will be described in section 3.4. The stability of the sensor is also a vital feature, which indicates the ability of the sensor to duplicate the same response to certain analytes for a considrable period. The optimum sensor should exhibit a high sensitivity, selectivity and stability, an extremely low LoD, a rapid response time and a low fabrication cost.

Regarding the sensing of waterborne analytes, many instruments employed atomic absorption spectroscopy [44], mass spectrometry [45] and atomic emission spectroscopy [46], as they are well-established methods for detecting a waterborne analyte at low concentrations. Moreover, these methods have also shown a high degree of accuracy and sensitivity [47][48]. However, the use of these techniques requires the provision of costly instrumentation and infrastructure, which are difficult to transport to the point of need [49]. The lowest LoDs that have been reached by using spectroscopy techniques were no lower than 1 nM [50]. The previously mentioned chemical sensors have attracted much attention during the last decades as a consequence of their advantages of good sensitivity, a low cost and portability owing to their small size [49]. More specifically, potentiometric sensors are the optimum type for identifying ion activity in a sample under study among chemical sensors [43].

A low cost, highly sensitive, easy operation, low power consumption, and portable potentiometric sensor has been investigated based on a thin-film transistor by Kergoat *et al.* [51]. Kergoat *et al.* operated a thin-film transistor across water as the electrolytic gate medium of the transistor; giving water-gated thin film transistor (WGTFT). This investigation has paved the way for detecting waterborne analytes, using a WGTFT as a new potentiometric transducer. To illustrate this point further, a WGTFT as a sensor allows the introduction of the waterborne analyte into the gate medium together with a suitable sensitiser (see sections 3.3.2 and 3.3.3)

within the WGTFT's architecture, resulting in a notable change in the transistor's characteristics, usually as a shift in the threshold voltage (V_{th}) (see section 3.2). This type of sensors has been widely applied to detect ionic species in aqueous media [34][35][52] and also in biosensor applications [53]. More recently, field-effect transistor-based sensor has found a role during the COVID-19 pandemic, which successfully detected coronavirus in clinical samples [54]. Achieving significant low LoDs that are required in the detection of the harmful ions is the key challenge facing all the potentiometric sensor including WGTFTs and that should be enhanced as aiming in this project.

1.4 Scope of the current research

The development and fabrication of low-cost, versatile, portable, highly sensitive sensors that can be employed for extremely low LoD is much more desirable when detecting toxic and harmful waterborne analytes, as reported in section 1.2. The incorporation of a unique sensitiser in the WGTFT transducer can achieve this goal. In this study, instead of the common organic macrocyclic ionophores, a new family of sensitiser materials, ion-exchange sorbents, are adopted in this work including zeolite and resin. Zeolites are widely used to extract toxic ions from water such as radioactive isotopes and heavy metals [8][55][56]. Mordenite zeolite experiences a good extraction of radioactive $^{137}Cs^{+}$ [57][58]. Accordingly, it was used to sensitise the membrane that emerged in the WGTFT sensor using a special design to detect the Cs^{+} cation analyte. The clinoptilolite zeolite has also been extensively utilised in heavy metal extraction from water [59][60]. Similarly, clinoptilolite was adopted in a WGTFT sensor to detect Pb^{2+} and Cu^{2+} cation analytes to monitor the 'Lead-and-copper-rule'. Moreover, an activated Puromet^{TM} MTS9501 chelating resin was used in a similar manner in the WGTFT sensor to detect F^{-} anion analyte, which showed good extraction of F^{-} from water [61]. The results of all these sensors will be presented in Chapters 6, 7 and 8, respectively.

Chapter 2 : Fundamentals of thin-film transistor (TFT) and potentiometric ion sensors

This chapter begins by describing thin-film transistor (TFT) in terms of structure and operation. Gating TFTs with electrolytes, instead of solid dielectrics, will be examined with a specific emphasis on 'an electric double layer' property of the electrolyte-gated TFTs. Some basic concepts of sensors as well as examples of potentiometric ion sensors are also demonstrated in this chapter.

2.1 Thin Film Transistors (TFTs)

2.1.1 Introduction

The transistor belongs to the class of semiconductor devices that have been utilized for many years in the modern electronic industry for several functions, such as switching or amplification of the electronic signal or regulating voltage or current. Moreover, the transistor can be a novel sensor technology showing excellent properties, as this project demonstrates.

Thin-film transistor (TFT) is well known as a modern semiconductor device that is extensively used in various types of integrated electronic technology, such as flat panel displays, video game systems, computers, and smart phones [62]. Moreover, TFTs are applied as an effective tool to detect biomolecules in bio-sensing applications [63]. The first TFT was demonstrated in 1962 by Weimer [64], based on an undoped semiconductor film of polycrystalline Cadmium Sulfide deposited on an insulating substrate. This TFT demonstration came two years after the fabrication of the first metal oxide semiconductor field-effect transistor (MOSFET), which commonly use high-doped crystalline silicon as a semiconductor. A TFT is similar to a MOSFET in that both are field-effect transistors that modulate the conductivity of a channel of semiconductors (and therefore current flow within the channel) by an electric field. However, TFTs are relatively easier to fabricate and cheaper than MOSFETs.

2.1.2 TFT structure

A TFT is a field-effect transistor, as mentioned earlier, constructed of an undoped polycrystalline or amorphous semiconductor thin film that acts as an active layer (carrying current), a dielectric layer (or electrolyte as displayed in section 2.2) as a gate insulator, and three electrical terminals: source (S), drain (D), and gate (G). Figure 2-1 displays the structures of TFT and MOSFET. The TFT device is fabricated on a non-conducting substrate, often glass and occasionally plastic, that does not have a role in TFT's operation. However, in MOSFET the silicon wafer acts as both semiconductor and substrate.

Figure 2-1(a) depicts the structure of TFT. The electrical terminals' 'source and drain' are deposited on the insulating substrate, and are used as metallic connections to an external circuit. Source and drain electrodes are separated by a channel with dimensions width (W) and length (L). The TFT's channel is directly connected by a thin film of semiconductor (reported in section 2.1.4) deposited on, or underneath, the source and drain contacts that supply and collect charge carriers to the channel, respectively. The third terminal, the 'gate electrode', is insulated from the semiconductor layer by electrical insulated materials referred to as gate insulators (gate medium). Hence, the latter is located between the gate electrode and the semiconductor thin film. Silicon dioxide (SiO_2) is a standard material applied as a gate insulator in MOSFETs due to its easy fabrication through thermal oxidation of the silicon substrate, and showing good dielectric properties [65]. On the other hand, the gate insulator can be an electrolyte, as we use in this work, instead of the gate insulator for sensing applications [34][66].

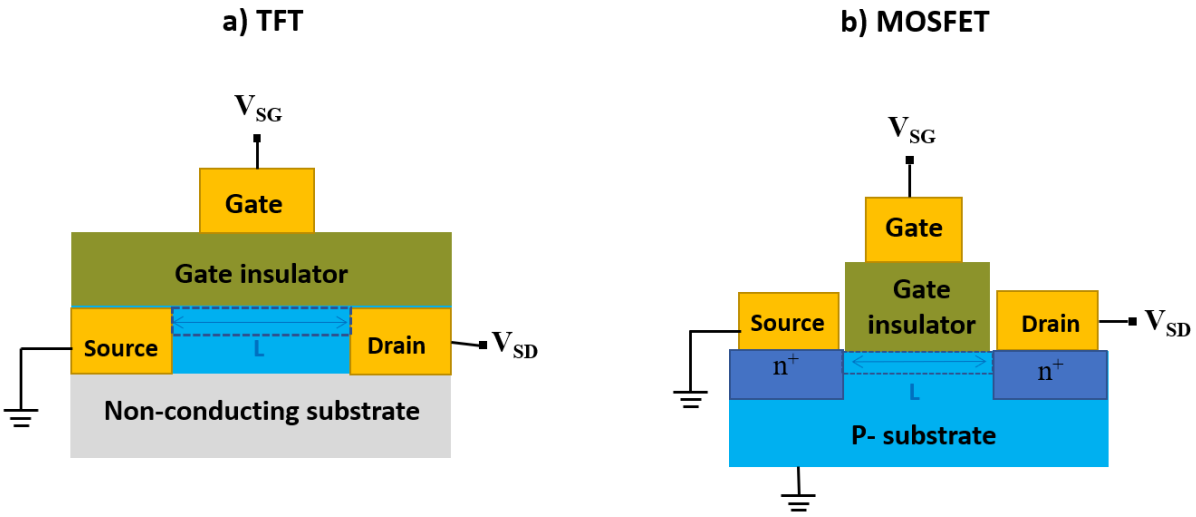

***Figure 2-1**: Construction of the a) thin- film transistor (TFT) and b) p-type MOSFET. The dashed squares indicate the semiconductor channels.*

Different configurations of TFT can be created based on the gate electrode location and the relative position of source-drain contacts in relation to the semiconductor location. Four possible geometries of TFT can be constructed and also divided into staggered and coplanar categories based on the source and drain contacts positions relative to the semiconductor/gate insulator interfaces. These variations are displayed in Figure 2-2. Each design has benefits and drawbacks and would be preferred for a specific application over others. For instance, in the architectures of a) and b), gate electrode and gate insulator can protect the channel against any damages or exposure to the light. Thus, it is favourable for applications of TFT in LCDs and TFTs based on hydrogenated amorphous silicon (a-Si: H) that is a light-sensitive semiconductor. Moreover, top gate configuration, is helpful in protecting TFT's components when exposed to the high temperature required for the deposition and crystallization process of the semiconductor film [67]. In this case, especially design a), the semiconductor layer is deposited before all other layers of TFT, thereby protecting the TFT's components from heat damage. Bottom gate structurers are extensively utilized for amorphous silicon-TFTs due to easier fabrication and improved performance [67][68]. However, protecting the back channel may be necessary to prevent undesired instability as a result of exposure to the atmosphere, and that can be achieved through adding an additional layer (passivation) [67][68].

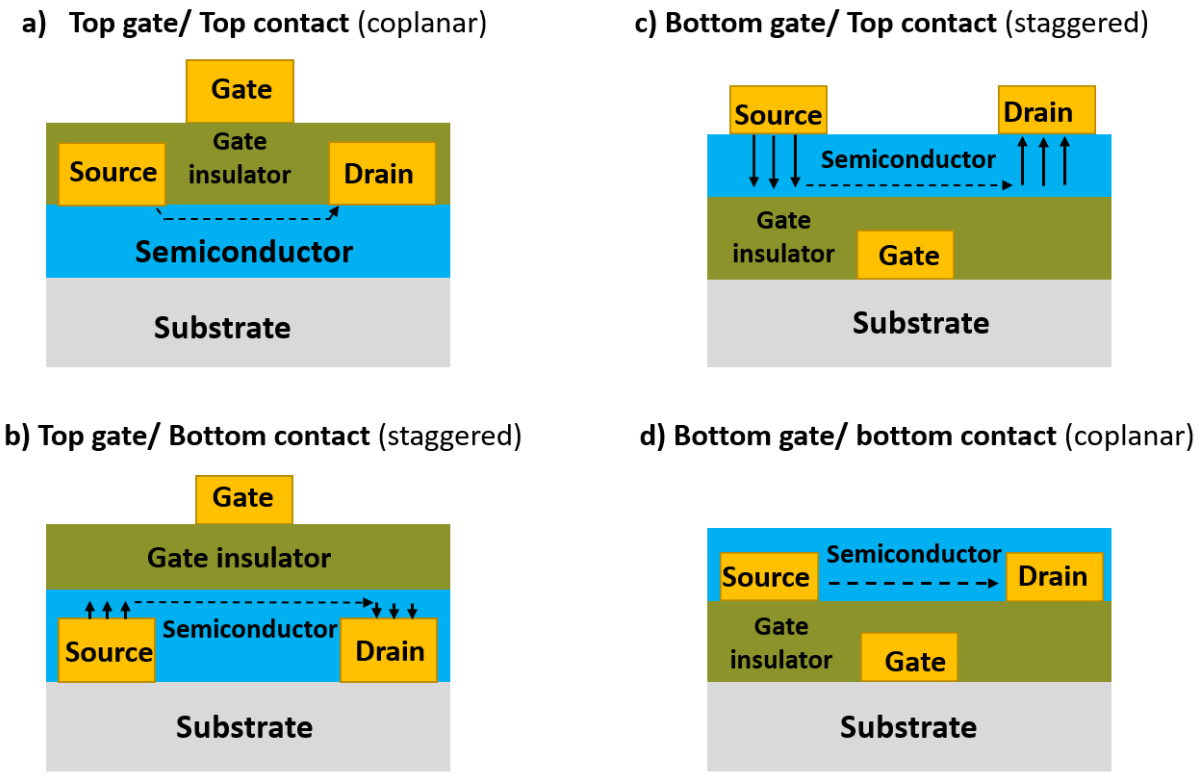

Figure 2-2: *Four possible designs of TFTs. The dashed arrows represent the charge carriers' flow direction in the channel.*

2.1.3 TFT operation

As a TFT is a field-effect transistor, its operation depends on the applied gate voltage to form a conductance channel and control the current flowing through it. The operation principles of TFT and MOSFET are similar in that both depend on the applied electric field to form and modulate the conductivity of the semiconductor channel at the semiconductor/gate insulator interface. However, due to employing doped semiconductors, MOSFETs operate on inversion mode, i.e., formation of n-type as a conductive layer in a p-type silicon substrate. TFTs normally operate on accumulation mode, as the vast majority of materials employed in TFTs as active layers are intrinsic semiconductors.

The three terminals of a TFT enables the application of two different voltages: source-gate voltage (V_{SG}) (or gate voltage V_G) and source- drain voltage (V_{SD}) (or drain voltage V_D). Once adequate gate voltage V_G is applied to the TFT's gate contact, charge carriers in the semiconductor film (electron or holes based on semiconductor type) are attracted to the semiconductor/gate insulator interface, leading to the creation of an accumulation layer of charge carriers at this interface. In this case a conducting channel will develop. The current

flows from source to drain through the semiconductor channel when a suitable drain voltage (V_D) is applied, giving drain current (I_D), as seen in Figure 2-3. For this process, the polarity of gate and drain voltages should oppose the semiconductor polarity, as presented in Figure 2-3. In this figure, positive gate and drain voltages are applied to the n-type TFT, resulting in formation of accumulation layers of electrons and vice versa. The minimum gate voltage needed to establish a conductance channel (accumulation layer) represents the threshold voltage (V_{th}) of the transistor, in which the TFT device 'switches on'. Threshold voltage and other key parameters of TFT will be demonstrated in section 3.2.

Note that the accumulation layer is very thin in comparison to the semiconductor film thickness. A few molecular layers (around one or two nm) is the thickness of the accumulation layer near the semiconductor/insulator interface, as reported for organic field-effect transistors (OFETs) [69]. The density of charge carriers within this thin accumulation layer is high, about 10^{17}-10^{19} /cm^3 [69][70].

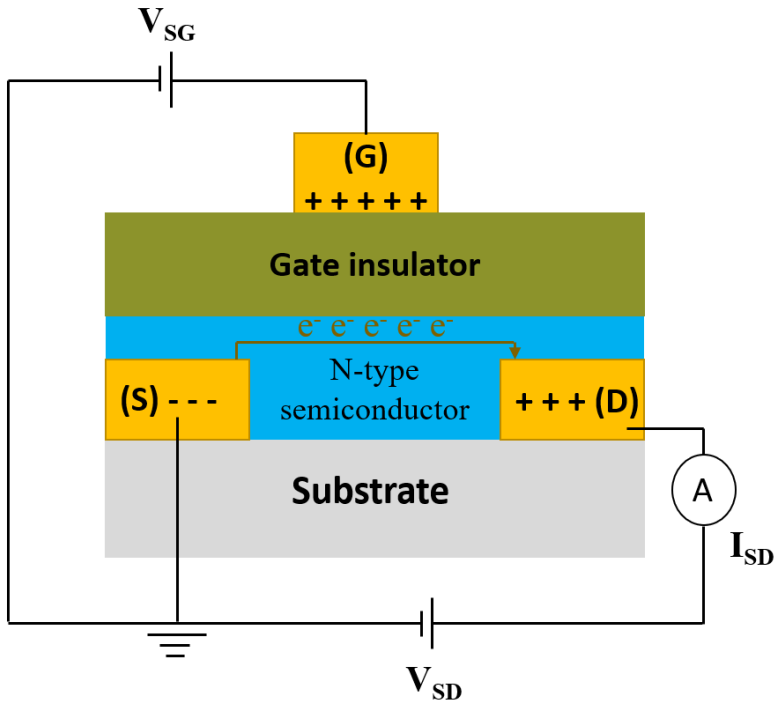

Figure 2-3: *The operation of TFT based on n-type semiconductor where (S),(D), and (G) are source, drain, and gate, respectively.*

2.1.4 TFT semiconductors

A variety of semiconductor materials have been utilized as an active layer in TFT devices. Cadmium Sulfide (CdS) and later Cadmium selenide (CdSe) were used as semiconductor film in TFTs, giving high charge mobility, in the early 1970s [71]. Nonetheless, these materials were not appropriate for large-scale processing. TFT technology experienced development in 1980-1989s by utilising hydrogenated amorphous silicon (a-Si:H) as semiconductor film-based TFTs, enabling their use in flat panel technology [72]. Polycrystalline silicon can be a semiconductor layer in TFTs, where amorphous and polycrystalline silicon are ideal for large scale processing. Polycrystalline silicon TFTs deliver higher charge carrier mobility ~ 100 cm/Vs than those with amorphous silicon [73], which polycrystalline silicon TFTs process under high temperature up to 1000 ^{o} C. The fabrication of TFTs based on the above-mentioned semiconductors requires costly technologies consisting of very high vacuum deposition system, *e.g.*, plasma-enhanced chemical vapour deposition (PECVD).

Moreover, many types of organic and inorganic semiconductor materials have been employed in TFTs in several studies [67][51][74]. The first organic semiconductor-based TFT was introduced in 1983 [75]. Interest in organic TFTs (OTFTs) has recently increased, resulting from some benefits. OTFTs can be constructed using low-cost techniques such as solution-based deposition (e.g., spin coating, solution casting) at low temperatures, no more than 200 ^{o} C. Furthermore, OTFTs are applicable for flexible display applications in which they can be deposited on flexible substrates, e.g., paper or plastic substrates [63]. Many organic semiconductors have been applied in TFTs, including polymers, e.g., poly (3-hexylthiophene) (P3HT) and oligomers, e.g., pentacene, mainly p-type OTFTs, providing good field effect mobility: 1-1.5 cm^2/Vs [76][77]. However, a major drawback of OTFTs is their poor stability under atmosphere [78].

Oxide semiconductors based on TFTs have been extensively studied to identify their optical and electrical behaviours. Advantages of oxide semiconductor TFTs appear in their excellent stability and superior electron charge mobility of ≥ 10 cm^2/ V s, even though when oxide semiconductor films are in an amorphous phase [79], those TFTs are based on amorphous silicon (a-Si)TFTs [67][80][68] and OTFTs. Also, oxide semiconductor TFTs can be prepared at relatively low temperatures, giving transparency to metal oxide film in visible light regions [73][81]. Thus, this type of TFT is a good candidate for LED, LCD, and large-area applications. In-Ga-Zn-O (IGZO) [82], ZnO [83], In_2O_3 and InZnO [84] are examples of metal oxide semiconductor-based TFTs. As an alternative to the conventional vacuum-based technologies

and expensive instrumentation, solution-processed metal oxide semiconductor films, forming polycrystalline films, are widely studied [83][85][86]. In this technique, precursor chloride, nitrate, and acetate are commonly used to produce oxide forms through pyrolysis, as displayed in section 4.3.

In this work, the solution-processed tin oxide (SnO_2) as a metal oxide semiconductor based on water-gated thin film transistor (WGTFT) is adopted. Some principal concepts of semiconductor materials and SnO_2 semiconductors will be demonstrated in section 3.1.

2.2 Electrolytes as gate media in TFTs

As mentioned in section 2.1.2, the gate insulator is a part of TFT's construction that insulates the gate metal from the semiconductor film. The gate insulator plays an essential role in enhancing the transistor performance resulting from the localization of accumulation layers at semiconductor/ insulator interface. The high specific capacitance of the gate insulators aids in increasing the charge carrier density and reducing the transistor threshold voltage and the operating power consumption. Two parameters can influence the insulator's specific capacitance (C_i): dielectric constant or the gate insulator's relative permittivity (k) and thickness of the gate insulator (d), in which C_i is proportional to (k) but inversely proportional to (d) according to:

$$C_i = \frac{\varepsilon_O k}{d} \qquad 2\text{-}1$$

Where ε_o denotes the vacuum permittivity.

It is known that silicon dioxide (SiO_2) is a traditional material applied as a gate insulator in TFTs exhibiting a satisfactory dielectric property. Nevertheless, SiO_2 shows a low dielectric constant (k) of ≈ 3.9 [87] and capacitance of 10 nF/cm^2 [88]. Also, an ultrathin layer of SiO_2 gives rise to the leakage current, i.e., the current flows through the insulator when voltage is applied [87]. There are multiple materials (organic and inorganic) that can be applied as a dielectric gate insulator with high k (≥ 8) and capacitance within the limit of 5-300 nF/cm^2, such as aluminium oxide (Al_2O_3), tantalum oxide (Ta_2O_5), and cyanoethylpullulan (CYEPL) [87][89].

Gating thin film transistors (TFTs) with electrolytes (as reported in section 2.2.2) has been the focus of much attention in view of their excellent performance and potential for use in sensing applications. Electrolyte refers to substances carrying free mobile ions or that can be dissolved in polar solvents such as salt (e.g., NaCl) dissolved in water. Dissolving salt in polar solvent results in breaking up this salt and releases separated charge ions: positive ions, 'cation', and negative ions, 'anions.' This is known as a dissociation process. Based on the degree of dissociation, partly or completely dissociation (ionizes), electrolyte (solute) can be classified as a 'weak' or 'strong' electrolyte, respectively.

The specific capacitance of electrolytes was demonstrated as typically in the range 1–10 $\mu F/cm^2$ [90], which is around three order of magnitude larger than for conventional dielectrics, as mentioned earlier. This great capacitance is induced, resulting from the formation of electric double layers (EDLs) on both electrolyte interfaces, as will be investigated in section 2.2.1.

2.2.1 Electric Double Layers (EDLs)

When a voltage is applied between two electrodes separated by an electrolyte, cations within the electrolyte migrate toward the negatively charged electrode while anions transfer to the positively charged electrode. Therefore, these two different charges resident on the electrode surfaces and electrolyte closely adjacent to the electrode form a thin double layer, known as Electric Double Layers (EDLs), of opposite polarity of charges on both sides of the electrode/electrolyte interface. The EDL can be cationic or anionic based on the type of charge ions (cations or anions) that reside close to the negatively or positively charged electrode, respectively.

EDLs are always present as pairs of two different polarities of charges close to each other, as shown in Figure 2-4. This configuration can be regarded as an electric double layer capacitor (EDLC). In other words, EDLs at interfaces can be seen as capacitors with a distance of the order of a nanometer. The important property of the EDL lies in providing high capacitance in the order of 10 $\mu F/cm^2$ due to the extremely low thickness of EDL $\leq$ 1 nm, and thus a much higher charge density will be obtained [91]. To estimate the total capacitance of EDLs, they can be characterized as a serial combination of capacitances.

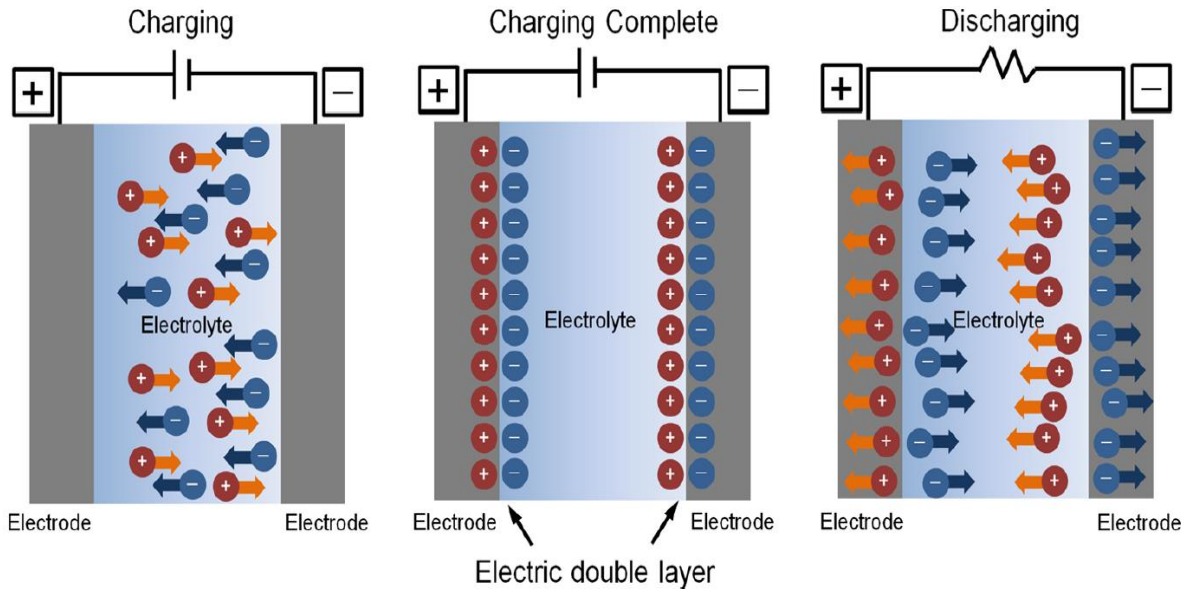

Figure 2-4: *Illustration of the EDLs' operation when charging electrodes, and the behavior of EDLs when electrodes are discharged* [65].

Figure 2-4 shows the mechanism of electric double layer capacitor (EDLC) operation. This example displays that a liquid or solid electrolyte containing free mobile ions – cations and anions – was deposited in between two electrodes. Two EDLs will build up on both electrolyte/electrode interfaces when an electric voltage is applied onto electrodes. When an external voltage begins to apply, a 'charging' process arises in which cations and anions in the electrolyte start to move toward electrodes based on their charge polarities. Thus, EDLs form when the charge is complete. Each double layer comprises two layers of ions of opposite charge polarities separated by a few Angstroms [92]. The capacitance of the EDL is proportional to its surface area because the capacitance is proportional to the area of electrodes. For this reason, specific capacitance is quoted (capacitance per unit area). Figure 2-4 also shows the discharging process whereby charges move away when the external voltage is removed.

Different models have been suggested to investigate the theory of EDL [65][93]. Von Helmholtz proposed the first model, the 'Helmholtz model', to describe the creation of double layers of opposite charges on the electrolyte being in contact with electrode's surface. This model indicates that counterions arrange in a thin layer close to the surface of the electrode, which surrounded by the molecules of solvent, when a voltage is applied between the two electrodes. The solvent molecules hinder ions from reaching the electrode's surface. This means that ions are isolated from the electrode's surface by a very small distance (d) in nm, as seen in Figure 2-5 a. This practice is called the Helmholtz plane. So the Helmholtz double layer

model indicates opposite charges resident on the electrode/electrolyte interface as a double layer, separated by an atomic distance. The resulting arrangement of counterions, cations or anions depending on the electrode's charge, near the electrode balances the electric charge on the electrode with polar opposite counterions, and thus the electrical potential Ψ within this layer decreases significantly and allows the overall potential of the bulk electrolyte to approximate zero. Consequently, the electric field is closely located at the EDL. On the other hand, this model does not assume the reliance of the measured capacitance on the concentration of ions in the electrolyte or the applied potential. Moreover, the neglect of interactions that arise away from the Helmholtz layer is another drawback of this model.

The Helmholtz model was followed by the 'Gouy-Chapman model' with improvements. This model takes into account the diffusion of ions through the electrolyte driven by the thermal motion. Therefore, Gouy-Chapman suggested the presence of a layer of counterions (both cations and anions) close to the electrode's surface, which is referred as the 'diffuse layer'. As a result, the electrical potential drops exponentially from the electrode to the bulk electrolyte (not abruptly), as seen in Figure 2-5 b. Although the Gouy-Chapman model provides an improvement and better reality in the double layer theory compared to the Helmholtz model, this model is still restricted since its measured capacitance does not correspond with the practical value of the capacitance.

The Gouy-Chapman model was further adjusted to give the 'Stern model'. In this model, Stern merged the two previous models, Helmholtz and Gouy-Chapman, combining the Helmholtz layer of ions next to the Gouy-Chapman diffuse layer to explore the distribution of ions in these regions [94]. Therefore, this model consists of an inner region, which is called Stern layer or compact layer, and a diffuse outer layer, as seen in Figure 2-5 c. The compact layer in turn contains adsorbed ions closest to and near the electrode surface distributed according to their size and charge. These ions are discriminated using the inner Helmholtz plane (IHP) and outer Helmholtz plane (OHP), as in Figure 2-5 c. The diffuse layer is similar to that in the Gouy-Chapman model, which extends from the Helmholtz plane to the bulk electrolyte. Thus, the charges on the electrode surface are not balanced by only ions in the Helmholtz layer but also by ions in the diffuse layer. In this case, the electrical potential falls abruptly at the OHP and then exponentially through the diffuse layer [65].

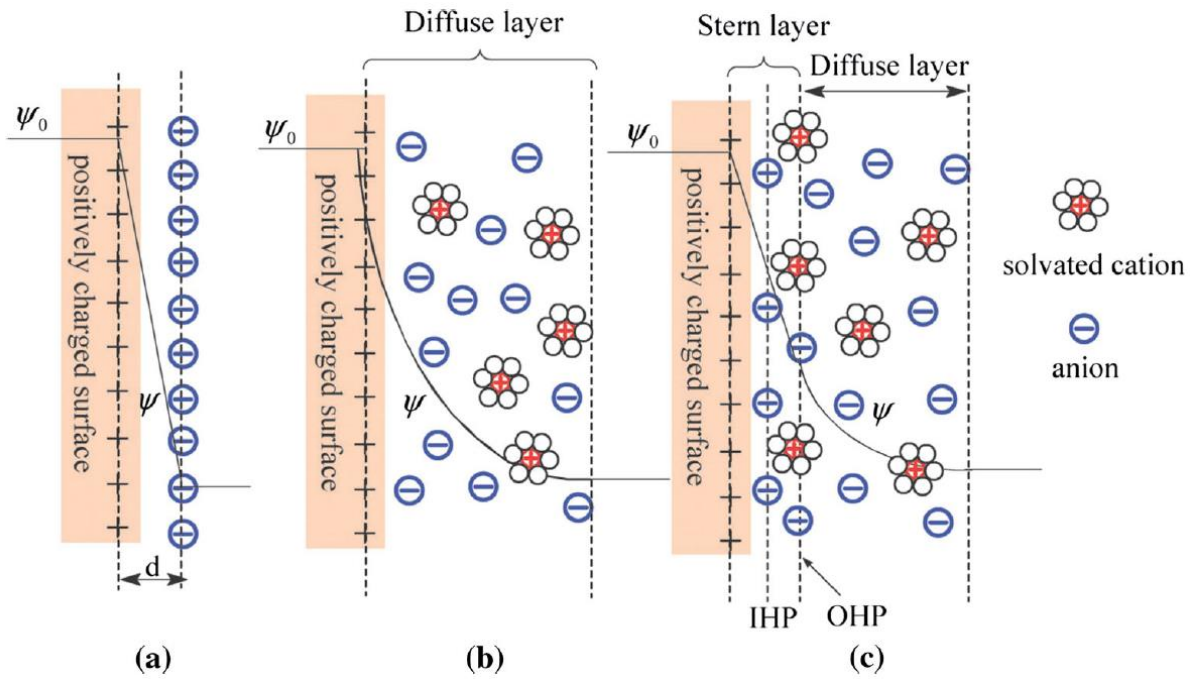

Figure 2-5: *Diagram of the three models that explained the EDL theory: (a) the Helmholtz model, (b) the Gouy–Chapman model, and (c) the Stern model* [65].

It is known that the existence of mobile ions in electrolytes are responsible for electrical conductivity. However, developing the EDLs prevents current from flowing through the electrolyte because the electrolyte's bulk is shielded by the EDLs. It is worth noting that electrolytes are conductors to AC while insulators to DC. Therefore, to measure the electrolyte conductivity, AC voltage should be applied to avoid EDL formation. Moreover, electrolytic substances can be destroyed (decomposed) electrochemically or broken down when high DC voltage is applied. This is known as an 'electrochemical window' property of electrolytes that should be taken into consideration when applying voltage. Water, for example, has an electrochemical window ≈ 1.23 V, which means no more than 1.2 V electrical potential should be applied [95].

2.2.2 Types of electrolytes

A number of electrolyte materials have been adopted for use as gate insulators in TFTs, such as pure water [51], salt solution [96][34][52], ionic liquid (IL) [97][98] and ion gel [99]. In this section, examples of common electrolytes will be demonstrated: DI water, Phosphate Buffered Saline (PBS), and ionic liquid (IL).

2.2.2.1 DI water

Deionised (DI) water is pure water with most of its naturally dissolved ions removed. Water is a weak electrolyte wherein a negligible quantity of water molecules (H_2O) are deprotonated to form hydroxide ions (OH^-) while other water molecules are simultaneously protonated to form hydronium ions (H_3O^+) by the free hydrogen atoms generated from water's autoprotolysis or auto-dissociation, as in the equation below [100], as reported in section 1.1:

$$2H_2O \leftrightharpoons OH^- + H_3O^+$$

The presence of H_3O^+ and OH^- ions allows the electrical conductivity of DI water, which make it an electrolyte. Furthermore, the exposure of DI water to the atmosphere enhances its conductivity due to the spontaneous dissolving of carbon dioxide (CO_2) from the air in DI water, which generates carbonic acid [101]. The conductivity of ordinary tap water (0.05 S/m) is much higher than that of DI water (5.5 µS/m) owing to the presence of acids and dissolved minerals [102]. The EDL capacitance of DI water that has been used as a gate insulator in an organic field effect transistor (OFET) was reported as being 3 µF/cm^2 [51]. This capacitance can be further enhanced by adding salt, e.g., NaCl, to be 10.6 µF/cm^2 at 0.5 V [95]. Moreover, the stability of water under applied voltage is restricted by the electrochemical window of water, 1.23 V, as stated above [95]. In this project, both tap water and DI water were used with TFTs where tap water includes several dissolved ions in different concentrations [103], giving higher EDL capacitance.

2.2.2.2 Phosphate Buffered Saline (PBS)

PBS is a buffer solution consisting of a water-based salt solution such as sodium hydrogen phosphate (Na_2HPO_4), potassium dihydrogen phosphate (KH_2PO_4), potassium chloride (KCl), or sodium chloride (NaCl). The main property of a buffer is that it serves to maintain the constant pH of the solution even if the chemical reactions release a small amount of acid or base owing to an acidic and basic substances included in the buffer. The pH of PBS buffer is about 7.4. The most common usage of PBS is in biological research. The ion concentrations in PBS match closely those in the human body. Hence, PBS is often used to simulate bodily fluids in biosensor applications [104][53]. Due to the higher concentration of PBS as electrolyte

compared to DI water, gating TFTs with PBS as a gate medium results in high drain current and small threshold voltage [86].

2.2.2.3 Ionic Liquid (IL)

The term ionic liquid indicates organic salts, including mobile ions - cations and anions - with melting points below room temperature. IL as electrolytes possesses some advantages, such as providing high EDL capacitance 5-17 µF/cm^2 [90][105], high thermal stability (below 450 ^{o}C) [106], nearly zero (no) volatility, and higher ionic conductivity 0.43 S/m [107] in comparison with DI water because, as mentioned above, the dissociation limitation of water molecules. The electrochemical window of IL is 4.10 -5.5 V [106], which is larger than the electrochemical window of aqueous electrolytes.

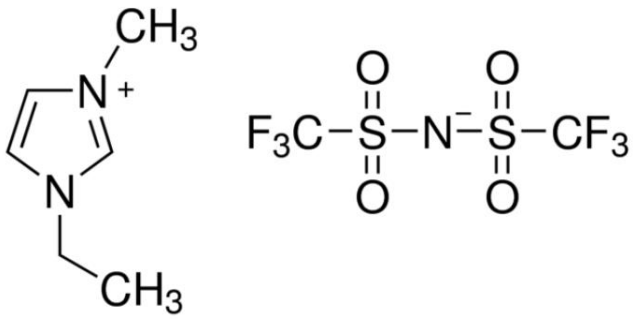

Figure 2-6: *The chemical structure of 1-ethyl-3-methylimidazolium-bis(trifluoromethyl-sulfonyl)imide ('EMITSFI') ionic liquid.*

Figure 2-6 shows the structure of an example of EMITSFI ionic liquid that has been employed to gate the OFET [105][108]. This IL yields higher capacitance of an electric double layer than aqueous electrolytes reached to 30 µF/cm^2 [108]. The result is lower power operation of the transistor, more charge carriers accumulated at the IL/semiconductor interface, and higher drain current.

2.2.3 Operation of EGTFTs

Operation of TFTs across electrolytes as gate medium, Electrolyte-Gated TFTs (EGTFTs), is a crucial development in TFT technology. Figure 2-7 shows the operation of EGTFT compared with dielectric-gated TFT. Electric double layers (EDLs) occur at gate/electrolyte and

electrolyte/semiconductor interfaces when gate voltage is applied, as seen in Figure 2-7 b. The formation of EDLs is similar to those shown in Figure 2-4; however, one of the capacitor plates is substituted with the TFT's semiconductor channel. This indicates that a very high electric field is induced at the semiconductor surface, resulting in the formation of the accumulation charge layer near the transistor channel/electrolyte interface at low applied voltage < 2 V [109]. So the accumulation layer is equivalent to the charge on this plate of capacitor 'semiconductor channel,' while another plate of this capacitor is the gate contact. The high capacitance of EDLs in EGTFTs results in some advantages as accumulating much higher charge density at the semiconductor/electrolyte interface, reducing threshold voltage, and hence operating at much lower voltage. These qualify electrolytes to be a good alternative to the conventional dielectrics due to their excellent performance and ability to enable sensing applications. Indeed, the development of EGTFTs opened the way for this technology to join sensing applications, as seen below in section 2.3.2.3 discussing water-gated thin film transistors (WGTFTs).

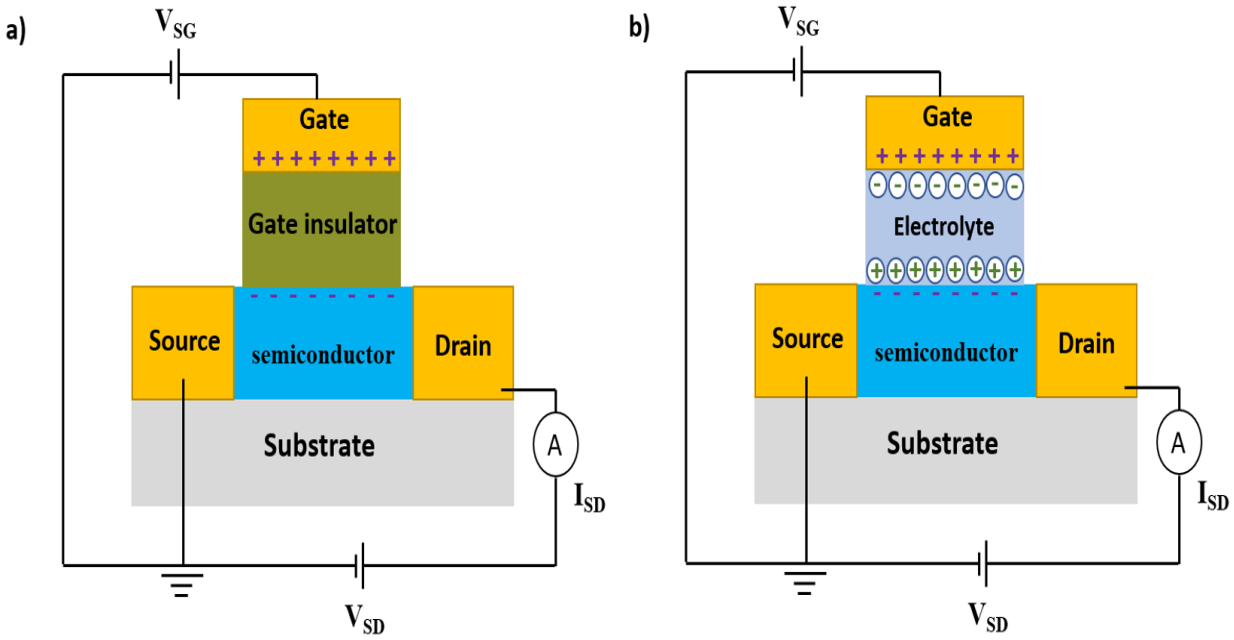

Figure 2-7: *Operation of TFT across (a) dielectric insulator and (b) electrolyte.*

In addition to the field effect mode of operation EGTFTs (referred to as EDL transistor), 'Electrochemical Transistor' (ECT) is another mode of operation. This mode is mainly dependent on the nature of the semiconductor material used in the channel of the transistor. For illustration, when a permeable semiconductor is used in EGTFT, the electrolyte's ions can transfer across the semiconductor/electrolyte interface to the semiconductor bulk, which dopes the bulk, once the gate voltage is applied. ECT mode differs from field effect mode whereby the latter employs impermeable semiconductors in EGTFTs that block ions of electrolytes from passing through the interface and dope the semiconductor bulk, as seen in Figure 2-8. A number of polymer semiconductors are known as electrochemical doping if they contact the electrolyte in the gate medium of the transistor [110][111]. These are called organic electrochemical transistors (OECTs). The field effect operation mode is only established in this project.

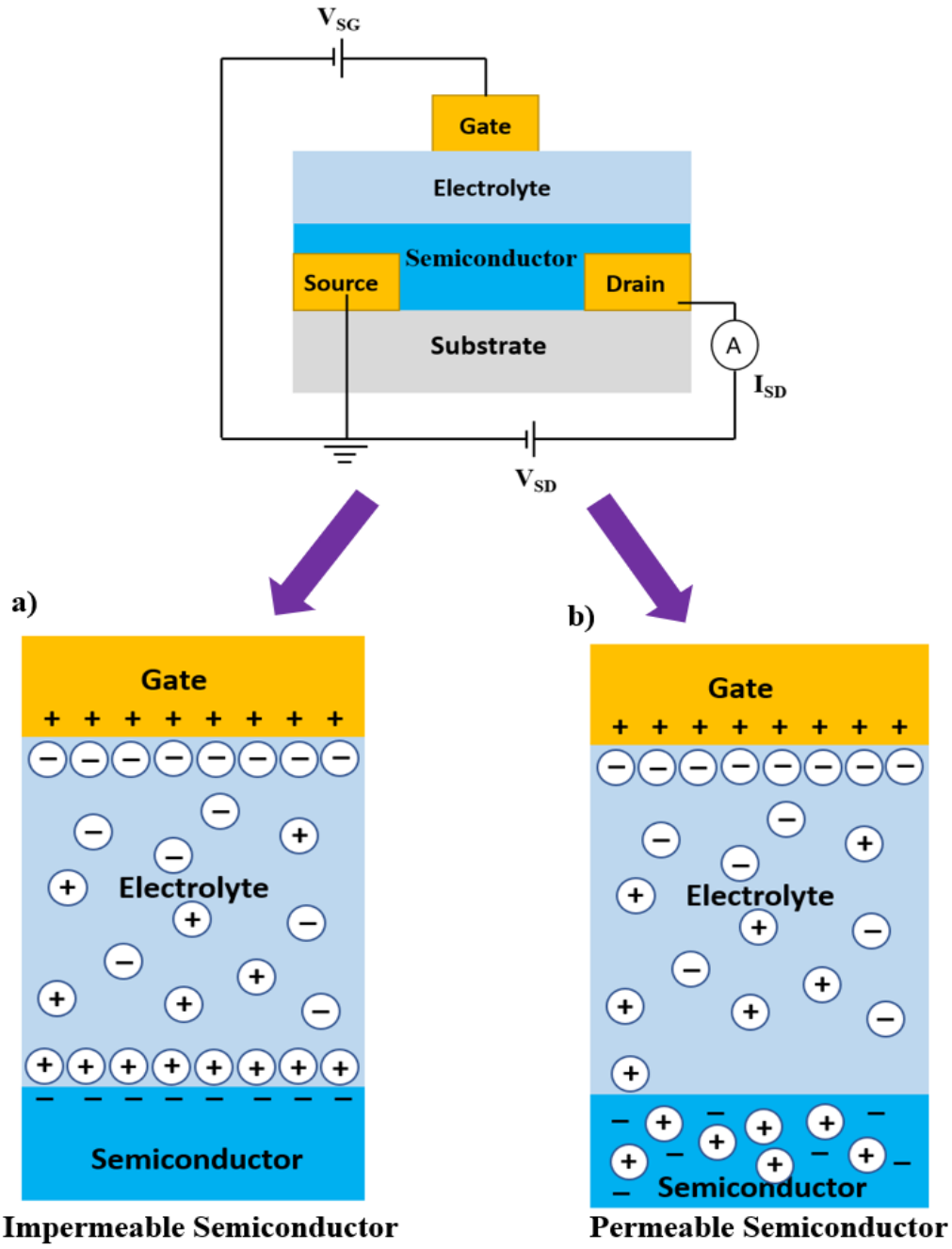

Figure 2-8: *Illustration of a) impermeable and b) permeable organic TFTs gated with an electrolyte, in the field effect mode (left) and electrochemical mode (right).*

2.3 Potentiometric ion sensors

2.3.1 Introduction

Sensors indicate measuring instruments or platforms that detect a concentration of specific analytes and respond to them in the test environment. Sensors can be operated under water or in the air as a common media. Sensor devices are widely known as detectors resulting from

detecting the target chemical substance known as ‘analyte’. As previously noted in section 1.3, electrochemical sensors are usually comprised of two essential elements: sensitiser (receptor) and transducer. The sensitiser is the principal part of the sensor that selectively binds certain analytes. This binding between sensitiser and analyte is transformed into a signal (physical property can be measured, e.g., voltage, current, capacitance,…) by the ‘transducer’. Macrocyclic as a common sensitiser are explained in section 3.3.2.

In potentiometric sensors, the interaction between sensitiser and analyte induces modification in the electrical potential of the transducer [112]. A phase transfer membrane is often the major part in potentiometric sensors in which ‘sensitisers’ are distributed within the membrane. Thus, a membrane potential builds up in response to combining the sensitiser with various concentrations of analyte (e.g., ions). The membrane potential is measured using a transducer that transduces the potential into a measurable electric signal, where the potential is proportional to the concentration of analyte. The phase transfer membrane and common sensitisers will be elaborated upon more fully in section 3.3. Potentiometric sensors exhibit some benefits including low consumption of energy, inexpensiveness, portability, and ease of fabrication [112][49]. Electrochemical cells and field-effect transistors (FETs) (transistor-based transducers) are common examples of potentiometric sensors, as will be outlined in the next section.

2.3.2 Examples of potentiometric sensors

2.3.2.1 Electrochemical cell

Use of electrochemical cells as potentiometric ion sensors is a common technique that determine the analyte concentration in the sample solution by measuring the electrical potential.

Figure 2-9 illustrates the construction of an electrochemical cell potentiometer. This structure contains two identical reference electrodes, one of which serves as a reference electrode while the other is used as an indicator electrode, which is an ion-selective electrode (ISE). Initially, reference electrode and ISE have the same potential. ISE normally contains a sensitised membrane that installs in between two solutions holding analyte: the test sample solution (unknown analyte concentration) and the inner reference solution (known analyte concentration). Membrane potential builds up across the sensitised membrane and that can be attributed to the difference of the analyte concentrations on both sides of the membrane,

changing the potential of the ISE. The potential of the reference electrode remains constant by using high concentrations of a bridge electrolyte (e.g., 0.1M KCl). Thus, ISE potential differs from the potential of the reference electrode by membrane potential, which is proportional to the analyte concentration in the sample solution [113]. A high impedance voltmeter is used to evaluate the difference in the potential between ISE and the reference electrode under near zero current flow between these electrodes.

In a potentiometric sensor's field, ISEs are one of the most popular topics due to their availability for a range of ions, simplicity of electrode design, and good selectivity [49][114]. The field of ISEs was developed in 1960 by Cremer [115], and they were initially used as a glass pH electrode, but since then they have been applied to determine various ions [49].

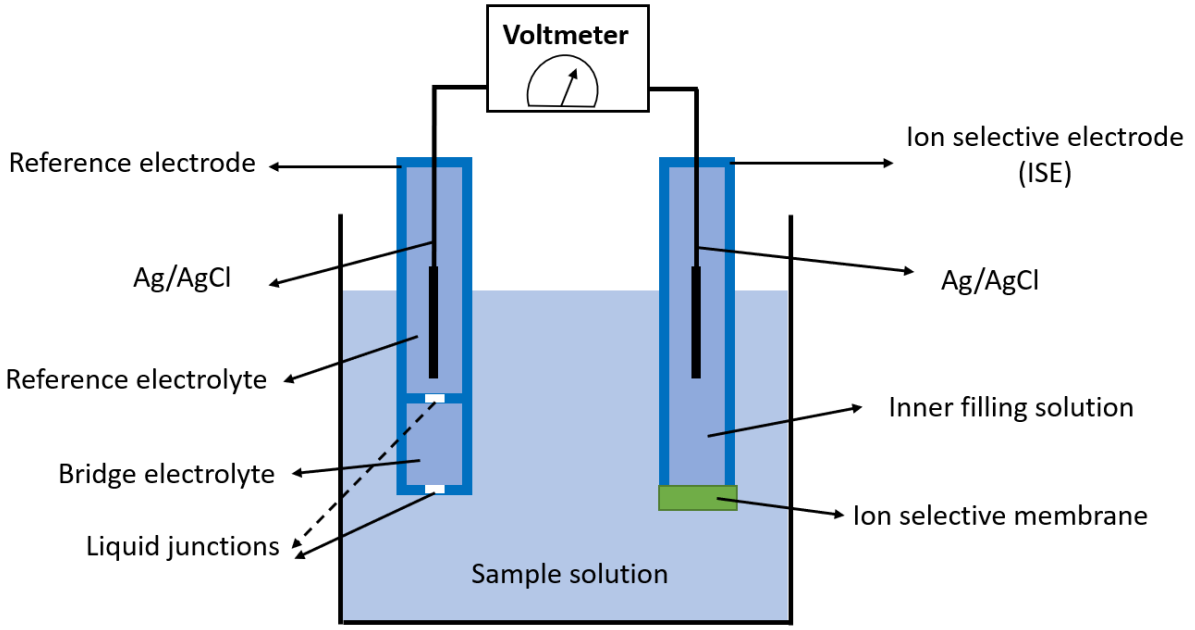

Figure 2-9: *Schematic representation of electrochemical cell transducer.*

2.3.2.2 The ion-selective field effect transistor (ISFET)

The ion-selective field-effect transistors (ISFETs) are a class of potentiometric ion sensor family, which was first developed as a form of transistor-based transducer by Bergveld in 1970 [116]. ISFETs have a similar structure and operation to metal oxide semiconductor field effect transistors (MOSFETs) (as reported about TFTs in section 2.1). However, in the ISFET, the gate electrode of MOSFET is replaced with a reference electrode immersed in aqueous solution

that is in direct contact with an insulating layer, as shown in Figure 2-10. The initial usage of ISFETs was as pH sensors where hydroxide groups on the gate oxide SiO_2 insulator act as binding sites. These sites can be protonated or deprotonated in response to hydrogen ion concentrations in electrolytes. Thus, by donating or accepting protons from or to the electrolyte solution, the initially neutral oxide surface can be altered to become a charged surface. This induces interfacial potential at the electrolyte/insulator (oxide surface) interface. This is considered to be a pH ISFET sensor [117][118]. However, the selectivity of the ISFET sensor can be modified to detect other metal ions, not just pH, by introducing specific ion selective membrane on the top of the gate insulator of the ISFET. That generates, for example, potassium ISFET and calcium ISFET sensors [119][120]. ISFET has also been widely applied in biosensor applications [121]. As a response to the change of surface potential, the drain current of the ISFET will be modified so that the current variation is proportional to the ion concentration in electrolyte.

Indeed, ISFET technology has garnered increasing interest as a consequence of its benefits as a potentiometric sensor in comparison with the ISE, such as small size, and short response time [122].

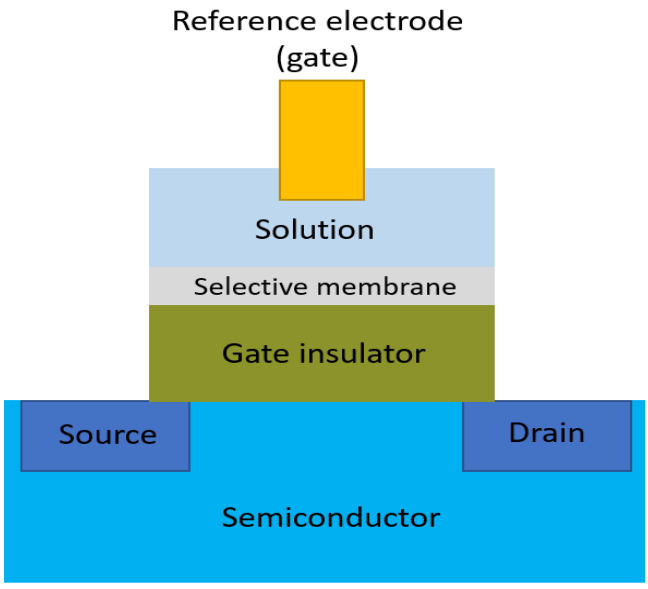

Figure 2-10: *Diagram illustrating the ISFET structure.*

2.3.2.3 WGTFTs

Water-gated thin-film transistors (WGTFTs) are EGTFTs, as shown in Figure 2-7 b and explained in section 2.2.3, in which the gate media is mainly water. The successful operation of TFT across DI water as a gate medium was demonstrated by Kergoat *et al.* in 2010 [51].

The invention of Kergoat *et al.,* WGTFT, opened the door for a new sensor technology for a range of analytes in water. Subsequently, WGTFTs can be utilized as a new potentiometric transducer that can transduce the presence and concentration of analytes dissolved in water in a gate medium into modification of the electrical characteristics of the transistor. For this purpose, to transform WGTFT into a sensor, selective sensitisers, 'ionophores', must be implanted in the WGTFT construction. Once analytes in the water gate media bind to the sensitisers introduced in the WGTFT design, the surface interfacial potential of the gate electrode or of the semiconductor will adjust, since the binding occurs on it, and hence the threshold voltage (V_{th}) of the transistor will shift. Surface dipoles or ions binding can induce this interfacial potential [52][53][123]. Many studies have been conducted using WGTFT as sensor to detect various analytes, whether ions ,*e.g.*, Na^+, K^+,Ca^{2+} [34][52][35], or molecules such as amine and dopamine [74][53].

Sensitisers in WGTFT sensors are often distributed within plasticised PVC membranes giving ion- selective membranes (displayed in section 3.3), which in turn are integrated into WGTFT architecture in different positions. List-Kratochvil *et al*. in 2014 [52] established a novel WGTFT sensor platform for selective ion detection of Na^+ in water. In this platform, the sensitised membrane was merged in the gate medium to separate the sample solution from the reference solution where the reference solution was in direct contact with the organic semiconductor channel of the transistor while the sample solution touched the gate electrode, analogous to the conventional electrochemical cell, as seen in Figure 2-11. This design facilitated the development of EGTFT as a sensor to detect various analytes with a simply integrated using suitable sensitised membrane. This design of WGTFT as a sensor is adopted in this project. A simpler way to turn WGTFT into a sensor is to introduce the ion-selective membrane on the gate electrode. The coating of the gate electrode of WGTFTs with the sensitised membrane was well established in 2014 by Melzer *et al.* [34]. In this approach, the gate electrode of a carbon-nanotube field-effect transistor was coated via K^+-/ Ca^{2+}-selective membrane and then immersed in a solution of the primary ion dissolved in DI water as a gate medium in concentration 10^{-1} M to 10^{-6} M. This work displayed the good performance of a simple design of ion selective WGTFT without the need to reference solution or electrode.

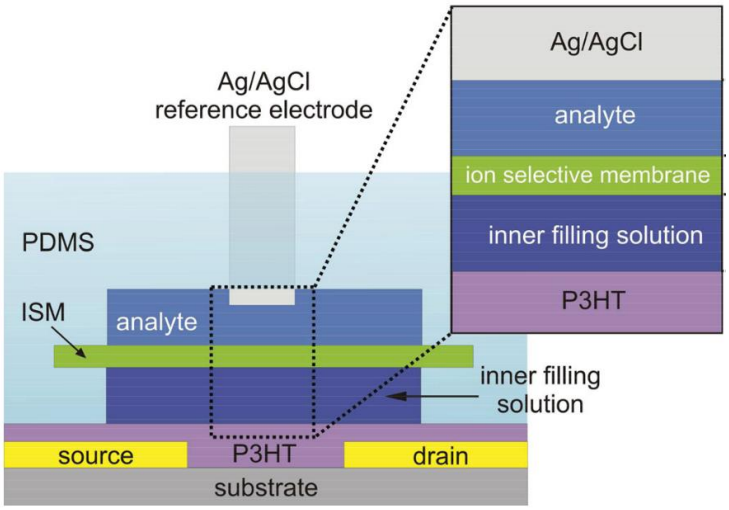

Figure 2-11: *Illustration of the ion-selective WGTFT that was formed by List-Kratochvil et al.* [52].

In the other hand, the sensitiser can be incorporated in the WGTFT architecture with free-membrane. The sensitiser can be dispersed within the semiconducting film. This was performed by Althagafi *et al.* in 2016 [123] when they distributed the Ca^{2+} ionophore in the P3HT processing solution, giving a good selectivity response to Ca^{2+} dissolved in the water in a gate medium comparable with devices sensitised with a sensitised membrane. Furthermore, the sensing element can reside on the gate contact, as conducted by Casalini *et al.* in 2013 to detect dopamine based on organic field-effect transistor and using PBS buffer as the gate medium [53].

Chapter 3 : Quantitative concepts and theory of TFT devices and sensors

After demonstrating the principles of the thin-film transistor (TFT) and potentiometric ion sensors in chapter 2, this chapter presents a description of the semiconductor as the critical part of the TFT device and the solution-processed semiconductors, namely SnO_2, adopted in this work. This follows with the quantitative explanation of the TFT device. The polyvinyl chloride (PVC) membrane matrix including ionophores (organic macrocycle and ion-exchange sorbent) , is also introduced as the core element of TFTs transducers. Finally, the sensing response characteristics for analytes are presented in section 3.4.

3.1 Fundamentals of semiconductors

Semiconductor components are the backbones of modern electronics. They allow the fabrication of devices that include light-emitting diodes (LEDs), solar cells, and transistors; these, in turn, are the building blocks of various electronic industries such as computers and phones. The key common feature of semiconductors is that their electrical conductivity can be modified by the application of an electric field and / or by the precise chemical composition of the material. This enables the control of a range of optical and electrical properties of the semiconductor [124].

It is well-known that the crystal lattice of semiconductors is assembled based on individual atoms' packing into an orderly pattern by sharing their valence electrons, joining together via a covalent bond. As a consequence of the collection of a large number of atoms in the material crystal structure, atomic orbitals combine to form the crystal orbitals. Those include the valence band (VB), or lower energy orbitals, and the conduction band (CB), or higher energy orbitals, with a gap in between known as the band gap or energy gap (E_g). The E_g represents the energy difference between the VB and CB, and it is the lowest required energy for an electron in VB to exist up to the state in the CB, to move freely and contribute to conduction. Based on the band gap's magnitude, materials can be classified as conductors, semiconductors, or insulators. In conductor materials, the VB and CB overlap, so that there is no band gap and valence electrons are free to move between the VB and CB. This mean, free electrons are abundant in

conductors and can act as mobile carriers of electrical current. Metals are typical conductors, characterised by a high density of mobile carriers and sufficient electrical conductivity. In contrast, a large band gap separates the VB electrons from the CB in insulator substances; this substantial energy gap prevents electrons from jumping to the CB and taking part in conduction. In semiconductors, the band gap is relatively small (e.g., $1.12\ eV$ for silicon) and the valence electrons can bridge it when they have sufficient energy to reach the CB [125]. For example, this can be achieved through thermal energy or excitation (e.g., heating or light photons) of the valence electrons or the electrical field [126]. The result is that the semiconductors' electrical properties are intermediates between those for insulators and metals, and electrons can flow through semiconductors under particular conditions.

Note that negatively charged free electrons and positively charged holes represent the current or charge carriers within the semiconductor crystal, indicating the bound electron motion. The semiconductors' electrical conductivity can be enhanced effectively by increasing the density of electrons or holes in the semiconductor crystal lattice by 'doping' impurities in their structures [124][127]. In the doping process, a small percentage of specific impurity elements (donor or acceptor atoms) known as dopants are added to the crystal structure, providing further free electrons or holes.

Semiconductor materials are generally categorised as intrinsic and extrinsic. The intrinsic semiconductors are pure semiconductor materials such as silicon (Si) and germanium (Ge) with equal concentrations of holes and free electrons where they come in pairs [125][127]. However, adding a minute quantity of dopants to the pure semiconductors creates the electrons or holes; this substance is known as an extrinsic semiconductor. Consequently, two classes of extrinsic semiconductors are derived with respect to the type of dopants: n-type and p-type semiconductors. Donor dopants, such as antimony when doping germanium, give a surplus of electrons in the semiconductor crystal structure that are readily available in the CB. On the other hand, acceptor dopants such as boron doping germanium, reduce available electrons so increase the holes in the VB, creating an opportunity for electrons to sequentially fill the holes and move in the opposite direction [127]. Therefore, most charge carriers in the n-type semiconductors are electrons, while holes are the charge carriers in case of p-type semiconductors.

Semiconductor materials can consist of a single element such as silicon (Si) and germanium (Ge) or several to form a compound semiconductor. Compound semiconductors include two

or more elements in their construction. Inorganic III-V compound materials formed by elements in the third and fifth columns in the periodic table e.g. GaAs, AlP, AlAs, II-VI compounds generated by combining elements in the second and sixth columns in the periodic table e.g. ZnO and CdS, and organic semiconductor polymers such as pentacene are examples of compound semiconductors [124].

Moreover, based on the degree of semiconductor crystallinity, semiconductors can be crystalline, polycrystalline or amorphous. When the atoms or molecules of the semiconductors are ordered or arranged regularly and repeatedly in one direction, crystalline semiconductors develop. However, amorphous semiconductors lack the long-range order of atoms, constituent atoms or molecules are not regularly arranged within the structure. The polycrystalline phase is in the middle between the crystal and amorphous phases and consists of crystals varying in size and orientation. The degree of semiconductor crystallinity plays a crucial role in a few of semiconductor parameters, such as charge carrier mobility [124][128].

3.1.1 Injection of charge carriers, transport and mobility

In many devices as the semiconductor films are the active components (e.g., transistors), optimal performances depend on the injection of charge carriers, whether electrons or holes, from metal electrodes into the adjacent semiconductor layer when so the crossing of metal/semiconductor interface is a fundamental requirement. This process relies on the electronic structure of the semiconductor and metal's work function. 'Injection barrier' is the critical parameter governing the injection of charge carriers between the metal and the semiconductor, which indicates the variance of the metal's work function and electron affinity (ionisation energy) for electrons (holes) in the semiconductor. There, they should be close enough to achieve the ideal metal-semiconductor junction [129]. Note that the electron affinity (E_a) denotes the energy obtained when electrons transition from the vacuum level to the bottom of the CB while the ionisation energy (Ip) constitutes the energy needed to inject the hole in the VB by removing the electron from the top to the VB to the vacuum level. Figure 3-1 illustrates the alignment of energy levels, namely the work functions for metals such as chromium (Cr) and platinum (Pt) and the electron affinity (E_a) of the tin oxide semiconductor (SnO_2). The Pt work function is adjacent to the SnO_2, close to its CB, and due to the work function of Pt is about 5.7 eV [130] and the electron affinity of SnO_2 is 4.5 eV [131], the injection barrier is estimated as 1.2 eV reflecting the difficulty of injecting electrons into the

SnO_2. However, the injection barrier disappears in the case of Cr because of the desired alignment of energy levels; electrons are easily injected into the SnO_2.

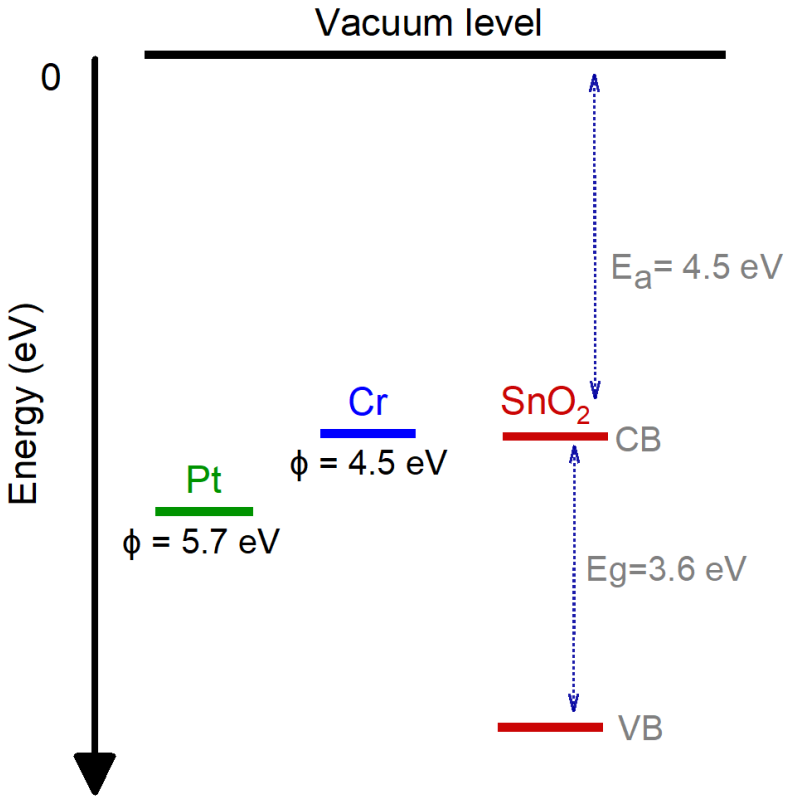

Figure 3-1:*Energy level of the SnO_2 semiconductor and the work function levels for Cr and Pt metals.*

For the carrier injection from the metal electrode into the semiconductor film, even in the presence the injection barriers, two mechanisms can be occurred: thermionic emission and field emission. In thermionic injection, charge carriers are thermally activated to overcome the injection barriers by receiving sufficient energy, strongly reliant on temperature. However, in the field emission mechanism, the carrier injection is conducted under quantum mechanical tunnelling, under high electric fields [132].

Once the charge carriers are injected into the semiconductor film, they should travel within the semiconductor from the source to drain electrodes in the transistor application. This yields the

drain current I_D. The movement of charge carriers within the semiconductor is affected by two key factors: the mobility of carriers and the presence of charge traps. In turn, the charge carrier mobility is largely dependent on the degree of crystallinity and the semiconductor's purity. Higher carrier mobility is found in more highly ordered crystalline semiconductors. In contrast, mobility declines in the case of polycrystalline semiconductors due to the existence of grain boundaries that perform as trap sites [133]. Applying the electric field (E) across the semiconductor film causes the movement of charge carriers with an average speed known as drift velocity (υ). Therefore, the mobility (μ) of charge carriers is defined as the average of the drift velocity (υ) per electric field unit, as presented in equation 3-1:

$$\upsilon = \mu E \qquad 3\text{-}1$$

The mobility of charge carriers induced by the electric field is measured in $cm^2/V.\ s$ unit.

3.1.2 Solution-processed inorganic semiconductors

Section 2.1.4 introduced the two types of organic and inorganic semiconductor materials that appear in TFTs architecture. Because of the benefits of metal oxide semiconductors as inorganic n-type semiconductors in TFTs, with low processing temperature, high mobility and good stability [134], this class was adopted for use in this study. In terms of preparation technologies, the solution-processed methods are preferred over the vacuum-based technologies from the standpoint of atmospheric processing, large-area and simpler fabrication and low cost [134][68].

Using metal salt precursors is a common approach to the deposition of oxide thin-films from solution [134][135]. The metal salt precursor-based solution processing technique can achieve high quality, homogenous, uniform films even in large-area applications [135]. In this method, the precursor-route semiconductors are prepared by dissolving metal salts in organic solvents, depositing the solution, and then heating the deposited oxide thin-film to dry the solvents and precipitate the active semiconductor resulting film, as will be shown in section 4.3. The chemical reaction occurs during the deposition of the precursor-route semiconductors, resulting in semiconductor film formation.

Several techniques are widely used to deposit the solution precursors to form the metal oxide semiconductors. Examples include spin-coating [86][136] and spray pyrolysis [137][138][35][83]. Spray pyrolysis will be demonstrated in section 4.3. ZnO [35][83], SnO_2

[139][140], and In_2O_3 [85] based TFTs are the majority metal oxide semiconductors reported to use the solution processing approach, exhibiting n-type characteristics and high electron mobility [72].

In this study, SnO_2, as a metal oxide thin-film semiconductor, is utilized as the semiconductor film in TFT construction, deposited using the spray pyrolysis technique of the precursor-route SnO_2. The structure and properties of SnO_2 will be discussed below in section 3.1.2.1. The electrical characteristics of SnO_2-based TFT will be presented in sections 5.2.1.1, 5.2.1.2 and 5.2.1.3.

3.1.2.1 SnO_2

Tin (IV) oxide, SnO_2 , is an inorganic semiconductor material widely used in essential technology applications such as solar cells, optoelectronic devices and gas sensors [141][142]. This widespread use is a consequence of its attractive properties, including high transparency, good electrical conductivity, high chemical stability and easy processing using the solution-processed method at relatively low temperature (200 ^oC) [143][144]. SnO_2 crystallography has a tetragonal rutile structure [80][145]. It has a wide band gap of 3.6 eV [142][143]. Figure 3-2 shows the unit cell structure of SnO_2 in which each tin atom surrounded by six oxygen atoms localised at the corners of a regular octahedron, while the oxygen atom is shared between three tin atoms at the corners of an equilateral triangle [80]. SnO_2 is an n-type semiconductor and the presence of impurities, which behave as acceptors or donors, in the SnO_2 structure results in enhanced electrical conduction. Oxygen vacancies might induce these impurities that play a role in providing electrons available at the CB [80].

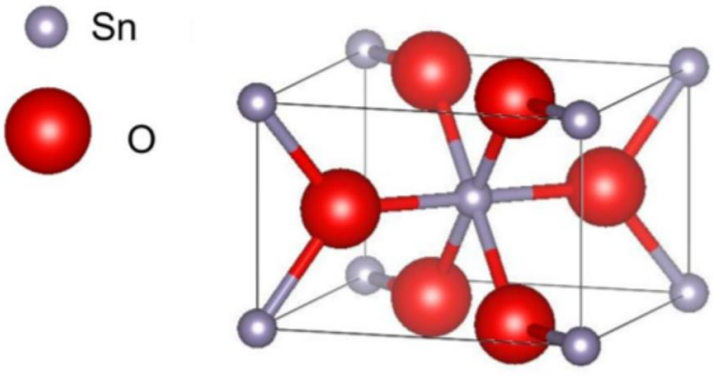

Figure 3-2: *SnO_2 unit structure [142]*

The first SnO_2 semiconductor based-TFT was reported by Klasens and Koelmans in 1964. This was the first use of the transparent conducting oxide material as the TFT channel [146], even before using ZnO, which has also been extensively used in the TFTs. In this work, SnO_2 was evaporated onto a glass substrate, with aluminium oxide (Al_2O_3) as a dielectric, and Al metal as gate, source and drain electrodes [147]. Aoki and Sasakura, in 1969, fabricated a SnO_2 TFT that operated in depletion mode, exhibiting poor electrical characteristics [148]. Improvement in the electrical characteristics of the SnO_2 TFT was documented in 1996, in depletion mode operation, achieving good mobility at 5 $cm^2/V.s$ and I_{on}/I_{off} ratio of about 60 [149]. The SnO_2 TFT operation in enhancement mode was conducted in 2004, yielding a drain current on-to-off ratio ~ 10^5 [150].

More investigation into SnO_2 TFTs was recently conducted using various technologies for SnO_2 fabrication, delivering superb electrical characteristics e.g., high electron mobility and I_{on}/I_{off} ratio [139][146][151]. The effective development of SnO_2 TFT devices is the operation under electrolytes as gate medium instead of dielectric insulators, giving desirable electric characteristics, namely low threshold voltage, good charge density and high stability [152][153]. Water-gated SnO_2 TFTs have not yet been reported in the literature, and this operation is being investigated by our group. The electrical characteristics of water-gated SnO_2 will be described in Chapter 5.

3.2 Quantitative description of TFT

The operational principle of a TFT is introduced in section 2.1.3. In this section, the quantitative operation of TFT is described. Three regimes characterise the operation of TFT based on the relative magnitude of the three critical voltages: threshold (V_{th}), gate (V_G), and drain (V_D).

As reported in section 2.1.3, when a TFT is operated in accumulation mode, the accumulation layer of charge carriers (electron or hole) will form at the gate insulator/semiconductor interface when sufficient and appropriate polarity gate voltage (V_G) is applied (positive or negative). The minimum gate voltage required to operate the transistor ('switch it on') resulting from the conductive channel's creation is known as the transistor's threshold voltage (V_{th}). Several parameters influence the V_{th} magnitude, as indicated in equation 3-2 [154]:

$$V_{th} = V_{fb} + \frac{qp_o d_s}{C_i} \qquad 3\text{-}2$$

Where V_{fb} represents the flat-band voltage, C_i is the specific capacitance of the gate insulator, d_s is the semiconductor film thickness, p_o is the density of trap in insulator/ semiconductor interface and semiconductor bulk, and q stands for one elementary charge.

It is clear that the flat-band voltage (V_{fb}) contributes to threshold voltage evaluation. V_{fb} , in turn, depends on the electrical structure of the semiconductor and gate metal, in particular, the electron affinity (E_a) or the ionization potential (I_p) of (n-type) or (p-type) semiconductors and the work function of the gate metal (Φ_M). Due to the differences in fermi levels between the metal and the semiconductor, and the bending of energy bands at the contact interface at zero gate voltage, this voltage should be increased to eliminate the bending. The increased voltage flattens the bands' bending, and thus permits the charge carrier to appear in the channel. This voltage is called flat-band voltage (V_{fb}) [155]. This flattening occurs before the formation of the accumulation layer. Quantitatively, V_{fb} can be expressed as $V_{fb} = \Phi_M - E_a$ or $V_{fb} = \Phi_M - I_P$.

Moreover, the capacitance per unit area of the gate insulator (C_i) effectively influences the threshold voltage, as seen in equation 3-2. C_i was presented earlier in section 2.2 as equation 2-1. As noted in section 2.2, the use of the electrolyte as a gate medium provides a high specific capacitance for the electrolyte-gated thin-film transistor (EGTFT) and, hence, provides a very desirable low threshold voltage [65]. The high C_i of such electrolyte-gating TFTs can also reduce the effect of charge traps. Consequently, the threshold voltage (V_{th}) can be modulated with V_{fb}; $V_{th} \approx V_{fb}$.

The first operation regime of TFTs is known as the subthreshold regime. In this regime, the magnitude of applied V_G is negligible compared to V_{th} ($|V_G| < |V_{th}|$); the formation of an accumulation layer does not occur yet, and the drain current (I_D) is extremely low. However, I_D enhances exponentially with increasing V_G until reaching V_{th} [154]. The drain current is given by equation 3-3 below:

$$I_D = K\mu C_i \frac{W}{L}\left(1 - e^{\frac{-qV_D}{K_B T}}\right) e^{\frac{qV_G}{n K_B T}} \qquad 3\text{-}3$$

Where K is a constant related to materials used and TFT design, W and L are the width and length of the transistor's channel, μ is the charge carrier mobility, q is the elementary charge, T indicates the absolute temperature, K_B is the Boltzmanns constant, and n is the ideality factor; the factor is given as ($n = 1 + C_s/C_i$), where C_i is the specific capacitance of the gate insulator, while C_s is the carrier trap's specific capacitance in the bulk and interface of the semiconductor.

Subthreshold swing (SS) is an essential parameter of TFT in the subthreshold region that reflects the required amount of V_G (in mV) to raise the drain current (I_D) by one decade that is an order of magnitude. It is defined as the inverse of (log I_D-V_G) plot's slop, as seen in equation 3-4 [80]:

$$SS = \left(\frac{\partial log_{10}(I_D)}{\partial V_G}\right)^{-1} \qquad 3\text{-}4$$

SS is measured in (mV/dec) unit. A low SS is more advisable and indicates the fast switching of TFT between off and on states and the reduction of power consumption (i.e., low applied V_G is needed) [67]. On the other hand, SS can be qualified using equation 3-5, which is related to the ideality factor (n) [156]:

$$SS = \ln(10)\frac{nK_BT}{q} \qquad 3\text{-}5$$

By replacing n with $(1 + C_s/C_i)$ then at room temperature ≈ 300 K, equation 3-5 can be written as:

$$SS = 60\ {}^{mV}/_{dec}\ (1 + \frac{C_s}{C_i}) \qquad 3\text{-}6$$

It is clear from equation 3-6 that both C_s and C_i have a role in reducing the magnitude of SS. Indeed, SS's magnitude has been determined for organic thin-film transistors as 760 mV/dec [157]. Lower SS can be achieved by gating the TFT with high dielectric capacitance [157][158]. TFTs based on metal oxide semiconductors and gating with high dielectric constants have also demonstrated preferable low SS < 114 mV/dec [159]. TFTs' gating with electrolyte offers more desirable SS values at about 68 mV/dec [160]. This value results from the high specific capacitance of electrolytes as the TFT's gate medium, based on the formation of electric double layers (EDLs), as reported in section 2.2.1.

Once V_G transcends the V_{th}, the charge carrier's accumulated layer will be established at the gate insulator/semiconductor interface; the conducting channel develops in this location of the semiconductor. In this case, I_D increases linearly with low V_D following Ohm's law, as displayed in Figure 3-3a. This regime is known as a linear regime, which describes the second operational regime of TFT. The linear drain current (I_D) can be expressed as equation 3-7 [154][161]:

$$I_{D,lin} = \mu C_i \frac{W}{L}\left((V_G - V_{th})V_D - \frac{V_D^2}{2}\right) \qquad 3\text{-}7$$

In case $V_D << V_G - V_{th}$, the term V_D^2 can be disregarded; hence, equation 3-7 can be written as equation 3-8:

$$I_{D,lin} = \mu C_i \frac{W}{L}(V_G - V_{th})V_D \qquad 3\text{-}8$$

On the other hand, when the difference between V_G and V_{th} is lower than V_D value ($V_D > V_G - V_{th}$), the charge density within the accumulation layer close to the drain contact will decrease, and the channel is pinched-off [154][42]. Under this condition, I_D will start to saturate, as seen in Figure 3-3b. I_D is no longer dependent on the applied V_D but simply depends on V_G. This is the third regime of the TFT operation, known as the saturation regime, as described in Figures 3-3b and c. I_D in the saturation regime is given by equation 3-9 [154]:

$$I_{D,sat} = \mu C_i \frac{W}{2L}(V_G - V_{th})^2 \qquad 3\text{-}9$$

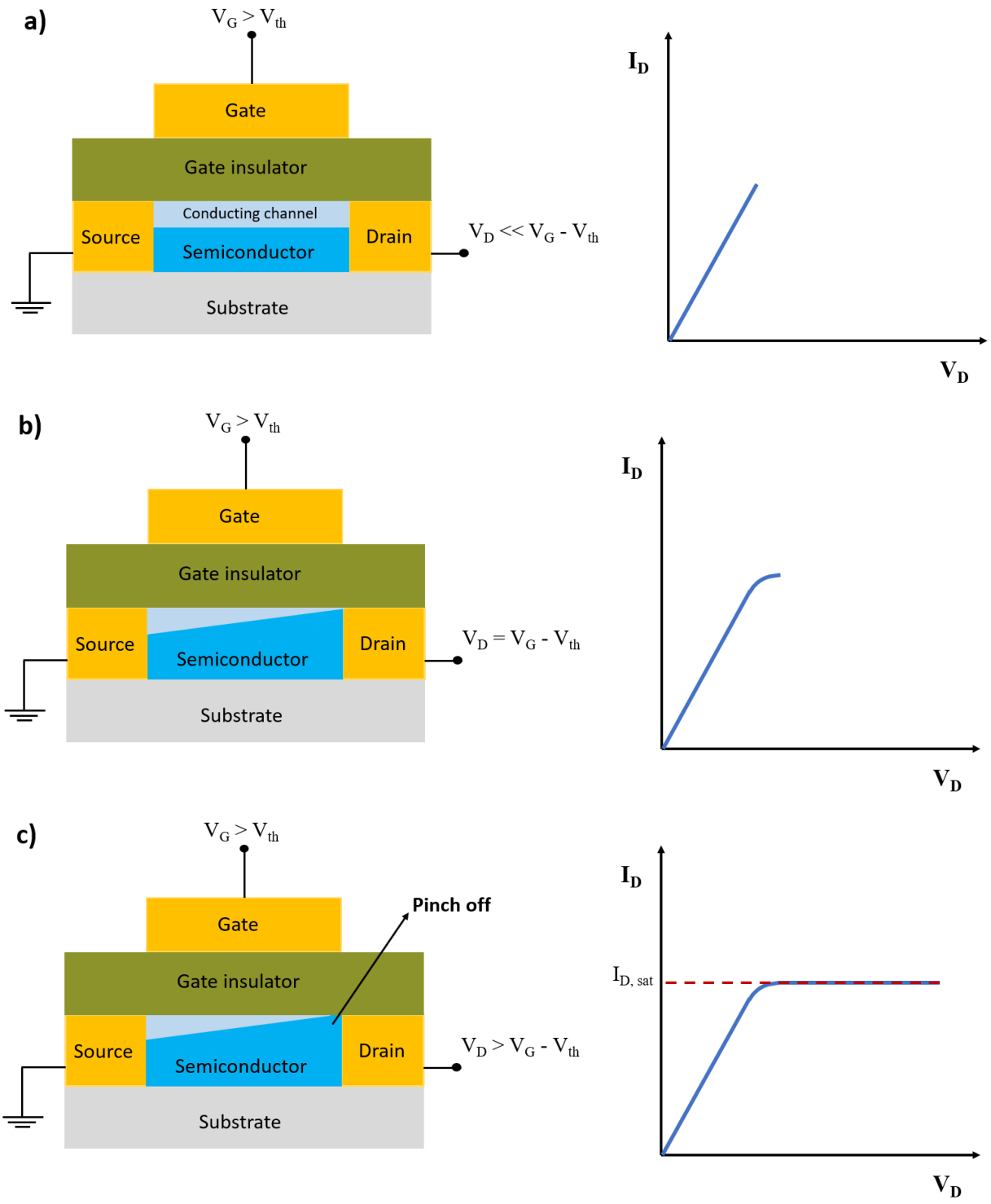

Figure 3-3: *TFT operational regimes displayed via the transistor's output characteristic in which (a) is the linear regime, (b) is the beginning of saturation, and (c) is the saturation regime.*

The practical measurement of TFT electrical characteristics is classified as output and transfer characteristics. The output characteristic describes the relationship between the I_D and V_D at constant V_G. The output is always presented as a group of curves recorded at different but constant V_G to examine the device quality. The transfer characteristic reveals the relation between the I_D and V_G at fixed V_D and can be presented in linear and saturation regimes. Figure 3-4 illustrates the example of (a) output and transfer characteristics of TFTs in (b) linear and (c) saturation regimes. The transfer characteristic can be analyzed to extract some vital parameters of the TFT device, such as threshold voltage (V_{th}), I_{on}/I_{off} ratio and mobility (μ). For this, plotting the saturation transfer characteristic on a logarithmic or square root scale is required, as seen in Figure 3-4c. Section 5.2 discusses the output and transfer characteristics and the evaluation of the previously mentioned parameters for SnO_2 TFT under water as gate medium.

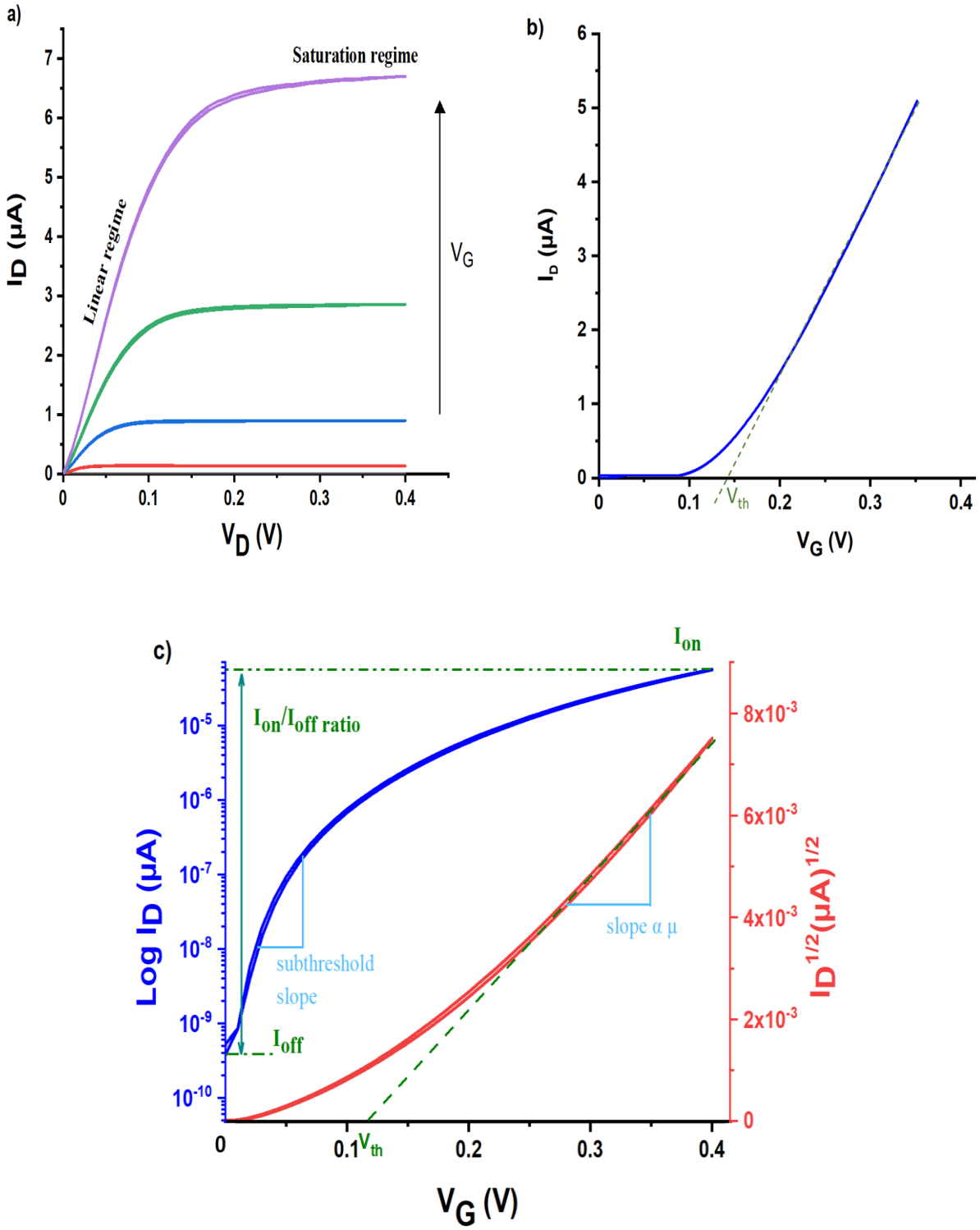

Figure 3-4: *Example of the typical a) output b) linear transfer and c) saturation transfer characteristics of TFT plotted in logarithmic and square root scales. The fitted lines show the evaluation approach of some parameters of TFT such as threshold voltage, subthreshold slope, I_{on}/I_{off} ratio, and charge carrier mobility as will be shown in section 5.2.*

3.3 The ion-selective phase transfer membrane

Section 2.3 explained that the sensitisers are the fundamental part of electrochemical sensors and are often inserted within a plasticised membrane as a solid phase medium. Additionally, as another critical part of the sensor platform, the analytes are commonly dissolved in a liquid phase medium. The interaction of the sensitiser within the membrane with the analyte in the liquid phase once they are in contact results in transferring the analyte from liquid to solid phase mediums. This membrane is known as the 'phase transfer membrane.' The ion-selective membrane is a common term referring to the phase transfer membrane. The term ionophore is frequently used to refer to the ion-selective sensitiser, notably in sensing ions.

The phase transfer membrane can be integrated within the potentiometric sensor platform between two solutions that include varying analyte concentrations. One of them is considered a reference solution holding a known concentration of analytes. In contrast, another solution contains an unknown analyte concentration (to be measured), referred to as the sample solution. The binding of analyte and sensitiser occurs on both interfaces of the phase transfer membrane with solutions, resulting in developing the difference in potential across the membrane, or 'membrane potential.' This potential can be electrically measured as a modification in the voltage or current.

3.3.1 Phase transfer membrane matrix

The polymeric matrix is a common class of the phase transfer membrane matrix reported in potentiometric sensors to detect cations and anions [162]. The polymer in such a polymeric membrane can offer desirable physical properties, such as mechanical stability and elasticity [162][113]. In addition, a variety of sensitisers can be integrated into this type of membranes for various applications of potentiometric sensors. Poly(vinylchloride) (PVC) is widely used as a polymer-based membrane and was adopted in this work.

The PVC membrane cocktail usually consists of PVC, plasticiser, and a sensitiser, in some situations, an ion exchanger may be used. A suitable polar solvent, such as tetrahydrofuran (THF), is frequently used to dissolve these components of the membrane cocktail. This results in the formation of a viscous solution that is then placed onto a flat surface. The THF evaporates leaving a thin film of sensitised PVC membrane. The resulting PVC membrane can then be easily inserted into the potentiometric sensor structure. Preparation of the sensitised PVC

membrane used in this study is explained in section 4.4.1. PVC membranes are typically plastics in potentiometric sensors. To generate a PVC membrane with the desired durability and flexibility, plasticisers are typically used in the manufacturing process [163].

Sensitised PVC membranes have been widely used in potentiometric sensors. The sensitised membranes exhibit good selectivity, not only for sensing ions, such as titanium [164], lead [33], and copper [165], but also for sensing molecules like trimipramine [166] and ascorbic acid [167].

3.3.2 Common ionophores

Ion-selective sensitisers ('ionophores') are the essential components in ion sensors and influence the sensors' selectivity. The most common class of sensitisers, particularly for ion sensing, is the organic macrocycle compounds. These ionophores bind analytes 'target ions' in their cavities based on the size of their holes and that of the ions. Crown ethers and calix[n]arenes will be discussed below as examples of this type of ionophores.

Crown ethers

A cyclic organic molecule containing a ring of various ether groups is known as the crown ether. The popular crown ethers are ethylene oxide cyclic oligomers, in which CH_2CH_2O is the repeating unit [168]. The presence of oxygen atoms within the crown ether's cavity results in the creation of binding sites with affinities for alkali and alkaline earth metal cations. Therefore, complex compounds are formed when crown ethers bind to the cation analytes [169]. The complex formation's stability relies mainly on the shape and size of the crown ether's cavity in relation to the cation size; hence, the selectivity of crown ethers will develop [169]. Figure 3-5 illustrates the chemical structure of '12-crown-4' and '18-crown-6' as examples of crown ethers in which '12' and '18' indicate the number of atoms included in the crown ethers' rings while '4' and '6' are the numbers of oxygen atoms in each ring, respectively. Regarding the selectivity of crown ethers, dibenzo-30-Crown-10 demonstrates excellent selectivity to potassium cations [35][170], while 15-crown-5 is a favourable option for Na^+-sensors [171].

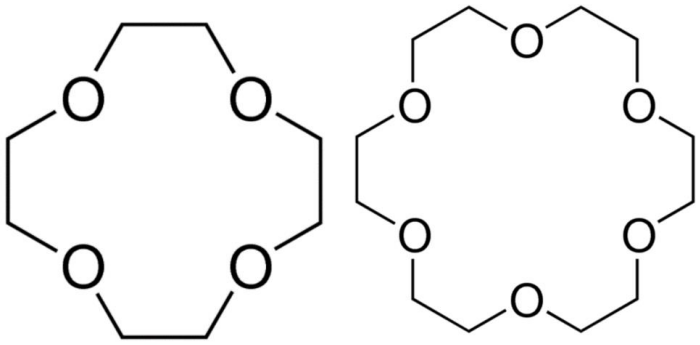

***Figure 3-5**: Chemical structure of 12-crown-4 (left) and 18-crown-6 (right).*

Calix[n]arenes

Calix[n]arenes are macrocycle compounds composed of formaldehyde and phenol in cyclic oligomer [172]. The name 'calix[n]arene' refers to the bowl shape of calix[n]arene molecule in which 'calix' relates to the vase shape in Greek and 'arene' refers to aromatic hydrocarbons in calix[n]arene's molecule. The 'n' in the square brackets stands for the number of units within the ring. Figure 3-6 illustrates the chemical structure of calix[4]arene and calix[6]arene as examples, showing different size cavities that can hold small molecules and ions. Larger cavities of calix[n]arenes provide suitable binding sites for larger metallic cations. As shown in Figure 3-6, the phenolic hydroxyl parts of the calix[n]arene molecule on the lower rim of the bowl and the aromatic portion of the upper rim can both act as receptors [173].

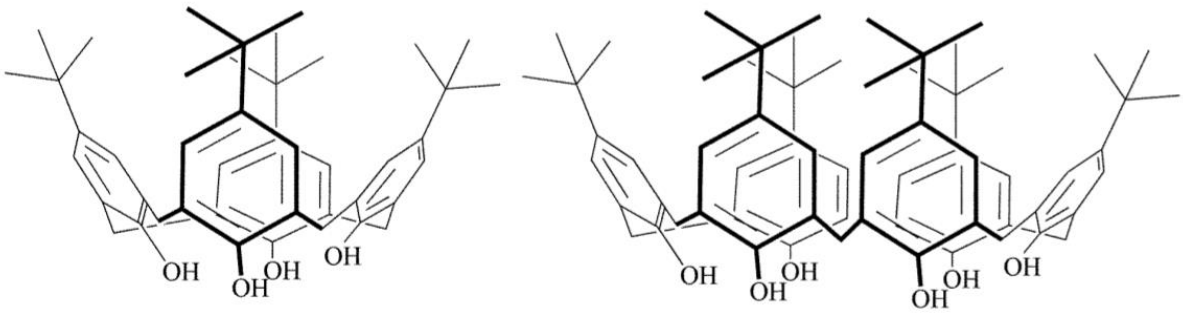

***Figure 3-6:** Chemical structure of calix[4]arene (left) and calix[6]arene (right)*[174].

Calix[n]arenes and their derivatives have been widely applied in potentiometric ion sensors to detect cations such as calcium [123], caesium [175], silver [32] and lead [176]. These potentiometric ion sensors include ion-selective electrode and the water-gated TFT sensor [123] due to the insolubility of calix[n]arenes in a water medium.

In this study, we adopted other types of receptors called 'zeolite' and 'resin' instead of the organic macrocyclic ionophores. They were incorporated in the water-gated thin film transistor (WGTFT) sensors within the plasticised membranes to detect several cations and anions. More details on zeolite and resin will be presented below.

3.3.3 Ion-exchange sorbents

Ion-exchange technology is widely used in water treatment for decontamination, purification, or softening water and wastewater. This technology is generally favoured for the treatment of large volumes of contaminated water due to its distinct advantages: simple operation, low cost, good selectivity, and high capacity [177]. In this method, the treatment is conducted by removing undesirable ionic species from water through an exchange process with acceptable ionic species having the same positive or negative electric charge from ion-exchange sorbents when the two phases come in touch. The ion-exchange sorbents are insoluble substances possessing high concentrations of exchangeable ions, which can be substituted for other ions from the solution. Ion-exchange practice is not a recent discovery. The ancient Greeks recognised the chemical modification of slightly salty waters when passed through certain types of sand [178]. Nevertheless, ion-exchange phenomena were investigated scientifically by Eichhorn (1858), who explored the reversible cation exchange reaction in natural zeolite [179]. Fifty years later, Gans synthesised the first aluminosilicate exchanger for water softening [180]. This has been widely employed for many years for water softening and nuclear waste treatment. This achievement led to the discovery of new industrial ion exchangers, resulting in the development of 'ion-exchange resins' in 1935 [181]. These resins then became an essential tool to address water problems such as deionisation and softening.

There is a wide diversity of ion-exchange sorbents, which can be organic or inorganic, natural or artificial, anionic or cationic. Of this range of materials, zeolites are the most commonly used ion exchangers and were the first materials to be used in ion-exchange processes. Organic

resins are the other type of ion exchanger most extensively used in water purification. Both substances will be presented below.

3.3.3.1 Zeolite

3.3.3.1.1 Structure

Zeolites are inorganic microporous minerals consisting of hydrated aluminosilicate crystals. Zeolite primary building units (PBUs) contain aluminium cations (Al^{3+}) and silicon cations (Si^{4+}), each surrounded by four anions of oxygen (O^{2-}) forming three-dimensional $(AlO_4)^{5-}$ and $(SiO_4)^{4-}$ tetrahedrons building blocks, as shown in Figure 3-7a. These PBUs are combined by sharing the four oxygen ions of each tetrahedron with those of adjacent tetrahedrons, where oxygen ions within the bounds of Al-O and Si-O link two cations, to produce the secondary building unit (SBU) (Figure 3-7b). The SBU is the main unit that describes the aluminosilicate structure of zeolites. The resulting SBUs combine to produce a crystalline zeolite framework containing open nanocavities or channels (Figure 3-7c) in different sizes and shapes with dimensions ranging from 0.2 nm to 0.8 nm [182].

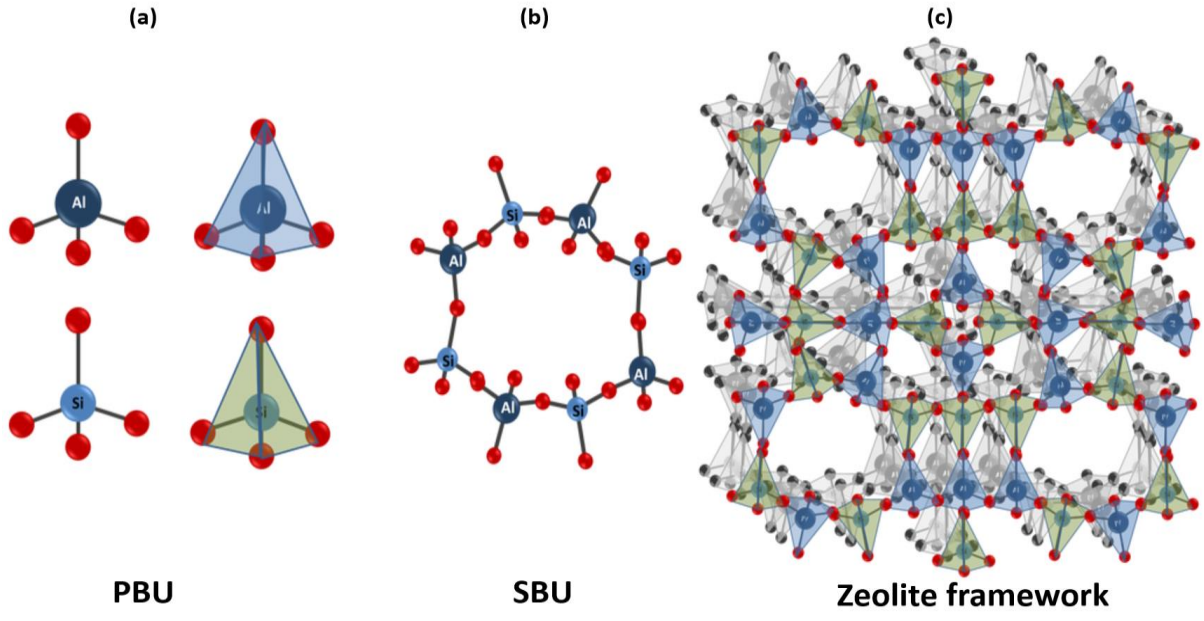

***Figure 3-7**: a) AlO_4 and SiO_4 tetrahedrons forming zeolite primary building units (PBUs). b) Tetrahedrons arranged in a ring to create secondary building units (SBUs). c) Joining SBUs produces the zeolite framework, which has cavities and channels of different size* [183].

The charges of the combination of SiO_4 tetrahedrons are completely balanced [182]. However, the replacement of some of the Si^{4+} by Al^{3+} in the SBUs leads to anionic (negative charge) frameworks of zeolites. The rise of negative charge when the tetrahedrons combine is a consequence of the valency differences between the $(AlO_4)^{5-}$ tetrahedron and $(SiO_4)^{4-}$ tetrahedron, which resides on one of the O anions in Al-O bonds. The resulting anionic frameworks are usually balanced by alkaline or/and alkaline earth cations such as K^+, Na^+, Ca^{2+} and Mg^{2+}. These counterions are located in zeolite channels and cavities, where they bind the aluminosilicate structure with electrostatic bonds [184], allowing exchange of ions to occur. Large nanocavities can also be occupied by water molecules, which surround the exchangeable ions. Note that the channel/cavity dimensions should be large enough to fit guest species. Therefore, the three main components of the zeolite structure are the aluminosilicate framework [$Al_x\ Si_y\ O_{2(x+y)}$], the exchangeable counterions [M^{n+} where is Na^+, K^+, Ca^{2+}, Mg^{2+}], and a number w of water molecules [wH_2O]. Hence, the general formula of aluminosilicate zeolites is $M_{x/n}\ [Al_x\ Si_y\ O_{2(x+y)}].\ wH_2O$ [185] [184]. Zeolites are typically cation exchangers; they can replace an identical number of counter cations on the surface with cations having the same charges from an adjacent solution, without any remarkable change in their structure.

3.3.3.1.2 Types

Zeolites occur naturally with varied morphologies and have been found in a diversity of geological sites around the world as volcanogenic sedimentary rock [185] [184] [186]. Natural zeolites have varied chemical compositions and cation exchange capacities due to different formation environments [185]. Clinoptilolite, mordenite, phillipsite, erionite and chabazite are the most common natural zeolites. Other zeolites are synthetic and are produced commercially with high purity and high cation exchange capacities, or with other specific properties (e.g. Na-zeolite form) [187][188]. P (GIS), X (FAU) and A (LTA) are examples of artificial zeolites. Zeolites are classified as cation exchangers according to the negative charge of their frameworks comprising cations as counterions. Alternatively, zeolite surfaces can be chemically modified to generate a net positive charge that is capable of binding anions in adjacent solutions instead of cations such as F^- and ClO_4^- [189][190].

3.3.3.1.3 Applications

Over the years, zeolites have received great interest due to their usefulness in various environmental, industrial, and scientific applications. They demonstrate excellent performance in water treatment, catalysis, the medical field and environmental monitoring applications [185] [187] according to their sorption properties as a satisfied capacitance for cation exchange and molecular sieve [8]. Zeolites act as ion exchangers when they substitute their counterions with other ions from the next phase. Because zeolite pores and cages possess different sizes and shapes, various molecular (and ionic) species can enter or be adsorbed by zeolites (acting as molecular sieves) when these species have a size similar to the zeolites' pores, and thus the large species will be rejected [184]. This enhances the selectivity of zeolite sorbents.

Zeolites have proven their efficacy in the purification of contaminated water against a variety of pollutants, including heavy metals, radionuclides, and organic and inorganic compounds as a result of their excellent radiation, thermal and chemical stability, availability, and low cost [184]. Water contaminated with heavy metals such as Hg^{2+}, Cd^{2+}, Pb^{2+}, and Cu^{2+} has been effectively purified using zeolites [59][60]. Natural zeolites can also selectively remove ammonium from wastewater [191][192]. Zeolites also play an important role in eliminating radioactive ions from wastewater such as $^{137}Cs^{+}$ and $^{90}Sr^{2+}$ that release to the environment resulting from nuclear incidents [55] [193].

The various types of zeolites vary in their affinity towards certain molecular or ionic species. For example, mordenite as a natural zeolite [$Na_3KCa_2(Al_8Si_{40}O_{96}).28H_2O$] [184][194] was effectively employed to selectively eliminate Cs^{+} from aqueous solution even in the presence of other cations (e.g. Na^{+} ,K^{+} [195], Na^{+}, NH_4^{+} [196]) and from sea water with high quantities of Na^{+}, Cl^{-}, Ca^{2+}, K^{+}, Mg^{2+}, SO_4^{2-} [57]. On the other hand, clinoptilolite [$(Na,K,Ca)_{3-6}(Al_6Si_{30}O_{72}).20H_2O$] [182][197] has a high removal efficiency for heavy metal cations Pb^{2+}, Cu^{2+}, Zn^{2+} and Cd^{2+} as evidence in the literature [59][60][198].

Zeolites have been incorporated in some potentiometric sensors, such as ion-selective electrode (ISE) [189][199] and ion-selective field effect transistor (ISFET) biosensors [200]. ISEs have been sensitised with zeolites as ionophores to detect several cationic and anionic substances in water, as presented in Table 3-1. The response characteristic of such sensor followed Nernstian response characteristic (section 3.4.1) and showed satisfactory selectivity with limit-of-

detections (LoDs) in the range of µM. This encourages to use zeolites as ion-exchange sorbents to be a sensitiser in the newer class of potentiometric sensors, WGTFTs, to detect several analytes. Mordenite and clinoptilolite were utilised as probable candidate sensitisers in WGTFT sensors for the selective detection of Pb^{2+} and Cu^{2+}as heavy metal cations and Cs^{+} as radioactive cations in water in this current study, as will be demonstrated in Chapters 6 and 7.

Table 3-1: *Some of the ISEs that were sensitised with zeolite ionophores to detect number of cations and anions in water, giving Nernstian response characteristic*

substance	***Zeolite ionophore***	***LoD [µM]***	***reference***
Thionine (cationic dye)	mordenite	0.8	[167]
Cs^{+}	Zeolite A	40	[199]
SO_4^{2-}	surfactant-modified clinoptilolite	70 *	[189]
ClO^{-}_4	surfactant-modified zeolite Y	0.4	[190]

*nM

3.3.3.2 Ion-exchange resins

Organic resins are another class of ion-exchange sorbents widely used for water treatment. Resins are insoluble polymers that effectively exchange their counterions (associated with their functional groups) with particular ions of the same charge that are being in the external solution. Resins are artificial polymer matrix (beads) with diameters in the 0.6 mm–1.0 mm range [8]. Resins usually consist of styrene and divinylbenzene as the backbone of the resin, where styrene molecules are the basis of the matrix, and divinylbenzene functions as a crosslink between the polystyrene chains, hence building a three-dimensional network structure (Figure 3-8). The degree of crosslinking determines the mesh-width of the matrix, i.e. the inner pore structure of the resins, which in turn may affect ion movements. Crosslinking also contributes to the insolubility and toughness of the resins. The amount of crosslinking varies in the 3-16% range [201].

The resin matrix carries a hydrophilic functional group charged with exchangeable ions, which is covalently bonded to phenyl groups at different locations (Figure 3-8). Ion-exchange resins are classified as cation or anion exchangers depending on the functional group type. If the functional group holds a negative charge, the exchange will involve cations. If the functional group is positively charged, resin will allow an exchange of anions. Resins are available with various formulas according to the diversity of the ionic groups. R-SO_3Na, R-COOH, R-PO_3H_2 are examples of cation exchanger resins, and R-NH_3OH is an example of an anion exchanger resin. Furthermore, the functional group of ion-exchange resin can form a multi-coordination complex with metal ions when it contains two or more electron donor atoms, such as oxygen (O), nitrogen (N), and sulphur (S). This type of resin is called chelating resin.

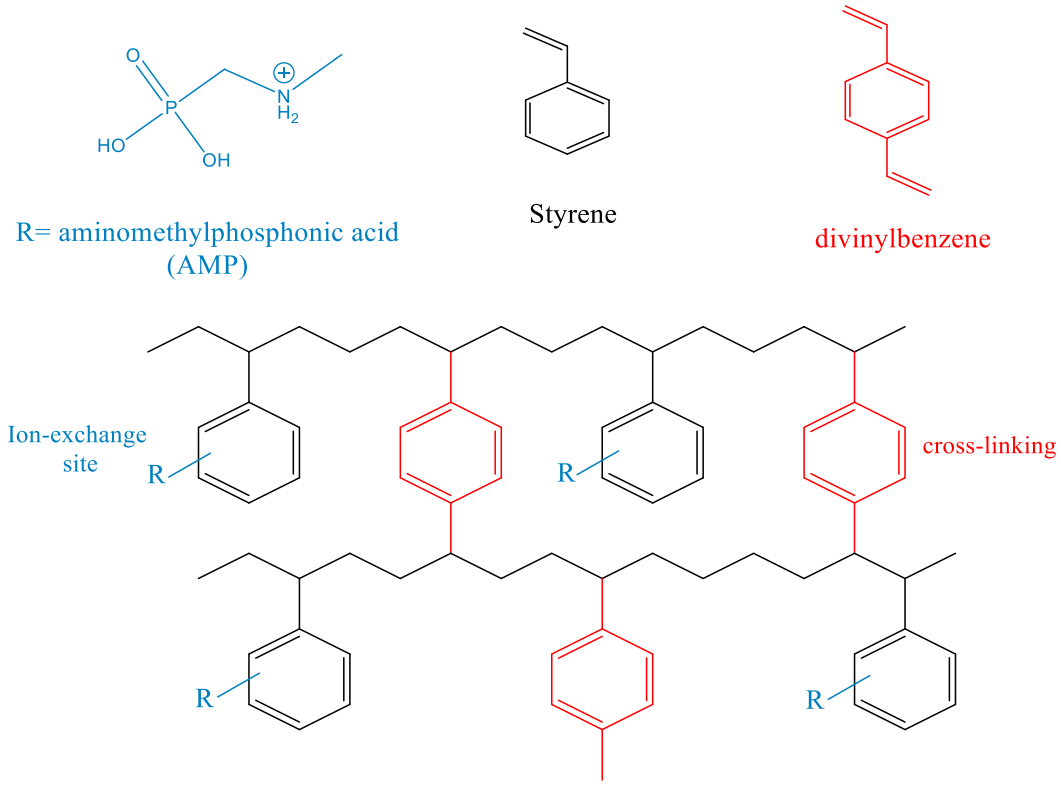

***Figure 3-8**: Illustration of the resin structure, which is typically divinylbenzene crosslinking polystyrene with covalently attached ionic functional groups.*

Resins are mostly used in water purification applications, such as softening [202] and demineralisation [203]. Remarkably, these resins can effectively remove toxic heavy metals, such as arsenic [204], mercury [205], and copper [206], and valuable metals, such as gold

[207], from water. Resins perform good selectivity and high thermal and chemical stability with low-cost advantages. This encourages employing this type of ion-exchange sorbent as a sensitiser in WGTFT sensors, similar to inorganic zeolites, in the current project (Chapter 8). According to our knowledge, this is the first time of merging resins as a sensitiser in the potentiometric sensors including WGTFTs.

3.4 Characteristics of sensing response

3.4.1 Nernst response characteristics

The response characteristics of most potentiometric sensors toward specific ions follow the Nernst equation presented below.

If the phase transfer membrane or the ion-selective membrane (ISM) is located between two solutions: sample (external) solution and reference (internal) solution, in which the sample or test solution is an unknown analyte concentration while the analyte concentration is known in the reference solution, the membrane potential will build up. For illustration, the analyte (ion) in both sides of the membrane interacts with the sensitiser loaded within the membrane. Due to the difference in ionic activities on both sides, a potential will arise across the membrane. Thus, the membrane potential is a consequence of the relative difference in the ionic activities between the external and internal solutions. This is calculated using the Nernst equation [208] as follows:

$$E_m = E_o + 2.3\frac{RT}{zF}\log\frac{a}{a_{ref}} \qquad (3\text{-}9)$$

In which E_m = ΔV represents the membrane potential i.e., the difference in potential between the two sides of the membrane. In the formula, E_o is the standard potential, R is the ideal gas constant (8.314 J/K mol), T is the temperature in Kelvin, F is the Faraday constant (9.643 × 10^4 C/mol), and z is the target ion valency (e.g., z = 2 for Mg^{2+} and 1 for Na^+). The 'a' and 'a_{ref}' in the equation refers to the activity of the target ion on external and internal solutions, respectively. Note that in some cases of the WGTFT sensors following the Nernst behaviour and due to E_o is a constant for the sensor, E_o does not contribute to the threshold shift evaluation [ΔV_{th} (c) = V_{th} (c) – V_{th}(c = 0)] as the sensor metric of the WGTFTs [35][123][209]. As a consequence, E_o can be neglected and rewrote the previous equation to be (equation 3-10):

$$\Delta V = 2.3\ \frac{RT}{zF}\ \log\frac{a}{a_{ref}} \qquad 3\text{-}10$$

The $2.3\ \frac{RT}{zF}$ represents the Nernst slope, which at room temperature (25℃ /298 K), is equivalent to $\frac{59\ mV}{z}$; that, in turn, yields 59 mV when z = 1 and 29.5 mV when z = 2. Therefore, equation 3-10 can be rewritten as equation 3-11:

$$\Delta V = \frac{59\ mV}{z}\ \log\frac{a}{a_{ref}} \qquad 3\text{-}11$$

The increased membrane potential is consistent with the activity of the target ion (a). The later denotes the effective concentration of ions. The relation between the ion concentration (c) and activity (a) can be expressed in equation 3-12 [208]:

$$a = \gamma\ c \qquad 3\text{-}12$$

in which γ is the activity coefficient; γ =1 in the case of the dilute system [210]. Subsequently, the ion activity is roughly equivalent to the concentration; $\frac{a}{a_{ref}} \approx \frac{c}{c_{ref}}$. Equation 3-11 can be rewritten as equation 3-13:

$$\Delta V = \frac{59\ mV}{z}\log\frac{c}{c_{ref}} \qquad 3\text{-}13$$

In reality, the ionophore cannot be entirely selective for one particular ion. However, the ionophore can interact with a distinct ion more strongly than other ions. Hence, the selectivity of the ionophore indicates the tendency of the ionophore to react with a specific ion over other interfering ions. The selectivity can be determined by considering the selectivity coefficient $K_{i,j}$, as seen in equation 3-14 below [211]:

$$K_{i,j} = \frac{a_i}{(a_j)^{\frac{z_i}{z_j}}} \qquad 3\text{-}14$$

Where a_i is the activity of the primary or target ion, a_j represents the activity of the interfering ion, z_i is the charge of the target ion, and z_j is the charge of the interfering ion. $K_{i,j}$ for the selective ionophore to the specific target ion a_i over the interfering ion a_j is larger than 1. However, when $K_{i,j}$ =1, the ionophore interacts equally with target and interfering ions.

When the interaction with the interfering ions was considered in addition to the target ion's interaction, the Nernst equation was modified to another equation called the Nikolsky-Eisenman equation [212], shown as equation 3-15:

$$\Delta V = \frac{59\,mV}{z}\log\left(\frac{a_i + K_{i,j}\,(a_j)^{\frac{z_i}{z_j}}}{a_{ref}}\right)$$

or $$\Delta V = \frac{59\,mV}{z}\log\left(\frac{a+a_{st}}{a_{ref}}\right) \Leftrightarrow \Delta V = \frac{59\,mV}{z}\log\left(\frac{c+c_{st}}{c_{ref}}\right) \qquad 3\text{-}15$$

in which $a_{st} = K_{i,j}.(a_j)^{\frac{z_i}{z_j}}$. The term $a_{st} = c_{st}$ is a property of the ion-sensitive system (sensor), equivalent to the limit-of-detection (LoD) concentration of such a sensor due to the presence of interfering ions.

Figure 3-9 illustrates the Nikolsky-Eisenman law as the relationship between the target ion's activity in logarithmic scale *vs* membrane potential. It is clear that, in the Nikolsky-Eisenman response, the membrane potential is a linear function for higher activity (or concentration) of the target ion $a_i \gg a_{st}$; this is identical to the Nernstian response. For lower ion activity $a_i \ll a_{st}$, the Nikolsky-Eisenman response is a flatline, differing from the Nernstian response. The latter gives an unrealistic infinite membrane potential when $a_i \to 0$. In addition, the Nikolsky-Eisenman behaviour is more realistic than the Nernstian response in terms of the existence of interfering ions in an aqueous medium that never reach 0, even in DI water as a result of autoprotolysis process described in sections 1.1 and 2.2.2.1. Therefore, c_{st} constitutes the LoD of the target ion. Practically, the electrolyte-gated field effect transistor (EGFET), which adopted the organic macrocycles ionophores, have been given LoDs within the limits of 100 nM - 1 µM [35][52][34].

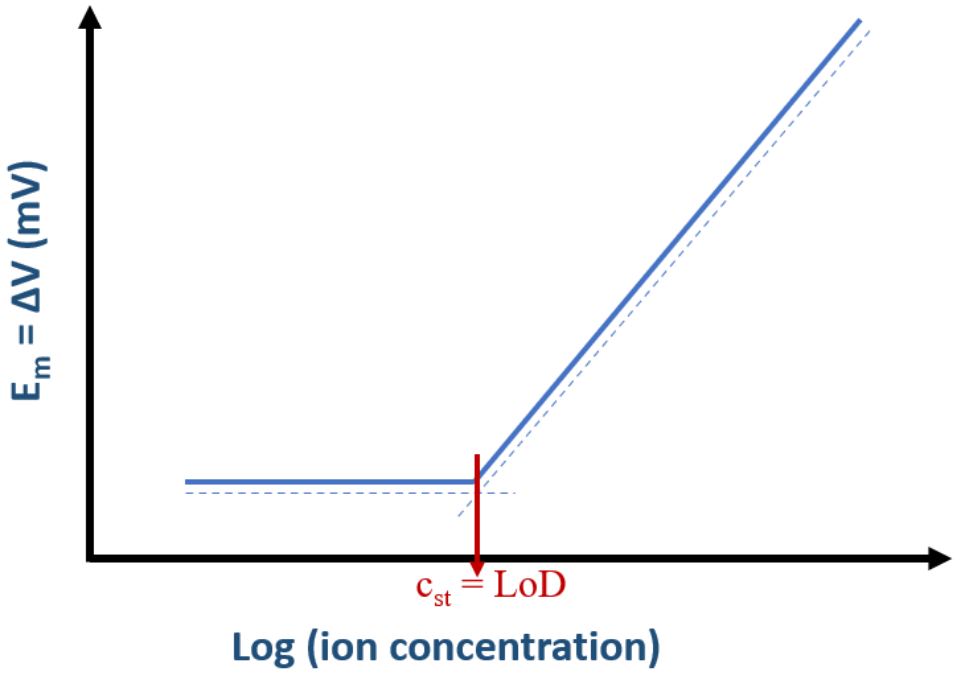

Figure 3-9: *Relationship of membrane potential vs ion concentration (proportional to ion activity) in logarithmic scale which undergoes the Nikolsky-Eisenman response and showing cst as LoD.*

3.4.2 The Langmuir adsorption isotherm

The Langmuir adsorption isotherm has been extensively applied to describe the adsorption equilibrium process. This model was initially designed to characterise the adsorption equilibrium of gas molecule adsorbates on the surface of a solid adsorbent by Irving Langmuir in 1916 [213]. The Langmuir isotherm presumes that the adsorption sites on the adsorbent's surface are all equivalent and identical with equal binding energy for each adsorbate leading to homogeneous adsorption. In addition, more assumptions are considered in the Langmuir isotherm, such that the adsorbates never interact or transmigrate between the adsorbent sites, and each site is occupied by one adsorbate, resulting in the creation of an adsorbed species monolayer covering the adsorbent surface [214].

In the adsorption process, ions or molecules of gas or liquid (adsorbate) adhere to the solid surfaces (adsorbent). Therefore, this technique includes two substances: 'adsorbate' that adsorbs on the adsorbent's surface, which can be ions or molecules of gas or solute dissolved in liquid, and 'adsorbent,' on which the adsorption is occurring on its surface. When the

adsorbate (X) adsorbs onto the vacant position or binding site on the adsorbent (M) surface, the dynamic equilibrium of this chemical reaction can be expressed as:

$$X + M_{surface} \overset{K}{\Leftrightarrow} XM_{surface} \qquad 3\text{-}16$$

$XM_{surface}$ represents the binding complex of X and M.

The equilibrium constant or binding constant (K) quantifies the strength of the interaction between the adsorbate X and binding site on the adsorbent surface M (equation 3-16) can be defined as:

$$K = \frac{[XM]}{[X]*[M]} \qquad 3\text{-}17$$

where brackets represent the concentrations of the corresponding compound [215]. $[X]$ and $[M]$ are proportional to the adsorbate concentration and available binding sites on the adsorbent; and $[XM]$ is proportional to the occupied sites binding with the analyte.

If the occupied adsorption sites denote the fractional surface coverage (θ) of the adsorbent, where $0 < \theta < 1$, the fraction of unattached sites on the surface can be expressed as $(1 - \theta)$. Therefore, the term $[XM]/[M]$ can be written as:

$$\frac{[XM]}{[M]} = \frac{\theta}{1-\theta} \qquad 3\text{-}18$$

By expressing $[X]$ as concentration 'c' of the adsorbate in relation to equation 3-18, equation 3-17 can be rewritten as:

$$K = \frac{\theta}{c\,(1-\theta)} \qquad 3\text{-}19$$

From equation 3-19, the equation that presents the Langmuir adsorption isotherm is:

$$\theta(c) = \frac{Kc}{Kc+1} \qquad 3\text{-}20$$

Figure 3-10 illustrates the Langmuir isotherm characteristic as a relationship between surface coverage (θ) and adsorbate concentration (c).

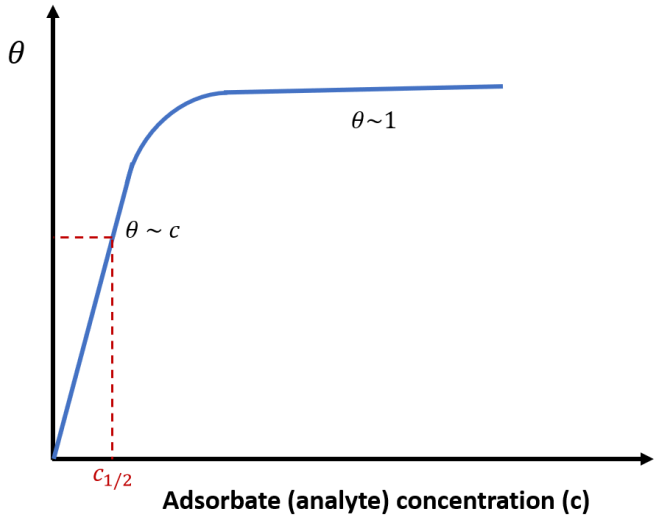

Figure 3-10: *The Langmuir isotherm characteristic and the extracting of* $c_{1/2}$ *characteristic.*

As seen in Figure 3-10, the $c_{1/2}$ characteristic can be easily extracted from the Langmuir isotherm characteristic, which defines the bonding (or occupying) of half the available binding sites on the adsorbent with the adsorbate. Thus, $\theta\left(c_{\frac{1}{2}}\right) = \frac{1}{2}$; $c_{1/2} = \frac{1}{K}$. It is clear that at low concentrations of adsorbate, $c \leq c_{1/2}$, the Langmuir isotherm is a linear relationship in which θ is proportional to c with slope K ($\theta \simeq Kc$) when $c << c_{1/2}$, while when $c >> c_{1/2}$, the Langmuir equation tends to $\theta = 1$. Note that if a sensor response exhibits the Langmuir isotherm characteristic, the adsorbate constitutes the analyte (e.g., the ion or molecule) and the adsorbent is the sensitiser; they are included in the sensor's architecture, and the same assumptions would be considered.

The maximum adsorption capacity (S_{max}), related to the adsorbent used, should be considered in the Langmuir equation. S_{max} implies the full occupation (saturation) of all available binding sites in the adsorbent (sensitiser) by the analyte, which is a constant property of the system being studied (sensor) [216], and can be extracted from the Langmuir response. The Langmuir equation can be written then as:

$$\theta(c) = \frac{S(c)}{S_{max}} = \frac{Kc}{Kc+1} \qquad 3\text{-}21$$

or $$S(c) = S_{max}\,\theta(c) = S_{max}\,\frac{Kc}{Kc+1} \qquad 3\text{-}22$$

in which $S(c)$ is the adsorption at analyte concentration c.

Equation 3-22 can be rearranged to be:

$$\frac{1}{S(c)} = \frac{1}{S_{max}\,K}\frac{1}{c} + \frac{1}{S_{max}} \qquad 3\text{-}23$$

If (1/S) is plotted against (1/c), this yields the Hildebrand-Benesi plotting [217], a linearised form of the Langmuir equation. The relationship of 1/S *vs* 1/c a straight line in the form $y = mx + b$ with $(m = 1/S_{max}K)$ as the line slope and $(b = 1/S_{max})$ as the intercept, is shown in Figure 3-11. The binding constant (K) and the maximum adsorption capacity (S_{max}) are important properties of the sensor and can be extracted using Figure 3-11 [217][218].

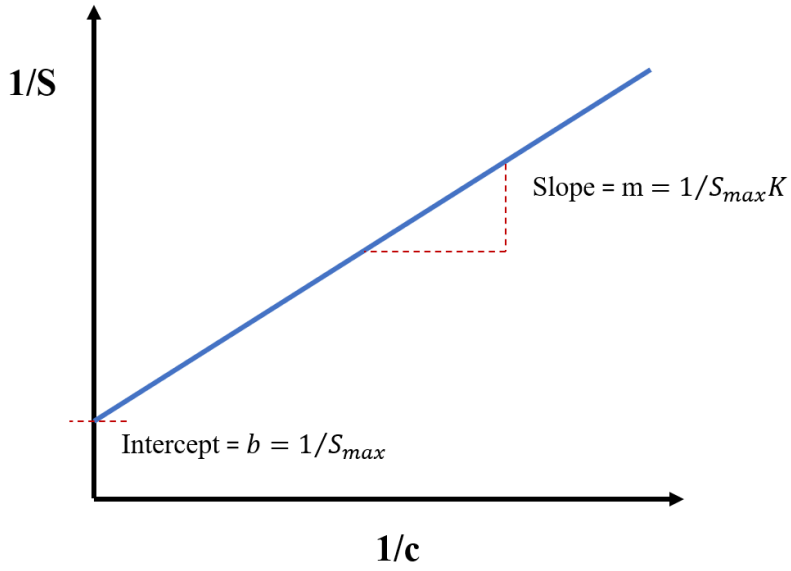

Figure 3-11: *The Hildebrand-Benesi plotting that illustrates the extracting of K and Smax characteristics of the sensor.*

As seen in Figure 3-11, K can be quantified as

$$K = \frac{b}{m} \qquad 3\text{-}24$$

and $$S_{max} = \frac{1}{b} \qquad 3\text{-}25$$

The LoD is the vital characteristic of sensors that implies the lowest analyte concentration to which the sensor can respond. To quantify the LoD of the sensor that follows the Langmuir response characteristic, the response characteristic should be linearised in the form y = mx + b (equation 3-22) by plotting $(Kc + 1).S(c)$ against the concentration (c); straight line with intercept near zero (b ± Δb) and slope (m) will be obtained in which Δb is the estimated standard error, as seen in Figure 3-12. Therefore, LoD is defined as [219]:

$$LoD = \frac{3\,\Delta b}{m} \qquad 3\text{-}26$$

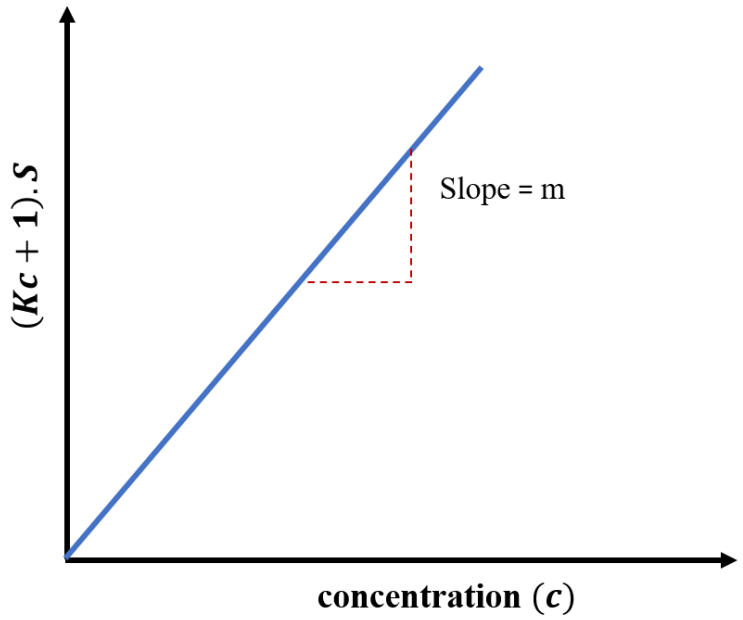

Figure 3-12: *The Limit-of-detection (LoD) determination.*

3.4.3 The Langmuir-Freundlich isotherm

The Langmuir-Freundlich isotherm is similar to the Langmuir isotherm with a modification. This isotherm is derived from the combination of the Langmuir and Freundlich adsorption isotherms [220][221], providing a flexible analytical model that is widely applied to characterise a variety of adsorption responses [220][222]. The Langmuir-Freundlich adsorption isotherm is written as:

$$S(c) = S_{max} \frac{(Kc)^{\beta}}{1+(Kc)^{\beta}} \qquad 3.27$$

where $S(c), S_{max}, K,$ and c are earlier defined, and β represents the inhomogeneity of the binding sites [221]. When the binding sites on the adsorbent surface (sensitiser) are homogeneous; $\beta = 1$ and K are equal for all binding sites and thus the equation 3.27 goes to the Langmuir adsorption isotherm (equation 3-22). However, when $\beta < 1$, the binding sites are in homogeneous and the adsorption response will follow the Langmuir-Freundlich adsorption isotherm (equation 3.27) due to using the heterogeneous adsorbents in the sensing system [220].

The Langmuir and the Langmuir-Freundlich adsorption isotherms have been widely used to characterise the uptake response of various analytes using e.g., zeolites [57][192], resins [223][61] and activated carbon [222] as adsorbents. In addition, a number of potentiometric sensors have been reported as following the Langmuir and the Langmuir-Freundlich isotherms as a response to the detection of various molecules such as amine [74] and others in potentiometric biosensors [224][225]. However, it does not represent yet a potentiometric sensor designed for ion detection that follows the Langmuir or the Langmuir-Freundlich isotherm models as we investigate in this study.

3.5 The project's aim

Water pollution with e.g., heavy metal and radioactive ions has become a matter of global concern. It is a growing threat all over the world as a consequence of several activities including waste disposal, industrial accidents and expansion of human activities, as reported in section 2.1. Various technologies are used for the monitoring of drinking water versus such pollutants such as inductively coupled plasma atomic emission spectrometry (ICP-AES), UV–Vis spectrometry, and atomic absorption spectrometry (AAS) [44][46]. These methods require costly instruments, pre-treatment of samples, and specially trained personnel [226][227].

In the field of electroanalytical chemistry, potentiometric techniques are important methods that are often used to determine various ions [228]. Potentiometric sensors offer considerable advantages including low-cost, ease of use, low LoD, short response time, and high selectivity and sensitivity [226][227][228]. These sensors, namely ion-selective electrodes ISEs (section 2.3.2.1), have been extensively used in water monitoring against a number of harmful ions. A significant number of macrocyclic compounds have been employed in the construction of potentiometric sensors to determine various ions. Table 3-2 demonstrates macrocyclic ionophores that have been used in the ISEs for the detection of heavy metals and radioactive ions in water. Such sensors exhibited Nernstian response characteristics (section 3.4.1) with LoDs presented in Table 3-2. This level of LoDs is not sufficient to monitor drinking water against Pb^{2+}, Cu^{2+}, and Cs^{+} pollutants.

Table 3-2: *LoDs obtained by ISE potentiometric sensors based on macrocyclic ionophores.*

Ion	***Ionophore***	***LoD [µM]***	***Reference***
Pb^{2+}	acridono-crown ether (ISE)	7.9	[226]
	15-crown-5	0.2	[229]
	1,3,7,9-tetraaza-2,8-dithia-4,10-dimethyl-6,12diphenylcyclododeca-4,6,10,12-tetraene (TDDDCT)	0.25	[230]
	2,3,4:10,11,12-dipyridine-1,3,5,9,11,13-hexaazacyclohexadeca-2,10-diene	1	[231]
	double-armed calix[4]arene amide derivatives	0.5	[232]
	5,11,17,23-tetrakis[(p- carboxyphenyl) azo]-25,26,27,28-tetrahydroxy calix[4]-arene	1	[176]
Cu^{2+}	5,10,15,20-tetrakis(4-allyloxyphenyl) porphyrin (TAPP)	0.8	[227]
	12-crown-4	17.8	[233]
	pyrido-pentapeptide derivatives	80 *	[234]
	3,6, 9,14-tetrathiabicyclo[9.2.1]tetradeca-11,13-diene	0.32	[235]
Cs^{+}	calix[4]crown ether ester	5	[236]
	dibenzo-24-crown-8 ether	5.2 *	[237]
	4´,4´´(5´)di-tert-butyldibenzo-18-crown-6 (DTBDB18C6)	4	[238]
	1,3-alternate thiacalix[4]biscrown-6,6	0.25	[175]

*nM

WGTFT sensors have recently belonged to the potentiometric sensors providing desired properties including low threshold voltage and low voltage operation. This is a consequence of the development of the electric double layers (EDLs) allowing high specific capacitance (in $\mu F/cm^2$), as reported in section 2.2.1. WGTFT sensors have been used to detect some ions in water such as Na^+, K^+, Ca^{2+} employing organic macrocyclic ionophores [34][35][52][123]. In this case, such sensors followed the Nernstian response characteristic with LoDs in the range of 100 nM - 1 µM. This level of the LoDs are acceptable for the previous mentioned ions that are commonly present in drinking water in millimolar concentration (Table 6-1) [239]. To implement WGTFTs as sensors for the detection of the heavy metals (e.g., Pb^{2+} and Cu^{2+}) and radioactive (e.g., Cs^+), macrocyclic ionophores (as reported in section 3.3.2 and Table 3-2) may not be the right choice to achieve LoDs much lower than that included in Table 3-2. Therefore, adaptation of another type of ionophores is required to achieve this goal.

Ion-exchange materials have extensively been used in water treatment. Zeolite and resin are the common examples of these materials. Mordenite and clinoptilolite zeolites show good selectivity extraction of Cs^{+} [57][195][196] and Pb^{2+}/Cu^{2+} heavy metals [59][60][198] from water, respectively, as reported in section 3.3.3. In addition, fluoride can cause fluorosis illness when high amounts are consumed (above the potability limit > 79 µm) [11][240][241].

Metal-activated Puromet^{TM} MTS9501 resin displayed excellent selectivity removal of fluoride anion from water [61]. The great results of extraction Cs^{+}, Pb^{2+}/Cu^{2+}, and F^{-} by mordenite zeolite, clinoptilolite zeolite, and activated Puromet^{TM} MTS9501 resin inspire us to utilise these ion-exchange materials to be ionophores in the WGTFTs for the first time to the best of our knowledge. Sensitised WGTFT sensors with ion-exchange sorbents as ionophores have achieved the main object of this study which is building a low-cost, portable, easy to operate, and high selectivity and sensitivity sensor to detect harmful ions in water such as heavy metal and radioactive ions, as presented in chapters 6,7 and 8.

Chapter 4 : Water-Gated Transistor Sensor Fabrication

This chapter presents the fabrication process of thin-film transistors (TFTs), including the supporting substrates and contact electrodes that clean and deposit, respectively. The deposition of the semiconductor thin film on the supporting substrates using a spray pyrolysis technique is also described. Such transistors are then ready to operate across water in the gate medium, as shown in Figure 4-1. The current chapter also shows the construction of the water-gated thin film transistor (WGTFT) as a sensor, with sensitised membrane placed horizontally into the transistor's gate medium, which separates the water in the gate medium into two chambers: the outer pool containing the sample solution and the inner pool containing the reference solution, creating the 'two-chamber design' of the WGTFT sensors, as seen in Figure 4-1 e, adopted in this work. The process of fabrication of sensitised PVC phase transfer membranes with ion-exchange sorbents, which were then incorporated into the architecture of the WGTFT sensor, in the two-chamber design, is reported in this chapter.

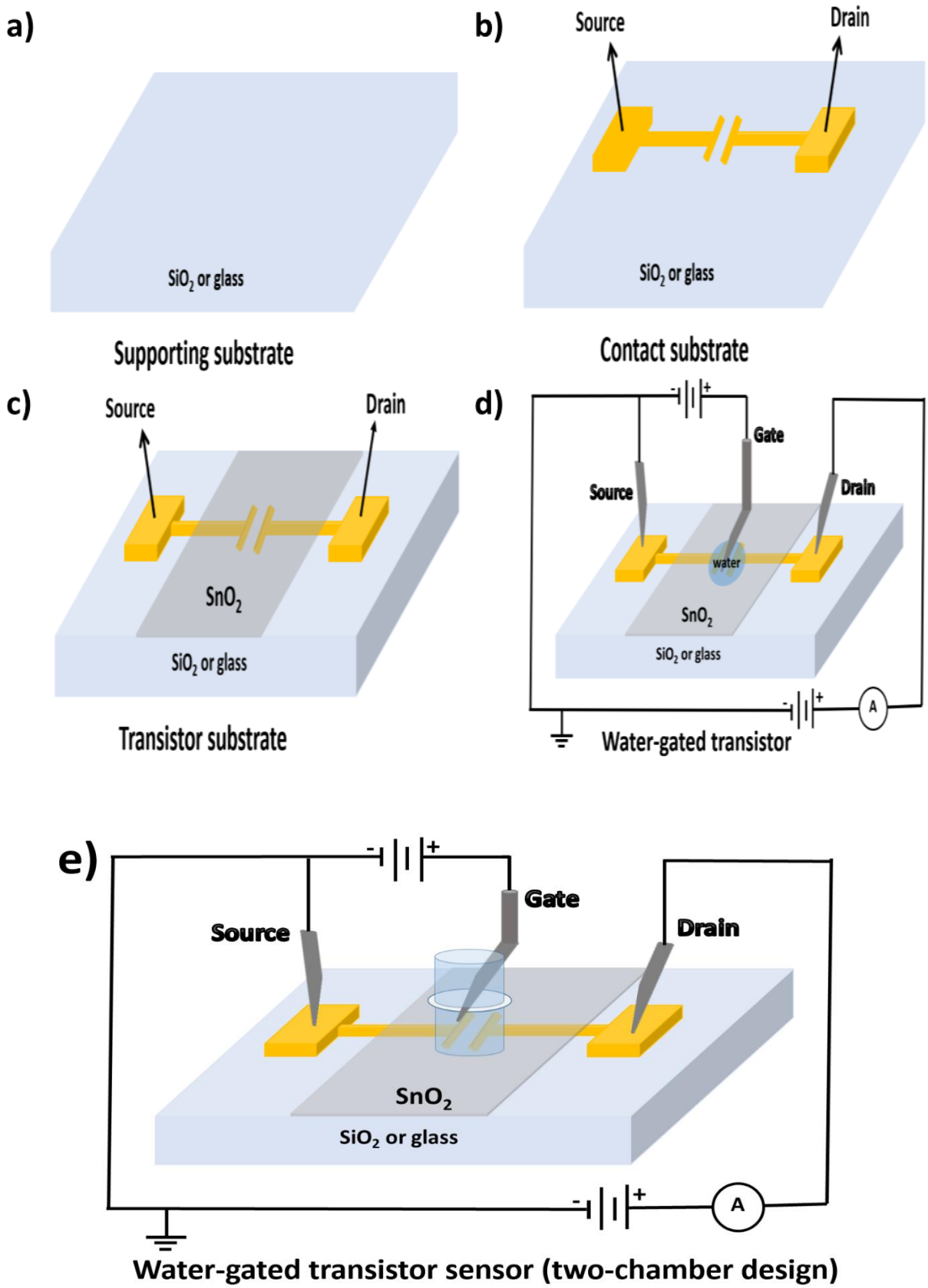

Figure 4-1: *Schematic representation of the construction stages of a water-gated transistor sensor: a) supporting substrate, b) contact substrate, c) transistor substrate, d) water-gated transistor, and e) two-chamber design of the water-gated transistor sensor.*

4.1 Supporting substrate

The preparation of transistor substrates (Figure 4-1 c), followed by the construction of the WGTFT sensor, was performed on a specific supporting substrate (Figure 4-1 a), consisting of flat glass slides (20 mm x 15 mm) with a thickness of 1.1 mm covered with 20 nm of SiO_2, which were supplied by Ossila Ltd, Sheffield, UK. Such substrates were used in this work to configurate top-gate and bottom-contact transistors.

4.1.1 Cleaning of the supporting substrate

Cleaning the supporting substrate slides is a crucial stage in transistor fabrication and must occur before any deposition process is attempted. The cleaning allows for proper adhesion of the contacts and semiconductor film, and results in higher-quality performance transistors. This particular procedure took place in a cleanroom, with sterile conditions under room temperatures, and performed with tweezers and gloves.

Organic residues present on the substrate slides were removed using various cleaning stages of organic solvents applications and ultrasonic baths. The supporting substrate slides were first inserted into a Teflon substrate holder, which holds them far enough apart to be cleaned effectively. The supporting substrates were then immersed into deionised (DI) water for five minutes. They were then extracted from the DI water and dried with dry nitrogen. In the second stage of the cleaning, the substrates were placed into a Teflon holder and submerged into an acetone -filled clean Teflon container, and then placed into an ultrasonic bath at 55^{o}C for 5 minutes. Following this, the supporting substrates were removed from both the ultrasonic bath and acetone, and dried with dry nitrogen. This step was repeated again using isopropanol instead of acetone. Finally, the supporting substrate slides were placed in a petri dish to be clean with UV ozone, which will be explained in the next section.

4.1.2 Ultraviolet (UV)ozone cleaning

Once the supporting substrates had been cleaned with organic solvents (using an ultrasonic bath as reported in the previous section), all remaining residual organic matter on the supporting substrate surfaces was eliminated using the UV ozone technique. Ozone is an effective oxidising agent [242] capable of breaking down any organic substances left on the substrate surface. To clean the supporting substrates with UV ozone, the petri dish that stored

these substrates was relocated to the ozone apparatus for 4.5 minutes. Figure 4-2 shows its construction. When the wavelength of the UV light is 184.9 nm, the atmospheric oxygen is consumed to produce ozone, and vice versa where the wavelength of the UV light is 253.7 nm.

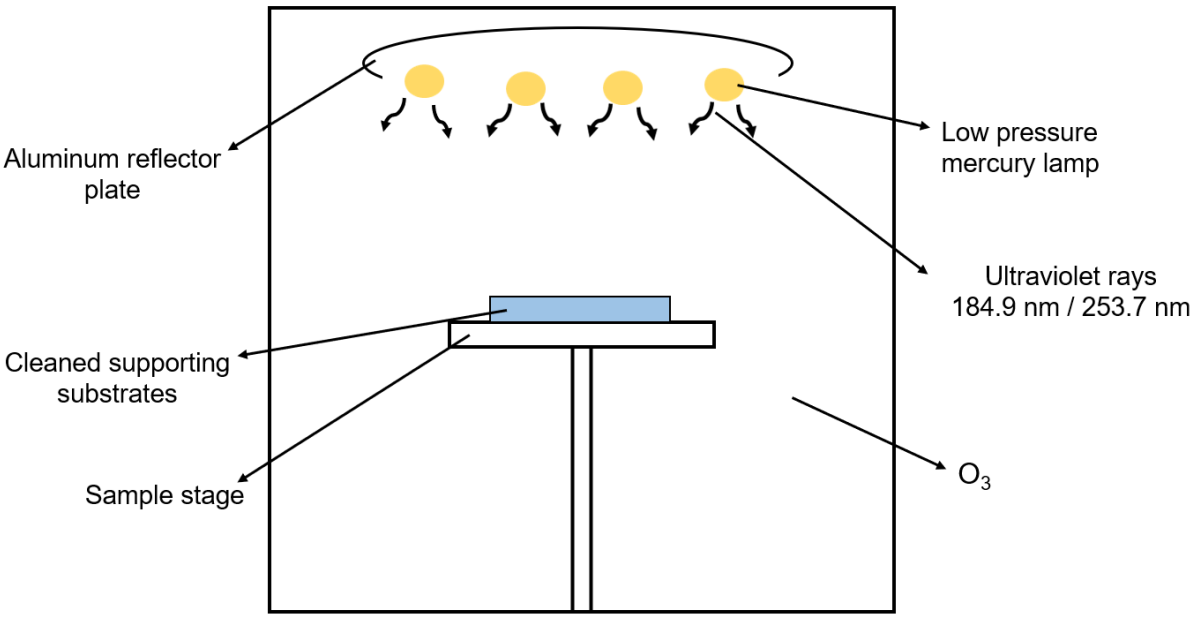

Figure 4-2: *Diagrammatic representation of the construction of the ultraviolet-ozone instrument used to clean the supporting substrate surface.*

4.2 TFT contacts deposition

Once the supporting substrate slides were cleaned, they were ready for the construction process, namely the transistor substrate fabrication. This section describes the thermal evaporation technique that was used to deposit the contact electrodes of the TFT on the supporting substrates to produce the contact substrates (Figure 4-1 b).

4.2.1 Thermal evaporation technique

Thermal evaporation, which is also known as physical vapour deposition (PVD), is a technique employed in this work and used, with a shadow mask, to deposit pairs of transistor contacts. The key point of the thermal evaporation is the heating of materials under a vacuum, with the goal of transitioning them from a solid to vapour stage. High vacuum is crucial in this procedure

to avoid any reaction that may occur between gas molecules and the evaporated elements, namely collisions or oxidation [243]. This reaction may cause a reduction in the long 'mean free path' of the evaporated atoms or molecules on their way from material source to substrate surface.

The mean free path length (λ) of travelling molecules or atoms can be evaluated with equation 4-1:

$$\lambda = \frac{k_B T}{\pi\sqrt{2}\ p\ d^2} \qquad 4\text{-}1$$

Where k_B stands for the Boltzmann constant, T is the absolute temperature, p represents the vapour pressure, and d denotes the molecule/atom diameter.

Under a pressure of 10^{-6} Torr, it can be estimated that the mean free path $\lambda \approx 44$ metres for a typical metal atom with 0.4 nm diameter. λ, in this case, is much longer than the distance in the evaporator between the heating terminal and the supporting substrates, just 15 cm, as shown in Figure 4-3a. Consequently, the vacuum operated in our thermal evaporation is more than sufficient for physical vapour deposition.

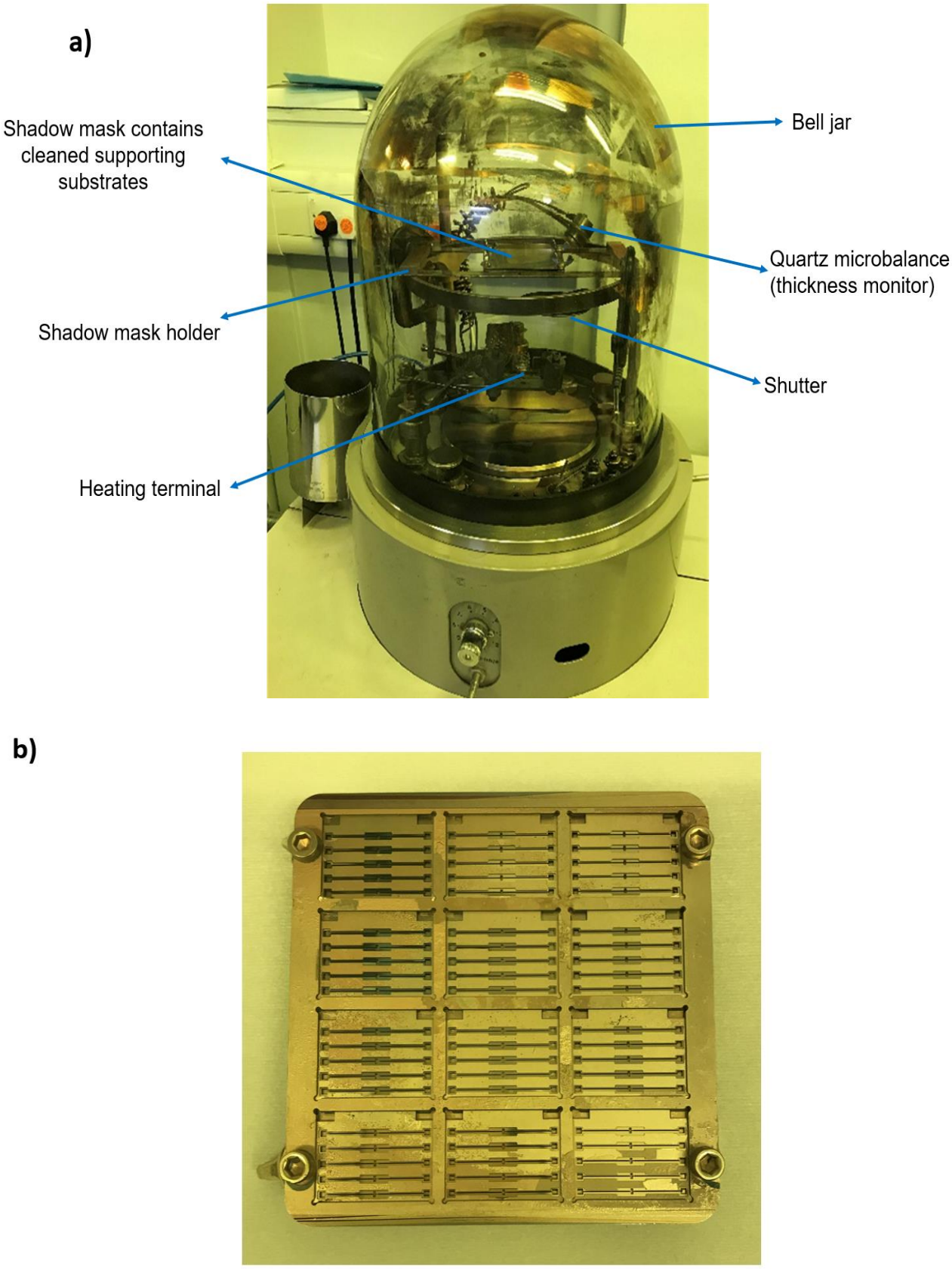

Figure 4-3: *Photos of a) Edwards (E306) thermal evaporator with labelling of some of its components, b) a shadow mask stack holding cleaned supporting substrates.*

Figure 4-3a shows the construction of the Edwards (E306) thermal evaporator. This type is typically used in the deposition of thin layers of metals, organic and inorganic materials of low molecular weight. The device consists of a glass bell jar 30.5 cm in diameter and 35.5 cm high. The substrate slide holder (Figure 4-3a) holds the shadow mask stack, which in turn contains 12 of the cleaned supporting substrates. There is a shutter disc in the evaporator, located between the surface of the substrates (held in the mask, which is the target surfaces) and the heating terminals. The thermal evaporation involves also the quartz crystal microbalance (QCM) placing at a short distance from both the evaporation source (heating terminals) and supporting substrates. The QCM plays an important role during the evaporation process, which will be discussed in the next paragraph. The pumping system is responsible for the intensity of the thermal evaporator's vacuum. This system at the bottom of the dome includes high-vacuum and rotary pumps. The two pumps are instrumental in reducing the chamber pressure, at a range of 10^{-5} – 10^{-8} Torr.

The QCM in the evaporator measures the thickness of the deposited film on the supporting substrates, as well as the rate of deposition. The QCM is made up of a thin quartz plate with metallic electrodes. The deposition of mass on the QCM's surface reveals a shift in the resonant frequency of the quartz crystal. In this situation, the film's thickness can be evaluated by the difference in resonant frequency, resulting in the accumulation of the mass on the quartz crystal surface, using the Sauerbrey equation [244] (equation 4-2)

$$\frac{\Delta f}{\Delta m} = -\frac{2f_o^2}{A\sqrt{\rho_q \mu_q}} \qquad 4\text{-}2$$

Where Δf refers to the modifications of frequency, f_o represents the resonant frequency, Δm denotes the mass change, A refers to the exposed quartz crystal area, ρ_q and μ_q stand for the quartz density, which is 2.648 g/cm^3, and the shear modulus of the quartz, which is 2.947x10^{11} g/cm. s^2.

4.2.2 TFT contact deposition using thermal evaporation

Two metal sources can be uploaded to the two thermal evaporation vessels, which facilitates the evaporation of two different metals (chromium [Cr] and gold [Au]) simultaneously, without needing to break the vacuum. For this process, pure gold wire is placed on a tungsten boat on one heating terminal, and a chromium-coated tungsten coil is placed on another. The choice of

tungsten (boat or coil) as the delivery medium due to its high melting point, thus enabling metals with lower melting points to be deposited onto it. The tungsten boat containing gold wire and the chromium-coated tungsten coil were both linked to the source of DC current, resulting in the resistive-Joule heating of the tungsten boat and coil, which in turn heats the metals. The current that flows for the thermal evaporation of the metals used in this work was in the range of 1.6 - 2.5 A.

The following process describes the production of a pair of contacts on the pre-cleaned supporting substrates (as illustrated in section 4.1) via thermal evaporation. The supporting substrates were first located on a steel frame, ensuring that the SiO_2-coated face of the substrates face the source of the metallic evaporation (chromium and gold) on the heating terminal. Next, a shadow mask (supplied by Ossila) was placed on the surfaces of the supporting substrates. The shadow mask can hold a dozen contact substrates, each of which includes five pairs of contacts, as shown in Figure 4-3b. The substrates, arranged on the shadow mask, were then positioned on a substrate slide holder in the evaporator. This holder consists of two parallel steel pieces placed in front of the thermal terminals. Approximately 4 cm of pure gold (Au) wire was placed on the centre of the tungsten boat, which had been bonded to the heating terminal connected to the current source. Due to the gold's poor adherence to the SiO_2 and oxide glass surfaces, Cr metal was used as an adhesive layer between the gold layer and the glass surface. For this, the tungsten coil, coated with Cr, was connected to heating terminal A of the evaporator. Once the supporting substrates, metals, and tungsten boat and coil were installed, the bell jar was then closed. The pressure inside the jar reduced to 10^{-7} Torr via a vacuum system. The DC current was increased manually for the Joule heating of the evaporation boats. At the beganing of evaporation and during the current adjustment, the evaporator shutter was closed to prevent any of the material source's residual and volatile pollutants from reaching the target surfaces. Once the adjustment of the deposition rate had been achieved, the shutter was opened, enabling Cr or Au vapor to deposit at a constant evaporation rate onto the slides and through the shadow mask. The deposited film's thickness, as well as the deposition rate, were monitored with the QCM, as reported earlier. After reaching the film's required thickness, the shutter was closed again, and the current was switched off. Chromium, used as an adhesive layer, was initially deposited on the supporting substrates at a rate of 0.2 Å/s, with a gold film deposited on the same substrates in a similar way at a rate of 1 Å/s. This process resulted in a 10-nm thin film of Cr beneath a 100-nm thin film of Au, which acted as the transistor's contact electrodes.

Figure 4-4 shows the resulting substrates the 'contact substrates' from this stage. The contact substrate contains five pairs of gold electrodes. A small channel in between the two electrodes in each pair was established, with the following dimensions: length (L) = 0.03 mm and width (W) = 1 mm; thus W/L is 33.3. The contact substrates, including the Au electrodes and adhesion layer Cr, were ready for the next stage of the semiconductor film deposition to produce the transistor substrate. Note that Au metal shows good resistance to corrosion and oxidisation, and there are slight barrier injections when it is aligned with the SnO_2 thin-film semiconductor (described in the next section), which negligibly affect the charge injection within the transistor, as illustrated in section 3.1.1. Although Cr and Al metals display free barrier injunctions with the SnO_2 semiconductor, they form oxide layers when they are exposed to high temperatures through the deposition of the semiconductor film [245].

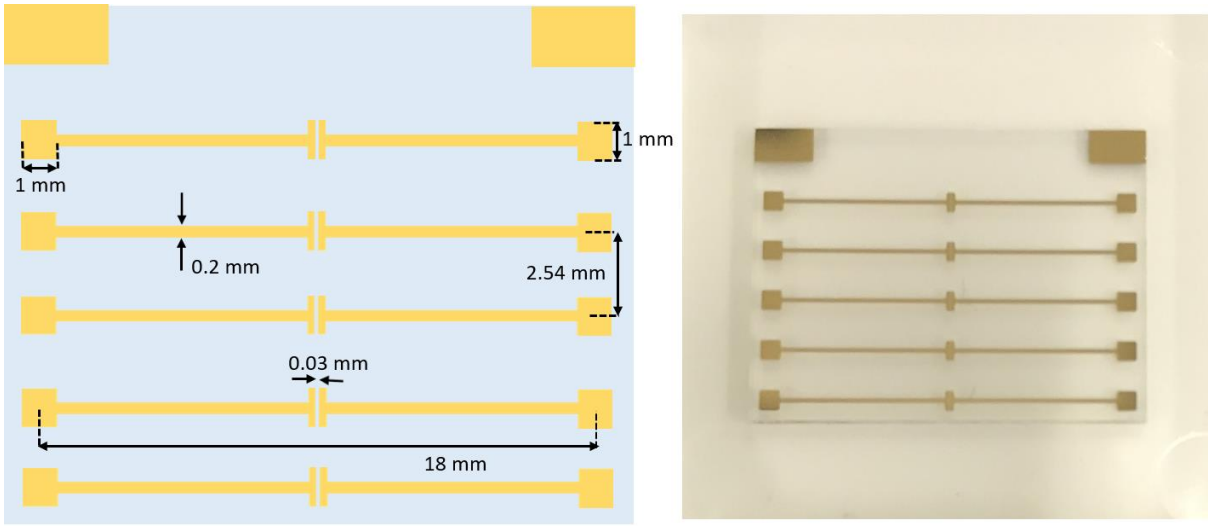

Figure 4-4: *The geometry of contact substrate (left) and a photograph of the supporting substrate with deposited chromium and gold contacts to produce the contact substrate with five gold contacts (right).*

4.3 The deposition of a semiconductor thin film using a spray pyrolysis technique

After the preparation of the contact substrates (using thermal evaporation) was completed (as explained in the previous section), a semiconductor film was applied onto the contact substrate that links the contact pair (source and drain electrodes) to yield a transistor substrate. Various techniques can be used for the semiconductor thin film deposition. This section explains the

‘spray pyrolysis’ as a solution-processed technique used to deposit the semiconductor film on the contact substrate.

4.3.1 Spray pyrolysis technique

Spray pyrolysis refers to a chemical technique that ends up forming a thin film layer by spraying appropriate precursor solution onto a hot surface, in which a suitable solvent is used to dissolve the precursor. The target film is derived once the precursor’s solvent evaporates and a corresponding pyrolysis reaction occurs [246]. This technique has been widely used to synthesise various materials in different applications, such as solar cells and TFTs [246][247][89]. For instance, metal oxide semiconductors (ZnO, SnO_2, In_2O_3) have been extensively fabricated using the spray pyrolysis method in previously mentioned applications [248][249][35][140][85].

In respect of other deposition techniques, spray pyrolysis offers some benefits, due to it being simple and cost- effective. Other benefits include the potential to spray over a wider area and coat various types of substrates with complex geometries [247]. Moreover, spray pyrolysis does not require high-quality substrates, and it can produce homogeneous films with a thickness of 0.1 – 1 μm [247][250].

The principal usage of the spray pyrolysis technique is to spray a precursor solution, using an atomiser which generates the required small droplets of the precursor and aim it towards a heated substrate; thus, the film will form on the substrate. Consequently, a typical system consists of a substrate heater, temperature controller, precursor solution, and atomiser. Various types of atomisers can be employed in this method, such as electrostatic, compressed air or ultrasonic atomisers [248]. In this study, a compressed air atomiser (also known as an airbrush) was used to spray the precursor solution through a jet of air. This can be seen in Figure 4-6.

When using spray pyrolysis for film deposition, several parameters are crucial to keep in mind, such as droplet size and speed, surface temperature, precursor solution concentration, and the distance between the nozzle and the substrate [35]. Figure 4-5 shows the spray mechanism of the pyrolysis for a precursor droplet exposed to a hot surface; we see it in four different scenarios within two stages, as reported by Falcony et al. [89]. In the first stage, a consistent size of droplet is exposed to different substrate- temperatures (gradually increasing from A to D), as shown in Figure 4-5a. In the second stage (Figure 4-5b), different droplet sizes, decreasing from A to D, are subjected to the fixed substrate- temperature. The deposition

mechanism in these two cases can be represented as follows: at a low substrate- temperature (or initially large droplet size), a small proportion of droplets evaporates when it reaches the substrate, since the solvent does not vaporise completely within the droplet. Once this droplet hits the substrate surface, it evaporates, leaving behind a dry precipitate in ring form, and the decomposition occurs (Process A). At low to intermediate substrate temperatures (or if the droplet size is a large to medium size), in Process B, the solvent is vaporised; thus, the dry precipitate strikes the substrate surface where the pyrolysis reaction has occurred. In Process C, where the substrate-temperature is medium-high (or the droplet size is medium-small), the droplet performs the previous Process B, and then the dry precipitate is vaporised close to the substrate surface, giving rise to a chemical vapour deposition (CVD) on the substrate surface. Finally, when the substrate temperature is high (the droplet size being small), the vaporised precipitate undergoes a chemical reaction within the vapour phase and is turned into a powder before it reaches the substrate surface (Process D). The resulting films from Processes A and B show a high quality and excellent adhesion to the substrate, as reported by Perednis and Gauckler [247].

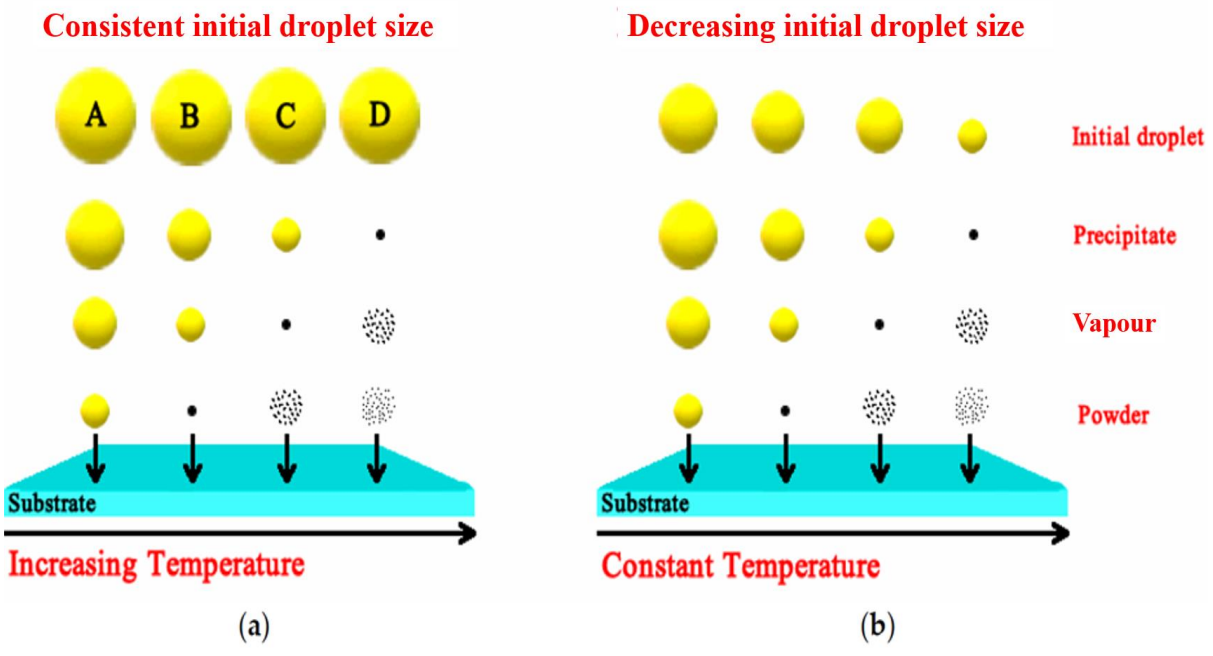

Figure 4-5: *Four different deposition mechanisms of the precursor droplets exposed to the substrate in two scenarios: (a) increasing substrate temperature and consistent size of the initial droplet, (b) decreasing initial droplet size and constant substrate temperature*

[89].

The substrate temperature, one of the key parameters of the spray pyrolysis deposition, play an important role in the resulting film properties, as early mentioned. Additionally, the crystallinity, electrical properties, morphology and visible transmission of the obtained film are influenced by the temperature of the substrate [247][251]. An example of this is ZnO film, which formed using aqueous zinc acetate precursor, exhibited modulation in its properties as a result of the substrate temperature variations [252]. High degrees of light transmittance and a thinner film were obtained when the substrate temperature increased to 490 ^{o}C. At higher temperatures, the crystallinity and homogeneity of the resulted film were enhanced, and thus improved charge mobility [252].

Moreover, some parameters such as the molar concentrations of precursor solution and salt, as well as solvent and additives in the precursor solution, can alter the properties of the sprayed film. To illustrate this, one needs to imagine low concentration precursors, with the smoother, thinner and more transparent films they obtain than when done in high concentrations [253]. Further, using various precursor salts such as Zinc nitrate ($Zn[NO_3]_2$), Zinc acetate (ZnAc) and Zinc chloride ($ZnCl_2$), dissolved in DI water to produce ZnO film, results in clear variations of transparency of ZnO and crystallinity. $ZnCl_2$ precursor yields better crystallinity and higher mobility while the ZnAc precursor shows higher transparent ZnO film [248][254]. In a similar example, SnO_2 films derived from pentahydrate tin chloride ($SnCl_4.5H_2O$) display lower resistivity than others that are produced from anhydrous tin chloride ($SnCl_4$) [255]. In terms of precursor solvents, copper oxide thin films sprayed from precursor dissolved in alcohol show higher transmittance than those produced from a precursor dissolved in distilled water [256]. Additives, or dopants, in the precursor solution can modify the film morphology. For example, adding acetic acid to the precursor solution changes the cracked TiO_2 film into free cracked film [247]. Aluminium doped into the SnO_2 thin film induces modification in the SnO_2 morphology, appearance of a smaller grain size in the film and reduction of film conductivity [257].

In this study, the SnO_2 thin film semiconductor was applied onto a contact substrate, as reported in section 4.2.2, to act as the transistor's semiconductor channel using spray pyrolysis technique. The SnO_2 precursor solution was conducted by dissolving 1.75 g of $SnCl_4.5H_2O$ in 100 mL of isopropanol to generate 0.05M of $SnCl_4.5H_2O$ as the best molarity of the precursor solution. Prior to depositing precursor-route SnO_2, a spray mask template was placed on the contact substrate to cover the contact electrodes and only those channels exposed to the

precursor solution, as shown in Figure 4-6. The contact substrate was heated to 400°C on a hotplate. The precursor solution was then sprayed onto the channel in the contact substrate (through the mask) using a commercial airbrush, with a nozzle of 0.2 mm at a pressure of 1.5 bar. The spraying process was performed in three short 'puffs', each lasting 1-2 seconds at intervals of one minute, from a distance of 20 cm from the substrate. The substrate remained on the hotplate for a further 30 minutes, leading to the development of the SnO_2 semiconducting film. Equation 4-3 describes the decomposition of precursors in forming the SnO_2 semiconductor film, as reported in [136]:

$$SnCl_4.5H_2O \rightarrow SnO_2 + 4HCl\uparrow + 3H_2O\uparrow \qquad 4\text{-}3$$

This preparation was carried out in the fume cupboard, using lab security gloves and glasses, and clean tweezers. Figure 4-6 illustrates the setup used to form the SnO_2 film by spray pyrolysis technique.

Hence, the transistor substrate, consisting of an SnO_2 thin film deposited on the contact substrate, was ready to be gated with water in order to operate the WGTFT. Note that the SnO_2 semiconductor WGTFT manifests excellent stability under water with a low threshold voltage [258]. The electrical characteristics of SnO_2 WGTFT will be elaborated upon in section 5.2. To the best of our knowledge, this operation, which was conducted by Nawal Alghamdi in our group, is the first to use SnO_2 in WGTFT [15].

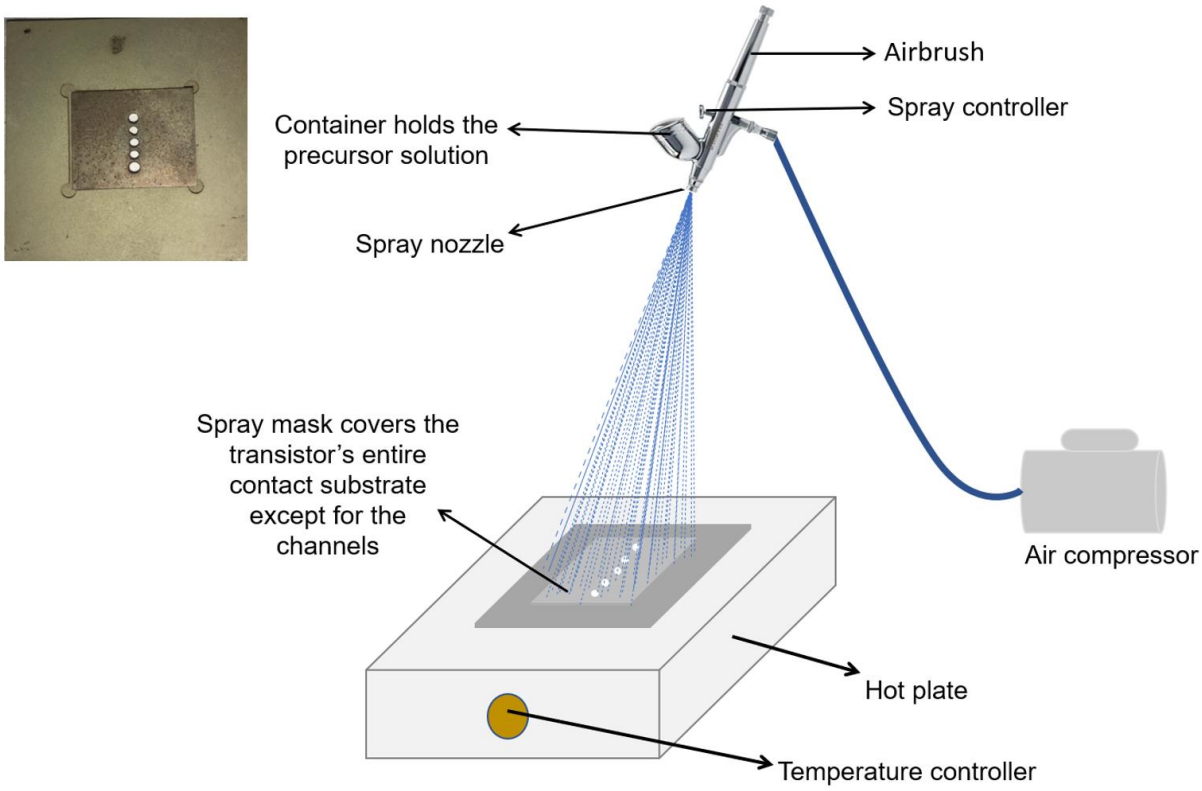

Figure 4-6: *Schematic representation of the technique used for the spray pyrolysis. It shows how the $SnCl_4.5H_2O$ precursor solution is sprayed on the contact substrate using airbrush in order to produce the transistor substrate. Inset: Photograph of the spray mask placed on top of the contact substrate.*

4.4 Two-chamber design of SnO_2 WGTFT as a sensor

The transistor substrate, its preparation described in section 4.3.1, was then used to design a 'two-chamber' setup to manufacture the WGTFT as a sensor. This design consists of an ion-selective membrane (explained in section 3.3) placed horizontally onto the transistor's gate medium, which separates two compartment units filling with solution. The lower chamber or inner pool was filled with reference solution (i.e., analyte-free water) and that was in contact with the SnO_2 transistor substrate at the bottom of the sensitised PVC membrane centre. This compartment remained filled with the analyte-free water as a reference during the sensing experiment. The upper chamber, or outer pool, was filled with the sample solution that was initially loaded with analyte-free water for sensor calibration and then subsequently replaced

with the same quantity of an increasing concentration of analyte solution to record the sensor response. The sample pool was in contact with a (L-shaped) tungsten (W) electrode, which functioned as the gate electrode of the transistor at the top of the sensitised PVC membrane centre. Source and drain contacts were also connected to the external circuit using tungsten needles to record the electrical characterisation of WGTFTs. It is worth noting that the sample pool was emptied after each measurement cycle and re-filled with samples of increased concentrations of salt. The preparation of the ion-selective membrane will be reported below in section 4.4.1. Figure 4-7 illustrates the 'two-chamber' setup of WGTFT sensors with a10-µL capacitance, 9- mm diameter and 0.5- cm height for each compartment.

The voltage applied to the gate contact is connected to the surface of the semiconductor across the membrane and water in both pools through interfacial electric double layers (EDLs), which was reported in section 2.2.1. The membrane develops the potential to respond to various concentrations of analyte in the sample- vs- reference solution. The membrane potential, which depends on analyte concentrations $V_M(c)$, is added to the applied gate voltage. Thus, the potential applied to the gate electrode differs from the potential on the semiconductor surface by membrane potential V_M. Due to the gate voltage required to turn the transistor from 'off' to 'on', known as the threshold voltage V_{th}, as reported in section 3.2, V_{th} thereby shifts by V_M as a result of the developed membrane potential. In this case, the analyte concentrations are increased in the sample pool, stepwise, and the membrane potential equilibrium takes place shortly thereafter (between 30 seconds and 6 minutes), as will be reported in Chapters 6, 7 and 8. The linear transfer characteristic of WGTFT was recorded for each analyte concentration to determine the modification in threshold voltage (ΔV_{th}), as a response of having changed the analyte concentrations in the sample pool, where, by definition, $V_M(c) = \Delta V_{th}$ (c). The evaluation routine of the threshold shift will be explained in section 5.2.1.5.

This design of WGTFT sensor is similar to the potentiometric ion selective electrode structure [199][259][260]. Schmoltner et al. [52] have demonstrated this novel sensor platform, based on electrolyte-gated organic field-effect transistors for selective ion detection, as the first ion-selective WGTFT. This innovative architecture is modular, enabling simple detection of various analytes by choosing a suitable sensitiser incorporated in the membranes. In this design, the analyte in the sample pool is never in contact with the semiconductor surface, which may lead to the interference of the analyte on the semiconductor film as in [209], giving a highly stable sensor. These benefits encouraged us to adopt the ion-exchange sorbents (zeolite or resin reported in section 3.3.3) as sensitisers in WGTFT, using this construction after failed attempts

to imbed the sensitised membrane with zeolite on the gate electrode as in [35][53] or incorporate such a sensitiser on the semiconductor film as in [123], as in previous designs of WGTFT sensors.

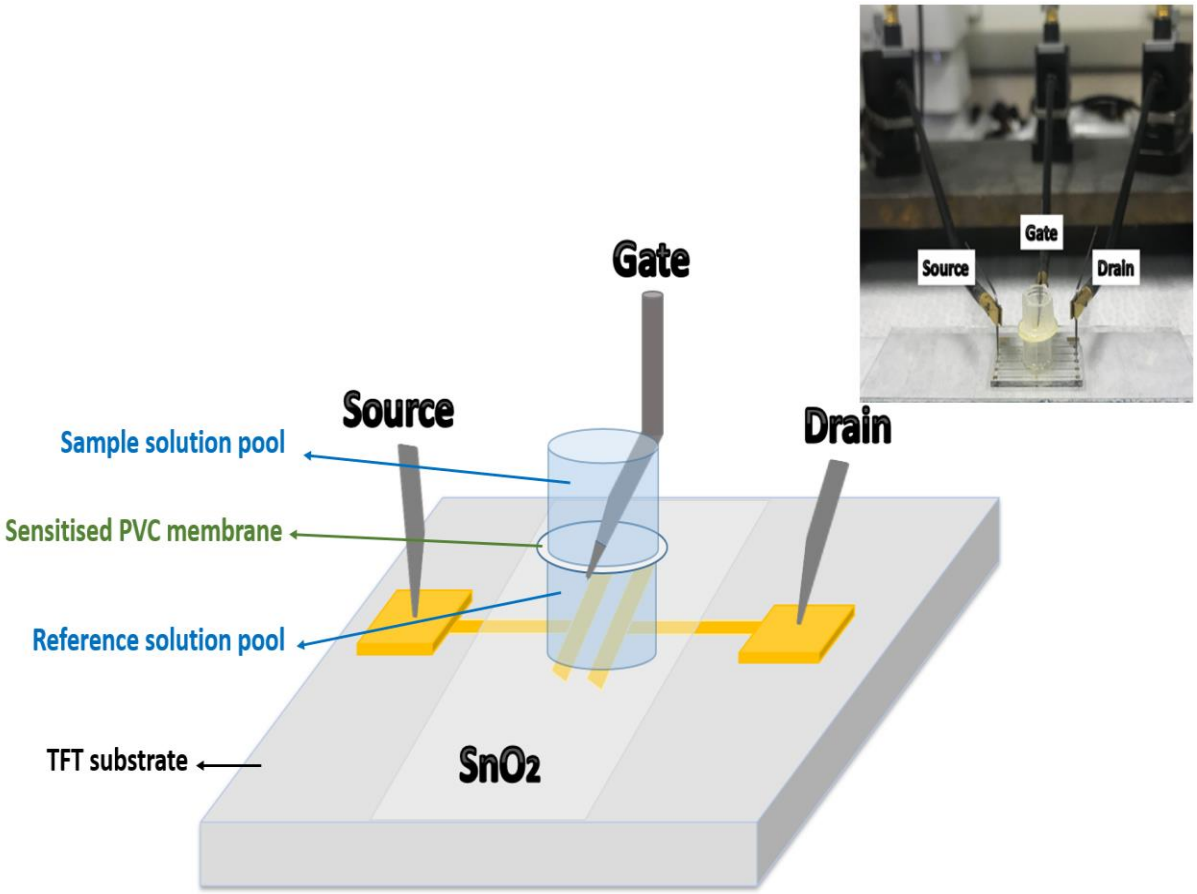

Figure 4-7: *Schematic diagram illustrating the construction of the 'two-chamber' design of the SnO_2 WGTFT sensor, involving the sample pool separated from the reference pool by a sensitised PVC membrane. Inset: Photograph of the design.*

4.4.1 Preparation of the ion-selective membrane sensitised with ion-exchange sorbents

As seen in section 4.4, the ion-selective membrane is the essential part of the WGTFT sensor design in this project. In the current study, inorganic zeolite (mordenite and clinoptilolite) and organic chelating resin (described in section 3.3.3) were embedded into plasticised PVC phase transfer membranes, as described in section 3.3.1, following the procedure described in [167].

The resulted sensitised membrane was then placed into the two-chamber design of WGTFT sensor (Figure 4-7).

The ion-selective PVC membranes were prepared by first dissolving 30 mg Poly(vinyl chloride) (PVC) and 65 µL 2-Nitrophenyl octyl ether (2NPOE) as a plasticiser into 3 mL tetrahydrofuran (THF). Then, 40 mg mordenite, 42 mg clinoptilolite or 39 mg metal-loaded MTS9501 chelating resin (explained in sections 8.2.1 and 8.2.2) was added to the mixture, which dispersed as a suspension. Next, 450 - 500 µL of membrane mixture solution was poured into a small vial and kept at room temperature overnight to allow solvent evaporation, resulting in membranes carrying approximately 7 mg/ 7 mg/ 5.6 mg of mordenite/clinoptilolite / metal-loaded MTS9501 resin each, respectively. The variation in the quantity of these ion exchangers (ionophores) in the plasticised PVC membranes can be attributed to the differences in their particle sizes, where mordenite and clinoptilolite were received as fine powder while the resin was coarse. Figure 4-8, shows the shape and diameter of the resulting membrane with a thickness of approximately 0.4 mm. The membranes were then conditioned overnight or for one day in tap water or deionised water based on the type of reference solution used in the WGTFT sensors. Finally, each membrane was introduced between the inner and outer pools into the WGTFT architecture, two-chamber design, with epoxy glue (as explained in section 4.4) to detect the following waterborne analytes: Cs^{+}, Pb^{2+} and Cu^{2+}, and F^{-}. The results of sensing these analytes will be shown in Chapters 6, 7, and 8, respectively.

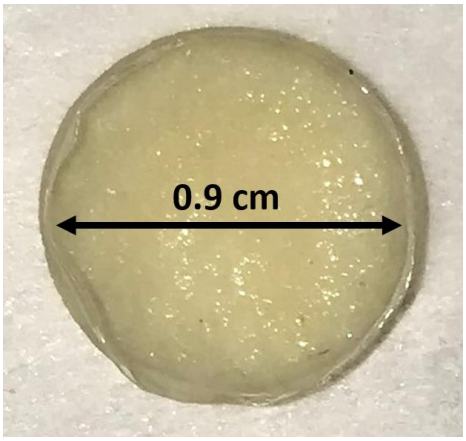

***Figure 4-8**: Image of La-loaded MTS9501 resin introduced in the PVC matrix.*

Chapter 5 : Equipment and electrical characterisations of the SnO_2 water-gated thin film transistor

This chapter starts with a description of the optical microscopy technique used to verify the quality of contact substrates before and after the deposition of the tin oxide (SnO_2) semiconductor thin film. Section 5.2 details the electrical characterisations of the SnO_2 water-gated thin film transistor (SnO_2 WGTFT) before introducing the sensitised PVC membrane into the WGTFT architecture. This chapter also includes an explanation of the method followed in this work to identify the key parameter in sensing specific analytes with WGTFT transducers.

5.1 Optical microscopy

Optical microscopy is a technique used to closely examine a sample using a magnifying lens with visible light. In this research, optical microscopy was employed to verify the quality of the contact substrate, the preparation of which was described in section 4.2.2. Prior to the deposition of SnO_2 semiconductor film on the contact substrate to generate the transistor substrate (reported in section 4.3.1), it is necessary to check the contact electrodes and channels for unwanted conductive links and any shorts or misalignment across the source and drain electrodes. Shorts might occur if the supporting substrates were incorrectly aligned relative to a shadow mask during the evaporation process. Figure 5-1 shows a typical contact substrate and perfect channel to build the transistor substrate.

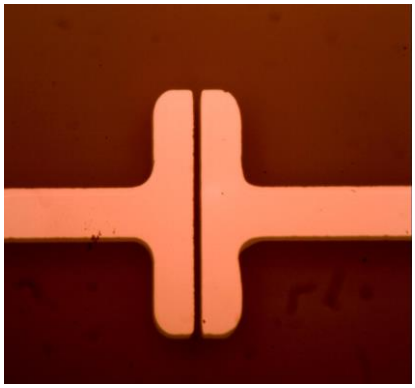

Figure 5-1: *Photo of the contact substrate with the channel region characterised using optical microscopy.*

Optical microscopy can also be exploited to examine the dispersion of ion-exchange sorbent sensitisers, such as powdered mordenite and coarse MTS9501 resin within the matrix of plasticised PVC membrane. The filling of the PVC matrix phase by these sensitisers should be considered during the preparation of the membrane. Figure 5-2 manifests the good distribution of mordenite (Figure 5-2 a) and La-loaded MTS9501 resin (Figure 5-2 b) particles within the PVC membranes. Such a microscope was also used to examine the change of grain size of La-loaded MTS9501 resin after grinding this coarse resin to be finer grains using mortar and pestle, as presented in section 8.3.2.

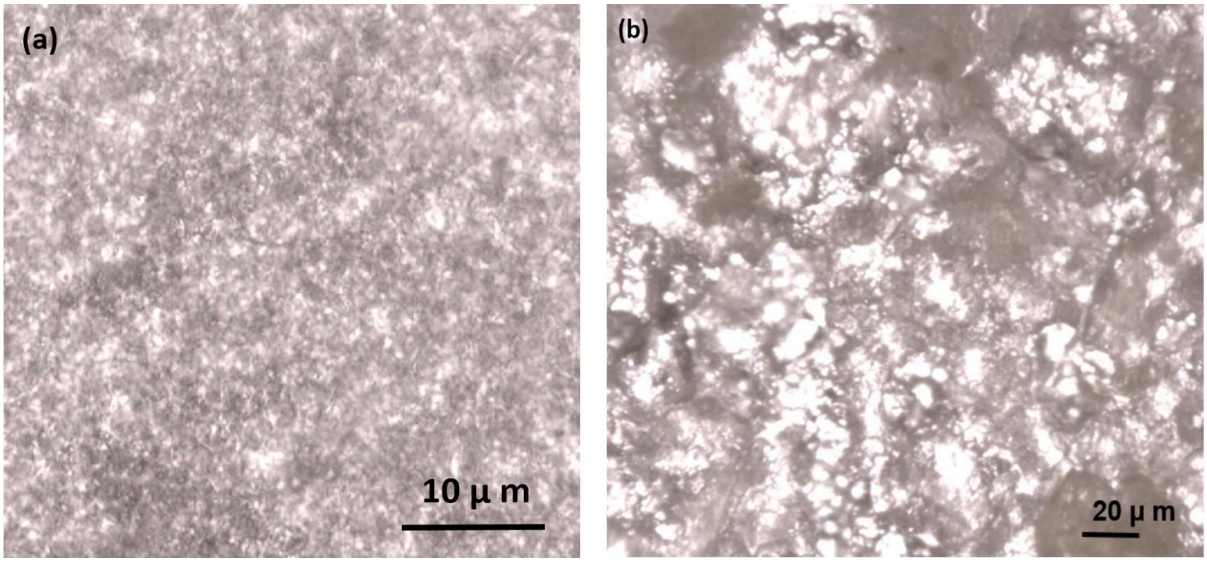

Figure 5-2: *Micrograph of (a) mordenite and (b) La-loaded MTS9501chelating resin dispersed in PVC phase transfer membrane.*

5.2 Electrical characterisation of SnO_2 WGTFT

The method used to manufacture the SnO_2 transistor substrate was reported in section 4.3. This section will present the process to record the electrical characterisations of an SnO_2 thin-film transistor (TFT) gated with a water droplet as an electrolyte, as shown in Figure 5-3, using Keithley units. The electrical characterisations, including the output and transfer characteristics of the SnO_2 WGTFT will be explored. Based on the analysis of these characteristics, some SnO_2 WGTFT parameters will be determined, such as the threshold voltage, charge carrier mobility and on/off ratio.

5.2.1 Source measure units to characterise WGTFTs

In this project, two Keithley 2400 source measure units (SMUs) controlled by bespoke LabView software were used to measure the electrical characterisations of WGTFT. Keithley units are used to source the current and measure the voltage driving the set current or to supply voltage and determine the resulting current by employing the 'current source-voltage meter' or 'voltage source-current meter' programming options, respectively. Only the second option, 'voltage source-current meter', was used in this project. The TFT was electrically connected to the Keithley units via coaxial cables, which in turn contact the transistor's electrodes using probe heads with fixed tungsten contact needles, as seen in the inset in Figure 5-3. As shown in Figure 5-3, Keithley SMU1 was connected to the source and gate electrodes of the TFT to supply the gate voltage (V_G), the source electrode of which was usually electrically grounded, and to record the gate current (I_G), which should be negligible (near zero). Keithley SMU2 was connected to the TFT's source and drain electrodes to supply drain voltage (V_D) and to record the drain voltage (I_D).

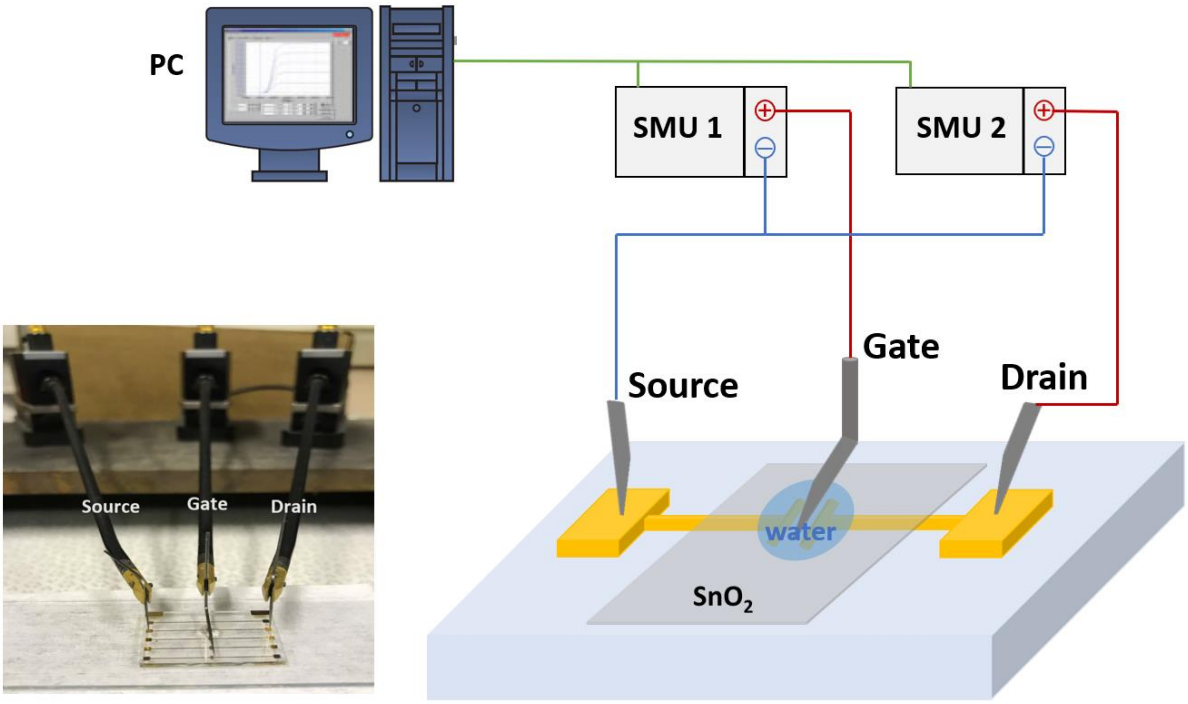

Figure 5-3: *Illustration of the connection of the SnO_2 WGTFT with Keithley 2400 source measurement units (SMU1 and SMU2) to record the electrical characterisations of SnO_2 WGTFT. Both units were used to supply voltage and measure the resulting current. Inset: Photo of SUSS MicroTec PH100 probe heads with fixed tungsten contact needles used to connect the TFT's electrodes with SMUs via coaxial cables.*

The Keithley units were linked to a PC running the bespoke LabView software by GPIB-PCI cables to record the electrical characteristics of the transistors. The software not only enables selection between the measurement of the output and transfer characteristics, but several measurement parameters can also be set, such as voltage range, delay time between steps, step size and repeated measurements of voltage from 0 to (+/-) value and back again to zero. The software begins the measurements automatically after the desired parameters are selected. The LabView software displays the applied voltages and resulting current data, which can be exported to a file for later detailed analysis in Excel format. In this chapter, the electrical characterisations (output and transfer) of SnO_2 WGTFT will be verified, as presented in sections 5.2.1.1 and 5.2.1.2. To record the output characteristics (drain current (I_D) vs. drain voltage (V_D) at constant gate voltage (V_G)) (see section 5.2.1.1), the setup parameters were selected as presented in Table 5-1 to record I_D. Table 5-1 also shows the selected parameters

in the case of recording transfer characteristics (I_D vs. V_G at constant V_D) in both linear and saturation regimes, as seen in section 5.2.1.2. The same parameters were also selected to record the linear transfer characteristics in terms of examining the performance of SnO_2 WGTFT as a sensor toward certain analyte; see section 5.2.1.5.

Table 5-1: *Example of input parameters to record I_D in both the output and transfer characteristics of SnO_2 WGTFT. The results are presented in Figures 5-4, 5-5 and 5-6.*

Parameter	**Output**			**Parameter**	**Transfer**	
V_D (V)	Start: 0	Rev start: 1		**V_G (V)**	Start: -0.8	Rev start: 0.8
	Stop:1	Rev stop: 0			Stop: 0.8	Rev stop: -0.8
	Step: 0.1	Step: -0.1			Step: 0.05	Step: -0.05
V_G (V)	Start: 0	Stop: 0.8	Step: 0.2	**V_D (V)**	0.1 (linear) 0.8 (saturation)	

5.2.1.1 Output characteristics

A TFT output characteristic is defined as a relationship between drain voltage (V_D) and drain current (I_D) carried at a collection of several consistent gate voltages (V_G).

The output is characterised by V_D sweeping from 0 to the V_D's maximum modulus (no more than 1.23 V in the case where water is the gate medium) in multiple small steps and then returning to 0 through reversed steps at a constant V_G, as seen in Table 5-1. Applying voltage $\geq$ 1.23 V results in the electrochemical decomposition of water molecules. The polarities of both drain and gate voltages must be in contrast to the polarity of the semiconductor carrier to characterise a transistor in accumulation mode, 'normally off'. This process is replicated for many V_G, producing I_D (V_D) characteristic family within different V_G, classified as TFT output characteristics. The output characteristics are linear $I_D \sim V_D$ at low V_D and saturated at high V_D, as explained in section 3.2.

Output characteristics are crucial in diagnosing the practical performance of TFTs, whether they correspond to the theoretical response of TFTs, as demonstrated in section 3.2, or when

there are deviations indicating that one or more of the transistor components have non-ideal characteristics, as reported in the next paragraph.

Figure 5-4 shows the output characteristics of the SnO_2 WGTFT device. For this, the SnO_2 semiconductor film, created by spraying $SnCl_4.5H_2O$ precursor solution on the transistor substrate, as explained in section 4.3.1, was gated via DI water, as seen in Figure 5-3. The SnO_2 semiconductor thin film enables good operation of a water-gated transistor showing good characteristics of an electron-transporting field-effect transistor. SnO_2 WGTFT output characteristics demonstrate the absence of contact limitation between SnO_2 film and contact electrodes and high on-current field-effect transistor, approximately 1.5 mA at V_G = 0.8 V. However, here I_D continues rising steadily at high V_D in the saturated regime because SnO_2 often exhibits some unintentional 'doping' in the transistor's channel. Hysteresis is also observed in the SnO_2 WGTFT characteristics and will be discussed in section 5.2.1.4.

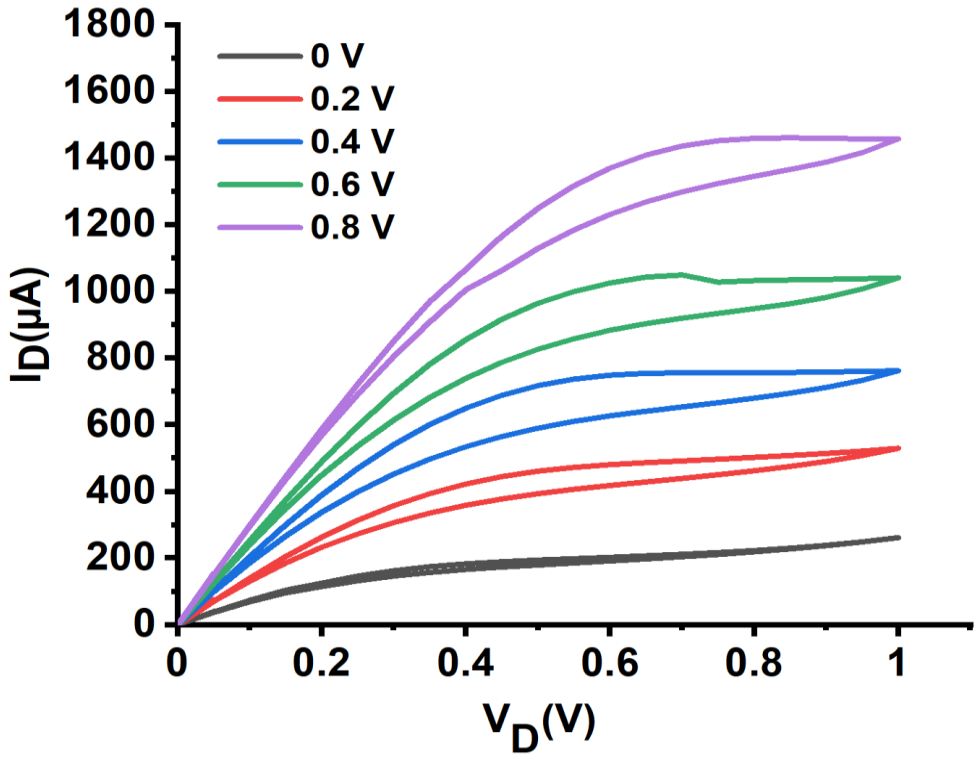

Figure 5-4: *Output characteristics of SnO_2 WGTFT at different gate voltages (V_G): 0, 0.2, 0.4, 0.6, and 0.8.*

5.2.1.2 Transfer characteristics

At a constant drain voltage (V_D), the relationship between the applied gate voltage (V_G) and the resulting drain current (I_D) indicates the transfer characteristic in linear (at low V_D) or saturation (at high V_D) modes. Linear and saturated transfer characteristics are demonstrated in more detail in section 3.2. The linear transfer characteristic emerges at a low drain voltage ($V_G >> V_D$), while the saturated transfer characteristic emerges at a high drain voltage ($V_G < V_D$).

Figure 5-5 shows the linear transfer characteristic of the SnO_2 WGTFT, where V_G was scanned from a high negative voltage (*i.e.* value well below V_{th}, when the transistor is clearly 'off') to a high positive voltage (where I_D increases linearly with V_G) as the off→on sweep and back from the same positive voltage to the negative voltage (on→off sweep) at V_D = 0.1 V. Note that we followed the same procedure to scan the linear transfer characteristic of the SnO_2 WGTFT as a sensor, after incorporating the sensitised membrane to sense certain analytes in the gate medium, as reported in section 4.4. The saturated transfer characteristic of SnO_2 WGTFT is plotted on the square root scale and logarithmic scale of (I_D) vs. (V_G), as displayed in Figures 5-5 (a) and (b), respectively, to extract mobility and the on/off ratio values, as explained in sections 5.2.1.3.2 and 5.2.1.3.3.

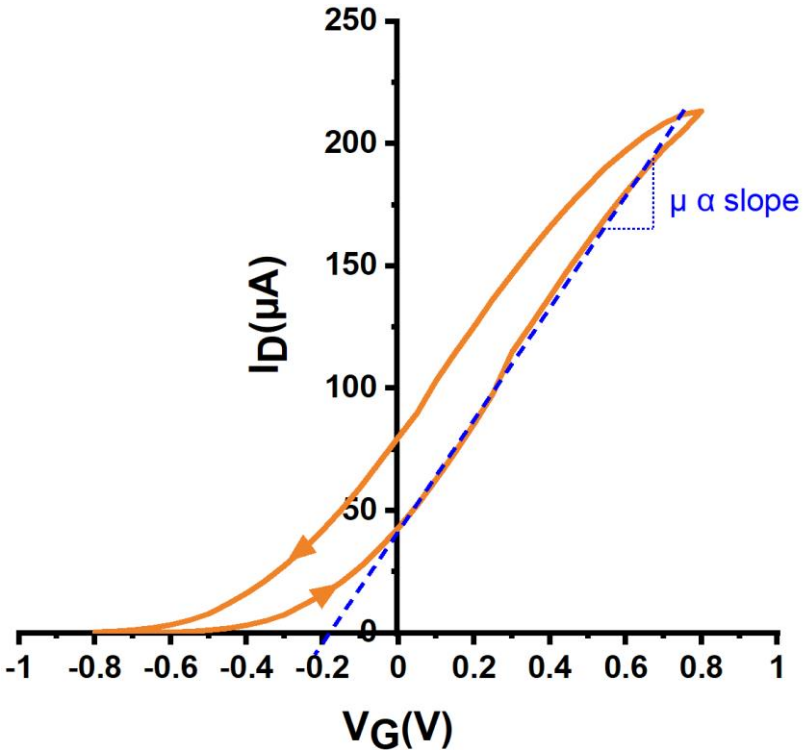

Figure 5-5: *Linear transfer characteristics of SnO_2 WGTFT. This illustrates the common method of determining the threshold value by fitting a straight line at high gate voltage. The intercept of the fitted line with the x-axis is V_{th}, as explained in section 5.2.1.3.1. In addition, the slope of the of the fitted line at high V_G is used to quantify the charge carrier mobility in the linear regime, as indicated by equation 5-1.*

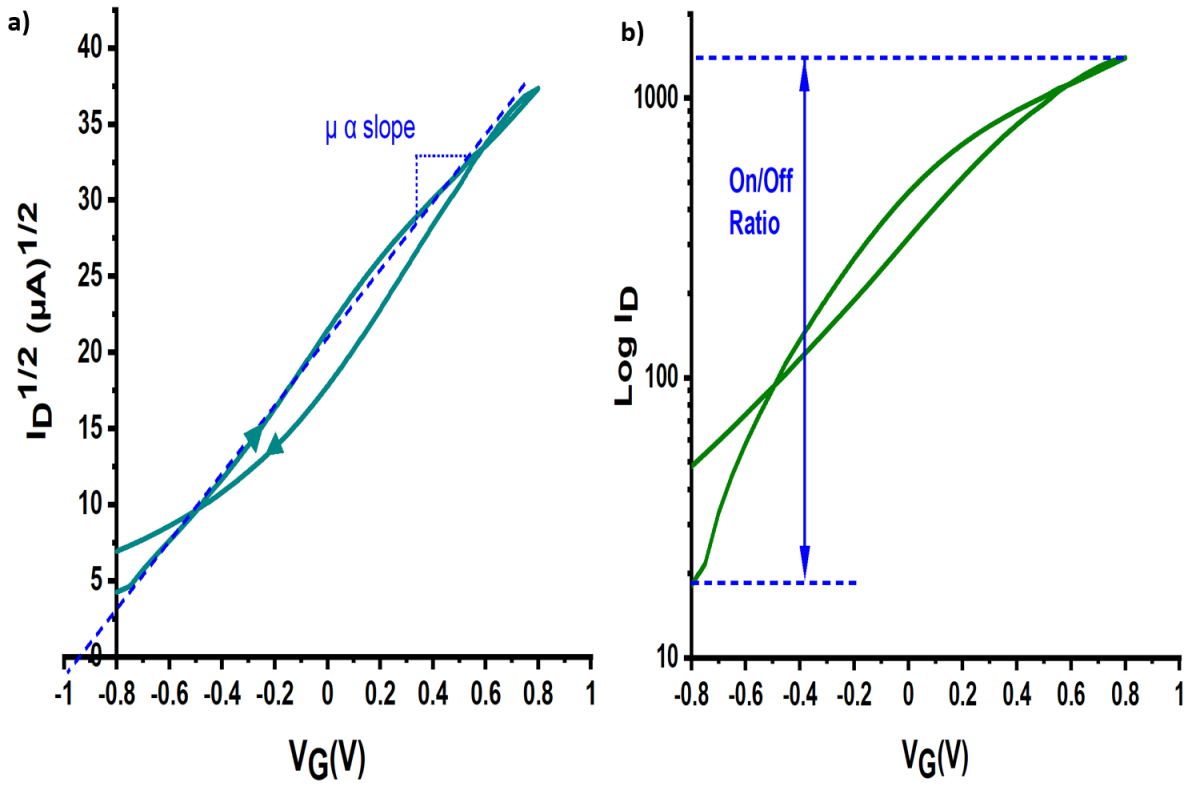

***Figure 5-6**: Saturated transfer characteristics of SnO_2 WGTFT plotted on (a) a square root ($\sqrt{I_D}$ vs V_G) scale and (b) a logarithmic scale (Log I_D vs. V_G) to evaluate the on/off ratio, mobility and threshold voltage in the saturation regime, as explained in section 5.2.1.3.*

5.2.1.3 Evaluation of SnO_2 WGTFT parameters

As mentioned above, various vital electrical parameters can be derived from the transfer characteristics, including the threshold voltage (V_{th}), charge carrier mobility (μ) and on/off current ratio (I_{ON}/I_{OFF}).

5.2.1.3.1 Threshold voltage

Threshold voltage (V_{th}) represents the gate voltage required to develop an accumulation layer in the transistor's channel to switch the transistor 'on' in accumulation mode, as explained in detail in section 3.2. This parameter is crucial in this study to detect the WGTFT sensor's response to analyte ions. The threshold voltage can be determined practically from the transfer characteristics I_D (V_G) using two possible approaches [65]: from the linear transfer characteristic by means of the intersection between the V_G axis and the extrapolated linear fit to the drain current (I_D) at high V_G or from the saturated transfer characteristic through the

intersection between the V_G axis and the extrapolated linear fit to ($\sqrt{I_D}$) at high V_G, based on equations 3-8 and 3-9. Figures 5-4 and 5-5 (a) show fitting the straight lines to the rising flank of the linear transfer characteristic (I_D vs. V_G) and the saturated transfer characteristic plotted on the square root of I_D ($\sqrt{I_D}$ vs. V_G), respectively, to extract the V_{th} of the SnO_2 WGTFT. It is clear that the SnO_2 WGTFT is 'on' (*i.e.* somewhat above threshold at V_G = 0) due to some doping in the SnO_2 semiconductor channel. Compared with a spray pyrolysed ZnO-based WGTFT, ZnO displayed a slightly higher threshold voltage of +0.4 V [258]. The low threshold voltage of the SnO_2 WGTFTs is favourable in this study, as the sensitised WGTFT sensor's response to analyte ions will promote a shift to a more positive voltage with the increase of analyte concentrations in the gate medium, as shown in Figures 6-3 a, 7-3 a and b, 8-2 c, 8-3 c, 8-5 c, 8-7 a, b and c, 8-8 and 8-9 a and b. However, the V_G's ranges for WGTFTs must be within the 'electrochemical window' of water ≈ 1.23 V [51][52]. Consequently, SnO_2 WGTFTs enable a large sensing range restricted only by the electrochemical window of water.

5.2.1.3.2 Charge carrier mobility

Charge carrier mobility (μ) describes the average speed of charge carriers' movement in the unit of the applied electric field [65], measured in cm^2/V s unit, as reported in section 3.2. Charge carrier mobility is one of the semiconductor's primary performance parameters rather than TFT [65].

Quantitatively, the carrier mobility (μ) can be derived from the linear and saturation regimes of the TFT's transfer characteristic as threshold voltage. The carrier mobility in the linear regime can be determined based on the linear transfer characteristic at high V_G, as demonstrated in equation 5-1:

$$\mu_{lin} = \frac{L}{WC_iV_D}\left(\frac{\partial I_D}{\partial V_G}\right) \qquad 5\text{-}1$$

where C_i is the specific capacitance of the gate medium of the transistor; L and W refer to the channel length and width, respectively; and I_D and V_G stand for drain current and gate voltage, respectively. The fitted line's slope at high V_G represents the derivative in equation 5-1.

The carrier mobility (μ) in the saturation regime can be evaluated using the saturated transfer characteristic at high V_G, as shown in equation 5-2:

$$\mu_{sat} = \frac{2L}{WC_i}\left(\frac{\partial\sqrt{I_{D,sat}}}{\partial V_G}\right)^2 \qquad 5\text{-}2$$

where $\frac{\partial\sqrt{I_{D,sat}}}{\partial V_G}$ is the fitted line's slope of the ($\sqrt{I_D}$ vs V_G) plot.

Therefore, the electron mobility in an SnO_2 semiconductor-based WGTFT can be determined from its transfer characteristics, namely, the slope of the best straight-line fitting at a high gate voltage of the linear transfer characteristic (I_D vs V_G) (Figure 5-5) and the saturated transfer characteristic in square root ($I_{D,sat}^{1/2}$ vs V_G) (Figure 5-6 a) plots, as well as the application of equations 5-1 and 5-2.

If we considered C_i (3 µF/cm^2) as reported for DI water as the gate medium of TFT in [51] and because W/L for our TFT equals 33.3 (see section 4.2.2), the electron mobility of the SnO_2-based WGTFT was determined as approximately 16.5 cm^2/V s in the linear regime. This is similar to the electron mobility of the spray pyrolysed ZnO-based WGTFT, which is 15 cm^2/V s [35].

5.2.1.3.3 On/off current ratio

The ratio between the highest and lowest drain current at the maximum and minimum values of V_G in the saturated transfer characteristic is the on/off drain current ratio (I_{on}/I_{off}). Equation 5-3 defines the on/off ratio of TFTs:

$$\frac{I_{on}}{I_{off}} = \frac{I_D\,(V_G,\max)}{I_D(V_G=0)} \qquad 5\text{-}3$$

The on/off ratio can be determined directly from the (Log I_D vs V_G) plot of the saturated transfer characteristic. A high on/off ratio is desirable for the fast switching of TFT devices. Figure 5-6 (b) shows the I_{on} and I_{off} of the SnO_2 WGTFT. Due to some doping in the SnO_2 semiconductor channel, the SnO_2 WGTFT presents a low on/off ratio ≈ 76. This ratio is much lower than the on/off ratio of the spray pyrolysed ZnO-based WGTFT of 300 [83]. However, the reduced on/off ratio of the SnO_2 WGTFT did not compromise the ability to determine the threshold shift as the main parameter in WGTFT sensors, as will be shown in section 5.2.1.5.

5.2.1.4 Hysteresis

Hysteresis commonly appears in TFT electrical characteristics, especially in electrolyte-gated transistors. Hysteresis explains the mismatch between the two sweeping directions in electrical characteristics when V_D or V_G is swept from 0 or negative voltage (*i.e.* the transistor is mostly 'off') to positive voltage (transistor is 'on') (off→on sweep) and then returned from 'on' to 'off' (on→off sweep), as shown in Figures 5-3 and 5-4. To put it another way, the dropping flank of the electrical characteristic is not identical to the rising flank. Hysteresis is mainly due to the charge trapping sites in the bulk of semiconductor film or at the gate medium-semiconductor interface [261][262]. Hysteresis can be clockwise or anticlockwise as a rotation direction between off→on and on→off sweeps [263]. As shown in Figure 5-5, the linear transfer characteristic of SnO_2 WGTFT exhibits anticlockwise hysteresis. In this work, due to the linear transfer characteristic is mainly used to extract V_{th} of WGTFTs, as will be explained in the next section, and the full characteristic (whole loop) often displays hysteresis, we dealt with one sweep of the whole loop 'rising flanks' (*i.e.* when the V_G sweeps from off to on) of the SnO_2 WGTFT linear transfer characteristic. The rising flanks of the linear characteristics more closely match the TFT theory for linear transfer characteristics. Therefore, for clarity, on→off sweeps of the linear transfer characteristic of the WGTFT sensor were omitted, and we only showed off→on sweeps to determine threshold voltages.

5.2.1.5 Evaluation of threshold voltage shift

The threshold voltage of the WGTFT as a potentiometric sensor is the key parameter in this study, reflecting the response of this sensor to the concentration of analytes in the gate medium. Based on the transfer characteristics, the threshold voltage can be determined using the linear or saturation transfer characteristics, as reported in section 5.2.1.3.1. Note that V_{th} is directly extracted from the transistor's linear transfer vs saturation transfer characteristics, in which plotting in square root scale is required. To evaluate the threshold shift (ΔV_{th}) as a difference between two threshold voltages of two different linear characteristic of the same transistor: linear transfer under zero analyte concentration (reference characteristic) and linear transfer under c concentration of the analyte, two approaches can be used. The first approach requires fitting straight lines to linear transfer characteristics at high V_G and extrapolating to an intercept with a V_G axis to extract the values of V_{th} and then calculating the difference between these two linear characteristics as $\Delta V_{th} = V_{th1} - V_{th2}$. The second approach is more precise and simple,

and does not require any theoretical models or fitting, as reported by Casalini et al. [53] and as will be elaborated in the next paragraph. This method of extracting ΔV_{th} from linear characteristics as a response of WGTFT sensors was adopted in our work. In particular, here we are not concerned with determining an exact threshold value but with the relative threshold shifts (ΔV_{th}) when we use different analyte concentrations with WGTFT sensors, as described in section 4.4.

Figure 5-7 shows an example of the simple method used to evaluate the ΔV_{th} of sensitised SnO_2 WGTFT for two different concentrations of analyte (Cu^{2+}) in the gate medium, as we do in this work. Figure 5-7a shows two linear transfer characteristics of the same transistor gating, first with 0 µM of $Cu(NO_3)_2$ aqueous solution and then with 0.5 µM of $Cu(NO_3)_2$ aqueous solution. To estimate the magnitude of the threshold shift, a better alternative method to fitting straight lines and finding intercepts is to regard the 0 µM as a reference characteristic (blue) and graphically shift the 0.5 µM (red) characteristic along the V_G axis until it best matches the 0 µM reference characteristic, as seen in Figure 5-7b. The required gate voltage shift for the best overlap is equivalent to the ΔV_{th} between the two characteristics, here ΔV_{th} = 140 mV. Good overlap between characteristics shows only a difference in threshold when gating with different concentrations. The change in specific capacitance or mobility of the charge carrier would result in modifying the slope at high gate voltage. Here, we observed them to be virtually identical.

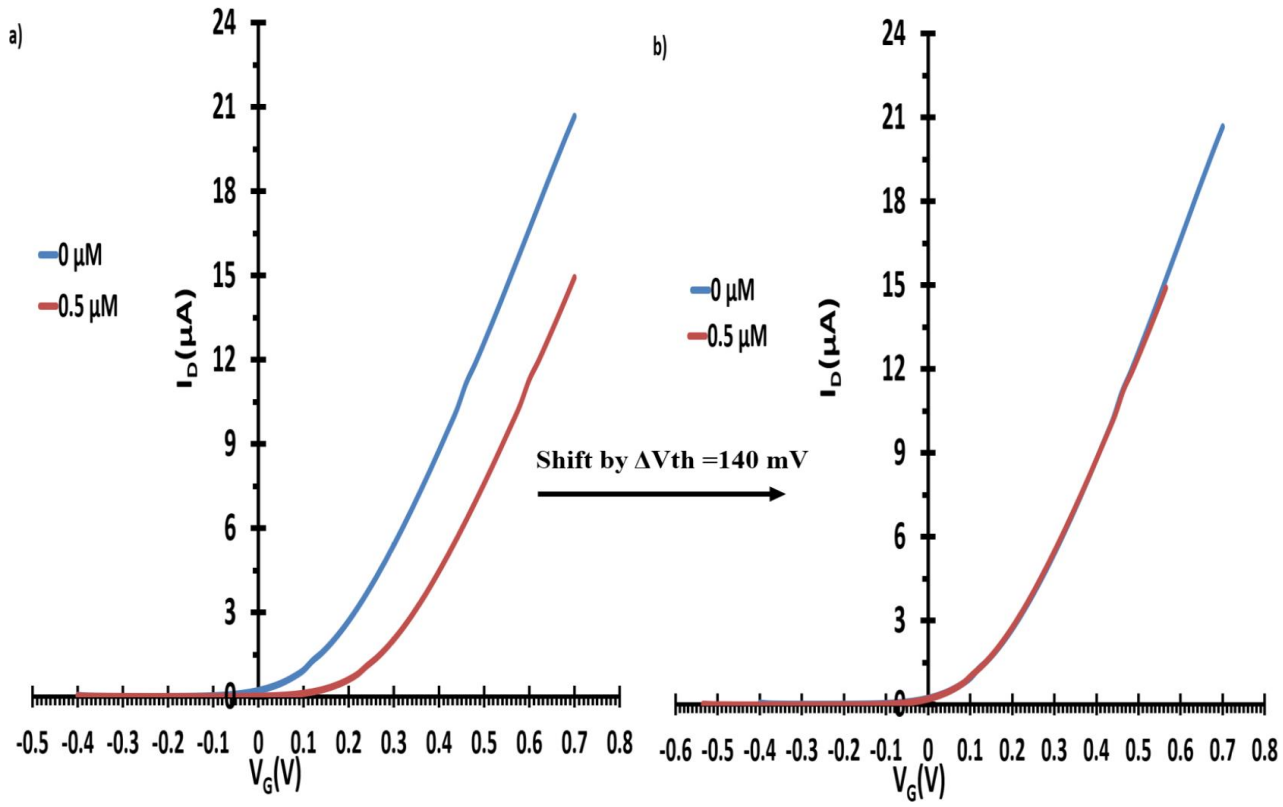

Figure 5-7: *Example demonstrating the threshold shift (ΔV_{th}) determination via a shift-and-match procedure of sensitised SnO_2 WGTFT to determine Cu^{2+}. a) The response characteristics (linear transfer characteristics) of one SnO_2 transistor substrate gating first with 0 µM of Cu (from $Cu(NO_3)_2$) and then with 0.5 µM of Cu.* ***b)*** *The 0.5 µM characteristic shifted along the V_G axis by 140 mV to best match with reference characteristic 0 µM. This shift presents ΔV_{th} (0.5 µM) = 140 mV.*

Similarly, if a set of linear transfer characteristics are obtained when gating with various salt concentrations (c), the linear transfer characteristic under 0 concentration is allocated as a reference, while the other characteristics are shifted along the V_G axis to best match with the reference by some voltage shift $\Delta V_{th}(c)$. Consequently, a 'master curve' is constructed in which the reference closely overlaps with all other characteristics under increasing of c in one curve. This approach is precise and does not depend on any specific mathematical model of the linear transfer characteristics. The threshold shift $\Delta V_{th}(c)$ required to create the master curve represents the response characteristic of the WGTFT sensor towards different analyte concentrations (c).

The errors of overlap were estimated through the threshold shift determination procedure, which means shifting characteristics more or less than the best overlap with the reference

characteristic until a visible mismatch formed. Figure 5-8 shows the method of identifying the overlap errors through determining the ΔV_{th} for the same example presented in Figure 5-7. According to Figure 5-7 b, the ΔV_{th} (0.5 µM Cu^{2+}) is 140 mV, resulting from identical overlap of the linear characteristic (0.5 µM Cu^{2+}) with the reference characteristic (0 µM Cu^{2+}). A more shift toward zero of the linear characteristics (0.5 µM) (as seen in Figure 5-8a) and a less shift far away from zero of the same characteristics (Figure 5-8b) relative to the reference characteristic result in visible mismatches by a voltage ≈ +/-10 mV as overlap errors. In this case, ΔV_{th} (0.5 µM) = 140 +/- 10 mV. The errors will be shown as error bars in the response characteristics of the WGTFT sensor (ΔV_{th} vs c) in Figures 6-3 a, 7-3, 8-2 c, 8-3 c, 8-5 c, 8-7, 8-8 and 8-9. The ΔV_{th}(c) response are plotted, including error bars, in the above-mentioned Figures in chapters 6, 7 and 8 using the nonlinear fit routine in Origin 2019.

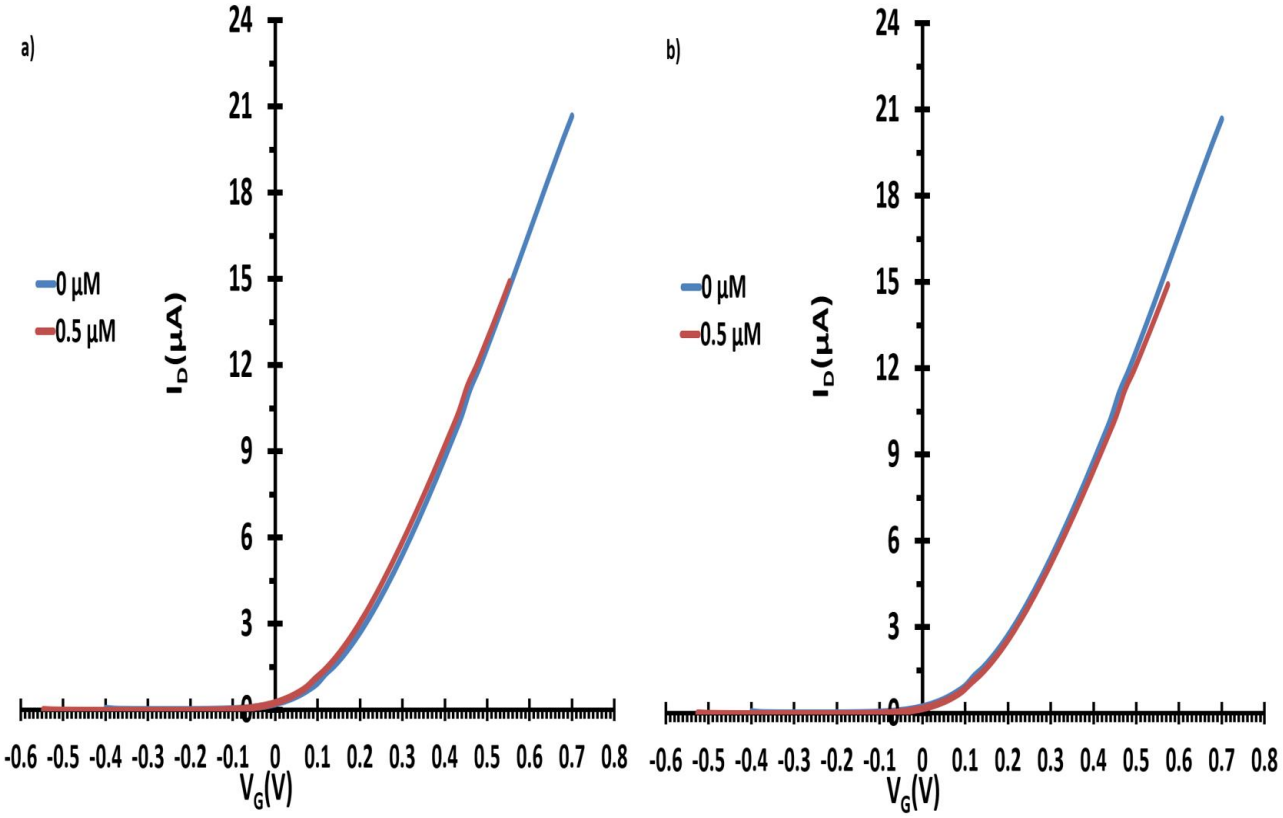

Figure 5-8: *Illustration of the overlap error of determining the threshold voltage ΔV_{th} (0.5 µM) extracted from Figure 5-7 b for sensing Cu^{2+} with the sensitised SnO_2 WGTFT. Figure 5-7 b shows the 0.5 µM Cu^{2+} characteristic shifted along the V_G axis by 140 mV for the best visual match to the c = 0 Cu^{2+} reference transfer characteristic. Shifting by 10 mV more (Figure 5-8 a) or less (Figure 5-8 b) gives a visible mismatch. Hence, in this example, ΔV_{th} (0.5 µM Cu^{2+}) = 140 +/- 10 mV.*

Chapter 6 : Sub-nanomolar detection of Caesium with water-gated transistor

6.1 Introduction

The operation of thin-film transistors (TFTs) under water acting as electrolyte gate media, (water-gated thin film transistor, WGTFT) was first reported by Kergoat *et al* [51]. This investigation developed a novel technology for sensing waterborne analytes present in the gate medium. For this, WGTFT was sensitised with a suitable receptor (sensitiser) to bind the analyte. The binding of the sensitiser and analyte results in a modification of the WGTFT characteristics; typically, a shift in threshold voltage (V_{th}). A number of such WGTFT sensors have been developed for e.g. dopamine and ion analytes [53][74][264]. Ion-selective WGTFTs are an important sub-category of WGTFTs, which first documented by Schmoltner et al. [52]. The usual sensitisers in such sensors are organic macrocyclic ionophores such as a calixarene [123], crown ether [35], or valinomycin [34] with Na^+, K^+, and Ca^{2+} being typical target ions. One approach to introduce the ionophore into the WGTFT is within a PVC membrane e.g. in a two-chamber design [52], as presented in section 4.4, like a classic electrochemical potentiometric sensors [265][266]. Other approaches include applying the membrane directly to the WGTFT's gate electrode [35]. Ion sensitive WGTFTs without a membrane have also been developed where the ionophore is embedded into the semiconductor in the channel [123]. Usually, WGTFT sensors are built with solution-processed semiconductors such as precursor-route metal oxides [35], polymer semiconductors [74][35][123], or carbon nanotubes [34]. The selective binding of the waterborne analyte present in water gate media to the ionophore results in a membrane potential (V_M), and thus a shift in V_{th}. This response follows the Nikolsky-Eisenman law (modified Nernstian) [35][267] such that the potential is flat below a certain concentration (c_{st}) on a logarithmic concentration scale and linear at high concentration ($c >> c_{st}$) (as presented in section 3.4.1); hence, the limit-of-detection (LoD) should be given $\approx c_{st}$:

$$V_M(c) = \Delta V_{th}(c) = 58\,mV/z\ \log[(c + c_{st})/c_{ref}] \qquad 6\text{-}1$$

where z represents the cation valency (for alkaline metals: z = 1), and $c_{ref} >> c_{st}$ refers to the concentration of ion in a reference solution. c_{st} is typically in the range 100 nM - 1µM [35][175][209], varying according to the ionophores and analyte concentrations. There is a distinct difference between the Nikolsky- Eisenman characteristic and the Langmuir adsorption isotherm. The latter measures the fractional surface coverage $\theta(c)$, where $0 < \theta(c) < 1$, on a surface of an adsorbent (adsorption sites) by adsorbates. Equation 6-2 gives $\theta(c)$ in Langmuir as follows:

$$\theta(c) = \frac{Kc}{Kc+1} \qquad 6\text{-}2$$

where K denotes the stability constant for the binding of the adsorbate and adsorption site, where $1/K = c_{1/2}$, in which $c_{1/2}$ known as $\theta(c_{1/2}) = ½$. Response characteristics of optical sensors are logically equivalent to equation 6-2, defined as the Hildebrand-Benesi law for optical absorption sensors (e.g. [219]). In potentiometric sensors obeying equation 6-2, threshold shift (ΔV_{th}) would be characteristic as defined by the following:

$$V_M(c) = \Delta V_{th}(c) = \Delta V_{th}(sat)\theta(c) = \Delta V_{th}(sat)\frac{Kc}{Kc+1} \qquad 6\text{-}3$$

in which $\Delta V_{th}(sat)$ is the saturation value of threshold shift in $c >> c_{1/2}$ limit, where $\theta(c >> c_{1/2}) \rightarrow 1$, as discussed in section 3.4.2.

In this work, we introduce mordenite zeolite into WGTFT architecture as an inorganic ionophore - instead of using an organic macrocycle ionophore - to detect caesium present in a water gated medium. The structure of the zeolite is fully elaborated in section 3.3.3.1. Briefly, mordenite displays a pronounced removal selectivity for the alkali metal caesium cation (Cs^+) even in the presence other cations such as Na^+ and K^+, when they are in high concentrations [195][196]. As a result, mordenite is a good choice to act as a sensitiser in WGTFTs for the detection of Cs^+. Despite caesium being uncommon in nature, the radioactive ^{137}Cs - with a half-life of about 30 years – can be released into the environment as a consequence of e.g. nuclear accidents, and causes harmful effects for decades to agriculture and livestock farming, and thus, human life [268][269]. Therefore, in areas that have experienced nuclear accidents, detection (and removal) of Cs^+ from drinking water is necessary for the protection of animal and human life. In a previous study that focused on the treatment of the contaminated water

with Cs^+ using mordenite, atomic absorption spectroscopy (AAS) was used to analyse mordenite after exposure to Cs^+ in water [195]. However, the WGTFT sensor as an instrument is low-cost and significantly lighter than AAS, and thus preferable. In this work, we find that the threshold shift as response of WGTFT sensors to increasing Cs^+ concentrations in water follows the Langmuir adsorption isotherm (equation 6-3), instead of the Nikolsky-Eisenman law (equation 6-1), with great stability constant (K) and extremely low limit-of-detection (LoD). Therefore, a Cs^+-WGTFT sensor with mordenite zeolite sensitiser is perfectly suited for water assessment against Cs^+ in respect of potability (safe drinking) limit of Cs^+ of 7.5 nM recommended by the Agency for Toxic Substances and Disease Registry [270].

6.2 Experimental

The methods of fabrication of an SnO_2 transistor and preparation of a sensitised PVC membrane with mordenite are explained in Chapter 4.

In this work, to prepare test solutions, the water samples were drawn from drinking tap water in our lab – at the University of Sheffield, for close simulation of a real-world scenario of using the Cs^+-WGTFT sensor. Tap water is usually contains potassium, sodium, calcium and magnesium as its most common cations [239] and as based on the analysis of the tap water taken from our lab using the Inductively coupled plasma electrospray mass spectrometry (ICP) [271] (Table 6-1) . Hence, the water samples were a cocktail of the common ions. Cs^+ stock solution (1 µM) was prepared by dissolving CsCl in tap water. The stock solution was then diluted to a number of desired lower concentrations (500, 300, 100, 50, 10, 1, 0.5, 0.4, 0.3, 0.2, and 0.1) nM Cs^+ via the addition of more tape water. The preparation of all the sample solutions was conducted using micropipette. The frequent calibrated micropipette is an accurate tool that can be used for sample preparations [272]. This accuracy appears in the smooth lining up of the data in the sensing response characteristics in Figures 6.3, 7.3, 8.1, 8.2, 8.4, 8.6, 8.7, and 8.8. NaCl was also used in the same way to prepare Na^+ solutions for the control experiment.

Table 6-1 *The concentration of common cations in the tap water supplied to our lab (by Yorkshire Water) that analyses by the Inductively coupled plasma electrospray mass spectrometry (ICP)*[271].

Cation	***Concentration (mg/L)***	***Cation***	***Concentration (mg/L)***
Ba	0.011	P	0.911
Ca	3.47	Pb	< 0.008
Cu	0.067	S	13.9
K	0.617	Si	2.37
Mg	2.54	Zn	0.146
Na	19.9	Cs*	0.011
Ni	0.020		

** Measured in µg/L*

A two-chamber design of WGTFT sensors, explained in section 4.4, was used to examine the response of mordenite-sensitised WGTFT to Cs^+. The sample pool in this design was first filled with tap water for calibration conditions and then replaced stepwise with increasing Cs^+ concentrations. The reference pool was kept full with tap water (Cs^+- free) throughout.

The membrane potential (V_M) can be obtained as a shift in the threshold voltage (ΔV_{th}) of the WGTFT due to V_M added to the applied gate voltage, as explained in section 4.4. For this, the linear transfer characteristics were recorded for each Cs^+ concentration after equilibrium had been reached (approximately 30 seconds) to identify the threshold voltage of WGTFT directly. The method of quantification of ΔV_{th} (c) is explained in detail in section 5.2.1.5.

6.3 Results and discussion

Figure 6-1 represents the linear transfer characteristics of the mordenite-sensitised SnO_2 WGTFT under increasing Cs^+ concentrations in the sample pool, as shown in Figure 4-7. All these linear characteristics resemble each other in terms of there being an increase in the threshold voltages as Cs^+ concentrations increase. Large threshold shifts can be observed even under only 100 pM Cs^+ , which is lower than the recommended potability limit ≈ 7.5 nM [270].

Moreover, this response was in the presence of alkali and alkaline earth ions e.g. K^+, Na^+, Mg^{2+}, Ca^{2+},…at high concentrations (much higher than 500 nM) in common tap water [239][273][274]. The threshold shifts saturated, no longer shift under further increasing of Cs^+ concentrations, at higher concentrations of $Cs^+ \geq 50$ nM. Figure 6-2 shows the best overlap of all characteristics after shifting them along V_G axis to match the c = 0 characteristic; thereby constructing a 'master curve' characteristic (see section 5.2.1.5). The clear overlap of characteristics on this single curve confirms that increasing Cs^+ concentrations in the sample pool only impacts the threshold voltages of the WGTFT. Hence, this allows to quantify the membrane potential by the required shift along V_G axis, $V_M(c) = \Delta V_{th}(c)$.

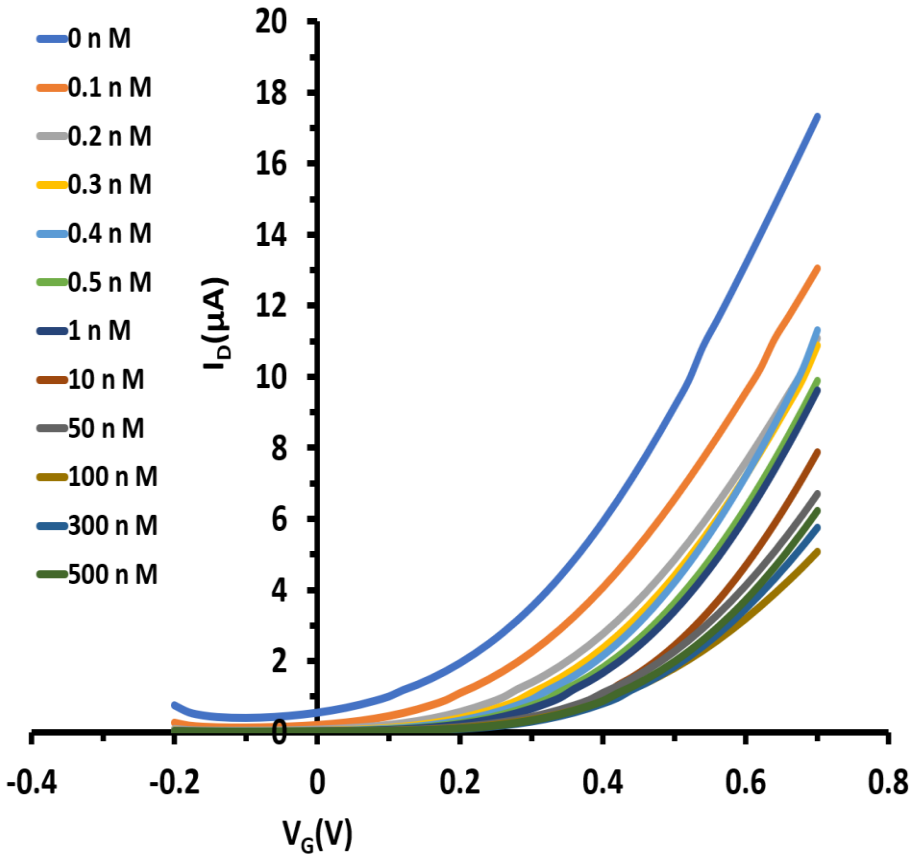

Figure 6-1: *Linear transfer characteristics of WGTFT sensitised with mordenite, under increasing Cs^+ concentrations in the sample pool.*

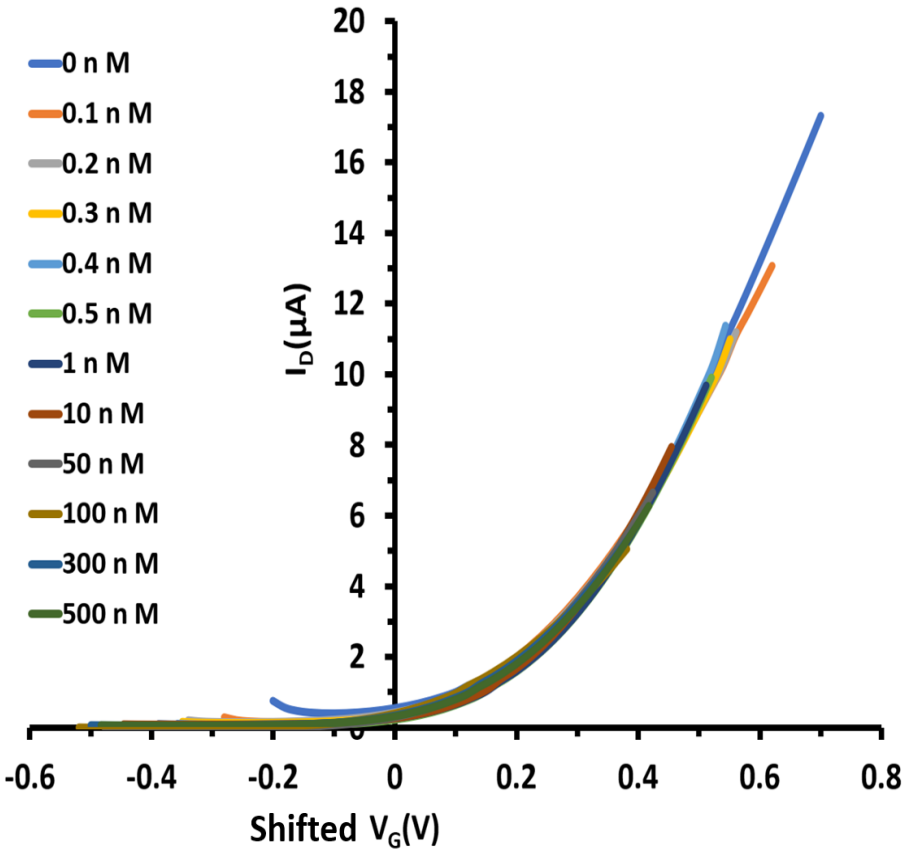

Figure 6-2:*Master curve characteristic constructed by shifting all characteristics in Figure 6-1 along the V_G axis to match the zero Cs^+ concentration characteristic.*

The procedure of shift-and-match for the linear transfer characteristics, as derived from Figure 6-1 to Figure 6-2, quantifies $\Delta V_{th}(c)$. The resulting $\Delta V_{th}(c)$ is shown in Table 6-2 and displayed in Figure 6-3 on a linear concentration scale. It is clear from Figure (6-3 a) that $\Delta V_{th}(c)$ for low Cs^+ concentration ($c << 50$ nM) rapidly increases (approximately linearly) until it saturates at $c \geq 50$ nM. Two additional SnO_2 substrates and mordenite membranes were prepared and exposed to 1 nM of Cs^+ concentration similar to the system used for Figure 6-1 to decide reproducibility. As shown in Table 6-2 also, all three devices exhibited similar threshold shift under 1 nM Cs^+, confirming good reproducibility.

Table 6-2: *Threshold shift values according to shift-and-match routine leading from Figure 6-1 to 6-2 gating with increasing Cs^+ concentrations in the sample pool along with the threshold shifts of two more devices under 1 nM Cs^+ to demonstrate reproducibility.*

c [nM]	***$\Delta V_{th}(c)$ [mV]***
0.1	80
0.2	130
0.3	160
0.4	170
0.5	200
1	220
1 (2^{nd} device)	205
1 (3^{rd} device)	210
10	260
50	270
100	310
300	300
500	300

The $\Delta V_{th}(c)$ characteristics in Figure 6-3 (a) differ clearly from the Nikolsky- Eisenman law (equation 6-1), the latter of which is linear at high concentrations ($c >> c_{st}$) on the logarithmic scale without saturation at high c, but flatlines at low concentrations ($c < c_{st}$) (see Figure 3-9). Rather, the threshold shift *vs.* concentration characteristic matches the Langmuir adsorption isotherm (equation 6-3). The similarity of the response characteristic to the Langmuir form is supported by the corresponding Hildebrand-Benesi plot. A good straight line fit on this plot [see Figure 6-3 (b)], $1/\Delta V_{th}(c)$ *vs.* 1/c, confirms the Langmuir response characteristic.

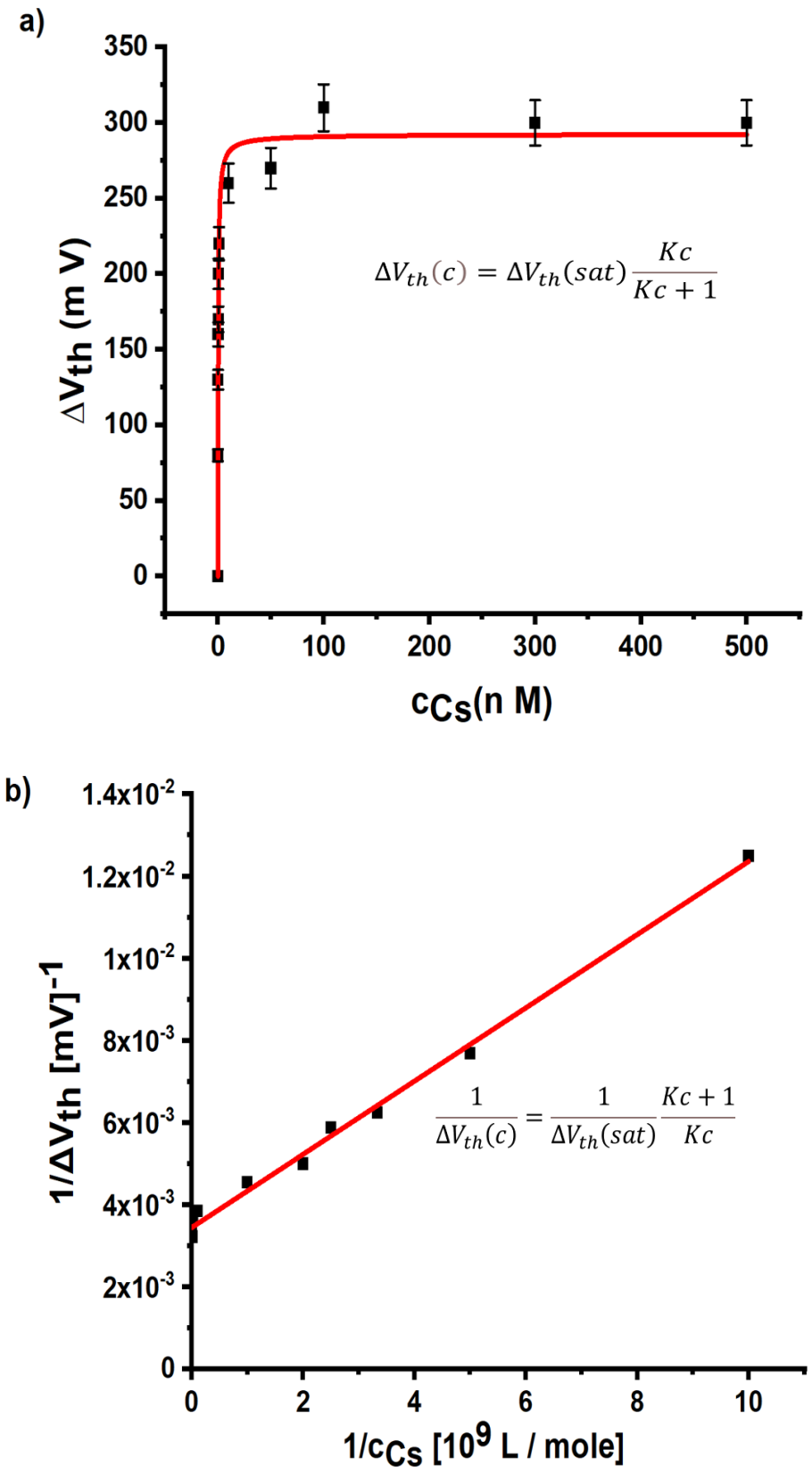

Figure 6-3: *(a) Threshold shift (ΔV_{th}) vs Cs^+ concentration (c_{Cs}) as the response characteristic of the mordenite-sensitised WGTFT, (b) Hildebrand- Benesi plot.*

The parameters of $\Delta V_{th}(sat)$ and K were extracted from the Hildebrand-Benesi plot [see Figure 6-3 (b)], in which $\Delta V_{th}(sat)$ represents the intercept with $1/\Delta V_{th}$ axis, and K is the ratio of intercept to slope (see section 3.4.2). The results are presented in Table 6-3. In comparison with optical sensors, which use organic ionophores for sensing waterborne analytes e.g. amine and potassium, K were 5 x 10^4 L/mole [275] and 10^5 L/mole [276], respectively, which is significantly smaller than K in this work. It can be concluded that the adsorption of cations into nanocavities within the zeolite structure is stronger than adsorption in holes in ring-shaped organic ionophores such as crown ethers [276]. It is worth stressing that the threshold shift response was due to the extraction of Cs^+ present in the sample by mordenite, and that, in turn, decreased the concentration of Cs^+ in the sample. The concentrations quoted here represent the initial Cs^+ concentration introduced, not partially extracted by mordenite. The significant high K can be interpreted also as the failure to recover this sensor when the mordenite in the membrane was exposed to Cs^+-free water after having been exposed to high Cs^+ concentration (500 nM) (see Figure 6-4). This is due to the extremely strong binding of Cs^+ with mordenite that cannot be reversed easily. Washing membranes with running Cs^+-free water may make recovery possible, but this process was not attempted. We suggest the use of a fresh membrane after Cs^+ is detected in water, but note that in real-world scenarios, this situation should be rare.

Table 6-3:*Response characteristic parameters: $\Delta V_{th}(sat)$, K, and $c_{1/2}$ extracted from the Hildebrand-Benesi plot (Figure 6-3 b).*

Parameter	***Result***
$\Delta V_{th}(sat)$ [mV]	290 +/-7
K [L/mol]	(3.9 +/- 0.4) x 10^9
$c_{1/2}$ [pM]	258 +/- 26

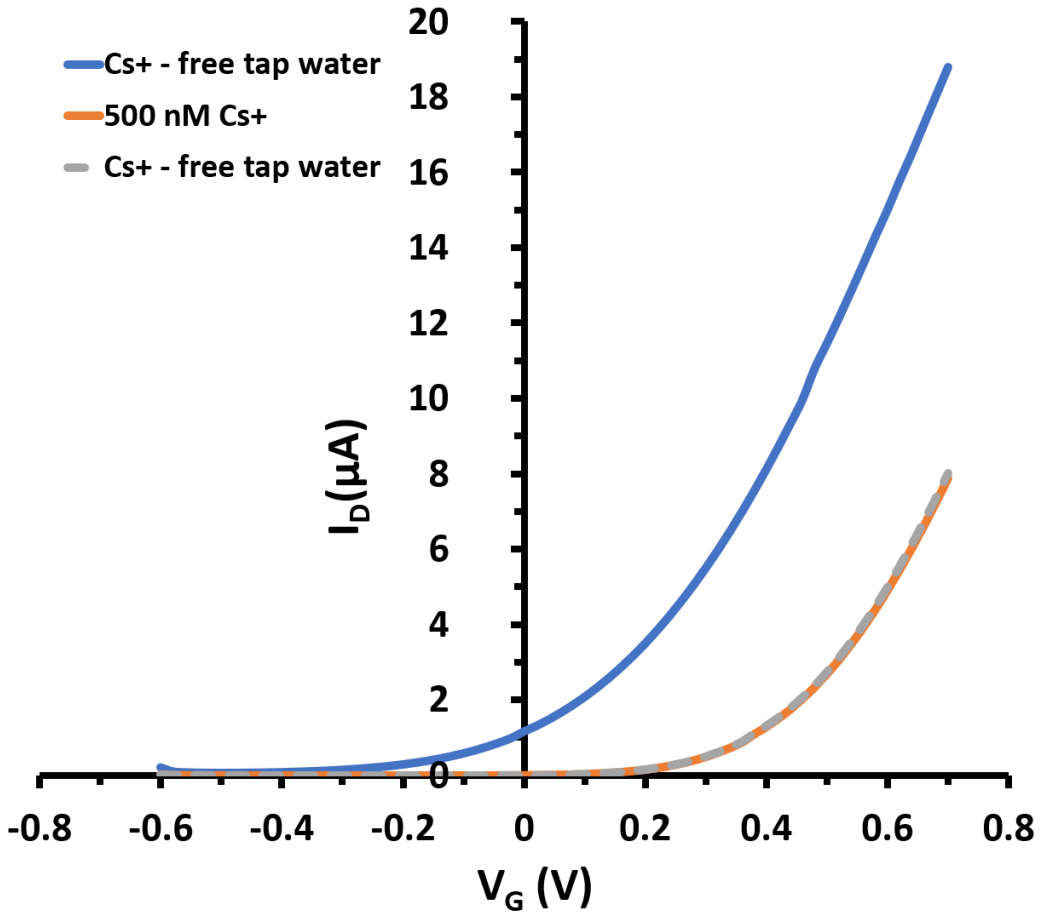

Figure 6-4: *Linear transfer characteristics of the mordenite-sensitised WGTFT under a test cycle of tap water (Cs^+- free) →500 nM Cs^+→ tap water (Cs^+- free) in the sample pool.*

The high K value enabled the detection of Cs^+ with an extremely low limit-of-detection (LoD). For LoD determination, we plotted (Kc + 1) $\Delta V_{th}(c)$ vs c_{Cs} in linearised form for small Cs^+ concentrations, as shown in Figure 6-5. This yielded a straight line in the form y = mx + b, according to equation 6-2, with the intercept near zero (b ± Δb) and slope (m). A good straight line fit was obtained with b = (12.8 +/- 11.8) mV and m = 1078 mV/nM, which in turn was used to evaluate LoD using the conventional '3 errors' criterion, (equation 6-4) [219]:

$$LoD = \frac{3\,\Delta b}{m} \qquad 6\text{-}4$$

Interestingly, we found extremely low LoD (33 pM). This is much lower - three orders of magnitude – than a typical LoD (c_{st}) for organic ionophore-sensitised WGTFTs to detect K^+

[35][209], and by four orders of magnitude for Cs^+- potentiometric sensors using organic ionophores [175][277].

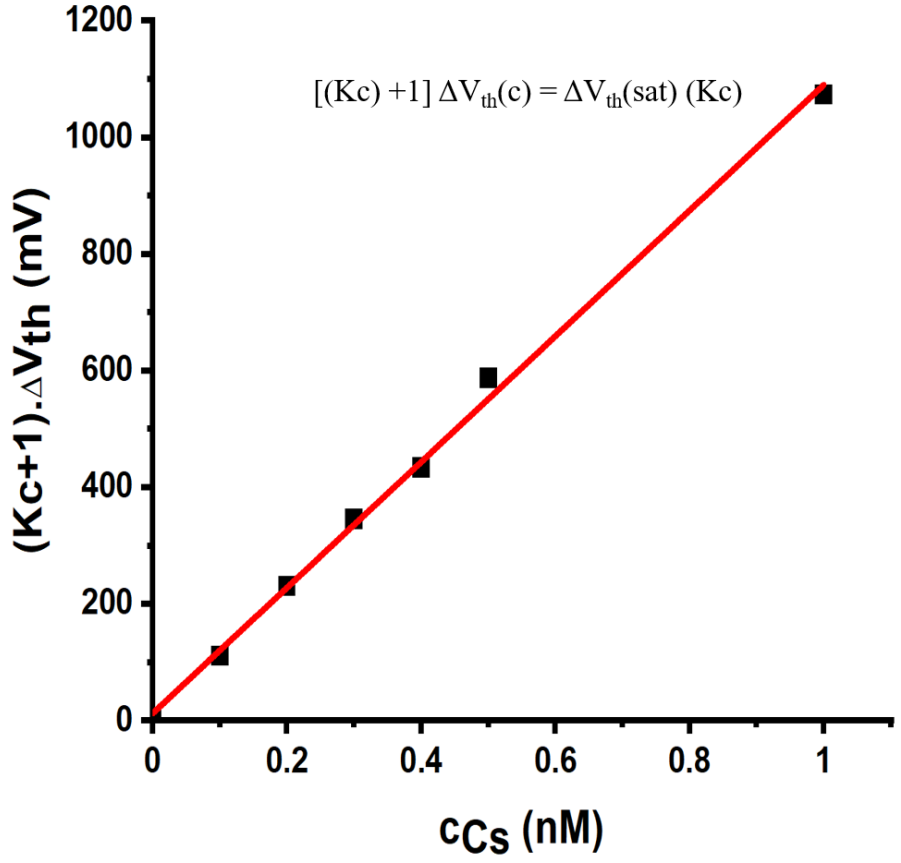

Figure 6-5: *Linearised plot - $(Kc + 1)\Delta V_{th}(c)$ vs c_{Cs} - of the response derived from Figure 6-3(a) at low Cs^+ concentrations to assess LoD.*

It is known that selectivity is a crucial feature of ionophores. Mordenite selectivity for Cs^+ has been well-established [195][196], and to confirm the selectivity of mordenite for Cs^+ over other alkali ions (e.g. Na^+), this was tested. Figure 6-6 exhibits the linear transfer characteristics of the mordenite-sensitised WGTFT under increasing Na^+ concentrations, similar to the experiment whose results are shown in Figure 6-1. This latter experiment was essentially repeated, but with Cs^+ replaced with Na^+ solution in the sample pool. As shown in Figure 6-6, all these characteristics are much the same without any systematic shift along the V_G axis. We

suppose that Na^+-mordenite form that used in this study is the reason behind the lack of mordenite-sensitised WGTFT response under increasing Na^+ concentration in the sample pool.

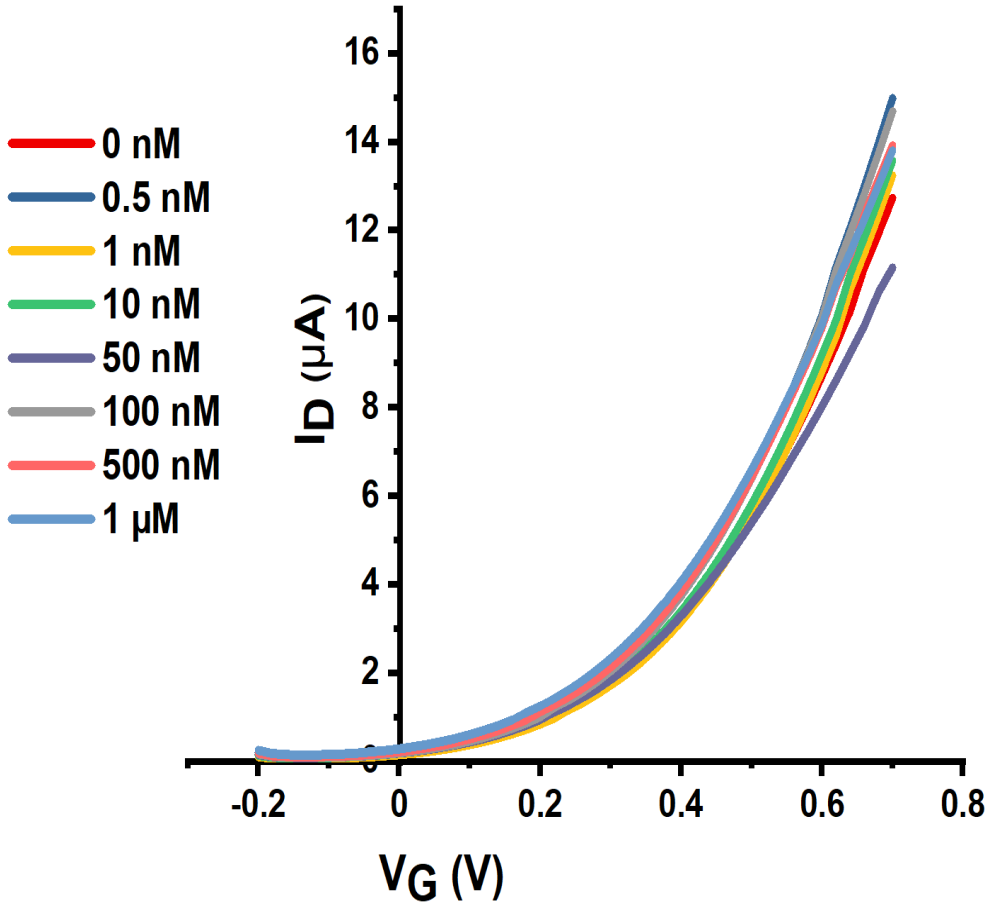

Figure 6-6: *Linear transfer characteristics of mordenite-sensitised WGTFT under increasing Na^+ concentrations in the sample pool instead of Cs^+, similar to the procedure followed in Figure 6-1.*

For further investigation of this unusual Langmuir response characteristic, two additional PVC membranes loaded with different mordenite quantities were prepared. Using these, similar response characteristics to those shown in Figure 6-1 were obtained, but saturated $\Delta V_{th}(sat)$ differently at high concentrations ($c >> 1/K$). The resulting $\Delta V_{th}(sat)$ increased with an increase in mordenite concentration, as seen in Figure 6-7. However, stability constants K remained at the same order of magnitude, as reported in Table 6-3. This is another difference found between the Langmuir response and Nikolsky-Eisenman behaviour, the latter of which is independent of sensitiser concentrations in the membrane but depends instead on analyte concentrations.

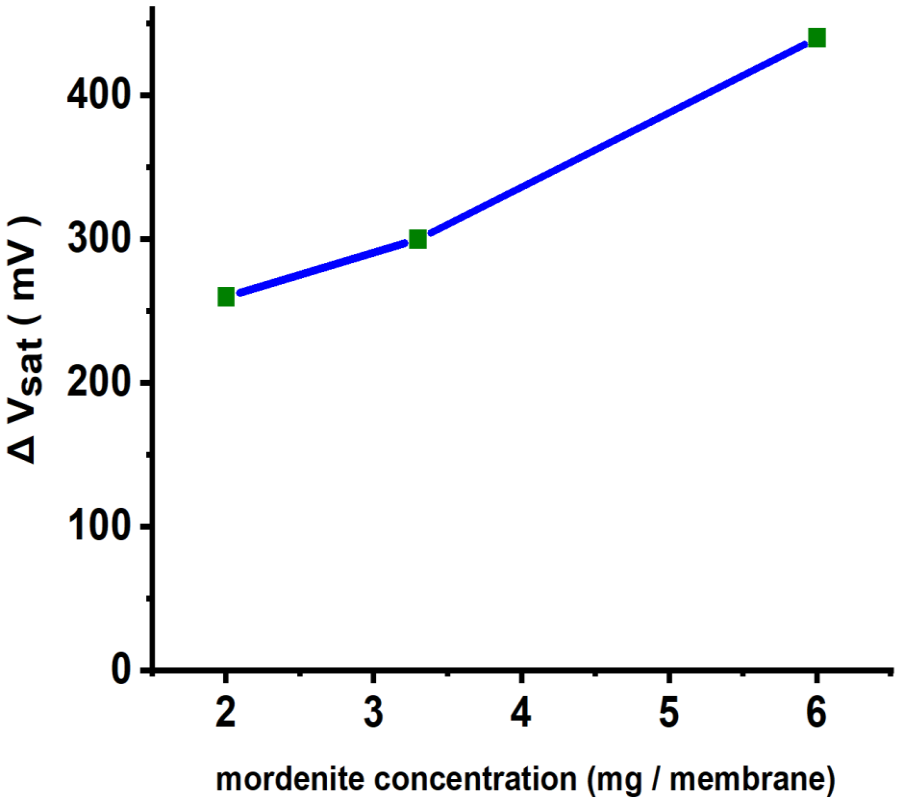

Figure 6-7: *ΔV_{th}(sat) for WGTFTs sensitised with different loading of mordenite in membranes (2, 3.3, 6 mg / membrane) using same procedure in Figure 6-1, under the same concentrations of Cs^+.*

6.4 Conclusion

Sensitised potentiometric sensors with organic ionophores to detect common waterborne analytes (e.g. Na^+, K^+, Ca^{2+}, Mg^{2+}) provide limit-of-detection (LoD) in the range (100 nM…1 µM) (e.g. [52][123][35][34][175][277]). According to their respective concentrations in the range (micro…milli) molar, this LoD is sufficient for detection. However, the detection of toxic or radioactive elements, such as Cd^{2+}, Pb^{2+}, $^{137}Cs^+$, Sr^{2+}, a LoD at or below nanomolar (nM) levels is required, which cannot be achieved with organic ionophores.

In this chapter, sub-nanomolar WGTFT potentiometric ion sensor for Cs^+ is demonstrated. Although Cs^+ is rare in nature, radioactive ^{137}Cs can often be released into drinking water following nuclear accidents. Mordenite, as an inorganic zeolite, was used to sensitise the PVC membrane, instead of organic ionophores, and then introduced to the WGTFT transducer architecture, as seen in Figure (4-7). The response characteristic found here is similar to a

Langmuir isotherm, with a significant stability constant, K = (3.9 +/- 0.4) x 10^9 L/mole. This is much larger than typical stability constants for cations forming complexes with organic macrocyclic ionophores by four to five orders of magnitude [275][276]. The high K resulted in very low LoD = 33 pM even with common cations in realistic interfering 'cocktail', where this work was conducted using tap water rather than DI water. In comparable with Cs^+-potentiometric sensors using organic crown ether sensitisers, the response characteristics fit Nikolsky-Eisenman behaviour, with LoDs of 380 nM [175] and 240 nM [277]. These were larger than LoD of the Cs^+-WGTFT sensitised with mordenite here by four orders of magnitude, and much higher than the potability limit of Cs^+. The Cs^+-WGTFT sensor's dynamic range extends from LoD = 33 pM to around 50 nM Cs^+ at saturation by three orders, which overlaps well with Cs^+ practically relevant potability limit ≈ 7.5 nM [270]. Although the actual reason behind the unusual Langmuir response characteristics requires additional investigation, these results show the investigation's usefulness in helping to drive LoD to the extremely low level required to monitor drinking water against potential traces of Cs^+ ions.

Chapter 7 : Monitoring the lead-and-copper rule with a water-gated thin-film transistor

7.1 Introduction

Industrial, mining, agricultural processes and waste disposal contaminate ground water and drinking water supplies with heavy metals. Despite these metals being present in natural water in trace amounts, some of them are toxic even at extremely low concentrations [278]. The heavy metal cations Lead (Pb^{2+}) and copper (Cu^{2+}) belong to the common low-level toxic pollutants in drinking water, which penetrate drinking water primarily through plumbing materials [279]. Moreover, in some developing countries, copper pots are still used to store bacteria-polluted water as sterilisation tool [280]. To monitor drinking water against these metals, the 'lead-and-copper rule' was reported in 1991 by the US Environmental Protection Agency (EPA), setting 'action levels' - at which water is considered no longer potable beyond these action levels- of 0.015 mg/L = 72 nM for lead and 1.3 mg/L = 20.5 μM for copper in the domestic water supply [281].

Water-gated thin-film transistors (WGTFTs) have recently been used as a unique potentiometric sensor for waterborne analytes (*e.g.* [52][35][123]). As reported in section 6.1, ion-selective WGTFTs incorporating the macrocyclic organic ionophores within a plasticised PVC phase transfer membrane, develop an ion concentration-dependent membrane potential $V_M(c)$ that leads to a threshold shift ΔV_{th} following the Nikolsky- Eisenman law [35][267], *i.e.* Nernstian (linear on a logarithmic concentration scale) at high ion concentrations ($c >> c_{st}$), but flatlining below a concentration $c_{st} \approx$ limit-of-detection (*LoD*):

$$V_M(c) = \Delta V_{th}(c) = 58\frac{mV}{z}\log[(c + c_{st})/c_{ref}] \qquad 7\text{-}1$$

Where z is the 'cation valency' and c_{ref} is the 'ion concentration in a reference solution', ($c_{ref} >> c_{st}$). c_{st} relies on both the ion and ionophore, but is commonly within the range 100 nM to 1μM [35][175][209]. This LoD is sufficient for common waterborne cations (*e.g.* Na^+, K^+, Ca^{2+}, Mg^{2+}), as these occur naturally at concentrations far higher than c_{st}. However, the

potability limit (highest acceptable concentration) of radioisotopes (*e.g.* Cs^+, Sr^{2+}) or heavy metals (*e.g.* Pb^{2+}, Cd^{2+}) is often significantly lower (*e.g.* 7.5 nM for Cs^+) [270]. Organic macrocycles cannot, therefore, be used for sensing such cations at the relevant low concentrations.

We have recently introduced an inorganic ionophore, a zeolite mineral called 'mordenite', into a WGTFT [258]. Mordenite is known to selectively extract Cs^+ ions from water [195][196] for treatment of water contaminated with the radioisotope $^{137}Cs^+$ [282]. We found a strong WGTFT threshold shift at very low Cs^+ concentrations, with response characteristics given by the Langmuir adsorption isotherm, equation 7-2, rather than equation 7-1:

$$\Delta V_{th}(c) = \Delta V_{th}(sat)\, Kc / (Kc + 1) \qquad 7\text{-}2$$

Where K is the stability constant for the analyte/sensitiser binding and $\Delta V_{th}(sat)$ the saturated value of threshold shift at the limit $c >> c_{1/2} = 1/K$, with $c_{1/2}$ defined as $\Delta V_{th}(c_{1/2}) = ½\, \Delta V_{th}(sat)$. We found a very large $K = 3.9 \times 10^9$ L/mole and very low LoD of 33 pM, well below the potability limit of 7.5 nM for Cs^+ [258].

In drinking water treatment, another zeolite, 'clinoptilolite', is used to extract Pb^{2+} and Cu^{2+} from water [60]. The structure and type of zeolite are described in section 3.3.3.1. Here, we show that WGTFTs sensitised with a clinoptilolite-filled membrane provide simple potentiometric sensors with very low limit-of-detection, suitable for monitoring the lead-and-copper rule. Response characteristics are described by a generalisation of equation 7-2, known as the 'Langmuir- Freundlich' (LF) isotherm, as in equation 7-3:

$$\Delta V_{th}(c) = \Delta V_{th}(sat)\, (Kc)^{\beta} / ((Kc)^{\beta} + 1) \qquad 7\text{-}3$$

The additional parameter $\beta < 1$ describes inhomogeneity in the analyte / ionophore binding sites [221]. $c_{1/2} = 1/K$ remains true regardless of the value of β. The ratio of K's for a target analyte *vs* an interferant (or the inverse ratio of $c_{1/2}$'s) quantifies the selectivity, S, of a sensitiser.

7.2 Experimental

The fabrication of the SnO_2 transistor and preparation of a PVC membrane sensitised with clinoptilolite are described in Chapter 4.

To simulate realistic conditions for practical use of our sensor, we did not work with deionised water, but drew water samples from drinking water taps at Sheffield University in March/April 2019. As reported in section 6.2, the most common cations in tap water are calcium, magnesium, sodium, selenium, and potassium [239]. For the assessment of water quality in the UK, the Drinking Water Inspectorate (DWI) releases an annual summary report [283], and our local supplier, Yorkshire Water, provides a list of ion concentrations in Sheffield tap water (see Table 6-1) [274]. A 1 mM Cu^{2+} stock solution was prepared by dissolving copper nitrate, $Cu(NO_3)_2$, in tap water; we then obtained the desired (low) concentrations used in the experiments by diluting this with more tap water to (300, 200, 100, 50, 10, 1, 0.5) µM Cu^{2+}. For Pb^{2+}, we prepared 1µM stock solution of lead nitrate, $Pb(NO_3)_2$, dissolved in tap water, and then diluted this to the desired low concentrations (0.5, 1, 5, 10, 25, 50, 100, 250) nM.

The construction of the clinoptilolite-sensitised WGTFT sensor to detect lead and copper is shown in Figure 4-7, using two-chamber design. As in the Cs^+ experiment, the water in the reference pool in the twin-pool gating setup was tap water as drawn, with no deliberately added ions. For sensor calibration, the sample pool was initially filled with tap water, but this was then subsequently replaced with solutions of known and increasing concentrations of lead or copper, while the reference pool remained filled with tap water. When a new sample is poured in the sample pool, we allowed two minutes for equilibrium to occur. The membrane potential ($V_M = \Delta V_{th}$) was determined as explained in section 5.2.1.5.

7.3 Results and Discussion

7.3.1 Lead and Copper sensing results

In Figure 7-1 (a), we show the linear transfer characteristics of SnO_2 WGTFT transistors sensitised with a clinoptilolite membrane. The reference pool was filled with tap water, and the sample pool - also filled with tap water - had increasing concentrations of Pb^{2+} added, up to 250 nM. Transfer characteristics clearly shifted to more positive gate voltages with increasing lead concentration, which indicates a lead concentration-dependent membrane potential. For quantitative analysis, we shifted all transfer characteristics under leaded water ($c_{Pb} > 0$) to

match the c = 0 characteristic, as described in section 5.2.1.5. The resulting 'master' transfer characteristic is shown in Figure 7-1 (b).

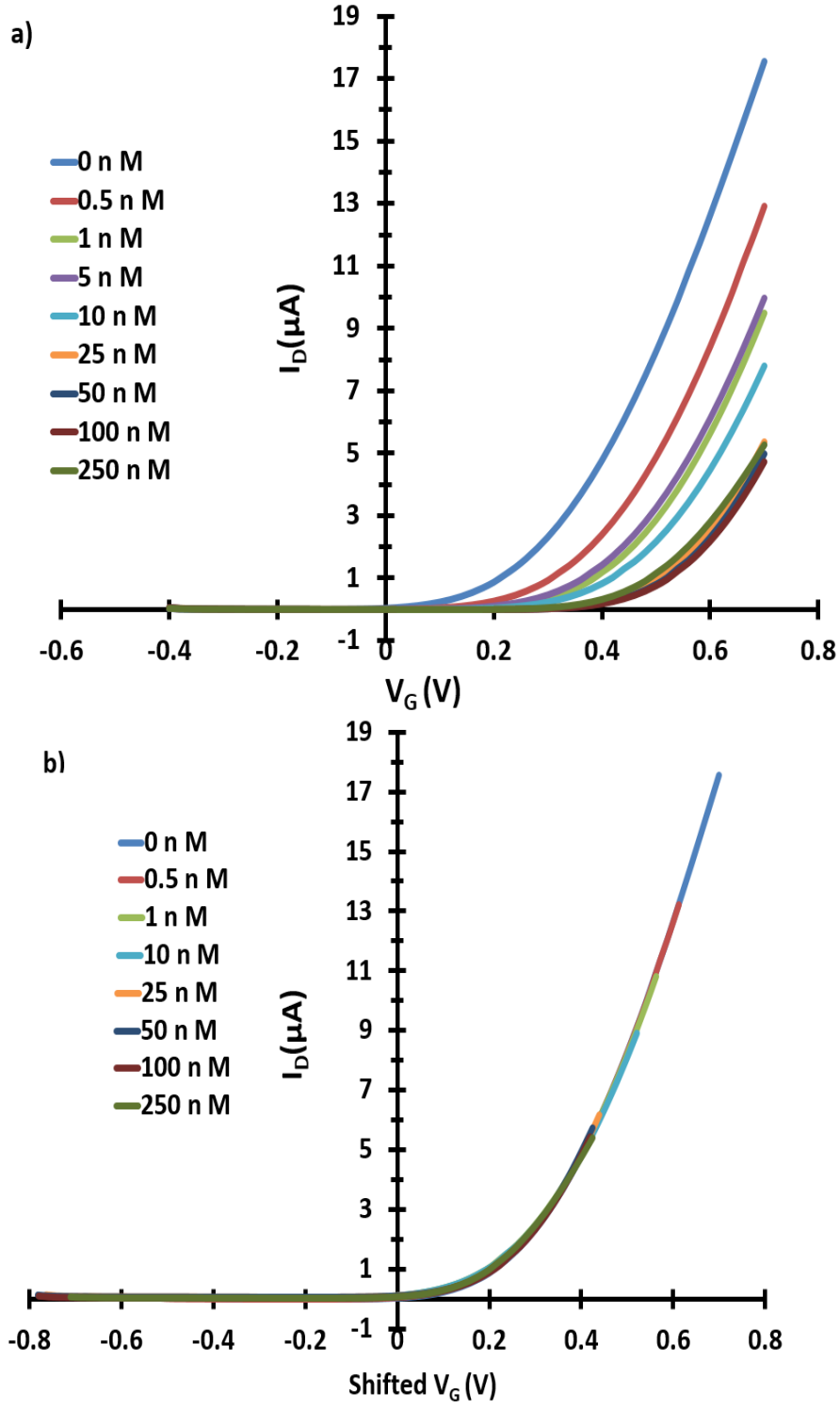

Figure 7-1: *Transfer characteristics of clinoptilolite-sensitised SnO_2 WGTFT gated under increasing Pb^{2+} concentrations in the outer pool. (b) 'Master' transfer characteristic after shifting transfers from Figure 7-1 (a) along the V_G axis for optimum overlap.*

Figure 7-1 (b) shows an excellent overlap of all transfer characteristics into a single 'master' curve. This typical master curve confirms that increasing lead concentration in the sample pool affects threshold voltage only, not any other WGTFT performance parameter. We identified the gate voltage shift required for best overlap as the WGTFT's threshold voltage shift under increasing lead concentration, $\Delta V_{th}(c_{Pb})$. These are shown and analysed in section 7.3.2 below.

We then repeated the above experiment using nominally identical transistors, but adding increasing concentrations of copper (Cu^{2+}) up to 300 μM rather than lead to the outer pool. Note the ~ 1000 times higher concentrations of Cu^{2+} *vs* Pb^{2+}. Corresponding results are shown in Figure 7-2.

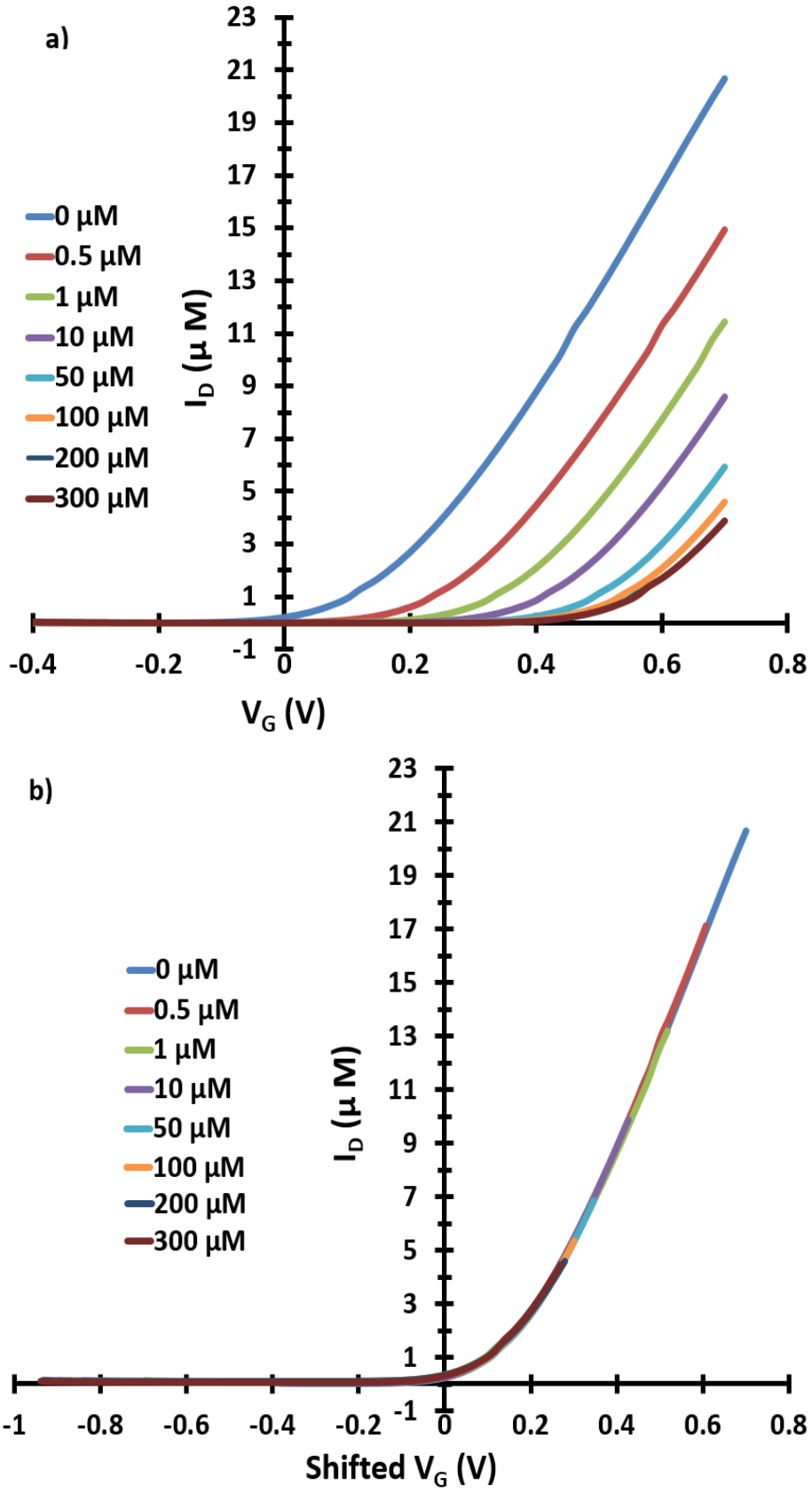

Figure 7-2: *(a) Transfer characteristics of clinoptilolite- sensitised SnO_2 WGTFT gated under increasing Cu^{2+} concentrations in the outer pool. (b) 'Master' transfer characteristic after shifting transfers from Figure 7-2 (a) along the V_G axis for optimum overlap.*

Figure 7-2 b again shows the excellent overlap of all transfer characteristics into a single 'master' transfer characteristic. Threshold shifts $\Delta V_{th}(c_{Cu})$ are shown and analysed in section 7.3.2.

7.3.2 Quantitative analysis of Pb^{2+} and Cu^{2+} sensing

Figure 7-3 shows $\Delta V_{th}(c_{Pb})$ and $\Delta V_{th}(c_{Cu})$ as evaluated from the shift of transfer characteristics along the V_G axis to construct 'master' characteristics.

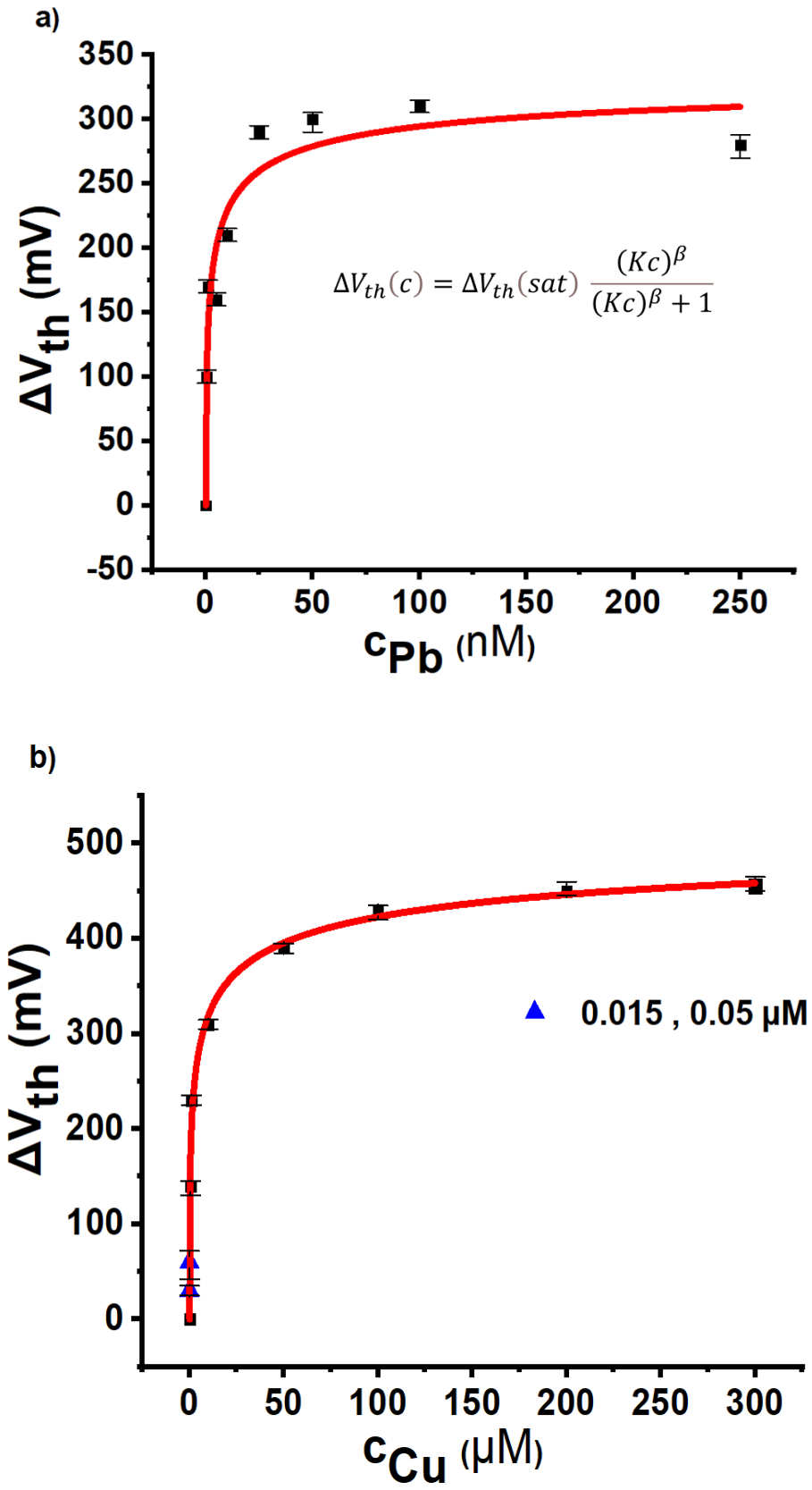

Figure 7-3: (a) *Squares with 'error bars': Threshold shift ΔV_{th} vs concentration of Pb^{2+}, c_{Pb}, as evaluated from Figure 7-1b. (b) Squares with error bars: Threshold shift ΔV_{th} vs concentration of Cu^{2+}, c_{Cu}, as evaluated from Figure 7-2b. Blue triangles with error bars: Data from a similar experiment at 15 nM and 50 nM. Solid red lines are fit to equation 7-3.*

Figure 7-3 shows the threshold shifts observed in clinoptilolite-sensitised WGTFTs with increasing concentration of Pb^{2+} and Cu^{2+}. These increase rapidly for low concentrations and approach saturation $\Delta V_{th}(sat)$ of several 100 mV at high concentrations. This response is different from the Nikolsky-Eisenman law (equation 7-1) but similar to our previous results with zeolite mordenite [258] albeit we required the LF isotherm, equation 7-3, rather than the simpler equation 7-2, for the fits shown in Figure 7-3. A satisfactory match for Pb^{2+} and an excellent match for Cu^{2+} are evident. The values for the fit parameters K, β, and $\Delta V_{th}(sat)$ from equation 7-3 for both Pb^{2+} and Cu^{2+} sensing are summarised in Table 7-1 below.

Table 7-1: *Fit parameters for best fit of equation 7-3 to the data in Figure 7-3*

Parameter ↓ / cation →	**Pb^{2+}**	**Cu^{2+}**
***K* [L mol^{-1}]**	$(4.3 \pm 0.4) \times 10^8$	$(2.5 \pm 0.2) \times 10^5$
$c_{1/2} = 1/K$	(2.3 ± 0.2) nM	(4 ± 0.3) µM
β	0.5 ± 0.2	0.4 ± 0.1
$\Delta V_{th}(sat)$ **[mV]**	341 ± 68	542 ± 74

The 3-orders-of-magnitude larger K for lead *vs* copper indicates the greater extraction of lead than copper by clinoptilolite, which is already evident from the concentration scales used in Figure 7-1 (nM) *vs* Figure 7-2 (µM). To determine values for the limit-of-detection (LoD), we re-plotted the data in Figure 7-3 in linearised form, $\Delta V_{th}(c)((Kc)^{\beta} +1)$ *vs* $(Kc)^{\beta}$ (Figure 7-4), using K and β for Pb^{2+} and Cu^{2+}, respectively, from Table 7-1. We then fitted straight lines of the form $y = mx + b$. The resulting parameters m (slope) and b (intercept) with their respective errors are listed in Table 7-2.

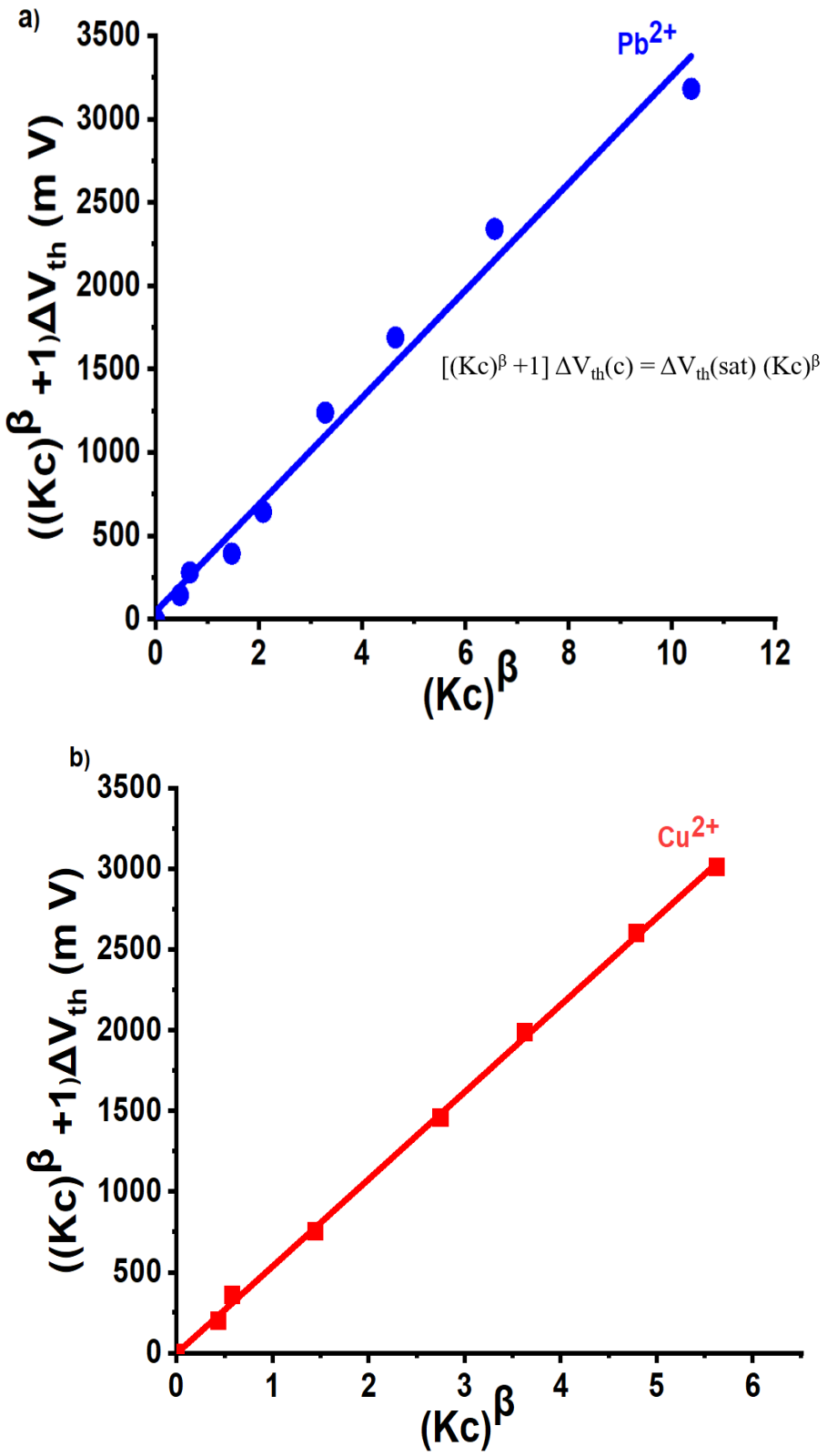

Figure 7-4: (a) *Linearised plot for the response characteristics (in Figure 7-3) of clinoptilolite-sensitised WGTFT threshold shifts, $\Delta V_{th}(c)[(Kc)^{\beta} +1]$ vs $(Kc)^{\beta}$, under Pb^{2+}. (b) The same plot for Cu^{2+}. Respective parameters K and β were taken from Table 7-1.*

Table 7-2: *Fitted slope (m) and intercept (b), with errors, for the linearised threshold shift plots in Figure 7-4.*

Parameter	**Pb^{2+}**	**Cu^{2+}**
***m* ± *Δm* [mV]**	321 ± 15	540 ± 6
***b* ± *Δb* [mV]**	50 ± 68	0.53 ±18.6
LoD	0.9 nM	14 nM

As expected from equation 7-3, b overlaps with zero within its error *Δb*. The concentration corresponding to LoD can be determined with the common '3 errors' criterion, equation 7-4:

$$(Kc_{LoD})^{\beta} = 3\Delta b/m \qquad 7\text{-}4$$

We here find LoD(Pb^{2+}) = 0.9 nM and LoD(Cu^{2+}) = 14 nM, which are already included in Table 7-2. To ensure that Cu^{2+} LoD is realistic value, we repeated the experiment shown in Figure 7-2 with very small Cu^{2+} concentrations (15 and 50 nM). Resulting threshold shifts are shown as blue triangles in Figure 7-3 (b). Note that the triangles agree well with the fit (red line), and that 15 nM is very close to the evaluated LoD and does lead to a recognisable threshold shift (≈ 30 mV); hence, the calculated LoDs for Cu^{2+} are realistic. It should be noted that the LoD for lead should be much smaller than for copper when compared to *1/K*. The relatively high LoD for lead reflects the larger scatter (poorer fit to the model equation 7-3) in the original data, particularly at higher concentrations. Visually, the lead LoD formally evaluated by equation 7-4 seems an overestimate when inspecting Figure 7-1 (a), which shows a clear threshold shift under LoD = 0.9 nM lead. Nevertheless, formally evaluated LoDs for both lead and copper are significantly smaller than the action levels of the lead-and-copper rule, which qualifies our sensors for its monitoring.

7.3.3 Sensor performance in acidic conditions

While the tap water drawn in our lab has near-neutral *pH* (*pH* = 7.2), measured with pH meter (CyberScan PH 300), drinking water generally may vary in *pH*, the permitted range for

drinking water being *pH* (6.5 … 8.5) [284]. Practically, water samples can be tested for *pH* using a *pH* meter and adjusted to *pH* 7 by adding small amounts of a strong base (or acid) before lead-and-copper testing. Contamination with Na^+ from NaOH, for example, will in itself not lead to significant threshold shift, as we show below in section 7.3.5. However, we here show that the impact of *pH* on sensing of lead and copper is small. We added a drop of acetic acid to our tap water to deliberately mildly acidify it, (to *pH* 5.2) as measured with the same *pH* meter. We then tested clinoptilolite-based WGTFTs to sense lead and copper in acidified tap water. Threshold shifts at one representative heavy metal concentration for as- drawn (*pH* 7.2) *vs* acidified (*pH* 5.2) tap water are compared in Table 7-3. Concentrations were chosen to lead to a near-saturated threshold shift, as shown in Figure 7-3.

Table 7-3: *Threshold shifts at selected lead and copper concentrations at pH 5.2 vs pH 7.2.*

Concentration	**ΔV_{th}(mV) at *pH* = 7.2**	**ΔV_{th}(mV) at *pH* = 5.2**
100 nM Pb^{2+}	310	255
300 µM Cu^{2+}	455	415

Heavy metal-induced threshold shifts under acidic conditions are slightly smaller than under near-neutral *pH*. This results from the increasing of hydrogen ions in the samples solution that may prevent Pb^{2+}/ Cu^{2+} cations to reach the binding sites. However, shifts are still significant at *pH* 5.2, which is more than one *pH* unit below the permitted *pH* range for drinking water. Clinoptilolite membranes are therefore suitable to detect lead and copper within the permitted *pH* range of drinking water.

7.3.4 Lead and copper extraction with clinoptilolite

As the usual application of clinoptilolite is for extraction of lead and copper pollution from the drinking water supply [60][59], we here used clinoptilolite membrane-sensitised WGTFTs to test extraction performance. We ‘spiked’ 15 mL of tap water with 1 µM lead and copper, respectively (at the same concentration to allow direct comparison of extraction), and then

attempted to extract the heavy metal again. For this, we added 100 mg of clinoptilolite to spiked water, agitated it, and left it to settle for 2 hr. We then tested water samples resulting from this spiking/extraction procedure in a WGTFT transistor sensitised with a clinoptilolite membrane, in the same manner described in section 7.3.1. The resulting transfer characteristics are shown in Figure 7-5, which for comparison, also includes the transfer characteristics for as-drawn tap water that had not been spiked / extracted.

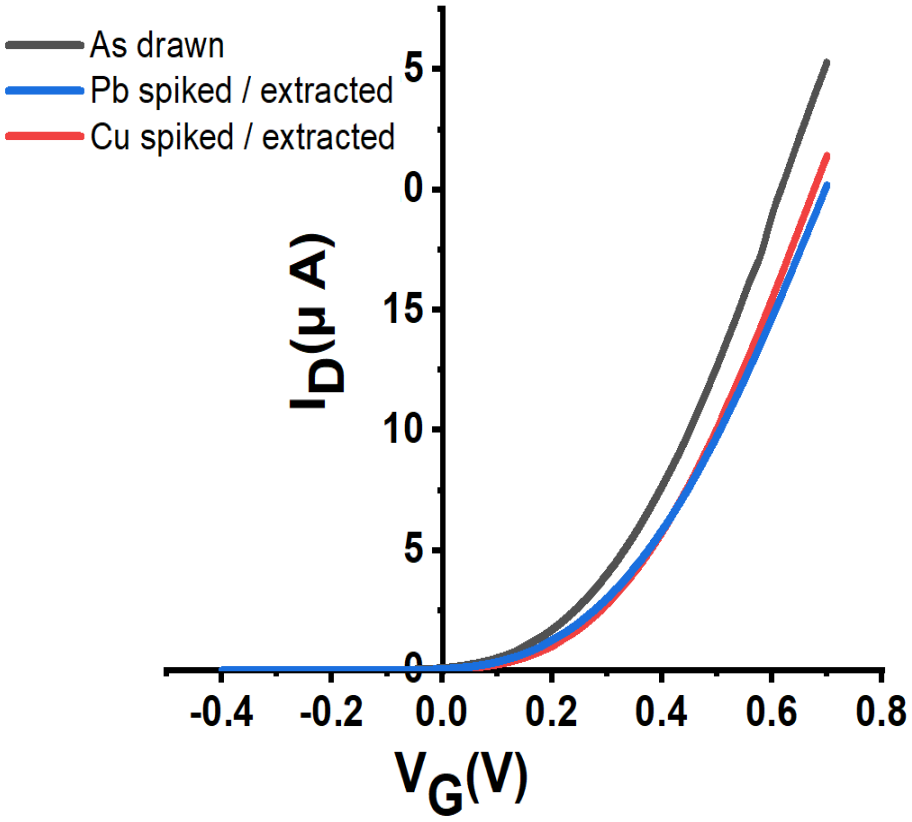

Figure 7-5: *Transfer characteristics for a clinoptilolite membrane-sensitised WGTFT gated by (1 µM heavy metal spiked / extracted) tap water sample vs tap water as-drawn. Blue: Pb^{2+} spiked / extracted, Red: Cu^{2+} spiked / extracted, Black: tap water as drawn.*

It is clear from Figure 7-5 that characteristics for both spiked/extracted samples do display a small threshold shift compared to the tap water sample that was not spiked. However, the shift is significantly lower than that found in section 7.3.1. This response suggests that the extraction procedure significantly reduced the initial 1 µM heavy metal concentration, even though a small amount of pollution remained. Results are summarised in Table 7-4, which also shows

the heavy metal concentration remaining after extraction. These are calculated using equation 7-3 from the measured threshold shifts after extraction, using the parameters listed in Table 7-1.

Table 7-4: *Threshold shift under 1 µM lead and copper vs threshold shift after extraction with clinoptilolite. Residual concentration calculated from threshold shift after extraction with equation 7-3 and the parameters from Table 7-1.*

Tap water spiked with...	**ΔV_{th} (mV) before extraction**	**ΔV_{th} (mV) after extraction**	**Residual concentration**
1 µM Pb^{2+}	340	60	106 pM
1 µM Cu^{2+}	230	50	13 nM

Table 7-4 shows that clinoptilolite is indeed effective at extracting lead and copper from drinking water. The remaining heavy metal pollution after extraction is far below the action level. The larger K for lead *vs* copper established previously is reflected again in the lower residual concentration after extraction.

7.3.5 Interference from common co-cations

Drinking water naturally contains common cations of alkaline and alkaline earth metals (*e.g.* Na^+, Ca^{2+}, Mg^{2+}) in concentrations typically ranging in the order (100 µM … 1mM). For example, our lab's water supplier, Yorkshire Water, quotes a typical 'cocktail' of 200 µM Ca^{2+}, 99 µM Mg^{2+}, and 783 µM Na^+, (see Table 6-1) [274]. These concentrations are significantly higher than the 'action levels' for heavy metals under the lead-and-copper rule, but alkaline and alkaline earth metal co-cations at these levels are not harmful and should not lead to false positives. As described in section 7.2, we accounted for the common tap water interference 'cocktail' by preparing calibration solutions and testing our WGTFTs using tap water rather than DI water. We did, nevertheless, study the interference from co-cations on our WGTFT heavy metal sensor. Figure 7-6 shows the transfer characteristics of a SnO_2 WGTFT transistor

sensitised with a clinoptilolite membrane when using tap water with deliberately added sodium (Na^+) ions (from NaCl) or calcium (Ca^{2+}) ions (from $CaCl_2$) in the sample pool *vs* tap water as-drawn in the reference pool.

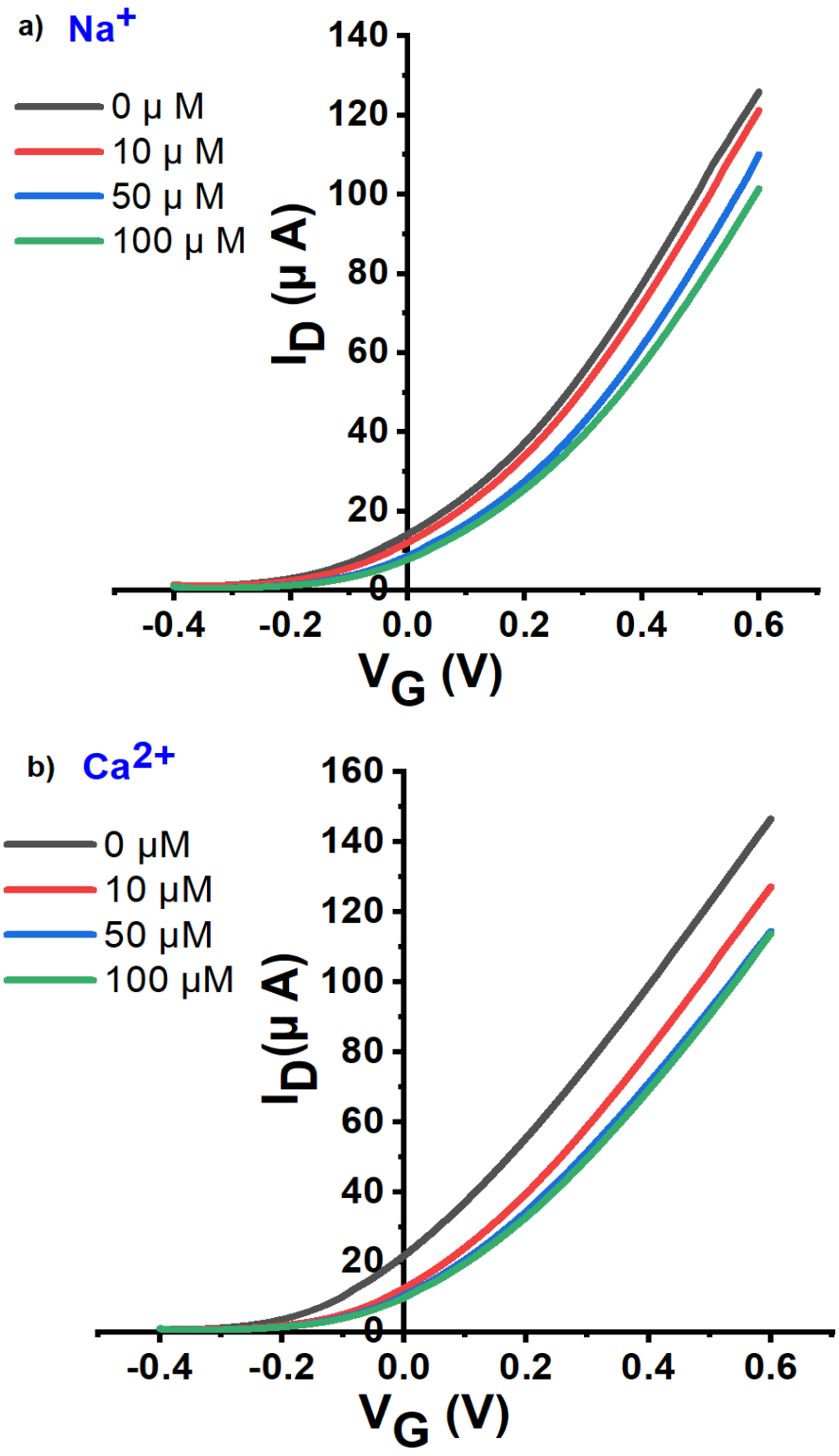

Figure 7-6: (a) *Transfer characteristics of a clinoptilolite-sensitised SnO_2 WGTFT under samples of tap water with deliberately added Na^+ at concentrations of (10, 50, and 100) µM.* ***(b)*** *The same as (a) for Ca^{2+} at concentrations (10, 50, and 100) µM.*

There are measurable threshold shifts under co-cations, as summarised in Table 7-5 below.

Table 7-5: *Threshold shifts under high concentrations of interferants Na^+ and Ca^{2+}.*

Concentration (µM)	ΔV_{th} **(mV) (Na^+)**	ΔV_{th} **(mV) (Ca^{2+})**
10	15	75
50	65	120
100	85	120

The results above show that the highest threshold shifts due to Na^+ and Ca^{2+} are significantly smaller than $\Delta V_{th}(sat)$ under Pb^{2+} or Cu^{2+}. At 100 µM, a shift of 85 mV for Na^+ and 120 mV for Ca^{2+} can be seen, while ΔV_{th} (100 µM) > 400 mV for Cu^{2+}. According to equation 7-3, with the parameters listed in Table 7-1, the action levels of 72 nM for lead and 20.5 µM for copper would lead to threshold shifts of 289 mV (lead) and 356 mV (copper), both significantly larger than 100 mV. Hence, at least qualitatively, we can still decide potability with respect to lead and copper despite interference. To quantify selectivity, we observe from Figure 7-6 (a) that $c_{1/2} \approx 30$ µM for Na^+; hence, selectivity S for lead over sodium is S(Pb^{2+} *vs.* Na^+) = K(Pb) / K(Na) = $c_{1/2}$(Na) / $c_{1/2}$(Pb) ≈ 13,000; log S ≈ 4.1.

7.3.6 Interferant matching by extraction

For sensor calibration in 7.3.1, co-cation (*i.e.*, interferant) concentration in the sample and reference were matched by calibrating sensors with sample solutions we prepared from the same tap water used for reference (*cf.* 7.2). Clinoptilolite selects nanomolar lead from a ~ millimolar interferant cocktail when the reference pool carries a matched cocktail. In section 7.3.5, we studied the practically unrealistic scenario of adding interferants to the sample solution without matching in the reference and found that such a mismatch would still allow lead and copper sensing, at least qualitatively. A more realistic interference 'loophole' arises,

not because we would deliberately add interferants to a sample, but because test samples taken in the environment would carry an *a priori* unknown interferant cocktail different from our tap water. If we, nevertheless, use our tap water in the reference pool, interferants in reference and sample would not be matched.

To address this interference loophole, we propose a procedure based on extraction, as described in section 7.3.4, to generate interferant (and pH) matched reference solutions. When obtaining a sample of unknown lead and/or copper content, we would first split it in two, and then generate an interferant-matched reference solution from one of the two by extracting lead and copper with clinoptilolite. We then first filled both the reference and sample pool with extracted (*i.e*. self-generated reference) solution and recorded a reference transfer characteristic, corresponding to the '0 nM / μM' curves in Figures 7-1 and 7-2. Then, we replaced the extracted solution in the sample pool with the non-extracted (*i.e.*, actual) sample and tested for threshold shift. We tested this procedure by applying it to a control and a sample contaminated with lead at potability limit (72 nM), Figure 7-7.

Figure 7-7 (a) displays the control experiment that was conducted by applying the above extraction procedure to Sheffield tap water (drawn on a different day as previously) without deliberately added lead. The two transfers in Figure 7-7(a) were both taken from the extracted 'reference' in the reference pool, but a comparison was carried out between the extracted 'reference' and non-extracted 'sample' in the sample pool. The two curves are virtually identical, reflecting that the 'sample' was, in fact, tap water with no added lead, like the reference. This control experiment shows that the extraction procedure itself does not introduce false positives (*e.g.* by unintended extraction of interferants). In Figure 7-7 (b), results are shown from the experiment in which we then applied the same procedure to a sample prepared by adding 72 nM lead (potability limit) from lead nitrate to tap water drawn on a different day; thus, not necessarily identical to the water used for Figures 7-1 and 7-2. We then split this 'spiked' sample and generated an interferant-matched reference by extraction. The reference pool was filled with extracted sample (*i.e.* the interferant-matched reference). The sample pool was first filled with the same extracted sample to record a reference transfer characteristic and was then replaced by the untreated 72 nM lead-spiked sample to record the transfer characteristics under sample exposure.

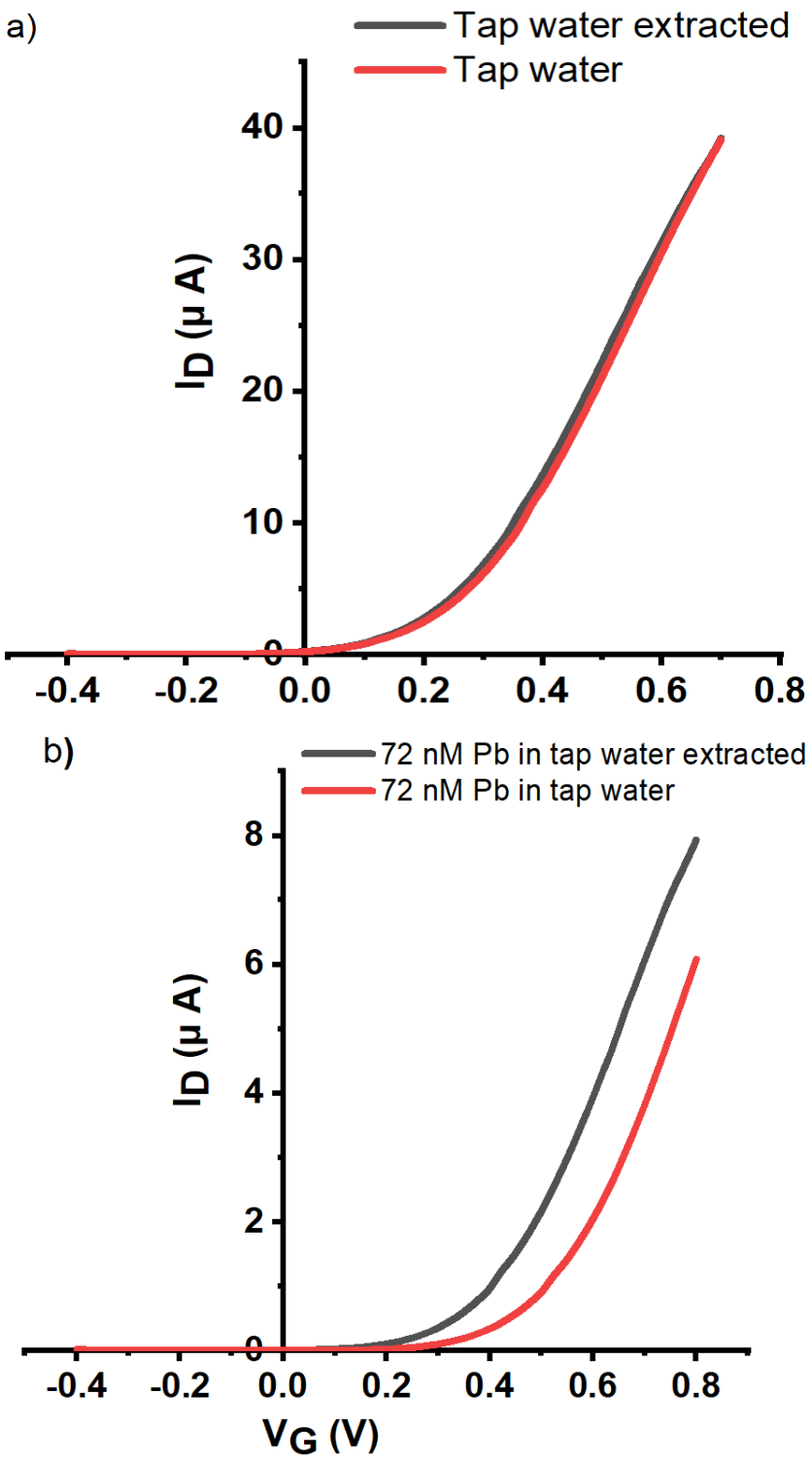
a)
Tap water extracted
Tap water
40
30
20
10
0
I_D (μ A)
-0.4
-0.2
0.0
0.2
0.4
0.6
0.8
b)
72 nM Pb in tap water extracted
72 nM Pb in tap water
8
6
4
2
0
I_D (μ A)
-0.4
-0.2
0.0
0.2
0.4
0.6
0.8
V_G (V)

Figure 7-7: (a) *Transfer characteristics with tap water vs 'extracted' tap water in the sample pool, with 'extracted' tap water in the reference pool.* ***(b)*** *Transfer characteristics with 72 nM lead- spiked tap water vs extracted spiked tap water in the sample pool, with extracted spiked tap water in the reference pool.*

Now we observe a significant threshold shift $\Delta V_{th} \approx 110$ mV between the reference (extracted sample) and actual sample in the sample pool. With the extraction procedure, we unambiguously detected lead at potability limit, relying only on clinoptilolite and the sample itself. The unknown interferant cocktail in the sample is accounted for by reference to an extracted sample with matching (albeit unknown) interferants.

7.4 Summary and conclusions

The cheap and naturally abundant zeolite clinoptilolite is not only useful for the extraction of the toxic heavy metals copper and lead from contaminated water but also for sensing and monitoring of the lead-and-copper rule. When powdered clinoptilolite was embedded into a plasticised PVC membrane that separate a sample and a reference pool in water-gated SnO_2 thin-film transistor, we observed a membrane potential that led to transistor threshold shift in response to the presence of either Pb^{2+} or Cu^{2+} in the sample pool. The threshold shift follows a Langmuir-Freundlich (LF) characteristic, equation 7-3. This contrasts to Nikolsky-Eisenman (NE) characteristics, equation 7-1, which are usually found for potentiometric membranes sensitised with organic ionophores (*e.g.* [52][35][34] [259][266]), but also in prior reports on zeolite-sensitised membranes (*e.g.* [199]). The NE characteristic flat lines at concentrations $c < c_{st}$, hence LoD $\approx c_{st}$, which is typically in the order (100 nM to 1 µM). The LF characteristic lacks such a lower cut-off and, in fact, shows the steepest slope of membrane potential with c in the limit $c \rightarrow 0$, opening a window to much lower LoDs. We here determine limits-of-detection (LoDs), which, for both Pb^{2+} and Cu^{2+}, are significantly smaller than the 'action levels' stipulated by the lead-and-copper rule [281], Pb^{2+}: LoD 0.9 nM *vs* 72 nM action level, Cu^{2+}: LoD 14 nM *vs* 20.5 µM action level. Threshold shift saturates for high ion concentrations; namely, at 341 mV (Pb^{2+}) and 542 mV (Cu^{2+}), which is high within the 1.23 V electrochemical window of water. Another finding is that the sensors work even in mildly acidic conditions. This qualifies clinoptilolite-sensitised WGTFTs as a low footprint sensor technology for monitoring the lead-and-copper rule, and to confirm the effectiveness of attempts to extract lead and copper from water. For the practical use of such sensors, potential interference from

common co-cations, such as Na^{+}, Ca^{2+}, and Mg^{2+}, is a more serious challenge than LoD. However, we have provided and verified a routine for generating interferant-matched reference solutions via the use of clinoptilolite as extractant as well as a sensitiser, closing the interference loophole.

The reason for the unusual but useful LF response characteristic warrants further study. We note an important difference between conventional macrocycle-sensitised potentiometric sensors and zeolite-based sensors; namely, macrocycles capture the target ion and, hence, charge the membrane. Zeolites are ion exchangers, so acquire no net charge under target ion exposure, but may well build up superficial dipoles.

Chapter 8 : Water-gated transistor using ion-exchange resin for potentiometric fluoride sensing

8.1 Introduction

In recent years, water-gated thin-film transistors (WGTFTs) have been developed into a novel potentiometric transducer for the sensing of waterborne ions. WGTFTs were sensitised with plasticised PVC phase transfer membranes loaded with ion selective sorbents such as organic macrocycles [52][34][35]. Macrocycles selectively 'accumulate' ions (usually cations) in their central cavity, and thus build up charge and potential following a Nikolsky-Eisenman (modified Nernstian) law, *i.e.*, potential is logarithmic with ion concentration down to a lower 'cut- off' $c_{st} \gtrsim 100$ nM, which sets a limit-of-detection (LoD). A similar characteristic applies to the classic potentiometric sensing of waterborne fluoride anions: Frant and Ross [285] reported electrodes constructed from LaF_3 giving Nikolsky-Eisenman characteristic with $c_{st} \sim 1$ µM and good selectivity for fluoride over other common anions. Alternatively, we have recently demonstrated WGTFT-based potentiometry using an ion-exchange sorbent in the phase transfer membrane, the caesium-selective zeolite 'mordenite' [258] and the lead-and-copper selective zeolite 'clinoptilolite' [286]. We found a membrane potential in response to increasing analyte concentration following a Langmuir- or Langmuir-Freundlich isotherm (to be introduced below), instead of a Nikolsky-Eisenman law. The different response characteristics allow a much lower limit-of-detection (LoD). The origin of the membrane potential remains unclear though: ion exchange does not accumulate a net charge on the membrane. This sets such membranes apart from membranes that are sensitised (*e.g.* with ion-selective organic macrocycles [52][34][35]), which give a Nikolsky-Eisenman membrane potential as a result of charge accumulation when exposed to a 'target' ion.

Here, we targeted the fluoride anion with another ion-exchange sorbent in a WGTFT membrane. Fluoride is naturally present in groundwater. Small quantities of fluoride are beneficial to health, but excessive fluoride intake can result in fluorosis [240][241], a serious illness. The World Health Organization (WHO) sets a maximum acceptable concentration ('potability limit') of 1.5 mg l^{-1} = 79 µM fluoride in drinking water [241]. The health hazards

associated with fluoride call for both methods of defluoridation and sensor technologies to detect fluoride hazards. Precipitation defluoridation results in large volumes of low-value slurry from which fluoride recovery is difficult [287]. Adsorption and ion-exchange techniques allow selective fluoride removal without generating waste. Numerous fluoride uptake studies have used sorbents such as alumina [288], activated carbon [289], synthesised microporous polymers [290], and layered double hydroxide clays [291].

Recently, sorbents have been developed from the macroporous Purolite™ MTS9501 chelating resin that allows metal loading through its aminophosphonic acid group (more details in section 8.2.1). Aluminium (Al)-loaded chelating resins have been investigated for fluoride-removal capabilities [292]. Robshaw *et al.* successfully trialled Lanthanum (La) loading [61]. Generally, sorbate extraction is quantified by relative sorbent mass uptake *vs.* sorbate concentration in solution, equation 8-1:

$$\frac{\Delta m(c)}{m(0)} = \frac{\Delta m(\infty)}{m(0)}\,\theta(c) \qquad 8\text{-}1$$

wherein c is the sorbate's concentration, $\frac{\Delta m(\infty)}{m(0)}$ the sorbent's capacity, *i.e.*, saturated relative mass uptake, and θ(c) a dimensionless monotonously increasing function with $\theta(0) = 0$ and $\theta(c \to \infty) = 1$. An often used, versatile approach to θ(c) is the Langmuir-Freundlich (LF) isotherm:

$$\theta(c) = \frac{(Kc)^{\beta}}{(Kc+1)^{\beta}} \qquad 8\text{-}2$$

which generalises the classic Langmuir isotherm (special case $\beta = 1$). K quantifies the strength of the interaction between a sorption site and the sorbate, $\beta \leq 1$, quantifies inhomogeneity between sorption sites ($\beta = 1$, K for all sorption sites is equal). A characteristic concentration $c_{1/2}$ is given by $\theta(c_{1/2}) = ½$. For the LF isotherm, $c_{1/2} = 1/K$, but $c_{1/2}$ can be read directly from measured characteristics without relying on a model. Note, for mordenite extracting Cs^+, $c_{1/2}$ is very much smaller for membrane potential [258] than for mass extraction [57].

Here, we introduce metal-loaded (La and Al) Purolite ion-exchange chelating resins into WGTFTs, the first example of an anion (Fluoride)-selective potentiometric WGTFT sensor. Chemically, the amorphous organic resin is different to inorganic crystalline zeolites such as

'mordenite' and 'clinoptilolite' zeolite minerals (as demonstrated in section 3.3.3.1) we used previously for Cs^+ [258] and Pb^{2+}/Cu^{2+} [286] sensing, respectively. However, they both exchange rather than accumulate ions, and we again found a response characteristic controlled by equation 8-2 with very low $c_{1/2}$ and LoD. We investigate the mechanism behind the build-up of an ion concentration-dependent potential in phase transfer membranes sensitised with ion-exchange sorbents despite the lack of a net charge on the sorbent, and tested a proposed model. Further, we explore practical aspects (*e.g.*, interference from other anions). Most importantly, our work sets a template for the use of a new family of sensitisers, namely ion-exchange resins, in WGTFT- based sensors for water pollutants. Such resins are available as sorbents for very harmful, or precious, water pollutants (arsenic, gold, copper, mercury, palladium [204][207][206][205][293]). Following this work, these sorbents can now easily be adapted for the sensing of such pollutants as well.

8.2 Experimental procedure and evaluation

8.2.1 Purolite™ MTS9501

Purolite™ MTS9501 is an example of a commercial ion-exchange resin consisting of styrene and divinylbenzene crosslinked copolymer, with aminomethylphosphonic acid (AMP) as a functional group as explained in section 3.3.3.2. This resin is a microporous chelating resin, available in spherical beads with particle sizes in the 300-1200 μm range. Purolite MTS9501 was kindly donated, as Na form, by the manufacturer 'Purolite' (Llantrisant, Wales) for the group in the Department of Chemical and Biological Engineering, The University of Sheffield. This group has successfully activated this cation exchanger resin for selective fluoride extraction via pre-loading with trivalent metal cations (lanthanum- La^{3+} and Al^{3+}) to the resin functional group [61], which is similar to the modification of this type of resin by aluminium metal (Al^{3+}) (Bhatt et al., 2004) [292], as will be described in section 8.2.2. The cations (La^{3+}/Al^{3+}) are bonded with the AMP group via chelation interaction while retaining several inner coordination sphere sites, which are occupied by hydroxyl and aqua ligands, as shown in Figure 8-1. Fluoride can be taken up through the ligand exchange mechanism in which one or two OH^- ligands coordinated to the metal-loaded resin can be substituted for F^- ligands as following:

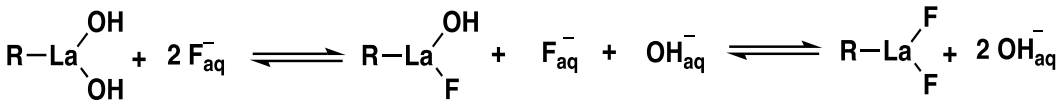

where R and ‘aq’ stand for resin functional group ligand and ions dissolved in water, respectively. We here adopted the La-/Al-loaded MTS9501 resin sorbent as a sensitiser in the WGTFT to develop the F^--WGTFT sensor. This activated resin was kindly donated to our group by Dr Mark D. Ogden and Dr Thomas Robshaw from the Department of Chemical and Biological Engineering, The University of Sheffield.

8.2.2 Preparation of metal- loaded chelating resin

To operate this resin to F^- uptake as described in [61], the resin is first converted to protonated form (H form) by preconditioning it with HCl. This is achieved by putting about 25 g resin (wet mass) in 1 L of 1M HCl and placing the mixture on an orbital shaker at 100 rpm for 24 h. The resin is then washed with 5 x 1 L deionised water. The resulting protonated resin is then loaded with La^{3+} ions by contacting about 25 g resin (wet mass) with 10 g/L La^{3+} solution (72 mM), made from $LaCl_3.7H_2O$ dissolved in deionised water, and placing that on an orbital shaker at 100 rpm for 24 hrs. The resin is then washed with 5 x 1 L deionised water. Excess water is removed, and the resin is ground with a mortar and pestle, then dried in an air-flow oven at 50 °C for a minimum of 24 h. The Puromet MTS9501 resin was loaded with Al by a similar procedure using $Al(NO_3)_3$ to produce 20 g/L Al^{3+} dissolved in deionised water, as described in [292]. Figure 8-1 below shows the loading and coordination of La ions to the resin functionality (Figure 8-1a) and the fluoride uptake mechanism, as explained in the previous section (Figure 8-1b).

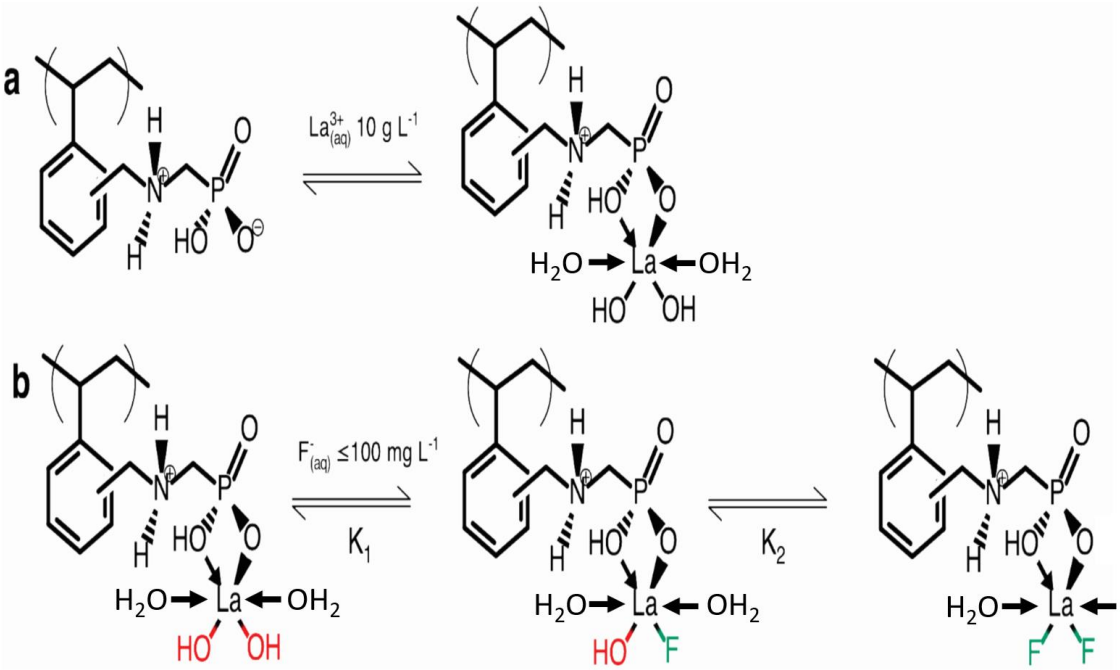

Figure 8-1: *a) Loading of trivalent metal (for example, La) to activate Puromet MTS9501 resin for later fluoride uptake. b) Ligand exchange (F- for OH-) when La-activated MTS9501 resin contacts with aqueous F- based on [59].*

As mentioned earlier, metal loading activates the resin for fluoride uptake via ligand exchange at low concentrations by replacing one or both hydroxyl (-OH) ligands in R-M(-OH)$_2$ (M = La or Al) with waterborne fluoride, F^-_{aq} (Figure 8-1b). We note that both the La-OH bond and the La-F bond are polar and thus contribute a dipole moment, but these will not be of the same magnitude. Hence, ion exchange of F^- for OH^- changes dipole moment, which can be detected with a potentiometric transducer. The characteristic concentration ,$c_{1/2}$, for the extraction of fluoride with Al-loaded Puromet® MTS9501 chelating resin was $c_{1/2}$ = 370 µM [292] while La-loaded chelating resin gave lower $c_{1/2}$ = 160 µM [61]. The lower $c_{1/2}$ for La- *vs*. Al-loaded resin is a quantitative measure for the stronger fluoride sorption by the La-loaded resin. Note the sorbent's capacity $\frac{\Delta\, m(\infty)}{m(0)}$ may nevertheless be larger for Al-loading as this is controlled by the extent of metal loading, not the strength of sorption. To prepare the resin for incorporation into the WGTFT, it was dried in a 50^{O}C air-flow oven for 24 hours, then ground to various degrees with pestle and mortar.

The La loading procedure, described above, results in 'heavily' La-loaded resins carrying 256 ± 2 mg of La per gram of resin. To prepare resins that are only 'lightly' loaded with La (to be used in section 8.3.4), a heavily loaded resin sample (25 g hydrated mass) was placed in a polypropylene bottle with 1 L of 1 M HCl. This was sealed and placed on an orbital shaker for a period of 24 hours, after which the resin was separated from the acidic solution, placed under gravity filtration and washed with at least 5 L of deionised water until the pH of the filtrate was near neutral. This procedure largely, but not completely, removed La centres from the resin.

8.2.3 Preparation of ion selective membranes and sample solutions

Metal loaded chelating resins were incorporated into plasticised PVC phase transfer membranes and then in the SnO_2 WGTFT architecture as explained in section 4.4.1. The preparation of SnO_2 WGTFTs was detailed in Chapter 4.

A 1 µM F^- stock solution was prepared by dissolving sodium fluoride, NaF, in deionised (DI) water; we then obtained the desired (low) concentrations used in the experiments by diluting this with more DI water to (500, 100, 10, 1, 0.1 and 0.01) nM F^-. NaCl and Na_2CO_3 were used in the same way to prepare Cl^- and CO_3^{2-} solutions for the control experiment.

8.2.4 Fluoride- sensitive water- gated thin film transistor (WGTFT) setup

In this work, the 'two-champers design' of WGTFT sensor (elaborated in section 4.4) was adopted. In this design, the lower 'reference' pool was filled with deionised (DI) water and the upper 'sample' pool was filled with samples containing calibrated amounts of fluoride or interferant (chloride or carbonate salts) dissolved in DI water. After each measurement cycle, the sample pool was then emptied and re-filled with a different sample, usually with increasing salt concentration. Note that drinking water commonly contains further anions (*e.g.* chloride, nitrate, and carbonate) that are far more concentrated than fluoride and can be tolerated up to millimolar potability limits, as detailed in [294][295]. We have, therefore, also conducted experiments to study interference from such ions in a similar manner as described above for fluoride.

8.2.5 Determination and evaluation of membrane potential with WGTFT

A voltage applied to the gate contact in Figure 4-7 is communicated across the water in both pools and the membrane to the semiconductor surface via interfacial electric double layers (EDLs), as mentioned in section 4.4. The membrane builds up a potential in response to different ion concentrations in the upper (sample) *vs*. the lower (reference) pool. This concentration-dependant membrane potential, $V_M(c)$, is added to the voltage applied to the gate. Thus, the potential at the semiconductor surface is different from the potential applied to the gate by $V_M(c)$. Consequently, the 'threshold' voltage V_{th}, *i.e*. the gate voltage at which the transistor turns from 'off' to 'on', shifts by V_M. We increased analyte concentration in the sample pool stepwise and allowed 6 minutes for the membrane to equilibrate. Then we recorded the WGTFT's linear transfer characteristics, as shown in section 5.2.1.2: at a small fixed positive source-drain voltage (source on ground, drain on + 0.1 V), we swept the gate voltage from a 'large' negative value (meaning, a value well below threshold, V_{th}, where the transistor clearly is 'off') to a 'large' positive value, where the drain current I_D increases linearly with gate voltage, while measuring and recording I_D. The resulting characteristic $I_D(V_G)$ is known as 'linear transfer characteristic' due to the linear I_D *vs* V_G relation at high V_G. Evaluation of linear transfers allows tracking V_{th}, as shown in section 5.2.1.3.1, which under increasing analyte concentration in the sample pool, shifted according to the membrane potential, $\Delta V_{th}(c) = V_M(c)$. We therefore graphically shifted measured characteristics along the gate voltage (V_G) axis until they best matched the zero fluoride (DI water) transfer, constructing a 'master' transfer characteristic, as explained in section 5.2.1.5. The shift needed to best match the characteristic under concentration, c, to the c = 0 characteristic, was identified as $\Delta V_{th}(c) = V_M(c)$. Finally, we plotted the $\Delta V_{th}(c)$ response, including error bars, and fitted to a Langmuir-Freundlich model, similar to that of sorbate mass uptake, using the nonlinear fit routine in Origin 2018:

$$V_M(c) = \Delta V_{th}(c) = \Delta V_{th}(sat)\ \theta(c) = \Delta V_{th}\frac{(Kc)^{\beta}}{(Kc)^{\beta}+1} \qquad 8\text{-}3$$

To determine the limit-of-detection (LoD), we plotted the same data in linearised form, $\Delta V_{th}(c)$ $((Kc)^{\beta}+1)$ *vs.* $(Kc)^{\beta}$, and fitted a straight line of the form $\Delta V_{th}(c)$ $((Kc)^{\beta}+1) = m(Kc)^{\beta} + b$, evaluating parameters m and b +/- Δb by Origin 2018's linear fitting routine. b was expected to overlap zero within +/- Δb. LoD was calculated from the common '3 estimated standard errors' criterion [219]:

$$(Kc_{LoD})^{\beta} = \frac{3\,\Delta b}{m} \qquad 8\text{-}4$$

8.3 Results and discussion

This section is structured into 4 sections. In part 8.3.1, we discuss our use of WGTFTs to establish membrane potential characteristics in response to fluoride concentration in water samples. The determined characteristics led us to a hypothesis for the underlying mechanism that we tested and confirmed, the results of which are presented in 8.3.2. In 8.3.3, we then address some of the practical issues for using chelating resins in WGTFT fluoride sensors; namely, recovery and interference. Finally, reducing interference from carbonate by diluting metal loading in the resin is presented in 8.3.4.

8.3.1 Fluoride response for WGTFTs using La- and Al- loaded resin membranes

Figures 8-2 and 8-3 show linear transfer characteristics of phase transfer membrane- sensitised WGTFTs under increasing concentrations of fluoride in the upper (sample) pool, using La-loaded (Figure 8-2) and Al-loaded (Figure 8-3) chelating resin membrane.

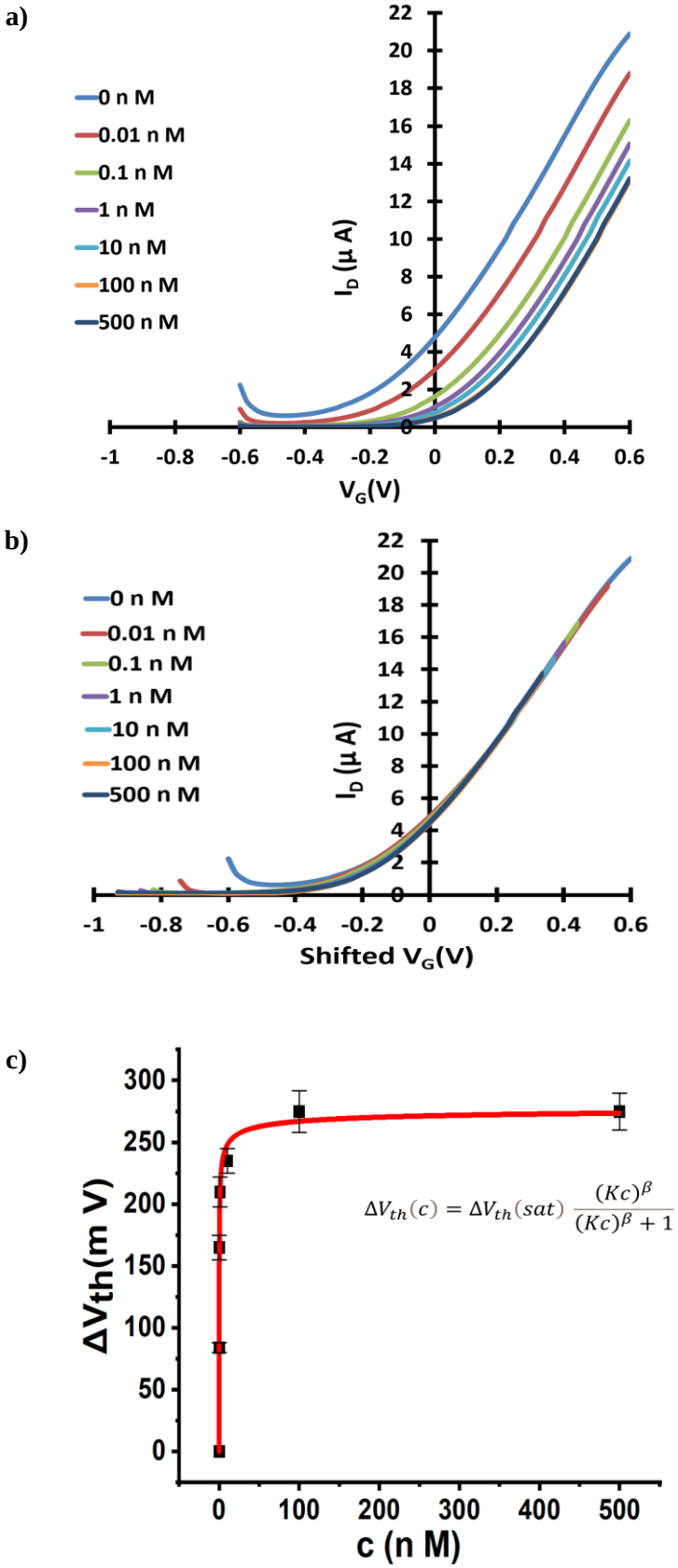

***Figure 8-2**: **(a)** Transfer characteristics of La-loaded chelating resin-sensitised SnO_2 WGTFT gated under increasing F^- concentrations in the outer pool. **(b)** 'Master' transfer characteristic after shifting transfers from Figure 8-2 (a) along the V_G axis for optimum overlap. **(c)** Response characteristic with fit to equation 8-3.*

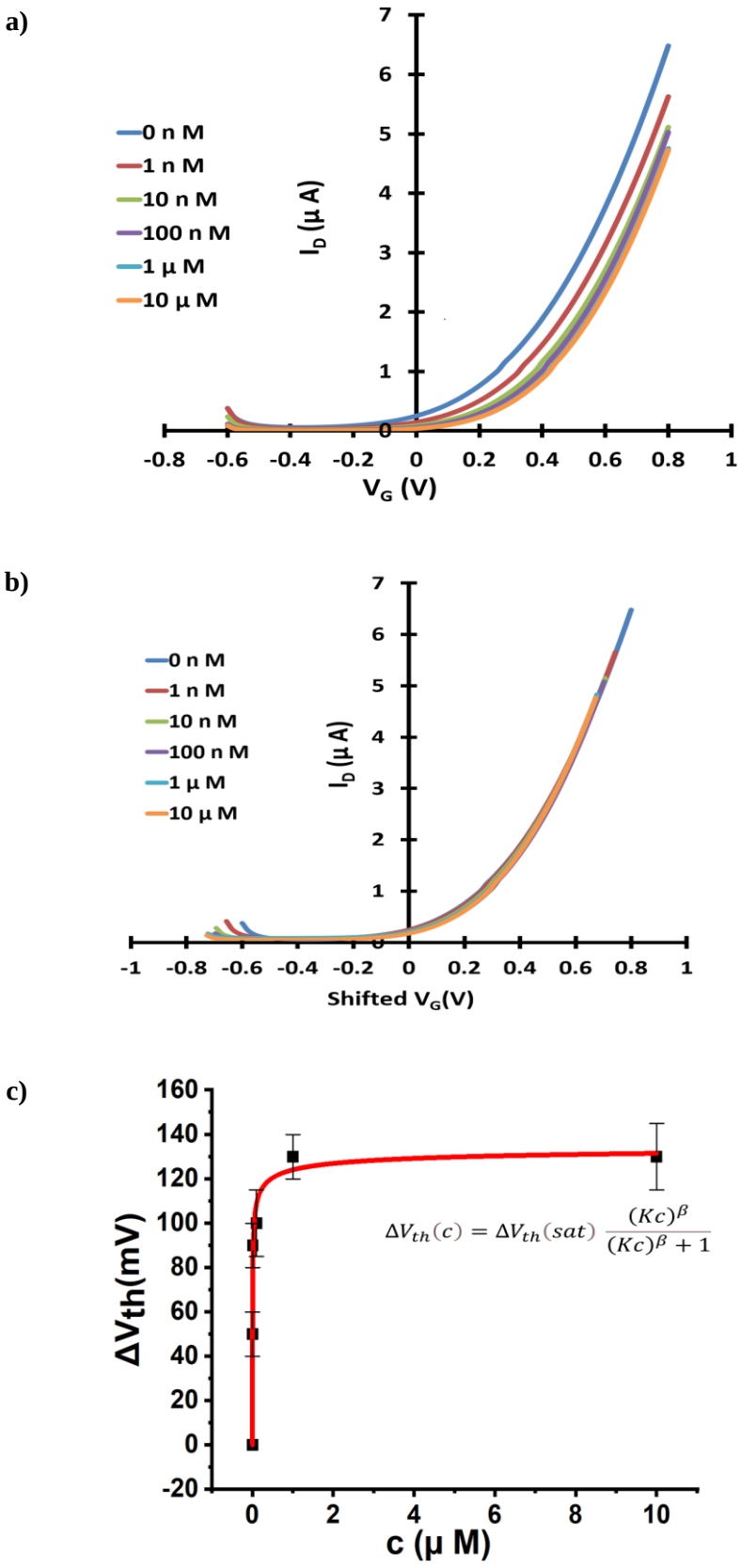

Figure 8-3: ***(a)*** *Transfer characteristics of Al-loaded chelating resin-sensitised SnO_2 WGTFT gated under increasing F^- concentrations in the outer pool.* ***(b)*** *Master transfer characteristic.* ***(c)*** *Response characteristic with fit to equation 8-3.*

For both La- and Al-loaded membranes, transfer characteristics clearly shift to more positive gate voltages under increasing fluoride concentration. For the La resin, this trend is already observed for a fluoride concentration of only 10 pM. This shows that metal-loaded membranes developed a potential in response to very small fluoride concentrations in the sample under test. Threshold shift was evaluated quantitatively, as described in sections 8.2.4 and 5.2.1.5. The resulting response characteristics for both La- and Al-loaded resin are shown in Figures 8-2 c and 8-3 c, respectively, including fits to the LF model (equation 8-3). Data line up on a smooth curve fitted well by the LF law, without random scatter. Table 8-1 summarises the parameters K, $c_{1/2} = 1/K$, $\Delta V_{th}(sat)$, and β for best fit to equation 8-3, as well as limits-of-detection (LoDs). Evaluation of LoD was as described in 8.2.4 and is shown in Figure 8-4.

Table 8-1: *K, $c_{1/2}$, $\Delta V_{th}(sat)$, β, and LoD for the response of WGTFTs sensitised with La- and Al-loaded chelating resins to fluoride. We only used coarse-ground resin-filled membranes. The results for fine-ground La-loaded resin from Figure 8-5 in section 8.3.2 below are previewed here but discussed only later.*

Metal loading (ground)	**K [10^8 L/mol]**	**$c_{1/2}$ [pM] / [nM]**	**$\Delta V_{th}(sat)$ [mV]**	**β**	**LoD [pM]**
La (coarse)	190 ± 80	(53 ± 22) pM	277 ± 14	0.43 ± 0.09	13
La (fine)	114± 72	(88 ± 55) pM	541 ± 37	0.3 ± 0.04	0.82
Al (coarse)	3 ± 1.8	(3.3 ± 2) nM	137 ± 11	0.4 ± 0.12	600

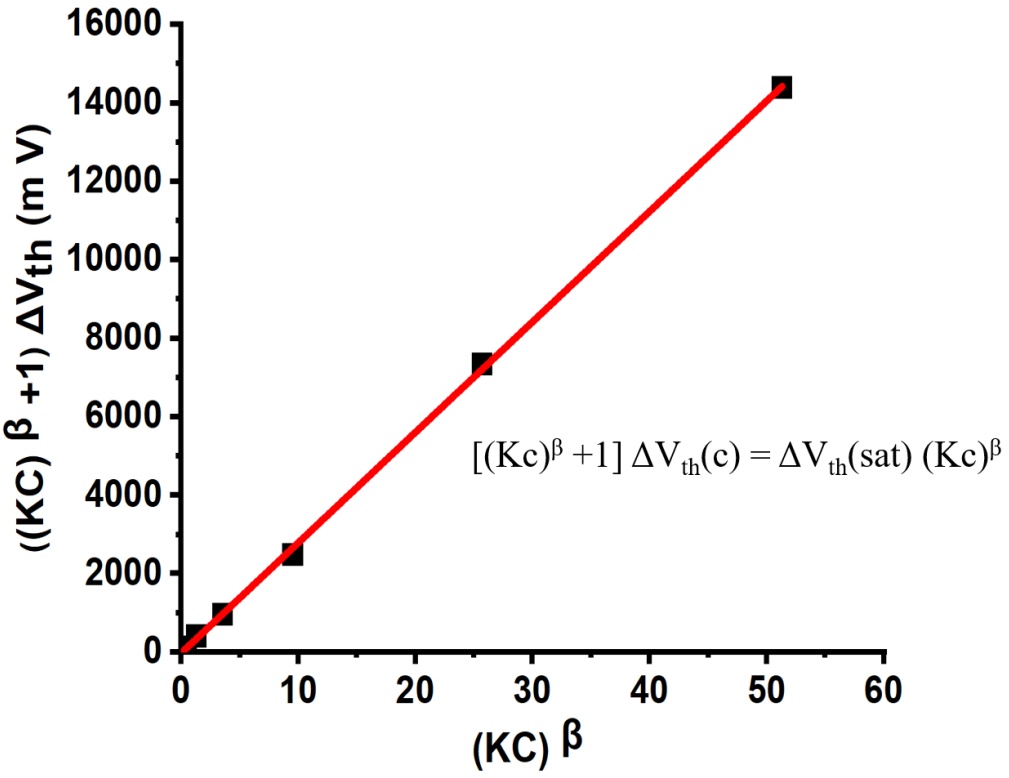

***Figure 8-4**: Linearised response characteristics plot, $\Delta V_{th}(sat)$ $((Kc)^{\beta}+1)$ vs. $(Kc)^{\beta}$, for the response characteristics, Figure 8-2 c, with straight- line- fits for determination of limit- of- detection (LoD) with equation 8-4. All other LoDs reported here were determined by similar plots and analysis.*

We note and discuss a number of interesting properties of the observed response characteristics. Threshold shifts (*i.e.* membrane potentials) are fitted well by a characteristic of the form equation 8-3, which is based on a Langmuir-Freundlich (LF) isotherm, albeit errors in some parameters are relatively large. This is common though for multiparametric non-linear fits [296][297]. The response following LF characteristics is distinctly different from the Nikolsky-Eisenman (Nernstian with lower limit ≈ LoD) characteristics typically observed for potentiometric sensors, including (cat)ion-selective WGTFTs sensitised with organic macrocycles (*e.g.*, [52][34][35]), and LaF_3 membrane-based fluoride potentiometers [285]. However, we have recently reported membrane potential and threshold shift with Langmuir characteristics [258] and LF characteristics [286] for a cation-selective WGTFT sensitised with zeolites. We suggest this difference is rooted in different sorption mechanisms: when an organic macrocycle complexes an ion (usually a cation) in its central cavity, it does so without ion exchange. Hence, the membrane usually accumulates positive charge, leaving behind an

excess of negative charge in the aqueous phase. The quantitative treatment of ion complexation from solutions of target ions with concentration c leads to the Nernst equation, with a logarithmic dependence of membrane potential on c. However, chelating resins and zeolite extract sorbate ions by ion exchange without build-up of net charge in the sorbent: e.g., La-activated Puromet resin returns a hydroxyl (OH^-) ion to the aqueous phase for every fluoride (F^-) ion it extracts from it (*cf.* Figure 8-1b). Neither the membrane nor aqueous phase accumulated net charge; hence, the assumptions of the Nernst law are not given. Ion exchange rather followed an LF adsorption isotherm (equation 8-2). How ion exchange can nevertheless lead to a membrane potential will be discussed below. First, we note a striking quantitative difference between the K's / $c_{1/2}$'s for sensing (*i.e.* threshold shift) and extraction (*i.e.* mass uptake) in ion-exchange sorbents: for La-loaded resin, Table 8-1 shows $c_{1/2}$ for threshold shift is 6½ orders-of-magnitude smaller (K correspondingly larger) than for mass extraction with the same sorbent [61]. K for threshold shift is also very large in comparison to K's found for the binding between metal cations and selective organic dyes (*e.g.*, [219]), which are of a similar order (or somewhat larger) to K's for mass extraction. We found a similar discrepancy in $c_{1/2}$ for Caesium-selective mordenite zeolite ion-exchange sorbent, $c_{1/2} \approx 260$ pM for threshold shift [258] *vs.* $c_{1/2} \approx 640$ µM for mass uptake [57]. For reasons not well understood at this stage, ΔV_{th} already saturates when only a small fraction of all available ion-exchange sites have exchanged hydroxyl for fluoride.

To address the fundamental question of how a membrane potential develops when neither membrane nor aqueous phase acquire a net charge under ion exchange, we note that the R-La-OH and the R-La-F bond have a different dipole moment. Hence ion exchange R-La-OH + F^- → R-La-F + OH^- leads to a change in the magnitude of the dipole moment at the exchanged site. The density of dipole moments represents a polarisation, P. We believe it is this polarisation, in particular at the surfaces of resin grains, that leads to a shift in threshold voltage. It is well established that polarisation can gate field-effect transistors, the most prominent example being memory transistors using ferroelectric or similar gate media (as in [298]). Such transistors can be 'on' even at zero applied gate voltage, solely due to the gate medium's remnant polarisation. A surface mechanism is suggested by the results presented in section 8.3.2 below.

While the discussion above applies to all ion exchangers, such as chelating resins and zeolites, we observed a minor difference in their response characteristics. While the generic Langmuir isotherm (special case of LF with $\beta = 1$) provides a good fit for threshold shift in WGTFTs

using zeolite ‘mordenite’ sorbent for Cs^+ [258], threshold shift characteristics for zeolite 'clinoptilolite' under lead and copper [286], and for chelating resin under fluoride as reported here, show β values significantly smaller than 1. Langmuir isotherm theory assumes all sorption sites have equal constant K, $\beta < 1$ in the LF isotherm accounts for dissimilar K within the same sorbent. Thus, the more inhomogeneous sorption sites there are, the smaller β becomes [220]. We suppose that while mordenite has a clearly defined chemical makeup as well as a defined crystalline unit cell, clinoptilolite may be has a degree of randomness in the sites available for ion exchange. This leads to a distribution of K's. Similarly, our organic chelating resin is an amorphous material, therefore different exchange sites will experience different microenvironments. Additionally, in the macroporous environment, in some cases, two metal centers may be adjacent and ‘share’ a fluoride-bridging ligand [299]. Overall, this again leads to a distribution of K's.

A significant difference is observed between La- and Al-loaded resins. The higher affinity of fluoride to exchange for OH^- from La-OH rather than an Al-OH, as also shown in the extraction characteristics presented in [292][61], is reflected in the lower $c_{1/2}$ for membrane potential and higher saturated threshold shift $\Delta V_{th}(sat)$ for La- rather than Al-loaded resin. While $c_{1/2}$s are different between mass extraction and membrane potential, they do scale in proportion.

$\Delta V_{th}(sat)$ for La-loaded resin of ~300 mV stands tall within the ‘electrochemical window’ of water (1230 mV). The remarkably large membrane potential under minute concentrations of fluoride leads to extremely small LoDs, many orders-of-magnitudes below the potability limit, and below the LoD with LaF_3-based potentiometry [285]. This justifies that we here studied sensing against a background of deionised water rather than against typical drinking water, as for instance in [258][286]. While our local tap water typically contains fluoride well below potability (3 µM *vs.* 79 µM potability) [300], this still far exceeds $c_{1/2}$ of our sensors and would push them into saturation.

8.3.2 Fluoride response using La- loaded resin of different grain sizes

To explore the importance of resin grain surfaces to the build-up of membrane potential (i.e., if the adsorption occurs on the resin surfaces), we compared La-loaded chelating resin phase transfer membranes carrying the same weight of resin, but with different grain sizes. This was

done by grinding the original coarse powder finer with pestle and mortar before loading into the membrane. As inset to Figure 8-5 a, we show micrographs of resin grains before and after grinding, displaying a finer texture after grinding. The resulting membranes hence carried the same mass and volume of resin, but the finer ground powder led to a larger sorbent surface area. Figure 8-5 shows the response characteristics of a WGTFT that is otherwise nominally identical to the WGTFT used for Figure 8-2, but with finer ground resin in the phase transfer membrane. Note that a corresponding test was not possible for the ‘mordenite’ [258] and 'clinoptilolite' zeolites [286], as they were delivered as a very fine powder which we could not grind any finer with pestle and mortar.

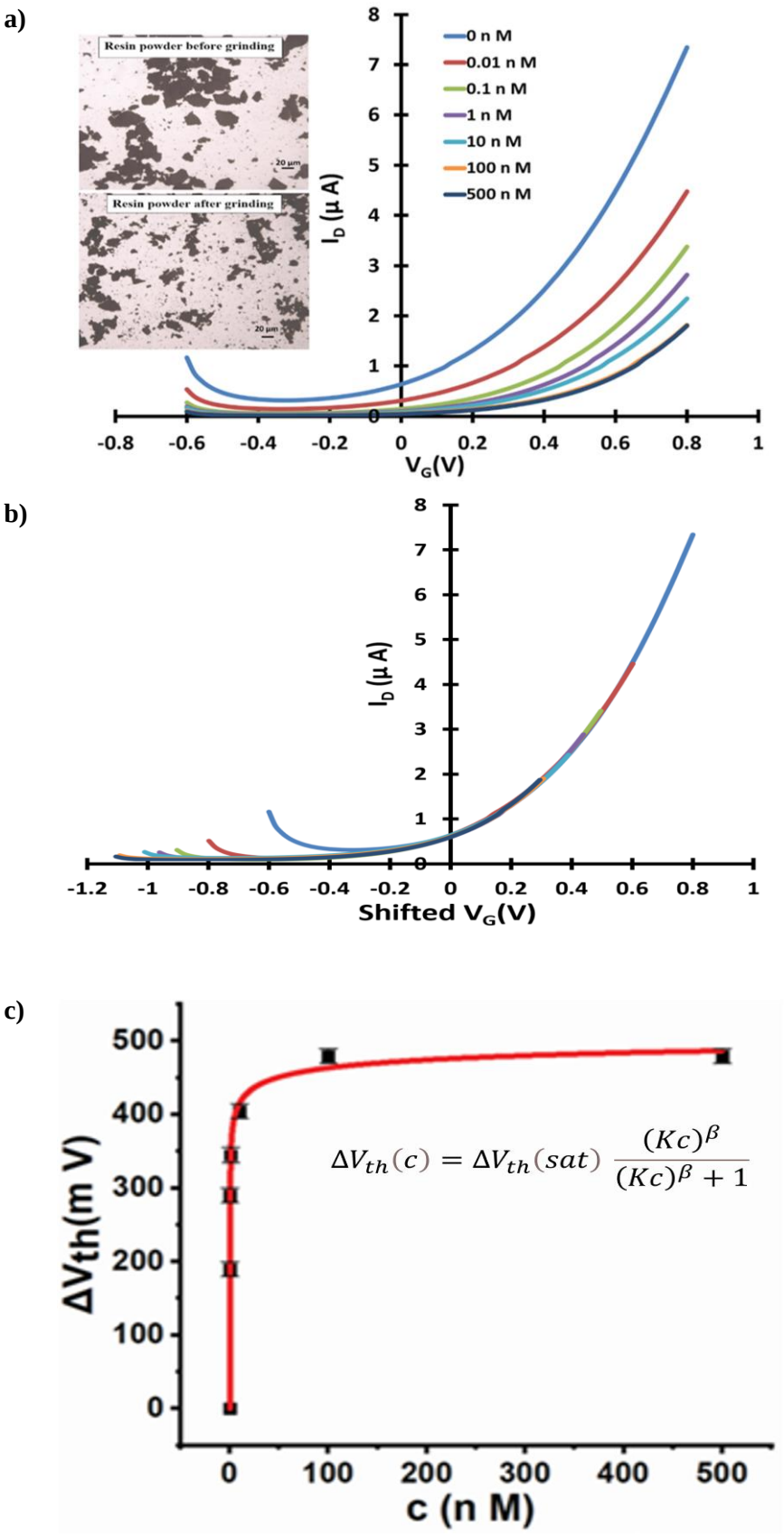

Figure 8-5: (a) *Transfer characteristics of finer-ground La-loaded chelating resin-sensitised SnO_2 WGTFT gated under increasing F^- concentrations in the outer pool. Inset to 8.5 a: Resin powder before / after grinding with pestle and mortar.* ***(b)*** *Master transfer characteristic.* ***(c)*** *Response characteristic with fit to equation 8-3.*

The parameters of the fit of response characteristics to equation 8-3 are included in Table 8-1 above in the 'La (fine)' row for direct comparison with 'La (coarse)' (*i.e.* parameters for the coarser powder). We found that within the margin-of-error, parameters K and β were not affected by grinding the powder finer. K describes the (average) strength of interaction between a single sorbent site and the sorbate, β, the inhomogeneity of such strengths in a disordered medium. Unsurprisingly, neither of these were affected by mechanical grinding that affects morphology on the size scale of μm. However, the saturated threshold shift, $\Delta V_{th}(sat)$, was significantly larger for the finer ground powder with larger sorbent surface area. This suggests that membrane potential in ion-exchange (rather than charge accumulating) sorbent membranes results from dipoles forming via sorption of sorbate on grain surfaces. Grinding ion-exchange media into finer powders allows the further increase of an already large $\Delta V_{th}(sat)$, which benefits LoD.

8.3.3 Recovery and interference from co- solutes

As $c_{1/2}$ for fluoride response established in 8.3.1 is more than 6 orders-of-magnitude smaller than the potability limit of 79 μM, practical sensing would require manifold (factor ~ 10^6) dilution of test samples with DI water to bring natural fluoride concentrations into the sensor's dynamic range (avoiding saturation). However, this is easily done. Note this would also dilute manifold any co-ions present in realistic samples, justifying our choice to use DI water as reference. More important practical considerations are the ability of a sensor to recover, and the resilience against interferants (other anions and cations) in water samples that may also lead to a threshold shift. To test for recovery, Figure 8-6 shows linear transfers for a WGTFT sensitised with La-loaded chelating resin under a test cycle of DI water (0 nM fluoride) ⇒ 500 nM fluoride ⇒ DI water (0 nM fluoride) again in the sample pool. It is evident from Figure 8-6 that a phase transfer membrane that was once exposed to a level of fluoride far larger than $c_{1/2}$ does not recover zero membrane potential when the sample pool is re-filled with DI water, but remains at or near saturated threshold shift. This is likely due to the strong analyte/sorbate binding, as quantified by large binding constant, K. Recovery may be possible by prolonged washing under dilute NaOH to reverse the fluoride/hydroxyl ligand exchange, but we have not attempted this. Since each membrane carries only a few milligrams of La-loaded resin, it is cheap enough to discard after single use.

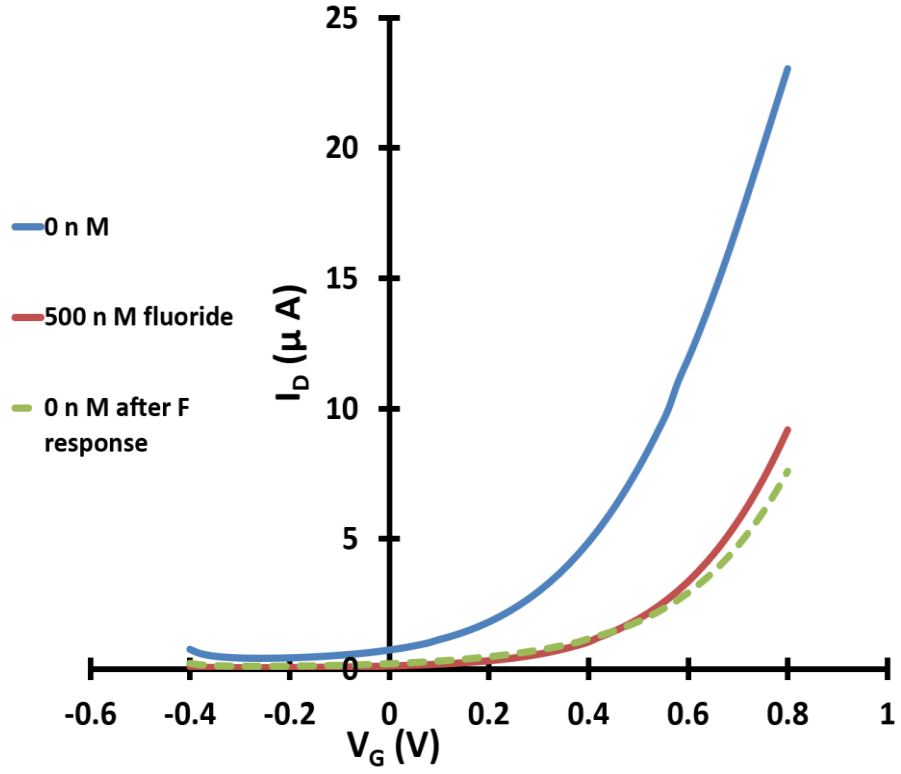

Figure 8-6: *Linear transfer characteristics for a WGTFT sensitised with La-loaded chelating resin under a test cycle of DI water (0 nM fluoride) ⇒ 500 nM fluoride ⇒ DI water (0 nM fluoride) again in the sample pool.*

To test for interference from other waterborne anions, we have measured the response of WGTFTs sensitised with La- and Al-loaded chelating resin to chloride (from NaCl), and for La-loaded phase transfer membrane to carbonate (from Na_2CO_3) in the same manner as done previously for fluoride. Chloride (Cl^-) is the most common monovalent anion in drinking water and is typically far more concentrated than fluoride: the potability limit for chloride is 7 mM [294], almost 2 orders-of-magnitude larger than for fluoride. Carbonate (CO_3^{2-}) is a common divalent anion, and the recommended range for drinking water is (0.3 … 4) mM [295], around one order-of-magnitude larger than for fluoride. Note that although we introduced this as a divalent carbonate anion from Na_2CO_3, at low concentration *(i.e., 'mild' pH)*, most 'carbonate' ions will in fact convert to the monovalent bicarbonate, HCO_3^-, rather than solvate as true carbonate [301]. Results are presented in Figure 8-7 below, clearly showing non-negligible membrane potential in response to chloride and carbonate.

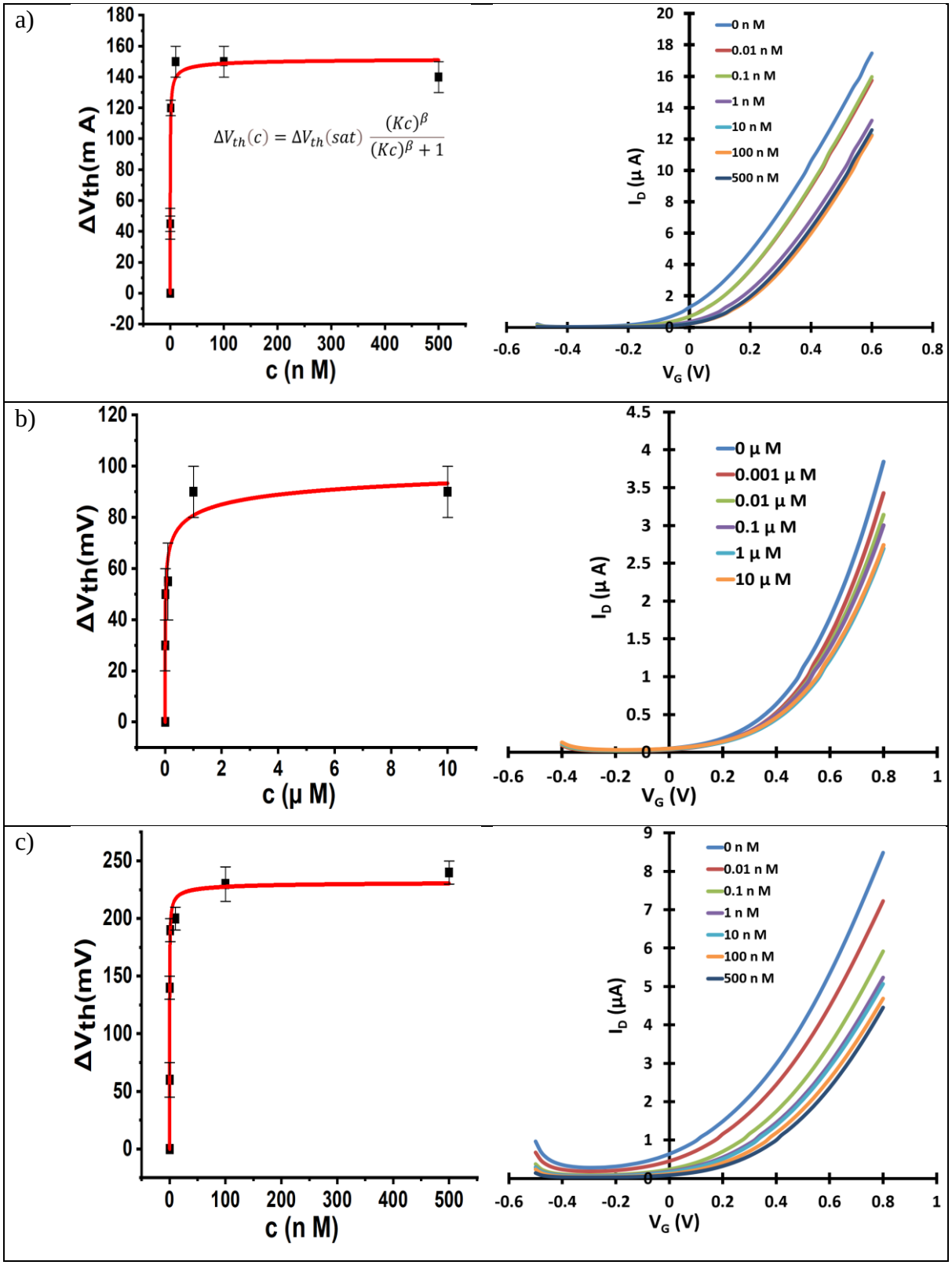

Figure 8-7: (a) *Response of La-loaded resin to chloride (right).* ***(b)*** *Response of Al resin to chloride (right).* ***(c)*** *Response of La resin to carbonate (right). Lefts: Response characteristics with fits to equation 8-3.*

Transfers in Figure 8-7 (right) were again shifted for best overlap into a master curve, and threshold shift characteristics with fits to equation 8-3 are shown in Figure 8-7 (left). We found that for chloride, the LF isotherm model equation 8-3 does not fit the data as well as previously in Figure 8-2. Therefore, some of the resulting 'LF' parameters carry large errors (particularly, K), and should be treated with caution. We still summarise them in Table 8-2, but prefer reading $c_{1/2}$ directly from response characteristics, without reliance on the LF (or any other) isotherm model.

Table 8-2: *K, $c_{1/2}$, $\Delta V_{th}(sat)$, β, and LoD for the response of WGTFTs sensitised with La- and Al-/ and La- loaded chelating resins to chloride/carbonate. *Due to the large error for K fitted by LF model, $c_{1/2}$ is read graphically, directly from response characteristics*

Metal loading	**Interferant**	**K [10^8 L/mol]**	**$c_{1/2}$ [pM / nM]**	**$\Delta V_{th}(sat)$ [mV]**	**β**	**LoD [pM / nM]**
La	Cl^- from NaCl	60 ± 40	720 pM*	152 ± 13	0.58 ± 0.2	0.5 nM
Al	Cl^- from NaCl	0.3 ± 0.7	28 nM*	112 ± 35	0.3 ± 0.1	1.1 nM
La	CO_3^{2-} from Na_2CO_3	167 ± 56	(60 ± 34) pM	233 ± 9	0.5 ± 0.09	55 pM

Again, response to chloride was stronger for La- *vs*. Al-loaded resin. For both Al- and La-loaded resins, $c_{1/2}$ is larger for chloride than for fluoride, but only by one order-of-magnitude. Since the typical concentration of chloride in common tap water is larger than fluoride, chloride could therefore still be a problematic interferant for the determination of fluoride. However, chloride ions are known not to act as inner-sphere ligands for La^{3+} aqueous complexes [302], suggesting a much smaller change in dipole moment for La-OH → La-Cl exchange than for La-OH → La-F exchange. This explains the larger ΔV_{th}(sat) when exchanging La-OH for fluoride than for chloride, *cf.* the discussion of the origin of threshold shift under ligand exchange in section 8.3.1. The larger ΔV_{th}(sat) for fluoride confers significant selectivity for

fluoride *vs.* chloride, despite the limited difference in $c_{1/2}$ / K: in a WGTFT sensitised with La-loaded resin, a threshold shift of more than ~150 mV (*i.e.*, more than $\Delta V_{th}(sat)$ for chloride) can only be explained by the presence of fluoride. Using equation 8-3 with the parameters from Table 8-1, to reach a threshold shift of 150 mV with fluoride, we required a fluoride concentration of ~ 80 pM. This gave a more practical LoD than the 13 pM we determined with La-loaded resin in interferant-free deionised water: beyond ~ 80 pM fluoride in water would give a threshold shift that cannot be due to chloride interferant. Still, this is 6 orders-of-magnitude below the fluoride potability limit of 79 µM. As a further interference test, we tested WGTFT response under the simultaneous presence of fluoride as analyte and chloride as interferant in the sample solution, which is more realistic than comparing response for analyte only *vs.* interferant only. Simultaneous testing allowed the checking of interactions between analyte and interferant from competition for binding sites. Figure 8-8 shows the response of WGTFTs with La-loaded chelating resin phase transfer membrane under samples containing both fluoride and chloride at equal concentration in the sample pool.

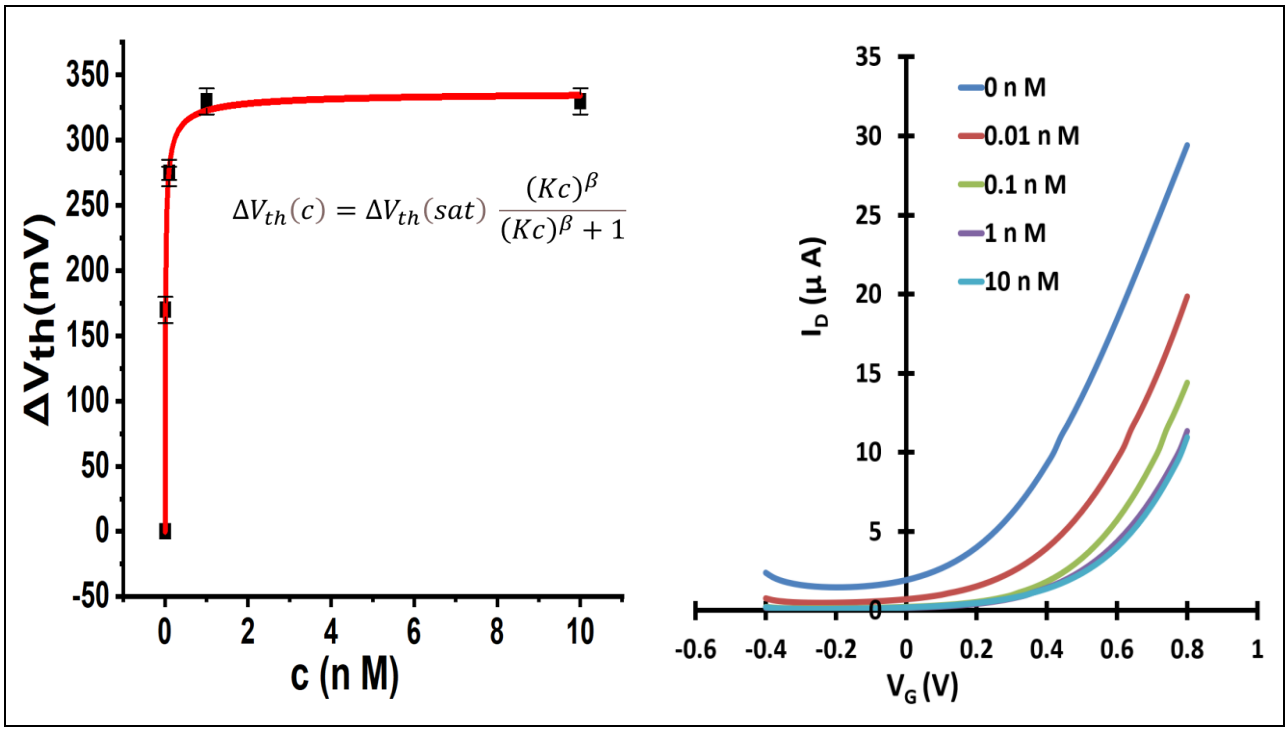

***Figure 8-8**: Response characteristics under simultaneous exposure to fluoride and chloride (right). The given concentrations apply to both fluoride and chloride: 1 nM means '1nM fluoride + 1nM chloride'. Left: response characteristics with fit to equation 8-3.*

The response to simultaneous exposure to analyte (fluoride) and interferant (chloride) was similar as for exposure to analyte alone (Figure 8-2), saturating at $\Delta V_{th}(sat) \sim 330$ mV. The presence of interferant therefore did not pull $\Delta V_{th}(sat)$ down from the level for fluoride alone, rather slightly increased it, but by far less than naive addition: $\Delta V_{th}(sat)$ (F^- and Cl^-) $\gtrsim \Delta V_{th}(sat)(F^-)$, but $\Delta V_{th}(sat)$ (F^- and Cl^-) $< \Delta V_{th}(sat)(F^-) + \Delta V_{th}(sat)(Cl^-)$. At least qualitatively, the presence of fluoride is therefore still evident despite the simultaneous presence of interferant.

Interference from carbonate was more serious though. $c_{1/2}$ is similar to that of fluoride, and $\Delta V_{th}(sat)$ exceeds 200 mV. $\Delta V_{th}(sat)$ from carbonate is only slightly smaller to $\Delta V_{th}(sat)$ for fluoride. Practically, to reduce the effect of carbonate interferent on F^--WGTFT sensor, carbonate removal prior to fluoride determination could be attempted (*e.g.* the 'Gyrazur'^{TM} process [303] is used for carbonate removal in commercial water treatment works). However, we advise a more direct way to minimise carbonate (and other) interference in section 8.3.4 below.

8.3.4 Reducing carbonate interference

We repeated fluoride (analyte) and carbonate (interferant) sensing experiments with a phase transfer membrane filled with an only 'lightly' La-loaded resin. The preparation of lightly La-loaded resin by partial La extraction from a conventionally (heavily) loaded resin was described in section 8.2.2. Figure 8-9a shows that a lightly La- loaded resin still strongly responds to fluoride. For response to carbonate (Figure 8-9b), we found a significantly reduced response for the lightly loaded resin than previously for the fully loaded resin (Figure 8-7c).

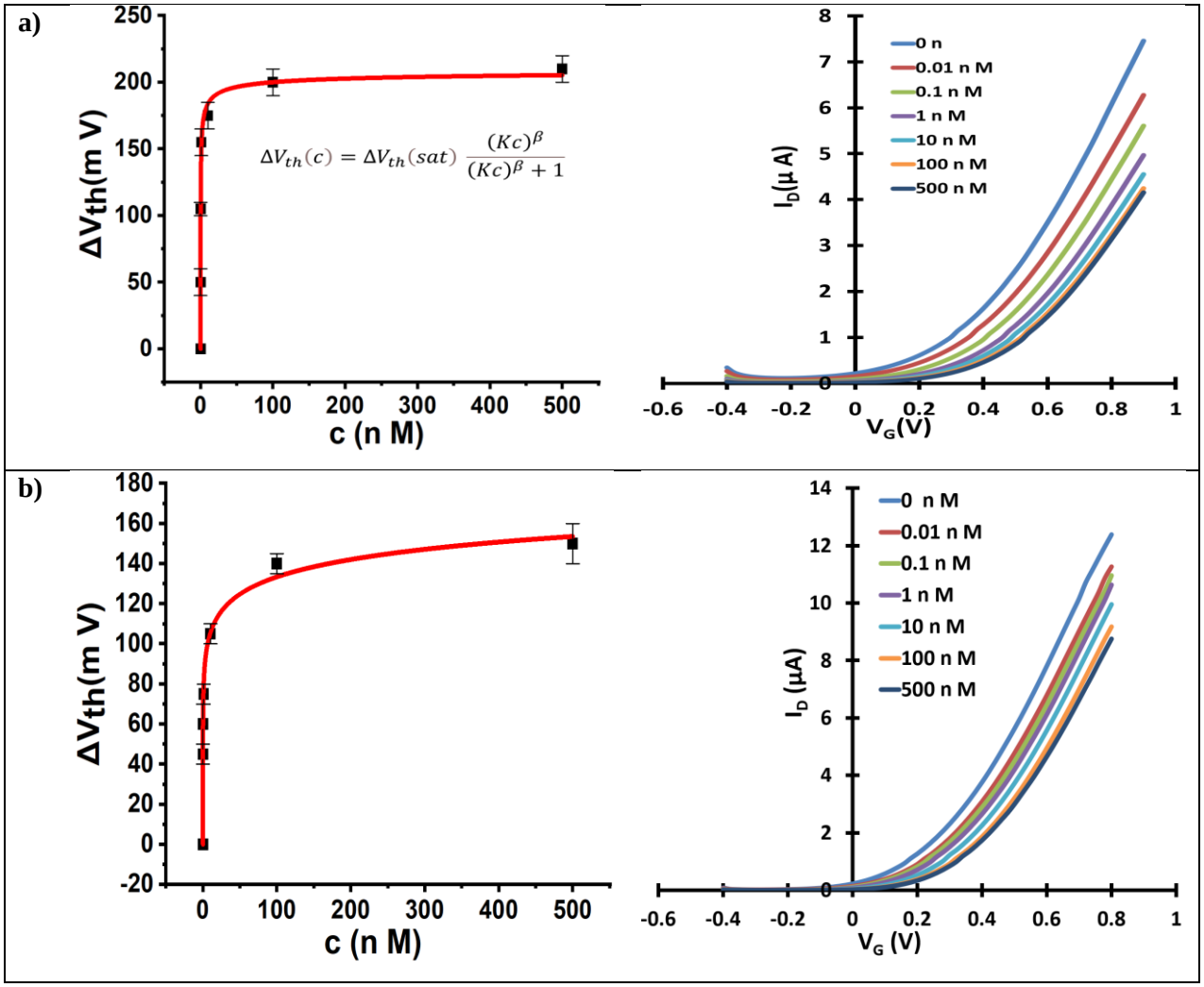

Figure 8-9: *Response of lightly La-loaded resin to* ***(a)*** *Fluoride and* ***(b)*** *Carbonate (right). Left: Response characteristics with fits to equation 8-3.*

Parameters of response characteristics for the lightly loaded resin are summarised in Table 8-3 and compared to parameters from fully loaded resin.

Table 8-3: *Parameters (K, $c_{1/2}$, $\Delta V_{th}(sat)$, β) for the response of WGTFTs sensitised with lightly La-loaded resin, extracted from Figure 8-9. For comparison, parameters for fully La-loaded resin are also shown (taken from Tables 8-1 and 8-2).*

	Fluoride		**Carbonate**	
Parameters↓	**Lightly load**	**Fully loaded**	**Lightly loaded**	**Fully loaded**
K [10^6 L/mol]	8500 ± 2100	19000 ± 8000	4.4 ± 20	16700 ± 5600
$c_{1/2}$	(118 ± 29) pM	(53 ± 22) pM	234 nM	(60 ± 34) pM
$\Delta V_{th}(sat)$ [mV]	211 ± 6	277 ± 14	288 ± 115	233 ± 9
β	0.43 ± 0.05	0.43 ± 0.09	0.2 ± 0.04	0.5 ± 0.09

We first note that $\Delta V_{th}(sat)$ are very similar for lightly and fully loaded resin, which at first sight is somewhat surprising. However, we established in section 8.3.1 that the characteristic concentration, $c_{1/2}$, for threshold shift is more than 6 orders-of-magnitude smaller than $c_{1/2}$ for fluoride extraction. Clearly, threshold shift saturates long before all available ion exchange sites have exchanged hydroxyl for fluoride. It appears that even the lightly loaded resin still has sufficient ion exchange sites to reach similar $\Delta V_{th}(sat)$ as the fully loaded resin.

There are remarkable and useful differences in K though between the lightly and the fully loaded resins' response to interferant carbonate: while K for the response to fluoride is not significantly reduced, K for carbonate response is at least 3 orders-of-magnitude smaller than for fully loaded resin. The stability constants of the equivalent La complexes favour ligand exchange for fluoride over carbonate: for the 1st La-F ligand binding, log K = 2.67 [304], but for the equivalent La-HCO_3 interaction, lower log K = 1.40 was established [305]. While this is true in both fully and lightly loaded resin, the preference for fluoride over carbonate is masked in the fully loaded resin: we note that all sensors with Langmuir or LF characteristics can only select between analyte and interferant at low analyte concentrations, c, because fractional coverage $\theta(c)$ scales with K at low c only. At high concentrations (c >> 1/K) the LF law saturates ($\theta(c) \rightarrow 1$) for both analyte and interferant; hence, selectivity is lost. A similar

saturation issue may occur under high concentration of sensitiser (ion exchange sites in the resin), rather than analyte / interferant: despite lower K, all interferant will still be ion-exchanged when the concentration of ion exchange sites is too high. The results presented in this section show that the procedure described in 8.2.1 had the intended effect: On the one hand, response to interferant is far weaker, which is evidence for the removal of most La centres. On the other hand, response to analyte is still strong, which is evidence for some residual La centres. Further evidence for the presence of some residual La centres even after the removal procedure described in section 8.2.2 comes from a control experiment shown in Figure 8-10. This shows no response to fluoride for a membrane filled with as- received Puromet^{TM} MTS9501 resin that was never loaded with La. The resin in the membrane used for Figure 8-10 therefore must have retained some La, otherwise it could not be responsive to fluoride. Overall, we find that diluting sensitiser opens a selectivity window that is closed at high sensitiser concentration.

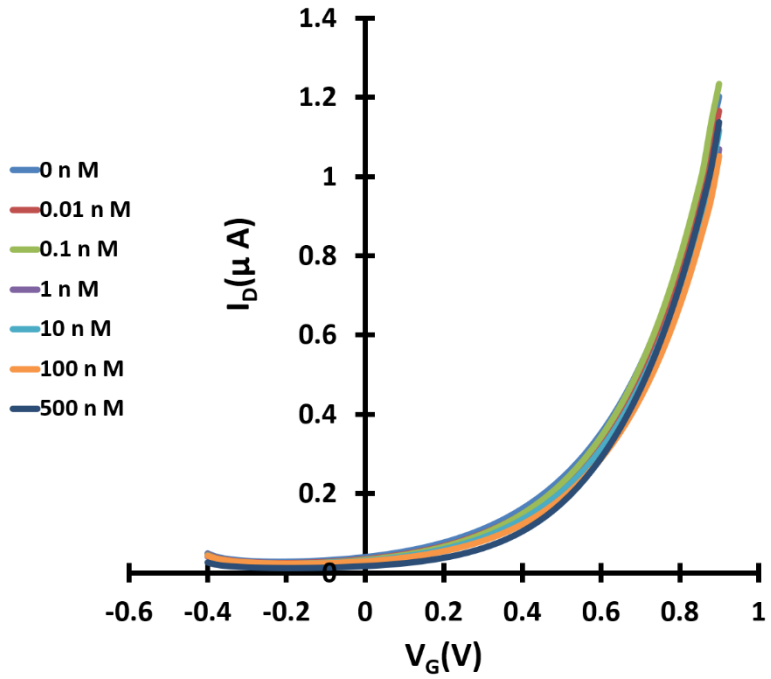

Figure 8-10: *Control experiment: WGTFT using a membrane loaded with as- received Puromet MTS9501 resin that was never activated with La. In the absence of La, no response to fluoride is observed.*

For a full assessment of interference, further tests (*e.g.*, sulfate, and nitrate) would have to be conducted to optimise the degree of La-loading for best overall selectivity. While this is beyond the scope of this work, we establish diluting activated centers in an ion exchange resin as a general approach for improved selectivity.

8.4 Conclusions

We have provided a second example of an ion-exchanging rather than charge-accumulating sorbent as sensitiser in the phase transfer membrane of a water-gated field effect transistor (WGTFT) for potentiometric ion sensing. The fluoride-selective sorbent used here was derived by metal loading (La or Al) of a commercial macroporous aminophosphate (AMP) resin, 'Puromet^{TM} MTS9501' to activate it for ion-exchange with fluoride. Despite being chemically different from the previously used ion-exchanging crystalline zeolite mineral 'mordenite' [258] and 'clinoptilolite' [286] and despite anion *vs.* cation sorption, we found very similar response characteristics for both ion-exchange media, which are distinctly different from the characteristics of charge-accumulating sensitisers (*e.g.* organic macrocycles, [52][34][35]): namely, that membrane potential, as revealed by WGTFT threshold shift, follows a Langmuir-Freundlich (LF) surface adsorption isotherm (equation 8-3) rather than a Nikolsky-Eisenman (modified Nernstian) law for charge accumulating ionophores. We also found that La-loaded resin is superior to Al-loaded resin. We assigned the membrane potential and consequential WGTFT threshold shift resulting from ion exchange to the different dipole moment of the exchanged (La-F) complex rather than original (La-OH) species, leading to a polarisation of the membrane. Moreover, grains ground to a finer powder led to larger saturated threshold shift at the same mass loading, suggesting a surface mechanism. The characteristic concentration, $c_{1/2}$, for threshold shift is 6 orders-of-magnitude smaller than for mass uptake. The reason for this discrepancy is not obvious, but it enabled us to achieve a limit-of-detection (LoD) that far undercuts practical requirements, which are sufficiently met by commercial solid state membrane sensors. The most important practical limitation of our sensor concept for fluoride sensing is interference from co-solutes, particularly from carbonate. We have shown a successful strategy to combat interference from carbonate by reducing the degree of La-loading of the ion exchange resin, which we believe can be generalised to other resin-based sensors with Langmuir or LF response characteristics.

Most importantly, with the example of fluoride, we established the general principle of extremely low limit-of-detection (LoD) potentiometric sensing using organic ion exchange resins as sensitisers. LoD for fluoride far undercuts practical requirements, which are sufficiently met by the established electrochemical fluoride sensors with Nikolsky-Eisenman (modified Nernstian) response. However, a number of similar ion exchange resins are available as sorbents for highly toxic or precious trace elements in water, where extremely low LoD is essential and cannot be achieved by electrochemical sensors with Nikolsky-Eisenman characteristics. Examples are sorbent resins for arsenic- and gold-containing anions [204][207], copper [206], mercury [205], and palladium [293] cations. Our work establishes a template for the way in which the entire organic resin sorbent family can be used as sensitisers in WGTFTs when ultra-low limit-of-detection is essential.

Chapter 9 : Overall Conclusion and Future Work

9.1 Overall conclusion

In this project, a close to ideal potentiometric sensor was developed to monitor drinking water against some toxic or harmful waterborne analytes. A SnO_2 WGTFT transducer with unique ion exchanger ionophores was implemented to produce highly effective sensors that detect cation (Cs^+, Pb^{2+} and Cu^{2+}) and anion (F^-) analytes. These sensors achieved the primary objective of this study, that is, to obtain capable sensors to detect radioactive or toxic elements (e.g. Cs^+, Sr^{2+}, Cd^{2+}, Pb^{2+}) at extremely low limit-of-detection (LoD), which match global guidelines to maintain the safety of drinking water. Another favourable feature of the sensors developed in this study was their excellent selectivity in several realistic sample situations.

The exploitation of ion-exchange sorbents as ionophore (sensitisers) clearly and demonstrably enhanced the performance of the WGTFT sensors in terms of the LoDs and selectivity for waterborne analytes. In this work, ion-exchange sorbents as sensitisers were embedded within phase transfer membranes (plasticised PVC membranes) which were placed across the gate medium of the WGTFTs in between a sample solution (in an outer pool) and a reference solution (in an inner pool). The interaction between the analyte in the sample solution and the ion-exchange sensitiser resulted in membrane potentials that were recorded as a shift in the WGTFT threshold voltage. This shift increased as the analyte concentrations in the sample solutions increased. This phenomenon occurred without any accumulation of charges in sorbents. We propose that the membrane potential may well have resulted from the change in the dipole moment magnitude on sorbents' surfaces during the exchange process, leading to membrane polarisation. The resulting response characteristics followed the Langmuir or Langmuir-Freundlich surface adsorption isotherm with steepest slope at low concentration ($c \leq c_{1/2}$) and saturation at a relatively high concentration ($c >> c_{1/2}$), enabling significantly low LoDs, which are, clearly, much to be desired in the detecting of radioactive or poisonous ions. By contrast, organic macrocyclic ionophores that have previously been used to sensitise the potentiometric ion sensors, including WGTFTs, can build the membrane potential based on the accumulation of charge in membranes. In this case, the response characteristics follow the Nikolsky- Eisenman (modified Nernstian) law with LoDs in the range of 100 nM - 1µM

[52][35][34]. That range of values of LoDs is insufficient to detect toxic or radioactive elements and the harmful threats they pose to humans and the environment.

In this work, the WGTFTs were sensitised with mordenite zeolite as a sensitiser in the phase transfer membrane to detect Cs^+ cations in tap water. The mordenite-WGTFT sensor successfully responded to Cs^+ analytes in a sample solution in a nanomolar dynamic range even in the presence of realistically interfering cations in high concentrations in tap water. The response of such a sensor followed the Langmuir isotherm with a superior stability constant that allowed an LoD (33 pM) that is remarkably lower than the potability limit (7.5 nM). This LoD has never been reached by Cs^+- potentiometric ion sensors that use organic ionophores and which exhibit response characteristics following the Nikolsky- Eisenman law [175][277].

Clinoptilolite zeolite, a useful sorbent for the extraction of the heavy metals Cu^{2+} and Pb^{2+}, was also employed in the WGTFT sensor as a sensitiser for the detection of these heavy metals, in a manner similar to that used in Cs^+- WGTFT sensors. The response characteristics of this sensor followed the Langmuir-Freundlich characteristic, allowing much lower LoDs to be achieved. The LoDs of Cu^{2+} (14 nM) and Pb^{2+} (0.9 nM) were considerably lower than the action levels (20.5 µM and 72 nM, respectively) enshrined in the lead-and-copper rule for the safety of drinking water established in 1991 by the Environmental Protection Agency [281]. The clinoptilolite-sensitised WGTFTs also exhibited high selectivity to Cu^{2+} and Pb^{2+} introduced in realistically sampling situations. These situations include high concentrations of interfering cations, such as Na^+, Ca^{2+} and Mg^{2+}, showing the potentially great practical usefulness of this sort of sensor in environments outside of the laboratory. These features clearly qualify clinoptilolite-sensitised WGTFTs to be directly applied to monitor instances governed by the lead-and-copper rule in the real world.

Puromet^{TM} MTS9501 resin is another ion-exchange sorbent adopted in this work to act as a sensitiser, in this case to detect fluoride anions (F^-). The Puromet^{TM} MTS9501 resin was activated to be selective to F^- by the loading of (La) metal and then embedded as a sensitiser in the phase transfer membrane of the WGTFT sensors in a similar manner to those used in Cs^+-/Pb^{2+} - or Cu^{2+} -WGTFT sensors. Although resin is chemically different from zeolite, the response of La-loaded resin-sensitised WGTFT to F^- in the sample solution also conformed to the Langmuir-Freundlich isotherm. Further of this, the grinding of resin grains to a smaller diameter/grade resulted in enhancing the saturated threshold shifts under the same condition of La mass loading. This result of the relative increase in surface area of the same sorbent directly

confirms the surface adsorption mechanism as crucial in ion-exchange sorbents. Interference from co-solutes, particularly from carbonate, is a significant challenge in fluoride- WGTFT sensors. Decreasing the degree of La-loading into the resin can be performed, successfully and routinely to effectively counteract this co-solutes interference. The extremely low LoD of the fluoride-WGTFT potentiometric sensor was far below the practical needs, which can be achieved using commercial electrochemical fluoride sensors. However, this investigation established the principle of the future incorporation of similar, available ion-exchange resins in WGTFT sensors for detecting highly toxic elements with extremely low LoDs, such as arsenic [204] and mercury [205] sorbates, unachievable by the electrochemical sensors following the Nikolsky- Eisenman characteristic.

In general, WGTFT sensors with ion-exchange sorbents following the Langmuir or Langmuir-Freundlich surface adsorption isotherm are a very promising category of sensor for the detection of toxic analytes in polluted water with highly desirable features, including high sensitivity, selectivity and stability; extremely low LoD; low-cost and designable for portability.

9.2 Proposed Future Work

Based on some investigations carried out in this work, a list of proposed future studies is suggested below:

1. Further investigations of the sensing mechanism of WGTFT sensors sensitised with ion-exchange sorbents are needed to interpret the variation values of $c_{1/2}$ characteristic between threshold shift and mass uptake. We found that $c_{1/2}$ is much lower for threshold shift than for mass uptake for unclear reason. Therefore, the threshold shift (ΔV_{th}) is saturated far below all available ion-exchange sites substitute their certain ions with analyte ions. However, the low $c_{1/2}$ enables to achieve a desirable of extremely low LoDs.
2. Strontium-90 (^{90}Sr) is a dangerously radioactive substance released into the environment as a consequence of nuclear accidents. The danger of ^{90}Sr is that it easily enters the body and behaving chemically very similarly to calcium. For instance ^{90}Sr substitutes for calcium in the bone in human and animal bodies [306]. For the removal

of ^{90}Sr from water, zeolite 4A shows good extraction and high selectivity for ^{90}Sr over calcium [307]. Therefore, zeolite 4A as an ionophore to sensitise WGTFT is likely to exhibit good performance for detecting ^{90}Sr with low LoD, as we have achieved in our Cs^{+}- WGTFT sensor.

3. As recommended in Chapter 8, several resin sorbents are available to remove precious or highly toxic elements, such as gold [207], arsenic [204] and mercury [205], where detecting them in significantly low LoDs is essential. This feature can be achieved using WGTFT sensors with such resin sorbents.
4. Other sorbents that can act as sensitisers in WGTFT sensors should be investigated. Clay minerals can act as an ion-exchange sorbents and are extensively used to remove heavy metals from wastewater, for instance, kaolin [308][309]. The Saudi clay mineral bentonite (prepared and activated with sulphuric acid) effectively extracted cobalt ions from water [310][311]. Therefore, the application of this clay mineral as a sensitiser in WGTFT sensors may well turn out to be useful in the detection of cobalt at favourably low LoDs.

References

[1] P. Senthil Kumar and P. R. Yaashikaa, “Introduction—Water,” in *Water in Textiles and Fashion*, Elsevier Ltd., 2019, pp. 1–20.

[2] K. A. Sharp, “Water : Structure and Properties,” *Encycl. LIFE Sci.*, 2001.

[3] J. S. Boyer and P. J. Kramer, “Functions and Properties of Water,” in *Water Relations of Plants and Soils*, San Diego: CA: Academic Press, 1995, pp. 16–41.

[4] “Water | Facts, Properties, Structure, Compounds & Summary.” https://alevelbiology.co.uk/notes/water/ (accessed Feb. 16, 2021).

[5] “Drinking Water Regulations and Contaminants | Safe Drinking Water Act (SDWA),” *US EPA*. https://www.epa.gov/sdwa/drinking-water-regulations-and-contaminants (accessed Feb. 23, 2021).

[6] J. Fawell and M. J. Nieuwenhuijsen, “Contaminants in drinking water,” *Br. Med. Bull.*, vol. 68, pp. 199–208, 2003, doi: 10.1093/bmb/ldg027.

[7] “Freshwater - Water, Ions, Sodium, and Chloride - JRank Articles.” https://science.jrank.org/pages/2857/Freshwater.html (accessed Mar. 02, 2021).

[8] S. Sharma and A. Bhattacharya, “Drinking water contamination and treatment techniques,” *Appl. Water Sci.*, vol. 7, no. 3, pp. 1043–1067, 2017, doi: 10.1007/s13201-016-0455-7.

[9] “Guidelines for Drinking-water Quality,” 2011. doi: 10.1007/978-1-4020-4410-6_184.

[10] “National Primary Drinking Water Regulation,” 2009. [Online]. Available: https://www.epa.gov/sites/production/files/2016-06/documents/npwdr_complete_table.pdf.

[11] S. Jagtap, M. K. Yenkie, N. Labhsetwar, and S. Rayalu, “Fluoride in drinking water and defluoridation of water,” *Chem. Rev.*, vol. 112, no. 4, pp. 2454–2466, 2012, doi: 10.1021/cr2002855.

[12] I. Adejumoke, A. Babatunde, O. Abimbola, A.-A. Tabitha, D. Adewumi, and O. Toyin, “Water Pollution: Effects, Prevention, and Climatic Impact,” in *Water Challenges of an Urbanizing World*, 2018.

[13] P. B. Tchounwou, C. G. Yedjou, A. K. Patlolla, and D. J. Sutton, “Heavy metal toxicity and the environment,” *Exp. Suppl.*, vol. 101, pp. 133–164, 2012, doi: 10.1007/978-3-7643-8340-4.

[14] B. Chouhan, P. Meena, and N. Poonar, “Effect of Heavy Metal Ions in Water on Human Health,” *Int. J. Sci. Eng. Res.*, vol. 4, no. 12, pp. 2015–2017, 2015, [Online]. Available: http://www.who.int/water_sanitation_health/factsfigures.

[15] V. Masindi and K. L. Muedi, “Environmental Contamination by Heavy Metals,” IntechOpen, 2018, pp. 115–133.

[16] “Soil and water pollution in Europe – A problem that concerns everyone – Metal-Aid,” *METAL-AID ESRS*, 2017. https://metalaidblog.wordpress.com/2017/02/27/pollution-europe/ (accessed Feb. 21, 2021).

[17] Y. Hu and H. Cheng, “Water pollution during China’s industrial transition,” *Environ. Dev.*, vol. 8, no. 1, pp. 57–73, 2013, doi: 10.1016/j.envdev.2013.06.001.

[18] R. Verma and P. Dwivedi, “Heavy metal water pollution- A case study,” *Recent Res. Sci. Technol.*, vol. 5, no. 5, pp. 98–99, 2013, [Online]. Available: http://recent-science.com/.

[19] M. A. Arefin and A. Mallik, “Sources and causes of water pollution in Bangladesh: A technical overview,” *Bibechana*, vol. 15, pp. 97–112, 2018, doi: 10.3126/bibechana.v15i0.18688.

[20] S. Nalatambi, “Determination of Metals in Tap Water Using Atomic Absorption Spectrometry : a Case Study in Bandar Sunway Residential Area,” *Sunw. Acad. J. 6*, pp. 33–46, 2006.

[21] L. M. Del Razo, M. A. Arellano, and M. E. Cebrián, “The oxidation states of arsenic in well-water from a chronic arsenicism area of Northern Mexico,” *Environ. Pollut.*, vol. 64, no. 2, pp. 143–153, 1990, doi: 10.1016/0269-7491(90)90111-O.

[22] J. Thomas, “A Short Note on Radioactive Pollution,” *J. Pollut. Eff. Control Short*, vol. 8, no. 4, p. 239, 2020, doi: 10.35248/2375-4397.20.8.250.Copyright.

[23] A. Thakur, M. Jadhav, N. Chavan, and A. Ranveer, “Radioactive Waste Management,” *Int. J. Innov. Eng. Res. Technol.*, vol. 2, no. 5, pp. 101–108, 2015, doi: 10.1016/B978-0-12-381475-3.10007-5.

[24] H. Tazoe *et al.*, “Radioactive pollution from Fukushima Daiichi nuclear power plant in the terrestrial environment,” *Radiat. Prot. Dosimetry*, vol. 152, no. 1–3, pp. 198–203, 2012, doi: 10.1093/rpd/ncs222.

[25] K. Osawa *et al.*, “Quantification of dissolved and particulate radiocesium fluxes in two rivers draining the main radioactive pollution plume in Fukushima, Japan (2013–2016),” *Anthropocene*, vol. 22, pp. 40–50, 2018, doi: 10.1016/j.ancene.2018.04.003.

[26] G. Hazra, “Radioactive Pollution : An Overview,” *Holist. Approach to Environ.*, vol. 8, no. 2, pp. 48–65, 2018.

[27] W. L. Robison, C. L. Conrado, K. T. Bogen, and A. C. Stoker, “The effective and environmental half-life of 137Cs at Coral Islands at the former US nuclear test site,” *J. Environ. Radioact.*, vol. 69, no. 3, pp. 207–223, 2003, doi: 10.1016/S0265-931X(03)00080-8.

[28] U. S. Environmental Protection Agency, “EPA facts about strontium-90,” p. 2, 2002.

[29] “CDC | Facts About Benzene,” *Centers for Disease Control and Prevention*. https://emergency.cdc.gov/agent/benzene/basics/facts.asp (accessed Feb. 23, 2021).

[30] “Benzene and drinking water,” 2015.

[31] T. Q. Trung and N. E. Lee, “Flexible and Stretchable Physical Sensor Integrated Platforms for Wearable Human-Activity Monitoringand Personal Healthcare,” *Adv. Mater.*, vol. 28, no. 22, pp. 4338–4372, 2016, doi: 10.1002/adma.201504244.

[32] L. Chen, X. Zeng, H. Ju, X. He, and Z. Zhang, “Calixarene derivatives as the sensory molecules for silver ion-selective electrode,” *Microchem. J.*, vol. 65, no. 2, pp. 129–135, 2000, doi: 10.1016/S0026-265X(00)00038-2.

[33] A. Jasiński, M. Guziński, G. Lisak, J. Bobacka, and M. Bocheńska, “Solid-contact lead(II) ion-selective electrodes for potentiometric determination of lead(II) in presence of high concentrations of Na(I), Cu(II), Cd(II), Zn(II), Ca(II) and Mg(II),” *Sensors Actuators, B Chem.*, vol. 218, pp. 25–30, 2015, doi: 10.1016/j.snb.2015.04.089.

[34] K. Melzer, A. M. Münzer, E. Jaworska, K. Maksymiuk, A. Michalska, and G. Scarpa, “Selective ion-sensing with membrane-functionalized electrolyte-gated carbon nanotube field-effect transistors,” *Analyst*, vol. 139, no. 19, pp. 4947–4954, 2014, doi: 10.1039/c4an00714j.

[35] A. F. Al Baroot and M. Grell, “Comparing electron- and hole transporting semiconductors in ion sensitive water- gated transistors,” *Mater. Sci. Semicond. Process.*, vol. 89, pp. 216–222, 2019, doi: 10.1016/j.mssp.2018.09.018.

[36] S. Wustoni, C. Combe, D. Ohayon, M. H. Akhtar, I. McCulloch, and S. Inal, “Membrane-Free Detection of Metal Cations with an Organic Electrochemical Transistor,” *Adv. Funct. Mater.*, vol. 29, no. 44, pp. 1–10, 2019, doi: 10.1002/adfm.201904403.

[37] A. H. Alshammari, Z. Alqahtani, F. B. Mohd Suah, S. A. Nizar, A. Dunbar, and M. Grell, “Low cost, high sensitivity detection of waterborne Al3+ cations and F− anions via the fluorescence response of a morin derivative dye,” *Anal. Chim. Acta*, vol. 1105, pp. 1–10, 2020, doi: 10.1016/j.aca.2020.01.070.

[38] S. Bayindir, “A simple rhodanine-based fluorescent sensor for mercury and copper: The recognition of Hg2+ in aqueous solution, and Hg2+/Cu2+ in organic solvent,” *J. Photochem. Photobiol. A Chem.*, vol. 372, pp. 235–244, 2019, doi: 10.1016/j.jphotochem.2018.12.021.

[39] X. Zhang, Y. Wang, H. Yuan, X. Guo, B. Dai, and X. Jia, “An acid-fluorescence and alkali-colorimetric dual channels sensor for Hg2+ selective detection by different coordination manners in aqueous media,” *J. Photochem. Photobiol. A Chem.*, vol. 373, pp. 12–19, 2019, doi: 10.1016/j.jphotochem.2018.12.009.

[40] X. Yan, H. Li, and X. Su, “Review of optical sensors for pesticides,” *Trends Anal. Chem.*, vol. 103, pp. 1–20, 2018, doi: 10.1016/j.trac.2018.03.004.

[41] A. Dey, “Semiconductor metal oxide gas sensors: A review,” *Mater. Sci. Eng. B*, vol. 229, pp. 206–217, 2018, doi: 10.1016/j.mseb.2017.12.036.

[42] L. Torsi, M. Magliulo, K. Manoli, and G. Palazzo, “Organic field-effect transistor sensors: A tutorial review,” *Chem. Soc. Rev.*, vol. 42, no. 22, pp. 8612–8628, 2013, doi: 10.1039/c3cs60127g.

[43] E. Bakker and E. Pretsch, “Potentiometric sensors for trace-level analysis,” *TrAC - Trends Anal. Chem.*, vol. 24, no. 3, pp. 199–207, 2005, doi: 10.1016/j.trac.2005.01.003.

[44] C. H. Chiu, Y. H. Sung, and S. Da Huang, “Simultaneous determination of manganese, iron and cobalt in copper with a multi-element graphite furnace atomic absorption spectrometer,” *Spectrochim. Acta - Part B At. Spectrosc.*, vol. 58, no. 3, pp. 575–580, 2003, doi: 10.1016/S0584-8547(02)00271-9.

[45] J. Wang, E. Harald Hansen, and B. Gammelgaard, “Flow injection on-line dilution for

multi-element determination in human urine with detection by inductively coupled plasma mass spectrometry," *Talanta*, vol. 55, no. 1, pp. 117–126, 2001, doi: 10.1016/S0039-9140(01)00397-6.

[46] E. A. Takara, S. D. Pasini-Cabello, S. Cerutti, J. A. Gásquez, and L. D. Martinez, "On-line preconcentration/determination of copper in parenteral solutions using activated carbon by inductively coupled plasma optical emission spectrometry," *J. Pharm. Biomed. Anal.*, vol. 39, no. 3–4, pp. 735–739, 2005, doi: 10.1016/j.jpba.2005.04.010.

[47] N. Spivey, "Analysis of Major Elements in Drinking Water Using FAST Flame Sample Automation for Increased Sample Throughput," 2015.

[48] D. Bradshaw and K. Neubauer, "Analysis of Minerals in Drinking Water with the PinAAcle 500 Atomic Absorption Spectrometer," 2015.

[49] Ö. Isildak and O. Özbek, "Application of Potentiometric Sensors in Real Samples," *Crit. Rev. Anal. Chem.*, vol. 8347, 2020, doi: 10.1080/10408347.2019.1711013.

[50] S. C. Wilschefski and M. R. Baxter, "Inductively Coupled Plasma Mass Spectrometry: Introduction to Analytical Aspects," *Clin. Biochem. Rev.*, vol. 40, no. 3, pp. 115–133, 2019, doi: 10.33176/AACB-19-00024.

[51] L. Kergoat *et al.*, "A water-gate organic field-effect transistor," *Adv. Mater.*, vol. 22, no. 23, pp. 2565–2569, 2010, doi: 10.1002/adma.200904163.

[52] K. Schmoltner, J. Kofler, A. Klug, and E. J. W. List-Kratochvil, "Electrolyte-gated organic field-effect transistor for selective reversible ion detection," *Adv. Mater.*, vol. 25, no. 47, pp. 6895–6899, 2013, doi: 10.1002/adma.201303281.

[53] S. Casalini, F. Leonardi, T. Cramer, and F. Biscarini, "Organic field-effect transistor for label-free dopamine sensing," *Org. Electron.*, vol. 14, no. 1, pp. 156–163, 2013, doi: 10.1016/j.orgel.2012.10.027.

[54] G. Seo *et al.*, "Rapid Detection of COVID-19 Causative Virus (SARS-CoV-2) in Human Nasopharyngeal Swab Specimens Using Field-Effect Transistor-Based Biosensor," *ACS Nano*, vol. 14, no. 4, pp. 5135–5142, 2020, doi: 10.1021/acsnano.0c02823.

[55] A. Nilchi, B. Maalek, A. Khanchi, M. Ghanadi Maragheh, A. Bagheri, and K. Savoji, "Ion exchangers in radioactive waste management: Natural Iranian zeolites," *Appl. Radiat. Isot.*, vol. 64, no. 1, pp. 138–143, 2006, doi: 10.1016/j.apradiso.2005.06.013.

[56] K. Margeta, N. Z. Logar, M. Šiljeg, and A. Farkaš, "Natural zeolites in water treatment–how effective is their use," in *Water treatment*, 2013, pp. 81–112.

[57] K. Y. Lee *et al.*, "Equilibrium, kinetic and thermodynamic study of cesium adsorption onto nanocrystalline mordenite from high-salt solution," *Chemosphere*, vol. 150, pp. 765–771, 2016, doi: 10.1016/j.chemosphere.2015.11.072.

[58] B. R. Figueiredo, S. P. Cardoso, I. Portugal, J. Rocha, and C. M. Silva, "Inorganic Ion Exchangers for Cesium Removal from Radioactive Wastewater," *Sep. Purif. Rev.*, vol. 47, no. 4, pp. 306–336, 2018, doi: 10.1080/15422119.2017.1392974.

[59] E. Erdem, N. Karapinar, and R. Donat, "The removal of heavy metal cations by natural zeolites," *J. Colloid Interface Sci.*, vol. 280, pp. 309–314, 2004, doi: 10.1016/j.jcis.2004.08.028.

[60] J. Peric´, M. Trgo, and N. Vukojevi, “Removal of zinc , copper and lead by natural zeolite — a comparison of adsorption isotherms,” *Water Res.*, vol. 38, pp. 1893–1899, 2004, doi: 10.1016/j.watres.2003.12.035.

[61] T. Robshaw, S. Tukra, D. B. Hammond, G. J. Leggett, and M. D. Ogden, “Highly efficient fluoride extraction from simulant leachate of spent potlining via La-loaded chelating resin. An equilibrium study,” *J. Hazard. Mater.*, vol. 361, pp. 200–209, 2019, doi: 10.1016/j.jhazmat.2018.07.036.

[62] A. Tixier-Mita *et al.*, “Review on thin-film transistor technology, its applications, and possible new applications to biological cells,” *Jpn. J. Appl. Phys.*, vol. 55, no. 4, pp. 0–9, 2016, doi: 10.7567/JJAP.55.04EA08.

[63] U. Zschieschang and H. Klauk, “Organic transistors on paper: A brief review,” *J. Mater. Chem. C*, vol. 7, no. 19, pp. 5522–5533, 2019, doi: 10.1039/c9tc00793h.

[64] P. K. Weimer, “The TFT A New Thin-Film Transistor,” *Proc. IRE*, pp. 1462–1469, 1962.

[65] H. Du, X. Lin, Z. Xu, and D. Chu, “Electric double-layer transistors: a review of recent progress,” *J. Mater. Sci.*, vol. 50, no. 17, pp. 5641–5673, 2015, doi: 10.1007/s10853-015-9121-y.

[66] M. Kaisti, “Detection principles of biological and chemical FET sensors,” *Biosens. Bioelectron.*, vol. 98, pp. 437–448, 2017, doi: 10.1016/j.bios.2017.07.010.

[67] L. Petti *et al.*, “Metal oxide semiconductor thin-film transistors for flexible electronics,” *Appl. Phys. Rev.*, vol. 3, no. 2, 2016, doi: 10.1063/1.4953034.

[68] J. S. Park, W. J. Maeng, H. S. Kim, and J. S. Park, “Review of recent developments in amorphous oxide semiconductor thin-film transistor devices,” *Thin Solid Films*, vol. 520, no. 6, pp. 1679–1693, 2012, doi: 10.1016/j.tsf.2011.07.018.

[69] C. Tanase, E. J. Meijer, P. W. M. Blom, and D. M. De Leeuw, “Local charge carrier mobility in disordered organic field-effect transistors,” *Org. Electron.*, vol. 4, no. 1, pp. 33–37, 2003, doi: 10.1016/S1566-1199(03)00006-5.

[70] C. Tanase, E. J. Meijer, P. W. M. Blom, and D. M. de Leeuw, “Unification of the hole transport in polymeric field-effect transistors and light-emitting diodes,” *Phys. Rev. Lett.*, vol. 91, no. 21, pp. 1–4, 2003, doi: 10.1103/PhysRevLett.91.216601.

[71] A. Tixier-Mita *et al.*, “Review on thin-film transistor technology, its applications, and possible new applications to biological cells,” *Jpn. J. Appl. Phys.*, vol. 55, no. 4, 2016, doi: 10.7567/JJAP.55.04EA08.

[72] S. R. Thomas, P. Pattanasattayavong, and T. D. Anthopoulos, “Solution-processable metal oxide semiconductors for thin-film transistor applications,” *Chem. Soc. Rev.*, vol. 42, no. 16, pp. 6910–6923, 2013, doi: 10.1039/c3cs35402d.

[73] H. Dong, *Microcrystalline silicon based thin film transistors fabricated on flexible substrate*. HAL, 2015.

[74] S. A. Algarni, T. M. Althagafi, A. Al Naim, and M. Grell, “A water-gated organic thin film transistor as a sensor for water-borne amines,” *Talanta*, vol. 153, pp. 107–110, 2016, doi: 10.1016/j.talanta.2016.01.068.

[75] B. G. Horowitz, “Organic Field-Effect Transistors,” *Adv. Mater.*, vol. 10, no. 5, pp. 365–377, 1998.

[76] C. Wang, H. Dong, W. Hu, Y. Liu, and D. Zhu, “Semiconducting π-conjugated systems in field-effect transistors: A material odyssey of organic electronics,” *Chem. Rev.*, vol. 112, no. 4, pp. 2208–2267, 2012, doi: 10.1021/cr100380z.

[77] M. Halik *et al.*, “Low-voltage organic transistors with an amorphous molecular gate dielectric,” *Nature*, vol. 431, no. 7011, pp. 963–966, 2004, doi: 10.1038/nature02987.

[78] A. Sharma, C. Madhu, and J. Singh, “Performance Evaluation of Thin Film Transistors: History, Technology Development and Comparison: A Review,” *Int. J. Comput. Appl.*, vol. 89, no. 15, pp. 36–40, 2014, doi: 10.5120/15710-4603.

[79] J. Y. Kwon, D. J. Lee, and K. B. Kim, “Review paper: Transparent amorphous oxide semiconductor thin film transistor,” *Electron. Mater. Lett.*, vol. 7, no. 1, pp. 1–11, 2011, doi: 10.1007/s13391-011-0301-x.

[80] E. Fortunato, P. Barquinha, and R. Martins, “Oxide semiconductor thin-film transistors: A review of recent advances,” *Adv. Mater.*, vol. 24, no. 22, pp. 2945–2986, 2012, doi: 10.1002/adma.201103228.

[81] C. W. Shih, A. Chin, C. F. Lu, and W. F. Su, “Remarkably High Hole Mobility Metal-Oxide Thin-Film Transistors,” *Sci. Rep.*, vol. 8, no. 1, pp. 1–6, 2018, doi: 10.1038/s41598-017-17066-x.

[82] K. Nomura, H. Ohta, A. Takagi, T. Kamiya, M. Hirano, and H. Hosono, “Room-temperature fabrication of transparent flexible thin-film transistors using amorphous oxide semiconductors,” *Nature*, vol. 432, no. 7016, pp. 488–492, 2004, doi: 10.1038/nature03090.

[83] T. M. Althagafi, A. F. Al Baroot, and M. Grell, “A New Precursor Route to Semiconducting Zinc Oxide,” *IEEE Electron Device Lett.*, vol. 37, no. 10, pp. 1299–1302, 2016, doi: 10.1109/LED.2016.2603520.

[84] W. Xu *et al.*, “Fully solution-processed metal oxide thin-film transistors via a low-temperature aqueous route,” *Ceram. Int.*, vol. 43, no. 8, pp. 6130–6137, 2017, doi: 10.1016/j.ceramint.2017.02.007.

[85] I. Isakov *et al.*, “Exploring the Leidenfrost Effect for the Deposition of High-Quality In2O3 Layers via Spray Pyrolysis at Low Temperatures and Their Application in High Electron Mobility Transistors,” *Adv. Funct. Mater.*, vol. 27, no. 22, pp. 1–9, 2017, doi: 10.1002/adfm.201606407.

[86] T. M. Althagafi, S. A. Algarni, A. Al Naim, J. Mazher, and M. Grell, “Precursor-route ZnO films from a mixed casting solvent for high performance aqueous electrolyte-gated transistors,” *Phys. Chem. Chem. Phys.*, vol. 17, no. 46, pp. 31247–31252, 2015, doi: 10.1039/c5cp03326h.

[87] R. P. Ortiz, A. Facchetti, and T. J. Marks, “High-k organic, inorganic, and hybrid dielectrics for low-voltage organic field-effect transistors,” *Chem. Rev.*, vol. 110, no. 1, pp. 205–239, 2010, doi: 10.1021/cr9001275.

[88] J. H. Oh, S. Liu, Z. Bao, R. Schmidt, and F. Würthner, “Air-stable n-channel organic thin-film transistors with high field-effect mobility based on N, N’-bis(heptafluorobutyl)-3,4:9,10- perylene diimide,” *Appl. Phys. Lett.*, vol. 91, no. 21, p.

212107, 2007, doi: 10.1063/1.2803073.

[89] C. Falcony, M. A. Aguilar-Frutis, and M. García-Hipólito, “Spray pyrolysis technique; High-K dielectric films and luminescent materials: A review,” *Micromachines*, vol. 9, no. 8, pp. 1–33, 2018, doi: 10.3390/mi9080414.

[90] S. H. Kim *et al.*, “Electrolyte-gated transistors for organic and printed electronics,” *Adv. Mater.*, vol. 25, no. 13, pp. 1822–1846, 2013, doi: 10.1002/adma.201202790.

[91] K. Ueno, H. Shimotani, H. Yuan, J. Ye, M. Kawasaki, and Y. Iwasa, “Field-induced superconductivity in electric double layer transistors,” *J. Phys. Soc. Japan*, vol. 83, no. 3, pp. 1–16, 2014, doi: 10.7566/JPSJ.83.032001.

[92] S. Fabiano, S. Braun, M. Fahlman, X. Crispin, and M. Berggren, “Effect of gate electrode work-function on source charge injection in electrolyte-gated organic field-effect transistors,” *Adv. Funct. Mater.*, vol. 24, no. 5, pp. 695–700, 2014, doi: 10.1002/adfm.201302070.

[93] Y. Huang, X. Liu, S. Li, and T. Yan, “Development of mean-field electrical double layer theory,” *Chinese Phys. B*, vol. 25, no. 1, 2015, doi: 10.1088/1674-1056/25/1/016801.

[94] E. Gongadze, S. Petersen, U. Beck, and U. van Rienen, “Classical Models of the Interface between an Electrode and Electrolyte,” in *Comsol Conference*, 2009.

[95] Y. Fujii, Y. Muramoto, and N. Shimizu, “Analysis of electric double layer in aqueous solutions of sodium chloride,” in *Annual Report - Conference on Electrical Insulation and Dielectric Phenomena, CEIDP*, 2010, pp. 22–25, doi: 10.1109/CEIDP.2010.5724027.

[96] S. Park *et al.*, “Sub-0.5 v Highly Stable Aqueous Salt Gated Metal Oxide Electronics,” *Sci. Rep.*, vol. 5, pp. 1–9, 2015, doi: 10.1038/srep13088.

[97] M. Singh *et al.*, “The double layer capacitance of ionic liquids for electrolyte gating of ZnO thin film transistors and effect of gate electrodes,” *J. Mater. Chem. C*, vol. 5, no. 14, pp. 3509–3518, 2017, doi: 10.1039/c7tc00800g.

[98] S. A. Algarni, T. M. Althagafi, P. J. Smith, and M. Grell, “An ionic liquid-gated polymer thin film transistor with exceptionally low ‘on’ resistance,” *Appl. Phys. Lett.*, vol. 104, no. 18, 2014, doi: 10.1063/1.4875746.

[99] J. Lee, M. J. Panzer, Y. He, T. P. Lodge, and C. D. Frisbie, “Ion gel gated polymer thin-film transistors,” *J. Am. Chem. Soc.*, vol. 129, no. 15, pp. 4532–4533, 2007, doi: 10.1021/ja070875e.

[100] A. V. Bandura and S. N. Lvov, “The ionization constant of water over wide ranges of temperature and density,” *J. Phys. Chem. Ref. Data*, vol. 35, no. 1, pp. 15–30, 2006, doi: 10.1063/1.1928231.

[101] A. Stirling and I. Pápai, “H2CO3 forms via HCO3- in water,” *J. Phys. Chem. B*, vol. 114, no. 50, pp. 16854–16859, 2010, doi: 10.1021/jp1099909.

[102] “Water conductivity - Lenntech.” https://www.lenntech.com/applications/ultrapure/conductivity/water-conductivity.htm (accessed Dec. 07, 2020).

[103] YorkshireWater, “Your water quality.” Accessed: Dec. 07, 2020. [Online]. Available: www.dwi.gov.uk.

[104] F. Buth, A. Donner, M. Sachsenhauser, M. Stutzmann, and J. A. Garrido, “Biofunctional electrolyte-gated organic field-effect transistors,” *Adv. Mater.*, vol. 24, no. 33, pp. 4511–4517, 2012, doi: 10.1002/adma.201201841.

[105] S. Ono, S. Seki, R. Hirahara, Y. Tominari, and J. Takeya, “High-mobility, low-power, and fast-switching organic field-effect transistors with ionic liquids,” *Appl. Phys. Lett.*, vol. 92, no. 10, pp. 90–93, 2008, doi: 10.1063/1.2898203.

[106] F. Endres and S. Zein El Abedin, “Air and water stable ionic liquids in physical chemistry,” *Phys. Chem. Chem. Phys.*, vol. 8, no. 18, pp. 2101–2116, 2006, doi: 10.1039/b600519p.

[107] P. Ma *et al.*, “Surface Functionalization of TiO2 Nanoparticles Influences the Conductivity of Ionic Liquid-Based Composite Electrolytes,” *ACS Appl. Nano Mater.*, vol. 3, no. 1, pp. 342–350, 2020, doi: 10.1021/acsanm.9b01980.

[108] S. W. Lee *et al.*, “Periodic array of polyelectrolyte-gated organic transistors from electrospun poly(3-hexylthiophene) nanofibers,” *Nano Lett.*, vol. 10, no. 1, pp. 347–351, 2010, doi: 10.1021/nl903722z.

[109] M. J. Panzer, C. R. Newman, and C. D. Frisbie, “Low-voltage operation of a pentacene field-effect transistor with a polymer electrolyte gate dielectric,” *Appl. Phys. Lett.*, vol. 86, no. 10, pp. 1–3, 2005, doi: 10.1063/1.1880434.

[110] L. Kergoat, B. Piro, M. Berggren, G. Horowitz, and M. C. Pham, “Advances in organic transistor-based biosensors: From organic electrochemical transistors to electrolyte-gated organic field-effect transistors,” *Anal. Bioanal. Chem.*, vol. 402, no. 5, pp. 1813–1826, 2012, doi: 10.1007/s00216-011-5363-y.

[111] A. Al Baroot, A. Alshammari, and M. Grell, “Electrochemical gating of a hydrophobic organic semiconductor with aqueous media,” *Thin Solid Films*, vol. 669, no. July 2018, pp. 665–669, 2019, doi: 10.1016/j.tsf.2018.11.032.

[112] N. R. Stradiotto, H. Yamanaka, and M. V. B. Zanoni, “Electrochemical sensors: A powerful tool in analytical chemistry,” *J. Braz. Chem. Soc.*, vol. 14, no. 2, pp. 159–173, 2003, doi: 10.1590/S0103-50532003000200003.

[113] A. Bratov, N. Abramova, and A. Ipatov, “Recent trends in potentiometric sensor arrays-A review,” *Anal. Chim. Acta*, vol. 678, no. 2, pp. 149–159, 2010, doi: 10.1016/j.aca.2010.08.035.

[114] E. Zdrachek and E. Bakker, “Potentiometric Sensing,” *Anal. Chem.*, vol. 91, no. 1, pp. 2–26, 2019, doi: 10.1021/acs.analchem.8b04681.

[115] M. S. Frant, “History of the Early Commercialization of Ion-selective Electrodes,” *Analyst*, vol. 119, pp. 2293–2301, 1994, doi: 10.1016/B978-0-443-06967-3.00001-6.

[116] P. Bergveld, “Thirty years of ISFETOLOGY: What happened in the past 30 years and what may happen in the next 30 years,” *Sensors Actuators, B Chem.*, vol. 88, no. 1, pp. 1–20, 2003, doi: 10.1016/S0925-4005(02)00301-5.

[117] M. Yuqing, G. Jianguo, and C. Jianrong, “Ion sensitive field effect transducer-based biosensors,” *Biotechnol. Adv.*, vol. 21, no. 6, pp. 527–534, 2003, doi: 10.1016/S0734-

9750(03)00103-4.

[118] J. C. Dutta, “Ion sensitive field effect transistor for applications in bioelectronic sensors: A research review,” *Proc. - 2012 2nd Natl. Conf. Comput. Intell. Signal Process. CISP 2012*, pp. 185–191, 2012, doi: 10.1109/NCCISP.2012.6189704.

[119] S. D. Moss, J. Janata, and C. C. Johnson, “Potassium Ion-Sensitive Field Effect Transistor,” *Anal. Chem.*, vol. 47, no. 13, pp. 2238–2243, 1975, doi: 10.1021/ac60363a005.

[120] S. D. MOSS, C. C. JOHNSON, and J. JANATA, “Hydrogen, Calcium, and Potassium lon-Sensitive FET Transducers : A Preliminary Report,” *IEEE Trans. Biomed. Eng.*, no. 1, pp. 49–54, 1978.

[121] C. S. Lee, S. Kyu Kim, and M. Kim, “Ion-sensitive field-effect transistor for biological sensing,” 2009.

[122] J. Artigas *et al.*, “Application of ion sensitive field effect transistor based sensors to soil analysis,” *Comput. Electron. Agric.*, vol. 31, no. 3, pp. 281–293, 2001, doi: 10.1016/S0168-1699(00)00187-3.

[123] T. M. Althagafi, A. F. Al Baroot, S. A. Algarni, and M. Grell, “A membrane-free cation selective water-gated transistor,” *Analyst*, vol. 141, no. 19, pp. 5571–5576, 2016, doi: 10.1039/c6an00967k.

[124] S. Dimitrijev, *Principle of Semiconductor Devices*, Second. OXFORD UNIVERSITY PRESS, 2011.

[125] D. R. Evans, *Basic Semiconductor Material Science and Solid State Physics*. 2014.

[126] J.-P. Colinge and C. A. Colinge, *PHYSICS OF SEMICONDUCTOR DEVICES*. Springer Science & Business Media, 2005.

[127] M. A. Rahman, “A Review on Semiconductors Including Applications and Temperature Effects in Semiconductors,” *Am. Sci. Res. J. Eng. Technol. Sci. ISSN*, vol. 7, no. 1, pp. 50–70, 2014.

[128] M. L. Lin, J. M. Huang, C. S. Ku, C. M. Lin, H. Y. Lee, and J. Y. Juang, “High mobility transparent conductive Al-doped ZnO thin films by atomic layer deposition,” *J. Alloys Compd.*, vol. 727, pp. 565–571, 2017, doi: 10.1016/j.jallcom.2017.08.207.

[129] S. Jung, C. H. Kim, Y. Bonnassieux, and G. Horowitz, “Injection barrier at metal/organic semiconductor junctions with a Gaussian density-of-states,” *J. Phys. D. Appl. Phys.*, vol. 48, no. 39, p. 395103, 2015, doi: 10.1088/0022-3727/48/39/395103.

[130] D. Gu, S. K. Dey, and P. Majhi, “Effective work function of Pt, Pd, and Re on atomic layer deposited HfO 2,” *Appl. Phys. Lett.*, vol. 89, no. 8, pp. 2004–2007, 2006, doi: 10.1063/1.2336718.

[131] M. N. Islam and M. O. Hakim, “Electron affinity and work function of polycrystalline SnO2 thin film,” *J. Mater. Sci. Lett.*, vol. 5, no. 1, pp. 63–65, 1986, doi: 10.1007/BF01671438.

[132] J. Li, W. Ou-Yang, and M. Weis, “Electric-field enhanced thermionic emission model for carrier injection mechanism of organic field-effect transistors: Understanding of contact resistance,” *J. Phys. D. Appl. Phys.*, vol. 50, no. 3, 2017, doi: 10.1088/1361-

6463/aa4e95.

[133] B. P. TYAGI and K. SEN, “Effective mobility of polycrystalline semiconductors,” *Int. J. Electron.*, vol. 58, no. 1, pp. 83–89, Jan. 1985, doi: 10.1080/00207218508939004.

[134] W. Xu, H. Li, J. Bin Xu, and L. Wang, “Recent Advances of Solution-Processed Metal Oxide Thin-Film Transistors,” *ACS Applied Materials and Interfaces*, vol. 10, no. 31. American Chemical Society, pp. 25878–25901, Aug. 08, 2018, doi: 10.1021/acsami.7b16010.

[135] J. W. Park, B. H. Kang, and H. J. Kim, “A Review of Low-Temperature Solution-Processed Metal Oxide Thin-Film Transistors for Flexible Electronics,” *Adv. Funct. Mater.*, vol. 30, no. 20, pp. 1–40, 2020, doi: 10.1002/adfm.201904632.

[136] M. Ganchev *et al.*, “Spin - Coating of SnO2 thin films,” *J. Phys. Conf. Ser.*, vol. 1186, no. 1, 2019, doi: 10.1088/1742-6596/1186/1/012027.

[137] S. F. Oboudi, N. F. Habubi, and S. S. Chiad, “Physical characterization of sprayed SnO2 thin films,” *Mater. Sci.*, vol. 10, no. 9, pp. 397–401, 2014.

[138] H. Y. Liu, W. C. Hsu, J. H. Chen, P. H. Hsu, and C. S. Lee, “Amorphous ITZO Thin-Film Transistors by Using Ultrasonic Spray Pyrolysis Deposition,” *IEEE Trans. Electron Devices*, vol. 67, no. 3, pp. 1009–1013, 2020, doi: 10.1109/TED.2020.2965949.

[139] D. Liang, B. J. Chen, B. Feng, Y. Ikuhara, H. J. Cho, and H. Ohta, “Optimization of Two-Dimensional Channel Thickness in Nanometer-Thick SnO2-Based Top-Gated Thin-Film Transistors Using Electric Field Thermopower Modulation: Implications for Flat-Panel Displays,” *ACS Appl. Nano Mater.*, vol. 3, no. 12, pp. 12427–12432, 2020, doi: 10.1021/acsanm.0c03069.

[140] J. Zhai, X. Zhang, F. S. Hai, X. Yu, R. Zhu, and W. Zhang, “Fabrication and characterization of thin-film transistors with SnO 2 channel by spray pyrolysis,” *Jpn. J. Appl. Phys.*, vol. 53, no. 6, 2014, doi: 10.7567/JJAP.53.066506.

[141] R. A. Casali, J. Lasave, M. A. Caravaca, S. Koval, C. A. Ponce, and R. L. Migoni, “Ab initio and shell model studies of structural, thermoelastic and vibrational properties of SnO2 under pressure,” *J. Phys. Condens. Matter*, vol. 25, no. 13, 2013, doi: 10.1088/0953-8984/25/13/135404.

[142] D. Mohanta and M. Ahmaruzzaman, “Tin oxide nanostructured materials: an overview of recent developments in synthesis, modifications and potential applications,” *RSC Adv.*, vol. 6, no. 112, pp. 110996–111015, 2016, doi: 10.1039/C6RA21444D.

[143] Q. Jiang, X. Zhang, and J. You, “SnO2: A Wonderful Electron Transport Layer for Perovskite Solar Cells,” *Small*, vol. 14, no. 31, pp. 1–14, 2018, doi: 10.1002/smll.201801154.

[144] T. Serin, N. Serin, S. Karadeniz, H. Sari, N. Tuğluoğlu, and O. Pakma, “Electrical, structural and optical properties of SnO2 thin films prepared by spray pyrolysis,” *J. Non. Cryst. Solids*, vol. 352, no. 3, pp. 209–215, 2006, doi: 10.1016/j.jnoncrysol.2005.11.031.

[145] B. Cojocaru, D. Avram, V. Kessler, V. Parvulescu, G. Seisenbaeva, and C. Tiseanu, “Nanoscale insights into doping behavior, particle size and surface effects in trivalent metal doped SnO2,” *Sci. Rep.*, vol. 7, no. 1, pp. 4–12, 2017, doi: 10.1038/s41598-017-

09026-2.

[146] C. Avis, Y. G. Kim, and J. Jang, “Amorphous tin oxide applied to solution processed thin-film transistors,” *Materials (Basel).*, vol. 12, no. 20, 2019, doi: 10.3390/ma12203341.

[147] H.A.Klasens and H.Koelmans, “oxide field-effect transistor,” *Solid. State. Electron.*, vol. 7, no. 9, pp. 701–702, 1964.

[148] A. Aoki and H. Sasakura, “Tin Oxide Thin Film Transistors,” *Jpn. J. Appl. Phys.*, vol. 9, no. 5, p. 582, 1970, doi: 10.1143/JJAP.9.582.

[149] M. W. J. Prins *et al.*, “A ferroelectric transparent thin-film transistor,” *Appl. Phys. Lett.*, vol. 68, no. 25, pp. 3650–3652, 1996, doi: 10.1063/1.115759.

[150] R. E. Presley, C. L. Munsee, C. H. Park, D. Hong, J. F. Wager, and D. A. Keszler, “Tin oxide transparent thin-film transistors,” *J. Phys. D. Appl. Phys.*, vol. 37, no. 20, pp. 2810–2813, 2004, doi: 10.1088/0022-3727/37/20/006.

[151] D. D. Liang, Y. Q. Zhang, H. J. Cho, and H. Ohta, “Electric field thermopower modulation analyses of the operation mechanism of transparent amorphous SnO2 thin-film transistor,” *Appl. Phys. Lett.*, vol. 116, no. 14, 2020, doi: 10.1063/5.0003153.

[152] J. Sun, W. Huang, C. Qian, J. Yang, and Y. Gao, “Mobility enhancement of SnO2 nanowire transistors gated with a nanogranular SiO2 solid electrolyte,” *Phys. Chem. Chem. Phys.*, vol. 16, no. 3, pp. 1084–1088, 2014, doi: 10.1039/c3cp54142h.

[153] I. Valitova, M. M. Natile, F. Soavi, C. Santato, and F. Cicoira, “Tin Dioxide Electrolyte-Gated Transistors Working in Depletion and Enhancement Modes,” *ACS Appl. Mater. Interfaces*, vol. 9, no. 42, pp. 37013–37021, 2017, doi: 10.1021/acsami.7b09912.

[154] S. D. Brotherton, *Introduction to Thin Film Transistors*. Springer, 2013.

[155] T. Ytterdal, Y. Cheng, and T. A. Fjeldly, *MOSFET Device Physics and Operation*. John Wiley & Sons, Ltd, 2003.

[156] Z. Bao and J. Locklin, *Organic Field-Effect Transistors*, 1st Editio. CRC Press, 2007.

[157] Q. Li, J. Zhao, Y. Huang, W. Tang, and X. Guo, “Subthreshold-Operated Low-Voltage Organic Field-Effect Transistor for Ion-Sensing System of High Transduction Sensitivity,” *IEEE Sensors Lett.*, vol. 2, no. 4, pp. 1–4, 2018, doi: 10.1109/lsens.2018.2863228.

[158] D. W. Chou, K. L. Chen, and S. F. Wang, “Pentacene bottom-contact thin film transistors with solution-processed BZT gate dielectrics,” *Microelectron. Reliab.*, vol. 91, pp. 323–329, 2018, doi: 10.1016/j.microrel.2018.03.016.

[159] L. Huang *et al.*, “High mobility transparent flexible nickel- doped zinc oxide thin-film transistors with small subthreshold swing,” *Electron. Lett.*, vol. 51, no. 20, pp. 1595–1596, 2015, doi: 10.1149/1.3589244.

[160] S. K. Garlapati *et al.*, “Electrolyte-gated, high mobility inorganic oxide transistors from printed metal halides,” *ACS Appl. Mater. Interfaces*, vol. 5, no. 22, pp. 11498–11502, 2013, doi: 10.1021/am403131j.

[161] B. Kumar, B. K. Kaushik, Y. S. Negi, P. Mittal, and A. Mandal, “Organic thin film

transistors characteristics parameters, structures and their applications," *2011 IEEE Recent Adv. Intell. Comput. Syst. RAICS 2011*, pp. 706–711, 2011, doi: 10.1109/RAICS.2011.6069402.

[162] F. Faridbod, M. R. Ganjali, R. Dinarvand, and P. Norouzi, "Developments in the field of conducting and non-conducting polymer based potentiometric membrane sensors for ions over the past decade," *Sensors*, vol. 8, no. 4, pp. 2331–2412, 2008, doi: 10.3390/s8042331.

[163] M. M. Zareh, *Plasticizers and Their Role in Membrane Selective Electrodes*. Shanghai: IntechOpen, 2012.

[164] M. Rezayi *et al.*, "Titanium (III) cation selective electrode based on synthesized tris(2pyridyl) methylamine ionophore and its application in water samples," *Sci. Rep.*, vol. 4, 2014, doi: 10.1038/srep04664.

[165] V. K. Gupta, L. P. Singh, R. Singh, N. Upadhyay, S. P. Kaur, and B. Sethi, "A novel copper (II) selective sensor based on Dimethyl 4, 4′ (o-phenylene) bis(3-thioallophanate) in PVC matrix," *J. Mol. Liq.*, vol. 174, pp. 11–16, 2012, doi: 10.1016/j.molliq.2012.07.016.

[166] M. Sharifi-Sistani, F. Faridbod, H. Rashedi, and N. Davarkhah, "PVC membrane and All-Solid-Sate Sensor for the Potentiometric Analysis of Trimipramine," *Int. J. Electrochem. Sci.*, vol. 14, pp. 10681–10692, 2019, doi: 10.20964/2019.11.01.

[167] S. Sohrabnejad, M. A. Zanjanchi, M. Arvand, and M. F. Mousavi, "Evaluation of a PVC-based thionine-zeolite and zeolite free membranes as sensing elements in ion selective electrode," *Electroanalysis*, vol. 16, no. 12, pp. 1033–1037, 2004, doi: 10.1002/elan.200302945.

[168] G. W. Gokel, W. M. Leevy, and M. E. Weber, "Crown ethers: Sensors for ions and molecular scaffolds for materials and biological models," *Chem. Rev.*, vol. 104, no. 5, pp. 2723–2750, 2004, doi: 10.1021/cr020080k.

[169] W. Walkowiak and C. A. Kozlowski, "Macrocycle carriers for separation of metal ions in liquid membrane processes-a review," *Desalination*, vol. 240, no. 1–3, pp. 186–197, 2009, doi: 10.1016/j.desal.2007.12.041.

[170] D. Lee and J. D. R. Thomas, "4′-Picrylamino-5′-Nitrobenzo-18-Crown-6 As a Sensing Reagent in Potassium Ion-Selective Electrode Membranes," *Talanta*, vol. 41, no. 6, pp. 901–907, 1994, doi: 10.1016/0039-9140(94)E0043-Q.

[171] K. Suzuki *et al.*, "Design and synthesis of sodium ion-selective ionophores based on 16-crown-5 derivatives for an ion-selective electrode," *Anal. Chem.*, vol. 68, no. 1, pp. 208–215, 1996, doi: 10.1021/ac950773j.

[172] V. Guérineau *et al.*, "The synthesis and characterization of giant Calixarenes," *Nat. Commun.*, vol. 10, no. 1, pp. 1–14, 2019, doi: 10.1038/s41467-018-07751-4.

[173] P. E. Georghiou *et al.*, "Synthesis of an upper- and lower-rim functionalized calix[4]arene for detecting calcium ions using a microcantilever sensor," *New J. Chem.*, vol. 37, no. 5, pp. 1298–1301, 2013, doi: 10.1039/c3nj00223c.

[174] F. Perret and A. W. Coleman, "Biochemistry of anionic calix[n]arenes," *Chem. Commun.*, vol. 47, no. 26, pp. 7303–7319, 2011, doi: 10.1039/c1cc11541c.

[175] Y. Choi, H. Kim, J. Kwang, S. Ho, H. Bin, and J. Seung, “Cesium ion-selective electrodes based on 1,3-alternate thiacalix[4]biscrown-6,6,” *Talanta*, vol. 64, no. 4, pp. 975–980, 2004, doi: 10.1016/j.talanta.2004.04.015.

[176] J. Lu, R. Chen, and X. He, “A lead ion-selective electrode based on a calixarene carboxyphenyl azo derivative,” *J. Electroanal. Chem.*, vol. 528, no. 1–2, pp. 33–38, 2002, doi: 10.1016/S0022-0728(02)00840-9.

[177] IAEA, *Application of Ion Exchange Processes for the Treatment of Radioactive Waste and Management of Spent Ion Exchangers*, no. 408. Vienna, 2002.

[178] F. Helfferich, *Ion exchange*. New York: McGRAW-HILL, 1962.

[179] H. Eichhorn, “On the reactions of silicates with dilute solutions of salts.,” *Pogendorf’s. Ann. Phys. Chem.*, vol. 105, p. 126, 1858.

[180] R. Gans, “Zeolites and similar compounds, their constitution and significance for technology and agriculture,” *Jahrb. Preuss Geol. Landesanst*, vol. 26, p. 179, 1905.

[181] S. B. Applebaum, *Demineralization by ion exchange: in water treatment and chemical processing of other liquids*. Elsevier, 2013.

[182] P. Baile, E. Fernández, L. Vidal, and A. Canals, “Zeolites and zeolite-based materials in extraction and microextraction techniques,” *Analyst*, vol. 144, no. 2, pp. 366–387, 2019, doi: 10.1039/c8an01194j.

[183] “Cages for nuclear waste,” *ChemBAM*. https://chembam.com/online-resources/experiments/cages-for-nuclear-waste/.

[184] M. Moshoeshoe, M. Silas Nadiye-Tabbiruka, and V. Obuseng, “A Review of the Chemistry, Structure, Properties and Applications of Zeolites,” *Am. J. Mater. Sci.*, vol. 7, no. 5, pp. 196–221, 2017, doi: 10.5923/j.materials.20170705.12.

[185] S. Wang and Y. Peng, “Natural zeolites as effective adsorbents in water and wastewater treatment,” *Chem. Eng. J.*, vol. 156, no. 1, pp. 11–24, 2010, doi: 10.1016/j.cej.2009.10.029.

[186] M. G. Valdés, A. I. Pérez-Cordoves, and M. E. Díaz-García, “Zeolites and zeolite-based materials in analytical chemistry,” *TrAC - Trends Anal. Chem.*, vol. 25, no. 1, pp. 24–30, 2006, doi: 10.1016/j.trac.2005.04.016.

[187] Sadaf Zaidi, “Ion exchange technology II: Applications,” in *Ion Exchange Technology II: Applications*, 2014, pp. 1–438.

[188] B. O. Hincapie, L. J. Garces, Q. Zhang, A. Sacco, and S. L. Suib, “Synthesis of mordenite nanocrystals,” *Microporous Mesoporous Mater.*, vol. 67, no. 1, pp. 19–26, 2004, doi: 10.1016/j.micromeso.2003.09.026.

[189] M. Danesh-Khorasgani and A. Nezamzadeh-Ejhieh, “PVC-zeolite nanoparticle-surfactant anion exchanger membrane: preparation, characterization, and its application in development of ion-selective electrode for detection of sulfate,” *J. Solid State Electrochem.*, vol. 20, no. 10, pp. 2827–2833, 2016, doi: 10.1007/s10008-016-3265-9.

[190] A. Nezamzadeh-Ejhieh and A. Badri, “Application of surfactant modified zeolite membrane electrode towards potentiometric determination of perchlorate,” *J.*

Electroanal. Chem., vol. 660, no. 1, pp. 71–79, 2011, doi: 10.1016/j.jelechem.2011.06.007.

[191] Y. F. Wang, F. Lin, and W. Q. Pang, "Ammonium exchange in aqueous solution using Chinese natural clinoptilolite and modified zeolite," *J. Hazard. Mater.*, vol. 142, no. 1–2, pp. 160–164, 2007, doi: 10.1016/j.jhazmat.2006.07.074.

[192] D. Karadag, Y. Koc, M. Turan, and B. Armagan, "Removal of ammonium ion from aqueous solution using natural Turkish clinoptilolite," *J. Hazard. Mater.*, vol. 136, no. 3, pp. 604–609, 2006, doi: 10.1016/j.jhazmat.2005.12.042.

[193] E. H. Borai, R. Harjula, L. malinen, and A. Paajanen, "Efficient removal of cesium from low-level radioactive liquid waste using natural and impregnated zeolite minerals," *J. Hazard. Mater.*, vol. 172, no. 1, pp. 416–422, 2009, doi: 10.1016/j.jhazmat.2009.07.033.

[194] R. T. Pabalan and F. P. Bertetti, "Cation-exchange properties of natural zeolites," *Rev. Mineral. Geochemistry*, vol. 45, pp. 453–517, 2001, doi: 10.2138/rmg.2001.45.14.

[195] M. W. Munthali, E. Johan, H. Aono, and N. Matsue, "Cs and Sr adsorption selectivity of zeolites in relation to radioactive decontamination," *J. Asian Ceram. Soc.*, vol. 3, no. 3, pp. 245–250, 2018, doi: 10.1016/j.jascer.2015.04.002.

[196] E. Johan, T. Yamada, M. Wazingwa, P. Kabwadza-, H. Aono, and N. Matsue, "Natural zeolites as potential materials for decontamination of radioactive cesium," *Procedia Environ. Sci.*, vol. 28, pp. 52–56, 2015, doi: 10.1016/j.proenv.2015.07.008.

[197] F. A. Mumpton, "La roca magica: Uses of natural zeolites in agriculture and industry," *Proc. Natl. Acad. Sci. U. S. A.*, vol. 96, no. 7, pp. 3463–3470, Mar. 1999, doi: 10.1073/pnas.96.7.3463.

[198] S. M. Shaheen, A. S. Derbalah, and F. S. Moghanm, "Removal of heavy metal from aqueous solution by zeolite," *Int. J. Environ. Sci. Dev. Vol. 3, No. 4*, vol. 3, no. 4, 2012.

[199] M. Arvand-Barmchi, M. F. Mousavi, M. A. Zanjanchi, and M. Shamsipur, "A PTEV-based zeolite membrane potentiometric sensor for cesium ion," *Sensors Actuators, B Chem.*, vol. 96, no. 3, pp. 560–564, 2003, doi: 10.1016/S0925-4005(03)00639-7.

[200] M. K. Shelyakina, O. O. Soldatkin, V. M. Arkhypova, B. O. Kasap, B. Akata, and S. V. Dzyadevych, "Study of zeolite influence on analytical characteristics of urea biosensor based on ion-selective field-effect transistors," *Nanoscale Res. Lett.*, vol. 9, no. 1, pp. 1–9, 2014, doi: 10.1186/1556-276X-9-124.

[201] Zbigniew Hubicki and D. Kołodyńska, "Selective Removal of Heavy Metal Ions from Waters and Waste Waters Using Ion Exchange Methods," in *Ion Exchange Technologies*, 2012, pp. 193–240.

[202] "6 Best Water Softener Resins | Highly Recommended in 2020." https://dwellingadvisor.com/best-water-softener-resin-reviews/ (accessed Jun. 25, 2020).

[203] "What Is Water Demineralization and How Does It Work?," 2018. https://www.samcotech.com/what-is-demineralization-and-how-does-it-work/ (accessed Jun. 25, 2020).

[204] "Arsenic removal using ion exchange resin | Purolite." https://www.purolite.com/industry/potable---groundwater/arsenic-removal-using-ion-exchange-resin (accessed Jun. 18, 2020).

[205] P. J. Lloyd-Jones, J. R. Rangel-Mendez, and M. Streat, "Mercury sorption from aqueous solution by chelating ion exchange resins, activated carbon and a biosorbent," *Process Saf. Environ. Prot.*, vol. 82, no. 4, pp. 301–311, 2004, doi: 10.1205/095758204323162328.

[206] P. Bulai, C. Bălan, D. Bîlbă, and M. Macoveanu, "Study of the copper (II) removal from aqueous solutions by chelating resin Purolite S930," *Environ. Eng. Manag. J.*, vol. 8, no. 2, pp. 213–218, 2009, doi: 10.30638/eemj.2009.030.

[207] N. van Nguyen, J. C. Lee, S. K. Kim, M. K. Jhac, K. S. Chung, and J. Jeong, "Adsorption of gold(III) from waste rinse water of semiconductor manufacturing industries using Amberlite XAD-7HP resin," *Gold Bull.*, vol. 43, no. 3, pp. 200–208, 2010, doi: 10.1007/bf03214987.

[208] K. N. Mikhelson, *Ion-Selective Electrodes*. Springer, 2013.

[209] T. M. Althagafi, S. A. Algarni, and M. Grell, "Innate cation sensitivity in a semiconducting polymer," *Talanta*, vol. 158, pp. 70–76, 2016, doi: 10.1016/j.talanta.2016.05.047.

[210] Julian B. Andelman, "Ion-selective electrodes - theory and applications in water analysis," *J. (Water Pollut. Control Fed.*, vol. 40, no. 11, pp. 1844–1860, 1968.

[211] E. Bakker, R. K. Meruva, M. E. Meyerhoff, and E. Pretsch, "Selectivity of Polymer Membrane-Based Ion-Selective Electrodes: Self-Consistent Model Describing the Potentiometric Response in Mixed Ion Solutions of Different Charge," *Anal. Chem.*, vol. 66, no. 19, pp. 3021–3030, 1994, doi: 10.1021/ac00091a600.

[212] F. Deyhimi, "A method for the determination of potentiometric selectivity coefficients of ion selective electrodes in the presence of several interfering ions," *Talanta*, vol. 50, no. 5, pp. 1129–1134, 1999, doi: 10.1016/S0039-9140(99)00194-0.

[213] I. Langmuir, "The constitution and fundamental properties of solids and liquids.," *J. Am. Chem. Soc.*, vol. 38, no. 11, pp. 2221–2295, 1916, doi: 10.1021/ja02268a002.

[214] R. Saadi, Z. Saadi, R. Fazaeli, and N. E. Fard, "Monolayer and multilayer adsorption isotherm models for sorption from aqueous media," *Korean J. Chem. Eng.*, vol. 32, no. 5, pp. 787–799, 2015, doi: 10.1007/s11814-015-0053-7.

[215] Y. Liu, "Some consideration on the Langmuir isotherm equation," *Colloids Surfaces A Physicochem. Eng. Asp.*, vol. 274, no. 1–3, pp. 34–36, 2006, doi: 10.1016/j.colsurfa.2005.08.029.

[216] D. G. Duff, S. M. C. Ross, and D. H. Vaughan, "Adsorption from solution: An experiment to illustrate the langmuir adsorption isotherm," *J. Chem. Educ.*, vol. 65, no. 9, pp. 815–816, 1988, doi: 10.1021/ed065p815.

[217] C. Yang, L. Liu, T. W. Mu, and Q. X. Guo, "The performance of the Benesi-Hildebrand method in measuring the binding constants of the cyclodextrin complexation," *Anal. Sci.*, vol. 16, no. 5, pp. 537–539, 2000, doi: 10.2116/analsci.16.537.

[218] S. Santhi, S. Amala, and S. M. Basheer, “Experimental and computational investigation of highly selective dual-channel chemosensor for Al(III) and Zn(II) ions: construction of logic gates,” *J. Chem. Sci.*, vol. 130, no. 11, pp. 1–13, 2018, doi: 10.1007/s12039-018-1541-1.

[219] K. A. Tuwei, N. H. Williams, and M. Grell, “Fibre optic absorbance meter with low limit of detection for waterborne cations,” *Sensors Actuators, B Chem.*, vol. 237, pp. 1102–1107, 2016, doi: 10.1016/j.snb.2016.05.065.

[220] G. P. Jeppu and T. P. Clement, “A modified Langmuir-Freundlich isotherm model for simulating pH-dependent adsorption effects,” *J. Contam. Hydrol.*, vol. 129–130, pp. 46–53, 2012, doi: 10.1016/j.jconhyd.2011.12.001.

[221] R. J. Umpleby, S. C. Baxter, Y. Chen, R. N. Shah, and K. D. Shimizu, “Characterization of Molecularly Imprinted Polymers with the Langmuir - Freundlich Isotherm,” *Anal. Chem.*, vol. 73, no. 19, pp. 4584–4591, 2001, doi: 10.1021/ac0105686.

[222] S. A. Al-Muhtaseb, M. H. El-Naas, and S. Abdallah, “Removal of aluminum from aqueous solutions by adsorption on date-pit and BDH activated carbons,” *J. Hazard. Mater.*, vol. 158, no. 2–3, pp. 300–307, 2008, doi: 10.1016/j.jhazmat.2008.01.080.

[223] I. H. Lee, Y. C. Kuan, and J. M. Chern, “Equilibrium and kinetics of heavy metal ion exchange,” *J. Chinese Inst. Chem. Eng.*, vol. 38, no. 1, pp. 71–84, 2007, doi: 10.1016/j.jcice.2006.11.001.

[224] M. Berto *et al.*, “EGOFET Peptide Aptasensor for Label-Free Detection of Inflammatory Cytokines in Complex Fluids,” *Adv. Biosyst.*, vol. 2, no. 2, pp. 1–8, 2018, doi: 10.1002/adbi.201700072.

[225] H. Yang, S. Nishitani, and T. Sakata, “Potentiometric Langmuir Isotherm Analysis of Histamine-Selective Molecularly Imprinted Polymer-Based Field-Effect Transistor,” *ECS J. Solid State Sci. Technol.*, vol. 7, no. 7, pp. Q3079–Q3082, 2018, doi: 10.1149/2.0131807jss.

[226] Á. Golcs, V. Horváth, P. Huszthy, and T. Tóth, “Fast Potentiometric Analysis of Lead in Aqueous Medium under Competitive Conditions Using an Acridono-Crown Ether Neutral Ionophore,” *Sensors*, vol. 18, no. 1407, 2018, doi: 10.3390/s18051407.

[227] D. Vlascici, I. Popa, V. A. Chiriac, G. Fagadar-Cosma, H. Popovici, and E. Fagadar-Cosma, “Potentiometric detection and removal of copper using porphyrins,” *Chem. Cent. J.*, vol. 7, no. 1, pp. 1–7, 2013, doi: 10.1186/1752-153X-7-111.

[228] O. Özbek, Ö. Isildak, M. B. Gürdere, and A. Cetin, “The use of crown ethers as sensor material in potentiometry technique,” *Org. Commun.*, vol. 14, no. 3, pp. 228–239, 2021, doi: 10.25135/acg.oc.110.2106.2114.

[229] E. Khaled, M. S. Kamel, and H. N. A. Hassan, “Novel Multi Walled Carbon Nanotubes /Crown Ether Based Disposable Sensors for Determination of Lead in Water Samples,” *Anal. Chem. Lett.*, vol. 5, no. 6, pp. 329–337, 2015, doi: 10.1080/22297928.2016.1143393.

[230] S. Mathew, L. Rajith, L. A. Lonappan, T. Jos, and K. G. Kumar, “A lead (II) selective PVC membrane potentiometric sensor based on a tetraazamacrocyclic ligand,” *J. Incl. Phenom. Macrocycl. Chem.*, vol. 78, no. 1–4, pp. 171–177, 2014, doi:

10.1007/s10847-013-0285-2.

[231] A. K. Singh, R. Singh, and P. Saxena, “Lead-selective potentiometric sensor based on macrocyclic ionophore [pyo2(16)diene N6],” *Anal. Lett.*, vol. 38, no. 4, pp. 589–600, 2005, doi: 10.1081/AL-200050269.

[232] L. Chen, J. Zhang, W. Zhao, X. He, and Y. Liu, “Double-armed calix[4]arene amide derivatives as ionophores for lead ion-selective electrodes,” *J. Electroanal. Chem.*, vol. 589, no. 1, pp. 106–111, 2006, doi: 10.1016/j.jelechem.2006.02.001.

[233] D. M. Kumar, J. Suresh, J. Neeraj, and B. Poonam, “A PVC- based Crown Ether Membrane Sensor for Cu2+,” *Res. J. Chem. Environ.*, vol. 17, no. 9, pp. 1–5, 2013.

[234] A. H. Kamel, A. E. G. E. Amr, A. A. Almehizia, E. A. Elsayed, and G. O. Moustafa, “Low-cost potentiometric paper-based analytical device based on newly synthesized macrocyclic pyrido-pentapeptide derivatives as novel ionophores for point-of-care copper(ii) determination,” *RSC Adv.*, vol. 11, no. 44, pp. 27174–27182, 2021, doi: 10.1039/d1ra04712d.

[235] M. H. Mashhadizadeh, A. Mostafavi, R. Razavi, and M. Shamsipur, “Highly selective Cu(II) PVC membrane electrode based on 3,6,9,14-tetrathiabicyclo[9.2.1]tetradeca-11,13-diene as a suitable neutral ionophore,” *Sensors Actuators, B Chem.*, vol. 86, no. 2–3, pp. 222–228, 2002, doi: 10.1016/S0925-4005(02)00191-0.

[236] R. K. Mahajan, M. Kumar, V. S. Bhalla, and I. Kaur, “Cesium ion selecti v e electrode based on calix [4] crown ether-ester,” *Talanta*, vol. 58, pp. 445–450, 2002.

[237] M. Shamsipur and H. R. Rajabi, “Flame photometric determination of cesium ion after its preconcentration with nanoparticles imprinted with the cesium-dibenzo-24-crown-8 complex,” *Microchim. Acta*, vol. 180, no. 3–4, pp. 243–252, 2013, doi: 10.1007/s00604-012-0927-x.

[238] S. Sadeghi and F. Fathi, “Polymeric membrane coated graphite cesium selective electrode based on 4′,4″(5′) di-tert-butyl di-benzo-18-crown-6,” *J. Incl. Phenom. Macrocycl. Chem.*, vol. 67, no. 1–2, pp. 91–98, 2010, doi: 10.1007/s10847-009-9679-6.

[239] “What chemical compounds might be present in drinking water?” https://www.open.edu/openlearn/ocw/mod/oucontent/view.php?printable=1&id=20880 (accessed Sep. 12, 2020).

[240] D. L. Ozsvath, “Fluoride and environmental health: A review,” *Rev. Environ. Sci. Biotechnol.*, vol. 8, no. 1, pp. 59–79, 2009, doi: 10.1007/s11157-008-9136-9.

[241] S. Ayoob and A. K. Gupta, *Fluoride in drinking water: A review on the status and stress effects*, vol. 36, no. 6. 2006.

[242] B. Kasprzyk-Hordern, M. Ziółek, and J. Nawrocki, “Catalytic ozonation and methods of enhancing molecular ozone reactions in water treatment,” *Appl. Catal. B Environ.*, vol. 46, no. 4, pp. 639–669, 2003, doi: 10.1016/S0926-3373(03)00326-6.

[243] “Mechanism of the vacuum thin film coating system | Thin Film Coating System | ShinMaywa Industries, Ltd.” https://www.shinmaywa.co.jp/vac/english/vacuum/vacuum_2.html (accessed Jul. 28, 2020).

[244] D. Johannsmann, *The Quartz Crystal Microbalance in Soft Matter Research*. 2014.

[245] M. A. Trunov, M. Schoenitz, and E. L. Dreizin, "Effect of polymorphic phase transformations in alumina layer on ignition of aluminium particles," *Combust. Theory Model.*, vol. 10, no. 4, pp. 603–623, 2006, doi: 10.1080/13647830600578506.

[246] J. Leng *et al.*, "Advances in nanostructures fabricated via spray pyrolysis and their applications in energy storage and conversion," *Chem. Soc. Rev.*, vol. 48, no. 11, pp. 3015–3072, 2019, doi: 10.1039/c8cs00904j.

[247] D. Perednis and L. J. Gauckler, "Thin film deposition using spray pyrolysis," *J. Electroceramics*, vol. 14, no. 2, pp. 103–111, 2005, doi: 10.1007/s10832-005-0870-x.

[248] N. Lehraki, M. S. Aida, S. Abed, N. Attaf, A. Attaf, and M. Poulain, "ZnO thin films deposition by spray pyrolysis: Influence of precursor solution properties," *Curr. Appl. Phys.*, vol. 12, no. 5, pp. 1283–1287, 2012, doi: 10.1016/j.cap.2012.03.012.

[249] R. Kumar, G. Kumar, and A. Umar, "ZnO nanostructured thin films: Depositions, properties and applications—A review," *Mater. Express*, vol. 5, no. 1, pp. 3–23, 2015, doi: 10.1166/mex.2015.1204.

[250] L. Filipovic *et al.*, "Modeling the growth of tin dioxide using spray pyrolysis deposition for gas sensor applications," *IEEE Trans. Semicond. Manuf.*, vol. 27, no. 2, pp. 269–277, 2014, doi: 10.1109/TSM.2014.2298883.

[251] S. W. Oh, H. J. Bang, Y. C. Bae, and Y. Sun, "Effect of calcination temperature on morphology , crystallinity and electrochemical properties of nano-crystalline metal oxides (Co 3 O 4 , CuO , and NiO) prepared via ultrasonic spray pyrolysis," *J. Power Sources*, vol. 173, pp. 502–509, 2007, doi: 10.1016/j.jpowsour.2007.04.087.

[252] T. P. Rao, M. C. S. Kumar, A. Safarulla, V. Ganesan, S. R. Barman, and C. Sanjeeviraja, "Physical properties of ZnO thin films deposited at various substrate temperatures using spray pyrolysis," *Phys. B Phys. Condens. Matter*, vol. 405, no. 9, pp. 2226–2231, 2010, doi: 10.1016/j.physb.2010.02.016.

[253] A. I. Hassan, A. J. Addie, and J. Admon, "Influence of precursor concentration on the optoelectronic properties of spray deposited SnO2/Si heterojunction," *Mater. Res. Express*, vol. 6, no. 9, 2019, doi: 10.1088/2053-1591/ab350b.

[254] E. Bacaksiz, M. Parlak, M. Tomakin, A. Özçelik, M. Karakiz, and M. Altunbaş, "The effects of zinc nitrate, zinc acetate and zinc chloride precursors on investigation of structural and optical properties of ZnO thin films," *J. Alloys Compd.*, vol. 466, no. 1–2, pp. 447–450, 2008, doi: 10.1016/j.jallcom.2007.11.061.

[255] V. Vasu and A. Subrahmanyam, "Electrical and optical properties of sprayed SnO2 films: Dependence on the oxiding agent in the starting material," *Thin Solid Films*, vol. 193, pp. 973–980, 1990, doi: 10.1016/0040-6090(90)90252-9.

[256] A. Y. Fasasi *et al.*, "Effect of Precursor Solvents on the Optical Properties of Copper Oxide Thin Films Deposited Using Spray Pyrolysis for Optoelectronic Applications," *Am. J. Mater. Synth. Process.*, vol. 3, no. 2, pp. 12–22, 2018, doi: 10.11648/j.ajmsp.20180302.12.

[257] G. K. Deyu *et al.*, "SnO2 Films Deposited by Ultrasonic Spray Pyrolysis : Influence of Al Incorporation on the Properties," *Molecules*, vol. 24, no. 15, p. 2797, 2019, doi: 10.3390/molecules24152797.

[258] N. Alghamdi, Z. Alqahtani, and M. Grell, “Sub-nanomolar detection of cesium with water-gated transistor,” *J. Appl. Phys.*, vol. 126, no. 6, 2019, doi: 10.1063/1.5108730.

[259] S. K. Menon, N. R. Modi, B. Patel, and M. B. Patel, “Azo calix[4]arene based neodymium (III)-selective PVC membrane sensor,” *Talanta*, vol. 83, no. 5, pp. 1329–1334, 2011, doi: 10.1016/j.talanta.2010.10.027.

[260] M. Esmaelpourfarkhani, G. H. Rounaghi, and M. H. Arbab-Zavar, “Construction of a new aluminum(III) cation selective electrode based on 12-crown-4 as an ionophore,” *J. Braz. Chem. Soc.*, vol. 26, no. 5, pp. 963–969, 2015, doi: 10.5935/0103-5053.20150058.

[261] W. Kim, A. Javey, O. Vermesh, Q. Wang, Y. Li, and H. Dai, “Hysteresis caused by water molecules in carbon nanotube field-effect transistors,” *Nano Lett.*, vol. 3, no. 2, pp. 193–198, 2003, doi: 10.1021/nl0259232.

[262] A. Di Bartolomeo *et al.*, “Hysteresis in the transfer characteristics of MoS2 transistors,” *2D Mater.*, vol. 5, 2017.

[263] M. Egginger, S. Bauer, R. Schwödiauer, H. Neugebauer, and N. S. Sariciftci, “Current versus gate voltage hysteresis in organic field effect transistors,” *Monatshefte fur Chemie*, vol. 140, no. 7, pp. 735–750, 2009, doi: 10.1007/s00706-009-0149-z.

[264] M. Singh *et al.*, “Bio-functionalization of ZnO water gated thin-film transistors,” *Proc. - 2015 6th IEEE Int. Work. Adv. Sensors Interfaces, IWASI 2015*, pp. 261–265, 2015, doi: 10.1109/IWASI.2015.7184944.

[265] S. K. Menon, N. R. Modi, B. Patel, and M. B. Patel, “Azo calix[4]arene based neodymium(III)-selective PVC membrane sensor,” *Talanta*, vol. 83, no. 5, pp. 1329–1334, 2011, doi: 10.1016/j.talanta.2010.10.027.

[266] A. Cadogan *et al.*, “All-Solid-State Sodium-Selective Electrode Based on a Calixarene Ionophore in a Poly(vinyl chloride) Membrane with a Polypyrrole Solid Contact,” *Anal. Chem.*, vol. 64, no. 21, pp. 2496–2501, 1992, doi: 10.1021/ac00045a007.

[267] A. Tarasov *et al.*, “Understanding the electrolyte background for biochemical sensing with ion-sensitive field-effect transistors,” *ACS Nano*, vol. 6, no. 10, pp. 9291–9298, 2012, doi: 10.1021/nn303795r.

[268] M. C. Honda *et al.*, “Dispersion of artificial caesium-134 and -137 in the western North Pacific one month after the Fukushima accident,” *Geochem. J.*, vol. 46, no. 4, pp. 1–9, 2012, doi: 10.2343/geochemj.1.0152.

[269] T. J. Yasunari, A. Stohl, R. S. Hayano, J. F. Burkhart, S. Eckhardt, and T. Yasunari, “Cesium-137 deposition and contamination of Japanese soils due to the Fukushima nuclear accident,” *Proc. Natl. Acad. Sci. U. S. A.*, vol. 108, no. 49, pp. 19530–19534, 2011, doi: 10.1073/pnas.1304997110.

[270] Atsdr.cdc.gov, “ATSDR - Public Health Statement: Cesium,” 2004. https://www.atsdr.cdc.gov/PHS/PHS.asp?id=575&tid=107 (accessed Sep. 12, 2020).

[271] N. H. Alghamdi, “Zeolites as sensitizers in water-gated thin film transistors sensors,” 2021.

[272] M. Frick-Engfeldt, B. Gruvberger, M. Isaksson, I. Hauksson, A. Pontén, and M. Bruze, “Comparison of three different techniques for application of water solutions to Finn

Chambers®,” *Contact Dermatitis*, vol. 63, no. 5, pp. 284–288, 2010, doi: 10.1111/j.1600-0536.2010.01797.x.

[273] A. Azoulay, P. Garzon, and M. J. Eisenberg, “Comparison of the mineral content of tap water and bottled waters,” *J. Gen. Intern. Med.*, vol. 16, no. 3, pp. 168–175, 2001, doi: 10.1111/j.1525-1497.2001.04189.x.

[274] “Yorkshire Water | Water hardness.” https://www.yorkshirewater.com/business/in-your-area-water-quality/ (accessed Mar. 22, 2021).

[275] A. K. Tuwei, N. H. Williams, M. Y. Mulla, C. Di Natale, R. Paolesse, and M. Grell, “‘Rough guide’ evanescent wave optrode for colorimetric metalloporphyrine sensors,” *Talanta*, vol. 164, no. September 2016, pp. 228–232, 2017, doi: 10.1016/j.talanta.2016.11.057.

[276] B. J. Müller, S. M. Borisov, and I. Klimant, “Red- to NIR-Emitting, BODIPY-Based, K+-Selective Fluoroionophores and Sensing Materials,” *Adv. Funct. Mater.*, vol. 26, no. 42, pp. 7697–7707, 2016, doi: 10.1002/adfm.201603822.

[277] K. KIMURA, H. TAMURA, and T. SHONO, “CAESIUM-SELECTIVE PVC MEMBRANE ELECTRODES BASED ON BIS(CROWN ETHER)S,” *J. Electroanal. Chem. Interfacial Electrochem.*, vol. 105, no. 2, pp. 335–340, 1979.

[278] Vhahangwele Masindi and Khathutshelo L. Muedi, “Environmental Contamination by Heavy Metals,” in *Heavy Metals*, IntechOpen, 2018.

[279] “Lead and Copper in Drinking Water.” https://mde.maryland.gov/programs/water/water_supply/Pages/Pb_and_Cu_Rule.aspx (accessed Sep. 16, 2020).

[280] V. B. P. Sudha, S. Ganesan, G. P. Pazhani, T. Ramamurthy, G. B. Nair, and P. Venkatasubramanian, “Storing Drinking-water in Copper pots Kills Contaminating Diarrhoeagenic Bacteria Bacterial strains,” *J. Health. Popul. Nutr.*, vol. 30, no. 1, pp. 17–21, 2012.

[281] EPA, “Lead and Copper Rule : A Quick Reference Guide Overview of the Rule,” *United States Environmental Protection Agency*, 2008. .

[282] I. Sato, H. Kudo, and S. Tsuda, “Removal efficiency of water purifier and adsorbent for iodine , cesium , strontium , barium and zirconium in drinking water,” *J. Toxicol. Sci.*, vol. 36, no. 6, pp. 829–834, 2011.

[283] Dwi.defra.gov.uk, “Drinking water 2017 Chief Inspector’s report for drinking water in England,” 2018. http://www.dwi.defra.gov.uk/about/annual-report/2017/Summary_CIR_2017_England.pdf (accessed Sep. 12, 2020).

[284] World Health Organisation, “pH in drinking-water,” 2007. doi: WHO/SDE/WHO/03.04/12.

[285] M. S. Frant and J. W. Ross, “Electrode for sensing fluoride ion activity in solution,” *Science (80-.).*, vol. 154, no. 3756, pp. 1553–1554, 1966, doi: 10.1126/science.154.3756.1553.

[286] Z. Alqahtani, N. Alghamdi, and M. Grell, “Monitoring the lead-and-copper rule with a water-gated field effect transistor,” *J. Water Health*, vol. 18, no. 2, pp. 159–171, 2020, doi: 10.2166/wh.2020.186.

[287] N. Ingle, H. Dubey, N. Kaur, and I. Sharma, “Defluoridation techniques: Which one to choose,” *J. Heal. Res. Rev.*, vol. 1, no. 1, pp. 1–4, 2014, doi: 10.4103/2394-2010.143315.

[288] L. M. Camacho, A. Torres, D. Saha, and S. Deng, “Adsorption equilibrium and kinetics of fluoride on sol-gel-derived activated alumina adsorbents,” *J. Colloid Interface Sci.*, vol. 349, no. 1, pp. 307–313, 2010, doi: 10.1016/j.jcis.2010.05.066.

[289] P. Wu, L. Xia, M. Dai, L. Lin, and S. Song, “Electrosorption of fluoride on TiO2-loaded activated carbon in water,” *Colloids Surfaces A Physicochem. Eng. Asp.*, vol. 502, pp. 66–73, 2016, doi: 10.1016/j.colsurfa.2016.05.020.

[290] Z. Li *et al.*, “Triarylboron-Linked Conjugated Microporous Polymers: Sensing and Removal of Fluoride Ions,” *Chem. - A Eur. J.*, vol. 21, no. 48, pp. 17355–17362, 2015, doi: 10.1002/chem.201502241.

[291] L. Lv, J. He, M. Wei, D. G. Evans, and Z. Zhou, “Treatment of high fluoride concentration water by MgAl-CO3 layered double hydroxides: Kinetic and equilibrium studies,” *Water Res.*, vol. 41, no. 7, pp. 1534–1542, 2007, doi: 10.1016/j.watres.2006.12.033.

[292] D. B. Bhatt, P. R. Bhatt, H. H. Prasad, K. M. Popat, and P. S. Anand, “Removal of fluoride ion from aqueous bodies by aluminium complexed amino phosphonic acid type resins,” *Indian J. Chem. Technol.*, vol. 11, no. 3, pp. 299–303, 2004.

[293] C. Paduraru, D. Bilba, I. Sarghie, and L. Tofan, “A sorption study of Pd(II) on aminomethylphosphonic purolite resin S-940,” *J. Serbian Chem. Soc.*, vol. 70, no. 10, pp. 1205–1212, 2005, doi: 10.2298/JSC0510205P.

[294] YorkshireWater, “Your water quality Drinking water quality standards explained,” Sheffield, 2018. [Online]. Available: https://www.yorkshirewater.com/sites/default/files/Drinking Water Quality Standards.pdf.

[295] “Commonly Found Substances in Drinking Water.” Accessed: Dec. 23, 2020. [Online]. Available: https://dph.illinois.gov/sites/default/files/publications/drinking-water-042716.pdf.

[296] X. Chen, “Modeling of experimental adsorption isotherm data,” *Inf.*, vol. 6, no. 1, pp. 14–22, 2015, doi: 10.3390/info6010014.

[297] J. Sreńscek-Nazzal, U. Narkiewicz, A. W. Morawski, R. J. Wróbel, and B. Michalkiewicz, “Comparison of Optimized Isotherm Models and Error Functions for Carbon Dioxide Adsorption on Activated Carbon,” *J. Chem. Eng. Data*, vol. 60, no. 11, pp. 3148–3158, 2015, doi: 10.1021/acs.jced.5b00294.

[298] R. Schroeder, L. A. Majewski, M. Voigt, and M. Grell, “Memory performance and retention of an all-organic ferroelectric-like memory transistor,” *IEEE Electron Device Lett.*, vol. 26, no. 2, pp. 69–71, 2005, doi: 10.1109/LED.2004.841186.

[299] T. Birk *et al.*, “Fluoride bridges as structure-directing motifs in 3d-4f cluster chemistry,” *Inorg. Chem.*, vol. 51, no. 9, pp. 5435–5443, 2012, doi: 10.1021/ic300421x.

[300] “Check your water Hardness | Yorkshire Water.” https://www.yorkshirewater.com/water-quality/check-your-water-hardness/ (accessed

Dec. 26, 2020).

[301] J. W. Morse and F. T. Mackenzie, “THE CO2-CARBONIC ACID SYSTEM AND SOLUTION CHEMISTR,” in *Geochemistry of sedimentary carbonates: Developments in Sedimentology*, no. 48, 1990, pp. 1–38.

[302] M. A. Marques, M. I. Cabaço, M. I. De Barros Marques, A. M. Gaspar, and C. M. De Morais, “Local order in aqueous solutions of lanthanum chloride and bromide by x-ray diffraction, EXAFS and raman spectroscopy,” *J. Phys. Condens. Matter*, vol. 13, no. 20, pp. 4367–4385, 2001, doi: 10.1088/0953-8984/13/20/301.

[303] “chemical carbonate removal with pellet reactor – Gyrazur™ - Degremont®.” https://www.suezwaterhandbook.com/degremont-R-technologies/drinking-water-production/carbonate-removal-softening/chemical-carbonate-removal-with-pellet-reactor-Gyrazur (accessed Dec. 27, 2020).

[304] M. P. Menon and J. James, “Stability constant for the lanthanide fluoride complexes in aqueous solution at 25°C,” *J. Solution Chem.*, vol. 18, no. 8, pp. 735–742, 1989, doi: 10.1007/BF00651806.

[305] S. K. Ciavatta LI, Ferri DI, Grenthe IN, Salvatore FR, “Studies on metal carbonate equilibria. 3. The lanthanum (III) carbonate complexes in aqueous perchlorate media,” *Acta Chem. Scand. A*, vol. 35, no. 6, 1981.

[306] C. Wong, “Strontium: Benefits, Side Effects, Dosage, and Interactions,” *verywell health*, 2020. https://www.verywellhealth.com/benefits-of-strontium-supplements-89516 (accessed Mar. 08, 2021).

[307] I. Smičiklas *et al.*, “Efficient separation of strontium radionuclides from high-salinity wastewater by zeolite 4A synthesized from Bayer process liquids,” *Sci. Rep.*, vol. 11, no. 1, pp. 1–14, 2021, doi: 10.1038/s41598-021-81255-y.

[308] K. O. Adebowale, I. E. Unuabonah, and B. I. Olu-Owolabi, “Adsorption of some heavy metal ions on sulfate- and phosphate-modified kaolin,” *Appl. Clay Sci.*, vol. 29, no. 2, pp. 145–148, 2005, doi: 10.1016/j.clay.2004.10.003.

[309] B. Jablońska, M. Busch, A. V. Kityk, and P. Huber, “Natural and chemically modified post-mining clays-structural and surface properties and preliminary tests on copper sorption,” *Minerals*, vol. 9, no. 11, pp. 1–20, 2019, doi: 10.3390/min9110704.

[310] S. S. Al-Shahrani, “Treatment of wastewater contaminated with cobalt using Saudi activated bentonite,” *Alexandria Eng. J.*, vol. 53, no. 1, pp. 205–211, 2014, doi: 10.1016/j.aej.2013.10.006.

[311] S. A. Al-Jlil, “Adsorption of cobalt ions from waste water on activated Saudi clays,” *Appl. Water Sci.*, vol. 7, no. 1, pp. 383–391, 2017, doi: 10.1007/s13201-014-0253-z.